ISSN 2525-2461

Vietnam Journal of Science, Technology and Engineering

DECEMBER 2019 • VOL.61 NUMBER 4

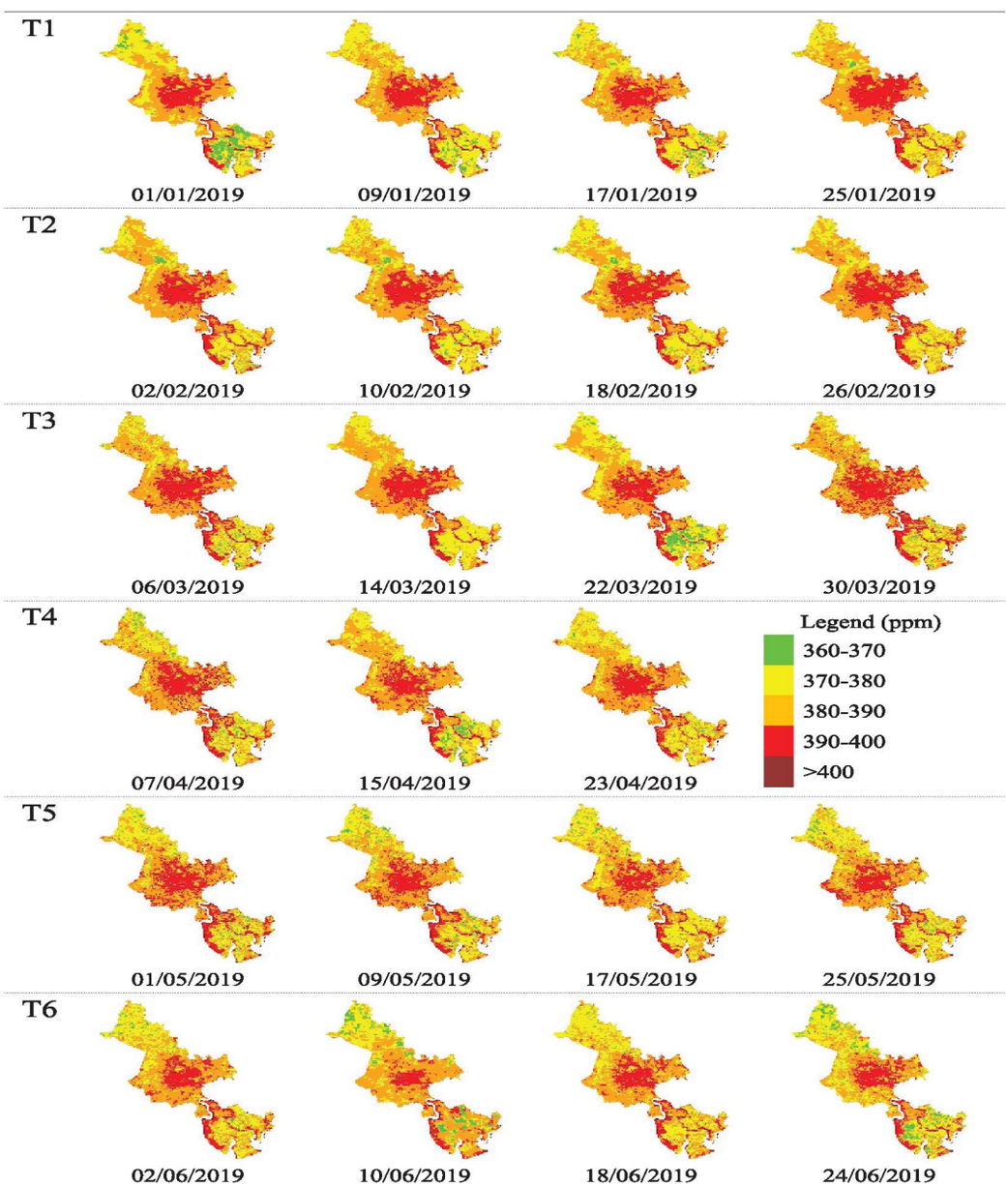

Remote sensing technology-based estimation of atmospheric CO_2 concentration to support efforts to reduce greenhouse gas emissions

Vietnam Journal of Science, Technology and Engineering (VJSTE) **is a quarterly double-blind peer-reviewed academic journal. VJSTE publishes research articles and review articles in all areas of science, technology and engineering with the focus on the life sciences and environmental sciences including the following topics:**

- **Agriculture**
- **Medicine**
- **Pharmacology**
- **Biology**
- **Biotechnology**
- **Ecology**
- **Climatology.**

CLASSIFICATION SCHEME

1. **Mathematics and Computer Science**
   - 1.1. Mathematics
   - 1.2. Computer Science
   - 1.3. Computational Science
2. **Physical Sciences**
   - 2.1. Physics
   - 2.2. Chemistry
   - 2.3. Engineering
3. **Life Sciences**
   - 3.1. Agriculture
   - 3.2. Medicine
   - 3.3. Pharmacology
   - 3.4. Biology
   - 3.5. Biotechnology
4. **Geosciences**
   - 4.1. Geography
   - 4.2. Geology
   - 4.3. Geophysics
   - 4.4. Oceanography
5. **Environmental Sciences**
   - 5.1. Ecology
   - 5.2. Climatology

CONTENTS

DECEMBER 2019 • VOL.61 NUMBER 4

22

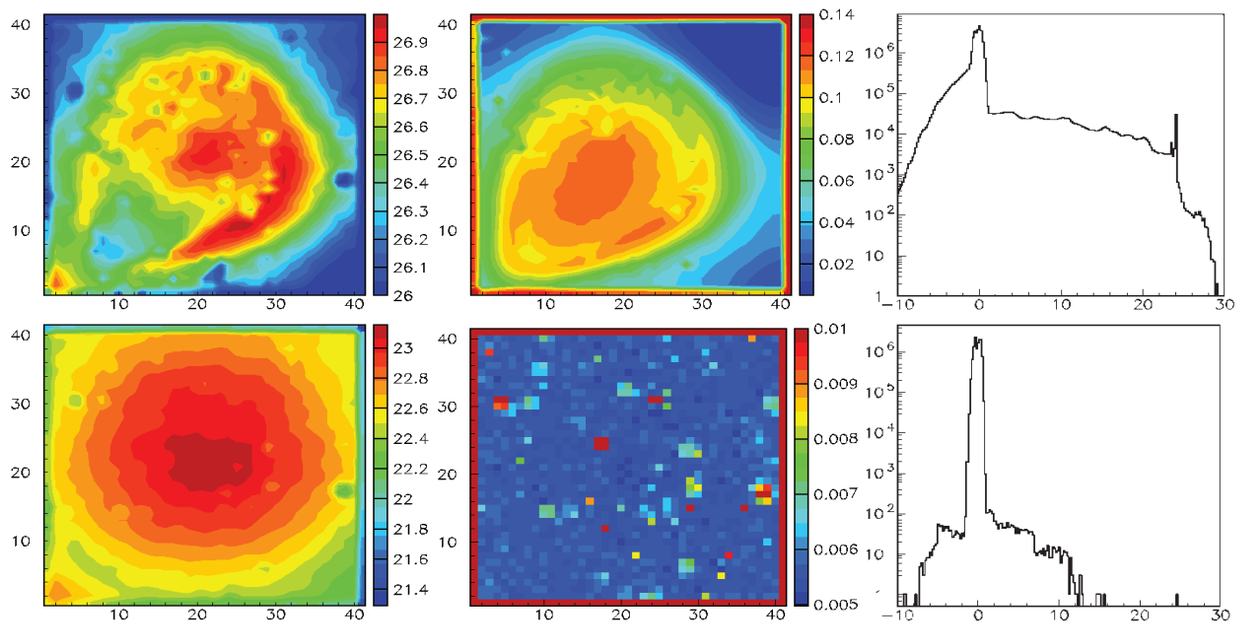

MATHEMATICS AND COMPUTER SCIENCE

PHYSICAL SCIENCES

LIFE SCIENCES

CONTENTS

DECEMBER 2019 • VOL.61 NUMBER 4

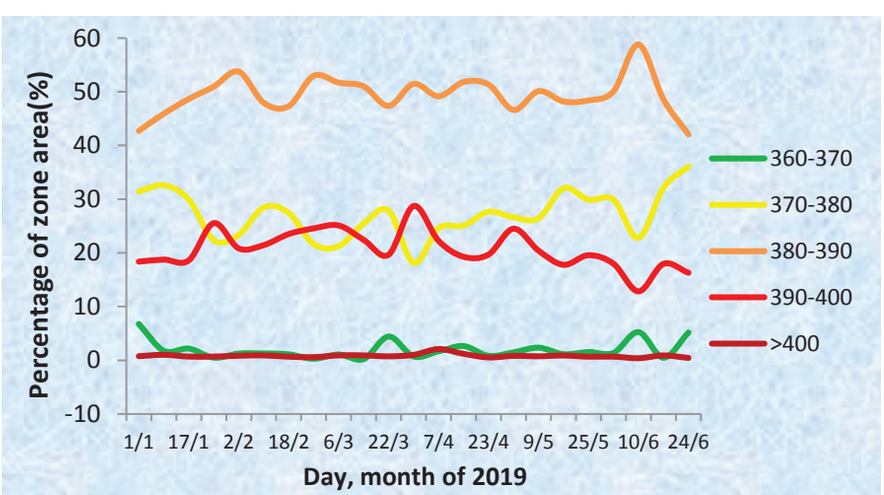

Doi: 10.31276/VJSTE.61(4).03-08

Finite-difference method for the Gamma equation on non-uniform grids

Le Minh Hieu[1*], Truong Thi Hieu Hanh[1], Dang Ngoc Hoang Thanh[2]

[1]*University of Economics, The University of Danang*
[2]*Hue College of Industry*

Received 1 August 2019; accepted 11 November 2019

Abstract:

We propose a new monotone finite-difference scheme for the second-order local approximation on a non-uniform grid that approximates the Dirichlet initial boundary value problem (IBVP) for the quasi-linear convection-diffusion equation with unbounded nonlinearity, namely, for the Gamma equation obtained by transformation of the nonlinear Black-Scholes equation into a quasilinear parabolic equation. Using the difference maximum principle, a two-sided estimate and an a priori estimate in the *C*-norm are obtained for the solution of the difference schemes that approximate this equation.

Keywords: **Gamma equation, maximum principle, monotone finite-difference scheme, non-uniform grid, quasi-linear parabolic equation, scientific computing, two-side estimates.**

Classification number: **1.1**

Introduction

In the theory of difference schemes [1-3], the maximum principle is used to study the stability and convergence of a difference solution in the uniform norm. Computational methods that satisfy the maximum principle are usually called monotone [1, 2]. The monotone schemes play an critical role in computational practice. They make it possible to obtain a numerical solution without oscillations even in the case of non-smooth solutions [4].

When constructing monotone difference schemes, it is desirable to preserve the second order approximation with respect to the spatial variable. Such schemes are constructed for parabolic and hyperbolic equations in the presence of lower derivatives. For example, a nonconservative scheme of second order approximation for linear parabolic equations of general form on uniform grids is given in [1, 2]. When solving two-dimensional partial differential equations in the free domain, we need to construct a difference scheme on a non-uniform grid. We must first confirm that a non-uniform grid is more general than a uniform grid. While one can easily convert a non-uniform grid to uniform grid, the inverse transformation is not so straightforward, and it cannot preserve the conservation properties [5]. For the nonlinear Black-Scholes equation, it is helpful to implement the grid to the payoff of the option, because the price of an option may be more sensitive in a precise area [6]. In this case, the uniform grid is not appropriate. In the case of non-uniform grids for equations in mathematical physics with variable coefficients without lower derivatives, a scheme was obtained in [7] for which the conditions of the maximum principle are fulfilled without relations on the coefficients and parameters of the grid (unconditional monotonicity). In [8], the unconditionally monotone and economical schemes of second order approximation were constructed on a non-uniform grid for non-stationary multidimensional convection-diffusion problems.

In the present work, the previously obtained results are

*Corresponding author: Email: hieulm@due.edu.vn

generalized to the construction of monotone difference schemes of second-order local approximation on non-uniform spatial grids for the Gamma equation for the second derivative of the option price in financial mathematics [9, 10]. The construction of such schemes is based on the appropriate choice of the perturbed coefficient, similar to [1, 2, 8]. Using the difference maximum principle, two-sided and a priori estimates are obtained in the normal C for solving difference schemes that approximate the above equation.

Problem setting and two-sided estimate of the exact solution

We consider the following quasilinear parabolic equation, which is called the Gamma equation [9, 10]:

$$\frac{\partial u}{\partial t} = \frac{\partial^2 \beta(u)}{\partial x^2} + \frac{\partial \beta(u)}{\partial x} + c\frac{\partial u}{\partial x}, \quad u = u(x,t), \quad 0 < t \leqslant T, \quad x \in \mathbb{R}, \quad c - const, \quad (1)$$

$$u(-\infty, t) = u(+\infty, t) = 0, \quad u(x,0) = u_0(x). \quad (2)$$

According to the studies in [9, 10], Eqs. (1)-(2) are obtained by transforming the nonlinear Black-Scholes equation for V(S,τ) such that

$$V_\tau + 0.5\sigma^2(t,S,V_{SS})S^2V_{SS} + (c-q)SV_{SS} - cV = 0, \quad 0 \leqslant S < \infty, \quad 0 \leqslant \tau \leqslant T. \quad (3)$$

The present paper will focus on some models related to nonlinear Black-Scholes equations for the European option whose volatility relies upon various factors like the stock price, the option price, the time, as well as their derivatives, due to the presence of transaction cost. The option's behaviour would be disclosed by a higher derivative of its price, which is mentioned as the Greeks in the financial literature. Reliable numerical methods are not only useful for providing a good approximation for the pricing option, but they are also essential for its derivatives because of the relevance of the Greeks to quantitative analysis.

For the case of European call options [10], V(S,τ) is a solution of Eq. (3) with q=0 and 0⩽S<∞, 0⩽τ⩽T. The initial condition and boundary conditions of the problem in Eq. (3) will be

$$V(S,T) = \max\{0, S-E\}, \quad 0 \leqslant S < \infty, \quad E > 0,$$
$$V(0,\tau) = 0, \quad 0 \leqslant \tau \leqslant T,$$
$$V(S,\tau) = S - Ee^{-c(T-\tau)}, \quad S \to \infty.$$

Note that σ is a parameter that depends on each concrete model, for example, $\sigma^2 = \sigma_{JS}^2$ (the Jandacka-Sevcovic model [9]) or $\sigma^2 = \sigma_F^2$ (the Frey model [11]), which can be written, respectively, as

$$\sigma_{JS}^2 = \sigma_0^2\left(1 + \mu(SV_{SS})^{\frac{1}{3}}\right), \quad \sigma_F^2 = \frac{\sigma_0^2}{1 - \rho SV_{SS}},$$

where $\mu = 3(C^2M/(2\pi))^{1/3}$, σ_0 is the volatility of the underlying asset, $M \geq 0$ is the transaction cost measure, $C \geq 0$ is the risk premium measure, and $\rho \geq 0$ is a parameter measuring the market liquidity. Using the change of independent variables $x = \ln(S/E)$, where $x \in \mathbb{R}$, $t = T-\tau$, $t \in (0, T)$ and substituting $u(x, t) = SV_{SS}$ in (3) for the two above models, we obtain problem (1)-(2). Then the function $\beta(u)$ and the initial condition $u_0(x)$ for the corresponding models will also become [9, 10]:

$$\beta_{JS} = \frac{\sigma_0^2}{2}\left(1 + \mu(u)^{1/3}\right)u, \quad u_0(x) = \delta(x),$$
$$\beta_F = \frac{\sigma_0^2}{2}\frac{u}{(1-\rho u)^2}, \quad u_0(x) = \delta(x),$$

where $\delta(x)$ is the delta function.

In order to find the approximate solution of problem (1)-(2), we must restrict it to a finite spatial interval $x \in (-L, L)$, where $L > 0$ is a sufficiently large number. Since $S=Ee^x$, we limit the interval $S \in (0, +\infty)$ by the interval $S \in (Ee^{-L}, Ee^L)$. In practical calculations, we can choose $L \approx 1.5$ to include important values of S. Thus, instead of (2), we consider the Gamma equation (1) with Dirichlet boundary conditions at $x = \pm L$ [9], i.e.,

$$u(-L,t) = u(L,t) = 0, \quad u(x,0) = u_0(x). \quad (4)$$

Let $u(x, t)$ be a solution of problem (1)-(2), and let $\overline{D}_u = [m_1, m_2]$ be a segment containing a set of its values, where $m_1 \leqslant u(x, t) \leqslant m_2$. If the function $\beta(u) \in C^3(\overline{D}_u)$ for $u \in \overline{D}_u$ is sufficiently smooth, then Eq. (1) can be written as

$$\frac{\partial u}{\partial t} = \frac{\partial}{\partial x}\left(k(u)\frac{\partial u}{\partial x}\right) + r(u)\frac{\partial u}{\partial x}, \quad (5)$$

with coefficients

$$k(u) = \beta'(u), \quad r(u) = k(u) + c. \quad (6)$$

We assume that the parabolicity condition of equation (5) on the solution [12] is satisfied such that

$$0 < k_1 \leqslant k(u) \leqslant k_2, \quad \forall u \in \overline{D}_u, \quad (7)$$

where k_1, k_2 are constants chosen based on each model, and

$$\overline{D}_u = \{u(x,t): \ m_1 \leqslant u(x,t) \leqslant m_2, \ (x,t) \in \overline{Q}_T\}.$$
$$\overline{Q}_T = \{(x,t): \ -L \leqslant x \leqslant L, \ 0 \leqslant t \leqslant T\}.$$

We assume in what follows that there exists a unique solution for problem (1)-(2) and all the coefficients in Eq. (5). We further assume the desired function to have continuous bounded derivatives of the required order as the presentation proceeds.

Using the technique from [13], we prove two-sided estimates for the exact solution of problem (1)-(2).

Theorem 1: let condition (7) be satisfied. Then, for the solution $u(x, t)$ of the problem (1)-(2), the following two-sided estimates are true:

$$m_1 = \min\left\{0, e^T \min_{-L\leqslant x\leqslant L} u_0(x)\right\} \leqslant u(x,t) \leqslant \max\left\{0, e^T \max_{-L\leqslant x\leqslant L} u_0(x)\right\} = m_2 \quad (8)$$

Proof: to prove (8), we make a transformation of the function $u(x, t)$ to the new function $v(x, t)$ associated with the equality

$$u(x,t) = v(x,t)e^{\lambda t},$$

where λ is an arbitrary number. The function $v(x, t)$ satisfies the equation

$$\frac{\partial v}{\partial t} + \lambda v - k\left(ve^{\lambda t}\right)\frac{\partial^2 v}{\partial x^2} - \frac{\partial k(ve^{\lambda t})}{\partial x}\frac{\partial v}{\partial x} - r\left(ve^{\lambda t}\right)\frac{\partial v}{\partial x} = 0, \quad (9)$$

with initial and boundary conditions

$$v(x,0) = u_0(x), \quad -L \leqslant x \leqslant L, \quad (10)$$

$$v(-L,t) = v(L,t) = 0, \quad t > 0. \quad (11)$$

Let the maximum of the solution, $v(x, t)$, of problem (9)-(11) be reached at some point $(x_0, t_0) \in (-L, L) \times (0, T]$

$$\max_{(x,t)\in Q_T} v(x,t) = v(x_0,t_0),$$

moreover, at the point (x_0, t_0), Eq. (9) and the following relations are satisfied

$$\frac{\partial v(x_0,t_0)}{\partial t} \geqslant 0, \quad \frac{\partial v(x_0,t_0)}{\partial x} = 0,$$
$$\frac{\partial^2 v(x_0,t_0)}{\partial x^2} = \lim_{\Delta x\to 0} \frac{v(x_0-\Delta x,t_0) - 2v(x_0,t_0) + v(x_0+\Delta x,t_0)}{\Delta x^2} \leqslant 0.$$

It follows that $v(x,t) \leqslant v(x_0,t_0) \leqslant 0, \quad \lambda > 0. \quad (12)$

If the maximum in Q_T value $v(x, t)$ is taken at the boundary $\{-L, L\} \times (0, T] \cup [-L, L] \times \{0\}$, then we obtain

$$v(x,t) \leqslant \max_{(x,t)\in Q_T} v(x,t) = \max\left\{0, \max_{-L\leqslant x\leqslant L} u_0(x)\right\}. \quad (13)$$

Thus, in all cases of Eqs. (12)-(13), the following estimate is valid

$$v(x,t) \leqslant \max\left\{0, \max_{-L\leqslant x\leqslant L} u_0(x)\right\},$$

from which it follows

$$u(x,t) \leqslant \max\left\{0, e^T \max_{-L\leqslant x\leqslant L} u_0(x)\right\}, \quad \lambda = 1.$$

The case of the minimum of the solution $u(x, t)$ is proved similarly. Thus, the theorem is proved.

Finite-difference scheme on non-uniform spatial grids

We introduce an arbitrary non-uniform spatial grid

$$\hat{\bar{\omega}} = \hat{\omega}_h \cup \gamma_h, \quad \hat{\omega} = \{x_i = x_{i-1} + h_i, i = 1,2,\ldots,N-1\}, \quad \gamma_h = \{x_0 = -L, x_N = L\},$$

and uniform grid by the time variable

$$\bar{\omega}_\tau = \{t_n = n\tau, \quad n = 0,1,\ldots,N_0, \quad \tau N_0 = T\} = \omega_\tau \cup \{T\}.$$

Taking into account the identity $(ku')' = 0.5((ku)'' + ku'' - k''u)$ and using standard notation [1]

$$h_+ = h_{i+1}, \quad h = h_i, \quad \hbar = (h_+ + h)/2, \quad v = v_i = v(x_i), \quad v_\pm = v_{i\pm1} = v(x_{i\pm1}),$$
$$v_x = (v_+ - v)/h_+, \quad v_{\bar{x}} = (v - v_-)/h, \quad v_{\bar{x}\hat{x}} = (v_x - v_{\bar{x}})/\hbar,$$
$$t = t_n, \quad \hat{t} = t_{n+1}, \quad v = v^n = v(t_n), \quad \hat{v} = v^{n+1} = v(t_{n+1}),$$

we construct a difference scheme for a quasilinear parabolic equation (5) on a non-uniform grid

$$\omega = \hat{\omega}_h \times \omega_\tau,$$
$$y_{t(\beta_1\beta_2)} = \kappa(y)A_1\hat{y} + b^+(y)a_+(y)\hat{y}_x + b^-(y)a(y)\hat{y}_{\bar{x}}, \quad (14)$$
$$y_i^0 = u_0(x_i), \quad y_0^{n+1} = y_N^{n+1} = 0,$$

where

$$v_{(\beta_k\beta_{k+1})} = \beta_k v_+ + (1-\beta_k-\beta_{k+1})v + \beta_{k+1}v_-,$$
$$A_1\hat{y} = 0.5\left[(k(y)\hat{y})_{\bar{x}\hat{x}} + k_{(\beta_1\beta_2)}(y)\hat{y}_{\bar{x}\hat{x}} - k_{\bar{x}\hat{x}}(y)\hat{y}_{(\beta_3\beta_4)}\right],$$
$$\beta_1 = 0.5\left(|\tilde{h}| + \tilde{h}\right)/h_+, \quad \beta_2 = 0.5\left(|\tilde{h}| - \tilde{h}\right)/h, \quad \tilde{h} = (h_+ - h)/3,$$
$$\beta_3 = 0.5\left(\tilde{h}k_{\bar{x}\hat{x}} - |\tilde{h}k_{\bar{x}\hat{x}}|\right)/(h_+k_{\bar{x}\hat{x}}), \quad \beta_4 = -0.5\left(\tilde{h}k_{\bar{x}\hat{x}} + |\tilde{h}k_{\bar{x}\hat{x}}|\right)/(hk_{\bar{x}\hat{x}}),$$
$$b^\pm(y) = \frac{1}{3}\left(\frac{r^\pm}{k}(y_-) + \frac{r^\pm}{k}(y) + \frac{r^\pm}{k}(y_+)\right), \quad r^\pm(y) = 0.5(r(y) \pm |r(y)|),$$
$$\kappa(y) = \frac{1}{1+R(y)}, \quad R(y) = \frac{h_+ + 2h}{6}b^+(y) - \frac{2h_+ + h}{6}b^-(y) \geqslant 0,$$
$$a(y) = 0.5\left(k(y) + k(y_-)\right), \quad a_+(y) = 0.5\left(k(y_+) + k(y)\right).$$

Approximation error: let us prove that the scheme (14) approximates problem (5) under the conditions of Eq. (4) in the second order with respect to the point $\bar{x}_i = x_i + \tilde{h}_i$ (in the case of a uniform grid $\bar{x}_i = x_i$). To do this, we focus on the relationship [7]

$$v_{\bar{x}\hat{x}} - v''(\bar{x}) = O(\hbar^2), \quad (15)$$

$$v_{(\beta_k\beta_{k+1})} - v(\bar{x}) = O(\hbar^2), \quad k \in \{1,3\}, \quad (16)$$

when the condition of variable in space weight factors is fulfilled β_k, β_{k+1},

$$\beta_k h_+ - \beta_{k+1}h = \frac{h_+ - h}{3} = \tilde{h}, \quad k \in \{1,3\}.$$

By virtue of (15)

$$(k(u)\hat{u})_{\bar{x}\hat{x}} - \frac{\partial^2(k(u)u)(\bar{x},\hat{t})}{\partial x^2} = O(\hbar^2+\tau), \quad k_{\bar{x}\hat{x}}(u) - \frac{\partial^2 k(\bar{x})}{\partial x^2} = O(\hbar^2). \quad (17)$$

In view of (16) we obtain

$$k_{(\beta_1\beta_2)}(u) - k(\bar{x}) = O(\hbar^2), \quad (18)$$

$$u_{t(\beta_1\beta_2)} - \frac{\partial u(\bar{x},\hat{t})}{\partial t} = O(\hbar^2+\tau). \quad (19)$$

From (15)-(18), it follows that

$$A_1\hat{u} - \frac{\partial}{\partial x}\left(k(u)\frac{\partial u}{\partial x}\right)(\bar{x},\hat{t}) = O(\hbar^2+\tau). \quad (20)$$

Using the Taylor series expansion

$$u_x = u'^{(\bar{x})} + \frac{h_+ + 2h}{6}u''^{(\bar{x})} + O(\hbar^2), \quad u_{\bar{x}} = u'^{(\bar{x})} - \frac{2h_+ + h}{6}u''^{(\bar{x})} + O(\hbar^2),$$
$$a_+(u) = k(\bar{x}) + \frac{h_+ + 2h}{6}k'(\bar{x}) + O(\hbar^2), \quad a(u) = k(\bar{x}) - \frac{2h_+ + h}{6}k'(\bar{x}) + O(\hbar^2),$$

we conclude that

$$a_+(u)u_x = (ku')(\bar{x}) + \frac{h_+ + 2h}{6}(ku')'(\bar{x}) + O(\hbar^2),$$

$$a(u)u_{\bar{x}} = (ku')(\bar{x}) - \frac{2h_+ + h}{6}(ku')'(\bar{x}) + O(\hbar^2).$$

Since

$$r^+(u) + r^-(u) = r(u),$$

$$b^+(u) + b^-(u) = \frac{1}{3}\left(\frac{r}{k}(u_-) + \frac{r}{k}(u) + \frac{r}{k}(u_+)\right) = \frac{r}{k}(\bar{x}) + O(\hbar^2),$$

then

$$b^+(u)a_+(u)u_x + b^-(u)a(u)u_{\bar{x}} = (ru')(\bar{x}) + R(u)(ku')'(\bar{x}) + O(\hbar^2). \quad (21)$$

Using (21) we get

$$b^+(u)a_+(u)\hat{u}_x + b^-(u)a(u)\hat{u}_{\bar{x}} = \left(r(u)\frac{\partial u}{\partial x}\right)(\bar{x},\hat{t}) + R(u)\frac{\partial}{\partial x}\left(k(u)\frac{\partial u}{\partial x}\right)(\bar{x},\hat{t}) + O(\hbar^2 + \tau). \quad (22)$$

Finally, from (19)–(20), (22) we find out that the approximation error is of second order in space

$$\psi(\bar{x},\hat{t}) = -u_{t(\beta_1\beta_2)} + \kappa(u)A_1\hat{u} + b^+(u)a_+(u)\hat{u}_x + b^-(u)a(u)\hat{u}_{\bar{x}}$$

$$= \frac{R^2(u)}{1+R(u)}\frac{\partial}{\partial x}\left(k(u)\frac{\partial u}{\partial x}\right)(\bar{x},\hat{t}) + O(\hbar^2 + \tau) = O(\hbar^2 + \tau).$$

Therefore, spatial approximation order of the difference scheme (14) is 2 and its temporal approximation order is 1.

Monotonicity, two-sided and a priori estimates

We write the difference scheme (14) in the canonical form [2]

$$A_i^n y_{i-1}^{n+1} - C_i^n y_i^{n+1} + B_i^n y_{i+1}^{n+1} = -F_i^n, i = 1,2,\ldots,N-1, \quad (23)$$

$$y_0^{n+1} = \mu_1(t_{n+1}), \quad y_N^{n+1} = \mu_2(t_{n+1}), \quad (24)$$

with coefficients defined as follows

$$A_i^n = -\beta_{2i} + 0.5\kappa_i^n\tau\left[\left(k_{(\beta_1\beta_2)}(y^n) + k(y_{i-1}^n)\right)/(\hbar_i h_i) - \beta_{4i}k_{\bar{x}\hat{x},i}(y^n)\right] - \tau b_i^-(y^n)a_i^n/h_i,$$

$$B_i^n = -\beta_{1i} + 0.5\kappa_i^n\tau\left[\left(k_{(\beta_1\beta_2)}(y^n) + k(y_{i+1}^n)\right)/(\hbar_i h_{i+1}) - \beta_{3i}k_{\bar{x}\hat{x},i}(y^n)\right] + \tau b_i^+(y^n)a_{i+1}^n/h_{i+1},$$

$$C_i^n = 1 + A_i^n + B_i^n, \quad F_i^n = y_{(\beta_1\beta_2)}^n, \quad \mu_1(t_{n+1}) = \mu_2(t_{n+1}) = 0.$$

The scheme (23)-(24) is monotone if the positivity conditions of the coefficients are satisfied [1], i.e.

$$A_i^n > 0, \quad B_i^n > 0, \quad D_i^n = C_i^n - A_i^n - B_i^n > 0. \quad (25)$$

Base on the maximum principle, similiar to the work of [14], we formulate the following results for the difference schemes (14):

Theorem 2 (Maximum principle): let positivity conditions for the coefficients in Eq. (25) be fulfilled. Then, for the solution of the difference scheme given by Eqs. (23)-(24), the following two-sided estimate is valid:

$$\min\left\{\mu_1^{n+1}, \mu_2^{n+1}, \min_{1\leqslant i\leqslant N-1}\frac{F_i^n}{D_i^n}\right\} \leqslant y_i^{n+1} \leqslant \max\left\{\mu_1^{n+1}, \mu_2^{n+1}, \max_{1\leqslant i\leqslant N-1}\frac{F_i^n}{D_i^n}\right\}, \quad i = \overline{0,N}. \quad (26)$$

Proof: suppose that the maximum of the solution, $y(x)$, of the difference problem (23)-(24) is reached on the boundary point such that

$$y_i^{n+1} \leqslant \max_{0\leqslant i\leqslant N} y_i^{n+1} = \max\{\mu_1^{n+1}, \mu_2^{n+1}\}. \quad (27)$$

If the grid function, $y(x)$, reaches its maximum at an interior grid-point x_{i^*}, $1 \leqslant i^* \leqslant N-1$, then

$$C_{i^*}^n y_{i^*}^{n+1} = A_{i^*}^n y_{i^*-1}^{n+1} + B_{i^*}^n y_{i^*+1}^{n+1} + F_{i^*}^n \leqslant (A_{i^*}^n + B_{i^*}^n)y_{i^*}^{n+1} + F_{i^*}^n.$$

In view of the conditions of the theorem $D_{i^*}^n = C_{i^*}^n - A_{i^*}^n - B_{i^*}^n > 0$, we have

$$y_i^{n+1} \leqslant \max_{0\leqslant i\leqslant N} y_i^{n+1} = y_{i^*}^{n+1} \leqslant \frac{F_{i^*}^n}{D_{i^*}^n} \leqslant \max_{1\leqslant i\leqslant N-1}\frac{F_i^n}{D_i^n}. \quad (28)$$

From Eqs. (27)-(28) we obtain the right-hand side of the estimate in Eq. (26). In a similar way, the lower bound can be proved. The theorem is proved.

Now we need to find a condition such that $y_i^n \in \bar{D}_u$ for all i, n. When $n = 0$, it is obvious that $y_i^0 = u_0(x_i) \in \bar{D}_u$. Assume that, for any arbitrary n, $y_i^n \in \bar{D}_u$, is also true for all i. From this assumption for the case of $\tilde{h} > 0$, $k_{\bar{x}\hat{x}} > 0$, (we do not consider trivial cases of $\tilde{h} = 0$ and $k_{\bar{x}\hat{x}} = 0$) we obtain the following concrete values of the weights

$$\beta_1 = \tilde{h}/h_+ > 0, \quad \beta_2 = \beta_3 = 0, \quad \beta_4 = -\tilde{h}/h < 0,$$

$$k_{(\beta_1\beta_2)}(y) = \frac{\tilde{h}}{h_+}k(y_+) + \left(1 - \frac{\tilde{h}}{h_+}\right)k(y) = \frac{\tilde{h}}{h_+}k(y_+) + \frac{2h_+ + h}{3h_+}k(y) > 0,$$

$$-\beta_4 k_{\bar{x}\hat{x}}(y) = \frac{\tilde{h}}{h}k_{\bar{x}\hat{x}}(y) > 0.$$

It follows that $A_i^n > 0$. It is easy to show that $B_i^n > 0$ at $\tau \geqslant \left(1 + 0.5\bar{h}c_0\right)\left|h_{i+1}^2 - h_i^2\right|/(6k_1)$, $\bar{h} = \max_{1\leqslant i\leqslant N} h_i$, and and $c_0 = \max_{u\in\bar{D}_u}\frac{|r(u)|}{k(u)}$. In a similar way we can investigate all the other cases.

Therefore, the inequality

$$\tau \geqslant \frac{(1+0.5\bar{h}c_0)\left\|h_+^2 - h^2\right\|_{\bar{C}}}{6k_1}, \quad \bar{h} = \max_{1\leqslant i\leqslant N} h_i, \quad c_0 = \max_{u\in\bar{D}_u}\frac{|r(u)|}{k(u)}, \quad (29)$$

guarantees the fulfilment of the positivity of the coefficients of Eq. (25) (i.e. the difference scheme (14) is monotone). According to Theorem 2 on the basis of the estimate of Eq. (26) for arbitrary $t = t_n \in \omega_\tau$ and all $i = 0,1,\ldots, N$, we have

$$\min\left\{0, \min_{1\leqslant i\leqslant N-1} y_{(\beta_1\beta_2)}^n\right\} \leqslant y_i^{n+1} \leqslant \max\left\{0, \max_{1\leqslant i\leqslant N-1} y_{(\beta_1\beta_2)}^n\right\}. \quad (30)$$

With the help of inequalities $\max\limits_{1\leqslant i\leqslant N-1} y^n_{(\beta_1\beta_2)} \leqslant \max\limits_{1\leqslant i\leqslant N-1} y^n_i$, $\min\limits_{1\leqslant i\leqslant N-1} y^n_i \leqslant \min\limits_{1\leqslant i\leqslant N-1} y^n_{(\beta_1\beta_2)}$ (since variable weight factors β_1, β_2, are non-negative) from Eq. (30) we have

$$\min\left\{0, \min_{0\leqslant i\leqslant N} y^n_i\right\} \leqslant y^{n+1}_i \leqslant \max\left\{0, \max_{0\leqslant i\leqslant N} y^n_i\right\}. \quad (31)$$

Using induction on n, according to Eq. (31) we acquire the two-sided estimate of the difference solution via the input data without assumption of its sign-definiteness

$$m_1 \leqslant \min\left\{0, \min_{-L\leqslant x\leqslant L} u_0(x)\right\} \leqslant y^{n+1}_i \leqslant \max\left\{0, \max_{-L\leqslant x\leqslant L} u_0(x)\right\} \leqslant m_2, \quad i = 0,1,\ldots N. \quad (32)$$

In view of Eq. (32) we conclude that $y^{n+1}_i \in \bar{D}_u$ for all $i = \overline{0,N}$. Therefore, the following theorem is proved.

Theorem 3: let the conditions of Eq. (29) be fulfilled. Then, the finite-difference scheme of Eq. (14) is monotone, and its solution belongs to the value interval of the exact solution $y \in \bar{D}_u$ and the above two-sided estimates of Eq. (32) hold.

With the help of the maximum principle we acquire the a priori estimate of the solution of the difference scheme of Eq. (14) in the C-norm:

Theorem 4: let the condition of Theorem 3 be fulfilled. Then, for the solution of the difference scheme of Eq. (14), the following a priori estimate holds

$$\|y^n\|_{\bar{C}} \leqslant \|u_0\|_{\bar{C}}. \quad (33)$$

Remark 1: note that the maximum and minimum values of the difference solution do not depend on the diffusion coefficient nor the convection coefficient.

Remark 2: the estimates obtained in Eq. (32) are fully consistent with the estimates of the exact solution of the differential problem given by Eq. (8).

Remark 3: if the grid is uniform in space ($h_+ = h$), then the scheme given by Eq. (14) is transformed into the well-known purely implicit scheme:

$$y_t = \kappa(y)(a(y)\hat{y}_{\bar{x}})_x + b^+(y)a_+(y)\hat{y}_x + b^-(y)a(y)\hat{y}_{\bar{x}},$$

for which the a priori estimates of Eqs. (32)-(33) have already been fulfilled without the restrictions of Eq. (29) on the relation between the grid steps (unconditional monotonicity). Here:

$$\kappa(y) = \left(1 + R(y)\right)^{-1}, \quad R(y) = 0.5h|r(y)|/k(y),$$
$$a(y) = 0.5[k(y) + k(y_-)], \quad b^{\pm}(y) = (r^{\pm}/k)(y).$$

Numerical implementation

Because the Gamma equation has no exact solutions (only analytical solutions), to assess the efficiency of the proposed difference scheme and to maintain the equality of the Gamma equation, we must add a residual term $f(x, t)$ to the right-hand side of Eq. (5). We consider Eq. (5) in the form

$$\frac{\partial u}{\partial t} = \frac{\partial}{\partial x}\left(k(u)\frac{\partial u}{\partial x}\right) + r(u)\frac{\partial u}{\partial x} + f(x,t), \quad (34)$$

with the boundary conditions:

$$u(-\pi,t) = u(\pi,t) = 0, \quad u(x,0) = u_0(x), \quad (35)$$

and input data:

$$k(u) = u^2 + 1, \quad r(u) = \sqrt{u+4}, \quad u = u(x,t), \quad x \in [-\pi,\pi], \quad T = 0.5,$$
$$f(x,t) = \frac{1}{4}e^t\left((8+e^{2t})sin(x) - 4cos(x)\sqrt{e^t sin(x)} - 3e^{2t}sin(3x)\right), u_0(x) = sin(x),$$

and suppose that an exact solution is $u(x, t) = e^t sin(x)$.

Obviously, we have $-e^{0.5} \leq u(x, t) \leq e^{0.5}$, i.e. $m_1 = -e^{0.5}$, $m_2 = e^{0.5}$. Then for all $u \in [-e^{0.5}, e^{0.5}]$ we obtain $0 < 1 \leq k(u) \leq e + 1$, and according to the condition of Eq. (7), Eq. (34) is parabolic (Fig. 1).

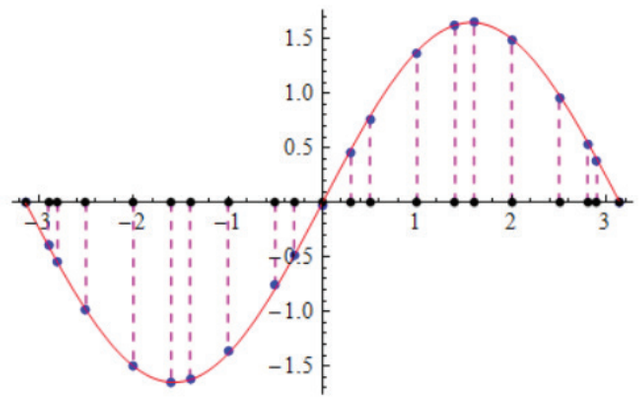

Fig. 1. Exact (red line) and approximate (blue nodes) solutions of the problem (34), (35) at $T = 0.5$ with $\tau = 0.01$.

In Table 1 we show the non-uniform spatial nodes and the error of the method in maximum norm

$$\|z\|_C = \|y - u\|_C = \max_{(x,t)\in\omega} |y(x,t) - u(x,t)|$$

for the difference scheme given in Eq. (14). The approximate solution of the problem given by Eqs. (34), (35) at t = 0.5, obtained by the difference scheme in Eq. (14), is shown on Fig. 1.

The computational experiment illustrates the higher accuracy of the new scheme on coarse space grids. For the scheme of Eq. (14) the accuracy of order $O(h^2+\tau)$ is reached on the coarse grids.

Table 1. Numerical results on non-uniform spatial grids for problem (34), (35) at $T = 0.5$ with $\tau = 0.01$.

x_i	$-\pi$	-2.9	-2.8	-2.5	-2	-1.6	-1.4	-1	-0.5	-0.3	
$\|\|Z\|\|c$	0	0.009	0.009	0.009	0.001	0.003	0.0004	0.01	0.02	0.01	
x_i	0	0.3	0.5	1	1.4	1.6	2	2.5	2.8	2.9	π
$\|\|Z\|\|c$	0.02	0.03	0.02	0.01	0.001	0.0001	0.008	0.02	0.02	0.015	0

Conclusions

Problems requiring a solution to nonlinear partial differential equations arise in elasticity theory, financial mathematics, physical chemistry, biology, and other fields. The demand to solve these problems has caused rapid development of numerical methods for their solution. By virtue of its comparative simplicity and versatility, the finite difference method is often used.

In the present paper we proposed a new second-order in a space monotone difference scheme on a non-uniform grid that approximates the Dirichlet IBVP for a quasi-linear parabolic equation, namely, the one-dimensional non-linear Gamma equation in financial mathematics. Under several constraints on the grid, two-side estimates of the solution of the scheme are established. Note that the proven two-side estimates of difference solution are fully consistent with estimates of the solution of the differential problem. Moreover, the maximum and minimum values of the difference solution are not dependent on the diffusion and convection coefficients.

ACKNOWLEDGEMENTS

This work was supported by University of Economics, The University of Danang (Project T2019-04-43).

The authors declare that there is no conflict of interest regarding the publication of this article.

REFERENCES

[1] A.A. Samarskii (2001), *The theory of difference schemes*, Marcel Dekker Inc., New York, Doi: 10.1201/9780203908518.

[2] A.A. Samarskii and A. Gulin (1989), *Numerical methods*, Nauka, Moscow (in Russian).

[3] P. Matus, D. Poliakov, and Le Minh Hieu (2018), "On the consistent two-side estimates for the solutions of quasilinear convection-diffusion equations and their approximations on non-uniform grids", *J. Comp. and Appl. Math.*, **340**, pp.571-581, Doi: 10.1016/j.cam.2017.09.020.

[4] P.P. Matus, V.T.K. Tuyen, and F.J. Gaspar (2014), "Monotone difference schemes for linear parabolic equations with mixed boundary conditions", *Dokl. Natl. Acad. Sci. Belarus*, **58(5)**, pp.18-22 (in Russian).

[5] O.V. Vasilyev (2000), "High order finite difference schemes on non-uniform meshed with good conservation properties", *Journal of Computational Physics*, **157(2)**, pp.746-761, Doi: 10.1006/jcph.1999.6398.

[6] J. Bodeau, G. Riboulet, and T. Roncalli (2000), "Non-uniform grids for PDE in finance", *SSRN Electronic Journal*, Doi: 10.2139/ssrn.1031941.

[7] A.A. Samarskii, V.I. Mazhukin, D.A. Malafei, and P.P. Matus (2001), "Difference schemes on irregular grids for equations of mathematical physics with variable coefficients", *Computational Mathematics and Mathematical Physics*, **41(3)**, pp.407-419 (in Russian).

[8] D. Malafei (2000), "Economical monotone difference schemes for multidimensional convection-diffusion problems on non-uniform grids", *Dokl. Natl. Acad. Sci. Belarus*, **44(4)**, pp.21-25 (in Russian).

[9] M. Jandacka and D. Sevcovic (2005), "On the risk-adjusted pricing-methodology-based valuation of vanilla options and explanation of the volatility smile", *J. of Appl. Math.*, **2005(3)**, pp.235-258, Doi: 10.1155/JAM.2005.235.

[10] M.N. Koleva and L.G. Vulkov (2013), "A second-order positivity preserving numerical method for Gamma equation", *Appl. Math. and Comput.*, **220**, pp.722-734, Doi: 10.1016/j.amc.2013.06.082.

[11] R. Frey (2000), "Market illiquidity as a source of model risk in dynamic hedging", *Model Risk*, pp.125-136, Risk Publications, London.

[12] A. Friedman (1964), *Partial differential equations of parabolic type*, Prentice-Hall Inc., Englewood Cliffs.

[13] O.A. Ladyzhenskaya, V.A. Solonnikov, and N.N. Uraltseva (1967), *Lineinye i kvazilineinye uravneniya parabolicheskogo tipa (Linear and quasilinear equations of parabolic type)*, Nauka, Moscow (in Russian).

[14] P. Matus, Le Minh Hieu, and L. Vulkov (2017), "Analysis of second order difference schemes on non-uniform grids for quasilinear parabolic equations", *J. Comp. and Appl. Math.*, **310**, pp.186-199, Doi: 10.1016/j.cam.2016.04.006.

Doi: 10.31276/VJSTE.61(4).09-13

New insights into the formation of amorphous molybdenum sulfide from a tetrathiomolybdate precursor

Anh D. Nguyen[1, 2*], Phuong T. Pham[2], An T. Dam[2], Phong D. Tran[2*]

[1]*Graduate University of Science and Technology, Vietnam Academy of Science and Technology*
[2]*University of Science and Technology of Hanoi, Vietnam Academy of Science and Technology*

Received 30 August 2019; accepted 7 November 2019

Abstract:

Amorphous molybdenum sulfide (MoS_x) is an attractive Pt-free catalyst for the hydrogen evolution reaction (HER) in both neutral and acidic pH electrolytes. Among the available approaches for the preparation of MoS_x, the electrochemical oxidation and reduction of a tetrathiomolybdate salt ($[MoS_4]^{2-}$) represents the most convenient. Herein we describe new insights onto the electrochemical oxidation of $[MoS_4]^{2-}$ to grow MoS_x thin films by employing an advanced technique called electrochemical quartz crystal microbalance (EQCM). These new findings enrich the current understanding of the structure, growth mechanism, redox property and catalytic operation of the MoS_x material.

One sentence summary: a new mechanism for growth of amorphous molybdenum sulfide thin films via the electrochemical polymerization of $[MoS_4]^{2-}$ is discussed.

Keywords: **EQCM, MoS_x formation, $[MoS_4]^{2-}$, $[Mo_3S_{11}]$ building block.**

Classification number: **2.1**

Introduction

Amorphous molybdenum sulfide, usually denoted as MoS_x, represents one of the most promising catalysts under investigation as the replacement for the Pt catalyst in the hydrogen evolution reaction (HER) of water. It shows excellent catalytic activity in both acidic and neutral pH electrolytes [1]. Its preparation can be achieved by different approaches like reactive magnetron sputtering [2], acidification of a $[MoS_4]^{2-}$ solution, electrochemical oxidation or electrochemical reduction of a deposition solution composed of $[MoS_4]^{2-}$ [3, 4], $[Mo_2S_{12}]^{2-}$ [5], or $[Mo_3S_{13}]^{2-}$ [5, 6]. In our previous work, we have demonstrated that MoS_x is a coordination polymer made of discrete $[Mo_3S_{13}]^{2-}$ building block clusters [4]. In the ideal circumstance where no structural defects like Mo-□ site are present within the polymeric structure of MoS_x, it could be described as a $(Mo_3S_{11})_n$ polymer. Treating MoS_x thin films or nanoparticles in an alkaline solution causes depolymerization that generates $[Mo_3S_{13}]^{2-}$ clusters that could be easily isolated, *e.g.* by adding Et_4N^+ cation [4]. Inversely, we recently demonstrated that electrochemical oxidation of the $[Mo_3S_{13}]^{2-}$ cluster *via* a two-electron process generated the MoS_x material [6]. A key elemental step was proposed to be the electrochemical elimination of the terminal disulfide ligand within the $[Mo_3S_{13}]^{2-}$ as the source of Mo-□ defects that subsequently served as anchoring sites for other $[Mo_3S_{13}]^{2-}$ clusters, thus driving polymerization. This means that during the growth of MoS_x materials, the $[Mo_3S_7]$ core skeleton is conserved.

$$[MoS_4]^{2-} \rightarrow MoS_3 + 1/8\ S_8 + 2e^- \qquad (eq.\ 1)$$

We then aim to revisit the polymerization of $[MoS_4]^{2-}$, namely a mononuclear species, into MoS_x which is made of $[Mo_3S_{13}]^{2-}$ building blocks. We note that the first discussion of the $[MoS_4]^{2-}$ to MoS_x polymerization mechanism was reported by Hu and co-workers [3, 7]. In that work, a rather simple reaction (*eq. 1*) was proposed based on the establishment of a relationship between the mass loss of the $[MoS_4]^{2-}$ precursor and the net charge consumed during the oxidation process. Furthermore, the amorphous molybdenum sulfide was described as MoS_3 which was not appropriate, as recent analysis has revealed the S: Mo atomic ratio within MoS_x should be closer to 4.0, e.g. ca. 3.7, rather than to 3.0 [4, 8]. We hypothesize the actual mechanism could be much more complicated than what has been described. In any case, the fundamental question of how the $[MoS_4]^{2-}$ mononuclear species can assemble into a

* *Corresponding authors: Email: nguyen-duc.anh@usth.edu.vn; tran-dinh.phong@usth.edu.vn*

$[Mo_3S_7]$ cluster within the MoS_x structure remains unclear.

Herein, employing an Electrochemical Quartz Crystal Microbalance (EQCM) analysis we show that the electrochemical oxidation of $[MoS_4]^{2-}$ precursor into MoS_x thin film occurs *via* a 10-electron process. Spectroscopic analyses clearly confirm the creation of the $[Mo_3S_{13}]^{2-}$ building block within MoS_x. A mechanism describing how $[MoS_4]^{2-}$ fragments assemble into the $(Mo_3S_{11})_n$ polymer, namely the MoS_x, is discussed.

Materials and methods

Materials

Ammonium tetrathiomolybdate ($(NH_4)_2[MoS_4]$) 99% and fluorine-doped tin oxide (FTO) coated glass were purchased from Sigma-Aldrich while Sulfuric acid (H_2SO_4), K_2HPO_4, KH_2PO_4, $K_3[Fe(CN)_6]$ and $K_4[Fe(CN)_6]$ were purchased from Xilong (99% purity). These chemicals were used as received without any further purification.

Electrochemical deposition and analyses

Electrochemical deposition and measurements were performed using a Biologic SP-50 potentiostat in a conventional three-electrode system. The working electrode was made of an FTO substrate for deposition of the MoS_x film which was then used for morphology and chemical composition characterization. For electrode mass change analysis, a AT-cut 5 MHz Au/Ti quartz QCM (S 1.31 cm^2) working electrode was used. A Pt plate was used as the counter electrode whereas the reference electrode was an Ag/AgCl (1 M KCl) electrode. All the potentials were reported on a normal hydrogen electrode (NHE).

The electrolyte solution consisted of 1 mM $(NH_4)_2[MoS_4]$ in a pH 7 phosphate buffer solution. Prior to use, the solution was filtered to remove any precipitates and then degassed by an N_2 flux for 30 min.

Cyclic voltammograms were recorded on the Au QCM electrode immersed in the electrolyte solution. The potential was polarized from 0 V towards 1.4 V then backwards to -1 V vs. NHE with a potential scan rate of 5 mV/s. The deposition of MoS_x was conducted using the chronoamperometric technique wherein the Au QCM electrodes were held at 0.33, 0.36 or 0.41 V vs. NHE. The total amount of charge passed through the working electrode for the MoS_x deposition was set at 10 mC/cm^2.

Bulk electrolysis

The number of electrons used per cluster during the oxidative deposition was determined using bulk electrolysis (chronoamperometric technique as aforementioned). During the electrolysis, the evolution of electrode mass was recorded. Because of the high sensitivity of QCM, a potential (e.g. 0.33 V) was only applied to deposit amorphous MoS_x on the electrode when the recorded mass was stable. We define a stable mass as changes less than 10^{-2} $\mu g/cm^2$ or lower. The deposition time was set for 500 s per cycle. The mass change was recorded in several repeated cycles.

Spectroscopic and microscopic characterization

The surface morphology of the MoS_x thin film was characterized by using a field emission scanning electron microscopy (FE-SEM, Hitachi S4800, Japan). Raman spectra were collected using a LabRAM HR Evolution Raman Microscope (Horiba) with the 532 nm green laser excitation. XPS analysis was conducted on a ULVAC PHI 500 (Versa Probe II) equipped with a monochromatic Al Kα (1486.6 eV) X-ray source.

Results and discussion

Electrochemical property of a $[MoS_4]^{2-}$ solution

We first re-investigated the electrochemical property of the $[MoS_4]^{2-}$ from the perspective of identification of suitable conditions for the electrochemical polymerization effect that generates MoS_x. Fig. 1 shows the first three consecutive cyclic voltammograms recorded on a clean FTO electrode immersed in a 1.0 mM $[MoS_4]^{2-}$ solution in pH 7 phosphate buffer. The potential polarization direction was set from the open circuit voltage towards the anodic potential with a potential scan rate of 50 mV/s. In the first cycle, two oxidation events are observed at potentials of 0 V and 0.95 V, while a reduction event is observed at -0.8 V vs. NHE (Fig. 1, blue trace). In the second and subsequent scans, the 0 V oxidation and the -0.8 V reduction events are unchanged. However, the 0.95 V oxidation event is no longer observable, and a new oxidation event at 0.41 V emerges (Fig. 1, red and green traces). Thus, to investigate the electrochemical polymerization of $[MoS_4]^{2-}$, we chose three potentials for chronoamperometry (CA) deposition, namely 0.33, 0.36 and 0.41 V vs. NHE, which corresponds to the foot-wave potential, half-wave potential and the peak potential of the latter oxidation event, respectively.

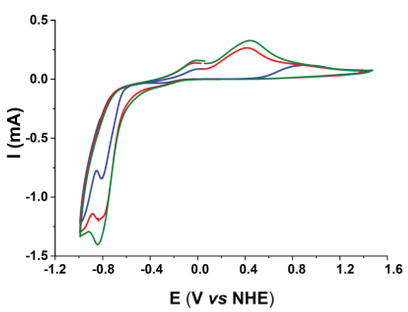

Fig. 1. Subsequent cyclic voltammograms (1st scan: blue trace; 2nd scan: red trace and 3rd scan: green trace) recorded on an FTO electrode immersed in a 1.0 mM $(NH_4)_2[MoS_4]$ solution in pH 7 phosphate buffer. The potential scan rate was 5 mV/s towards the anodic scan direction.

Characterization of deposited MoS_x films

In the same 1.0 mM $[MoS_4]^{2-}$ solution in pH 7 phosphate buffer, a clean FTO electrode was held at 0.33, 0.36 or 0.41 V vs. NHE for 2 hours to deposit brown-coloured MoS_x thin films.

Figure 2 shows the SEM images of these films. It can be seen that the obtained MoS_x films consist of clumps arranged close together in different shapes and sizes. The variation in clump shape and size are likely due to the different in the grown rate of MoS_x at different applied potential. There is no difference of morphologies observed between films prepared at various anodic potentials.

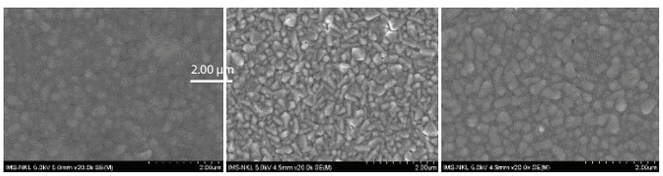

(A) (B) (C)

Fig. 2. SEM images of MoS_x grown at 0.33 (A), 0.36 (B), and 0.41 V vs. NHE (C).

Raman spectra clearly show all the characteristic features of a MoS_x polymeric thin film with $[Mo_3S_{13}]^{2-}$ building block clusters, as previously reported (Fig. 3) [4]. Vibrations at 284-382 cm^{-1} are assigned to the Mo-S bond, whereas the one at 450 cm^{-1} is attributed to the νMo_3-S_{apical} vibration mode. Vibrations of bridged or shared disulfide $(S\text{-}S)_{br/sh}$ and terminal disulfide $(S\text{-}S)_t$ are observed at 555 and 525 cm^{-1}, respectively.

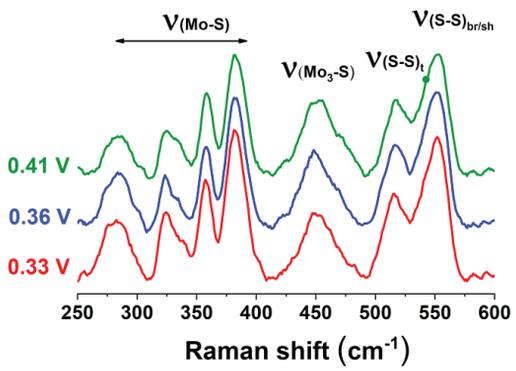

Fig. 3. Raman spectra recorded on the MoS_x films grown on FTO electrode at: 0.33 V (red trace), 0.36 V (blue trace), and 0.41 V vs. NHE (green trace).

In XPS analysis, Mo^{IV} species is characterized by a doublet having $Mo3d_{5/2}$ of 229.38 eV. The doublet at higher binding energy, $Mo3d_{5/2}$ of 230.30 eV, is attributed to Mo^{V} species, *e.g.* due to the presence of Mo^{V}=O defects. The presence of some Mo^{VI} species, like excess $[MoS_4]^{2-}$ or MoO_3, within the deposit is also likely as a doublet having $Mo3d_{5/2}$ of 232.44 eV is observed. The $(S\text{-}S)_{br/sh}$ disulfide ligand and the apical sulfide are characterized by a doublet having $S2p_{3/2}$ of 163.18 eV. While the doublet at $S2p_{3/2}$ of 162.07 eV is assigned to the terminal $(S\text{-}S)_t$ disulfide ligand (Fig. 4). The binding energies of Mo and S from XPS results are in consensus with the reported literatures [4, 6] and proving the obtained materials is amorphous molybdenum sulfide, labeled as MoS_x.

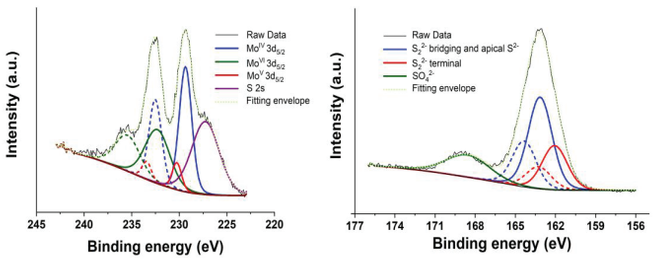

(A) (B)

Fig. 4. (A) Mo- and (B) S- core levels of a MoS_x film grown at 0.36 V vs. NHE. Similar features were recorded for the films grown at 0.33 V and 0.41 V.

These results confirm that at the potentials applied, $[MoS_4]^{2-}$ is electrochemically oxidized, which grows the MoS_x thin film consisting of $[Mo_3S_{13}]^{2-}$ building block clusters. In following section, we employ EQCM analysis to identify the number of electrons involved in each elemental electrochemical oxidation event.

Electrochemical quartz crystal microbalance analysis

A clean Au QCM electrode was first equilibrated in a 1.0 mM $[MoS_4]^{2-}$ solution in a pH 7 phosphate buffer for 30 minutes at the open circuit voltage. Subsequently, an anodic potential of 0.33 V vs. NHE is applied for a period of 500 s. We observed a linear increment of the electrode mass (Fig. 5A) that indicated growth, by electrodeposition, of material on the Au QCM electrode surface. When the applied potential was removed, no mass increment was recorded. This clearly confirmed that the MoS_x deposition is solely driven by the applied oxidation potential. From the mass increment we are able to deduce the amount of MoS_x deposited in moles under the assumption that the MoS_x is a perfect $(Mo_3S_{11})_n$ polymer without any structural defects or impurities. At the same time, the amount of charge involved in the process was recorded. We then plot the number of electrons (in mol) against the amount of Mo_3S_{11} clusters deposited (Fig. 5B). A slope of 9.65 is found. The same value was determined when we repeated the same deposition-relaxation process on the same electrode for several cycles (Figs. 5C, D).

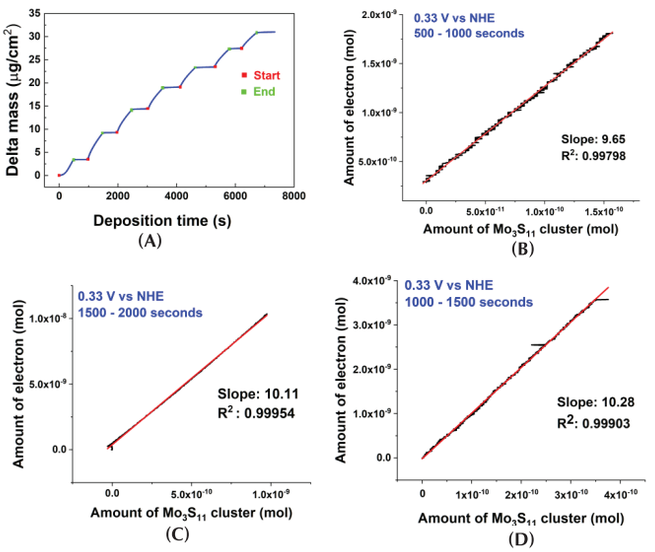

Fig. 5. EQCM analysis conducted on an Au QCM electrode held in a 1 mM $[MoS_4]^{2-}$ solution at 0.33 V vs. NHE. (**A**) evolution of the mass of the electrode as function of deposition time; (**B**, **C**, **D**) plots the electrode mass increment against the amount of electrons involved for different deposition periods.

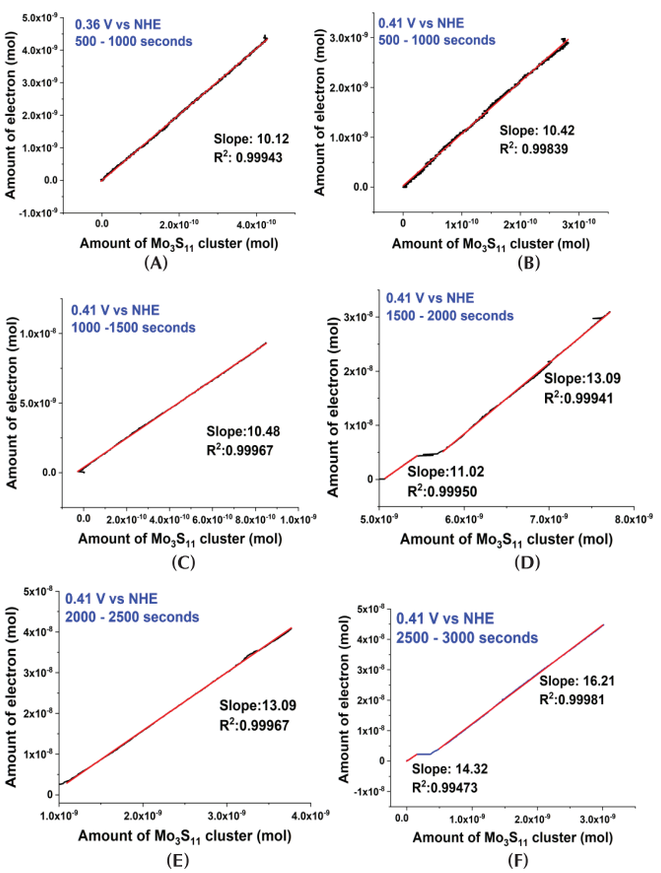

Fig. 6. Plot of electrode mass against the amount of electrons involved. (**A**) MoS_x film grown at 0.36 V and (**B**) 0.41 V vs NHE for a deposition period of 500-1,000 s. (**C**, **D**, **E**, **F**) MoS_x film grown at 0.41 V vs NHE for longer deposition periods.

At a higher applied potential, namely 0.36 V and 0.41 V vs. NHE, we observed the same phenomenon and a similar value of ca. 10 electrons over a (Mo_3S_{11}) cluster was determined (Figs. 6A, B). When the deposited film got thicker, e.g. after longer deposition time, the number of electrons involved was higher to generate the same (Mo_3S_{11}) cluster (Figs. 6C-F). This observation can be explained by the fact that MoS_x is not a good conductor. Thus, a thick layer of MoS_x may inhibit the electron transfer process. A similar phenomenon was also observed for the case of MoS_x films grown via an electrochemical oxidation of $[Mo_3S_{13}]^{2-}$ clusters [6].

Thus, based on the available data, we conclude that the MoS_x thin film is grown from the $[MoS_4]^{2-}$ solution via a 10-electron oxidation process during the early stages of deposition when the MoS_x film is not too thick. In other words, each Mo_3S_{11} unit comprising the MoS_x film is created *via* a 10-electron oxidation. This result is different compared with that reported by Hu, et al. [3, 7] where a 2-electron oxidation process was proposed (*eq. 1*) [3, 7]. The 10-electron oxidation process is given below:

$$3[MoS_4]^{2-} \rightarrow Mo_3S_{11} + 1/8S_8 + 10\ e^- \qquad (eq.\ 2)$$

Proposed mechanism for the growth of MoS_x film

We propose a mechanism for the growth of the $(Mo_3S_{11})_n$ polymer, namely the MoS_x film, *via* the electrochemical oxidation of $[MoS_4]^{2-}$. Our primary focus is on the mechanism behind the construction of a $[Mo_3S_{11}]$ skeleton by assembling three $[MoS_4]^{2-}$ fragment species through a 10-electron oxidation process. Firstly, a $[MoS_4]^{2-}$ molecule adsorbs to the electrode surface and loses 1 electron to create a Au-S covalent bond (Fig. 7A). Two other $[MoS_4]^{2-}$ molecules approach (Fig. 7B) and remove 6 electrons, which create three $(S\text{-}S)^{2-}$ ligands as well as a $Mo_3\text{-}S_{apical}$ mode (Fig. 7C). Actually, each $(S\text{-}S)^{2-}$ is generated from two S^{2-} ligands *via* a two-electron reaction:

$$2S^{2-} \rightarrow (S\text{-}S)^{2-} + 2e^- \qquad (eq.\ 3)$$

$$Mo^{VI} + 2e^- \rightarrow Mo^{IV} \qquad (eq.\ 4)$$

Here, the $[Mo_3S_7]$ skeleton grafted onto the electrode surface via a sulfide covalent bond is readily (Fig. 7D). In this $[Mo_3S_7]$ species, two Mo atoms are bound to two terminal S^{2-} ligands. These S^{2-} ligands could also be oxidized *via* a two-electron reaction, creating the terminal $(S\text{-}S)^{2-}$ ligand. This oxidation can also occur in parallel with the reduction of Mo^{VI} into Mo^{IV} (*eq. 4*). Alternatively, a S^{2-} ligand is oxidized by a two-electron process producing elemental sulfur and leaving a coordination vacancy on the Mo atom (Fig. 7E). Indeed, the presence of an elemental sulfur impurity in the MoS_x film has been discussed elsewhere [9, 10]. This vacancy then acts as an anchoring position to host a new $[MoS_4]^{2-}$ molecule. At this step, a

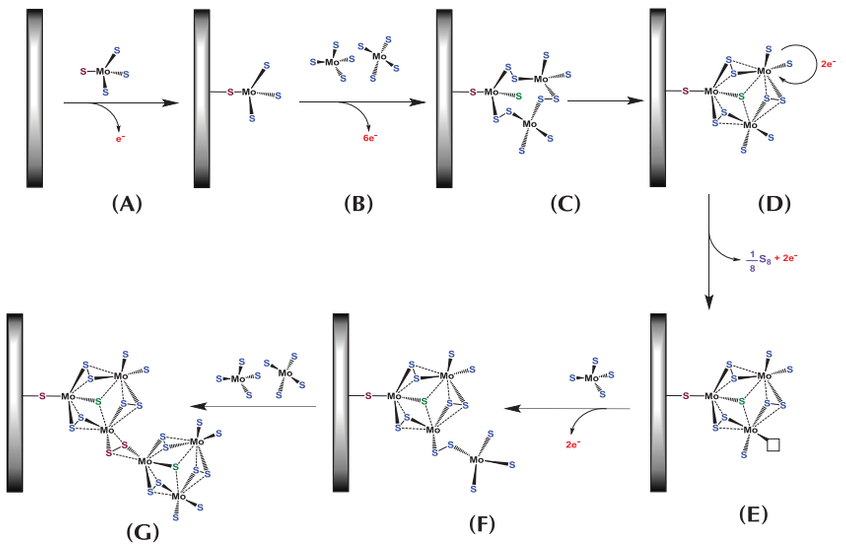

Fig. 7. Proposed mechanism of electro-oxidation synthesis of a-MoS_x from $[MoS_4]^{2-}$ precursor.

new $(S\text{-}S)^{2-}$ ligand is generated after removing two more electrons (Fig. 7F). The newly $[MoS_4]^-$ species grafted on the $[Mo_3S_7]$ cluster now continues its reaction in the same manner as the $[MoS_4]^-$ grafted on the Au electrode described above (Fig. 7G). Through such a reaction sequence, the $(Mo_3S_{11})_n$ polymer is grown on the Au electrode surface via a 10-electron oxidation process as determined experimentally in this work.

Conclusions

To conclude, the electrochemical oxidation of a $[MoS_4]^{2-}$ solution in neutral pH can grow an amorphous molybdenum sulfide (MoS_x) thin film, which is constructed of $[Mo_3S_{13}]^{2-}$ building blocks. Employing an electrochemical quartz crystal microbalance (EQCM) analysis, we revealed that the $[MoS_4]^{2-}$ molecule goes through a 10-electron oxidation process to create the (Mo_3S_{11}) structure unit and subsequently the $(Mo_3S_{11})_n$ polymer. A mechanism has been proposed to describe the elemental steps of such a 10-electron oxidation process. This work enriches the current knowledge of the formation, structure, and attractive redox property of the MoS_x.

ACKNOWLEDGEMENTS

This work is supported by Graduated University of Science and Technology (GUST - VAST) via project GUST. STS.DT 2017 - HH11. We acknowledge Dr. Nguyen Thu Loan and Prof. Ung Thi Dieu Thuy (Institute of Materials Science - VAST) for experimental support.

The authors declare that there is no conflict of interest regarding the publication of this article.

REFERENCES

[1] D.E. López, Z. Lou, N.V. Rees (2019), "Benchmarking the activity, stability, and inherent electrochemistry of amorphous molybdenum sulfide for hydrogen production", *Adv. Energy Mater.*, **9**, 1802614, Doi: 10.1002/aenm.201802614.

[2] F. Xi, P. Bogdanoff, K. Harbauer, P. Plate, C. Höhn, J. Rappich, B. Wang, X. Han, R. van de Krol, S. Fiechter (2019), "Structural transformation identification of sputtered amorphous MoS_x as an efficient hydrogen-evolving catalyst during electrochemical activation", *ACS Catal.*, **93**, 2368, Doi: 10.1021/acscatal.8b04884.

[3] D. Merki, S. Fierro, H. Vrubel, X. Hu (2011), "Amorphous molybdenum sulfide films as catalysts for electrochemical hydrogen production in water", *Chemical Science*, **2(7)**, pp.1262-1267.

[4] Phong. D. Tran, T.V. Tran, M. Orio, S. Torelli, Q.D. Truong, K. Nayuki, Y. Sasaki, S.Y. Chiam, R. Yi, I. Honma, J. Barber, V. Artero (2016), "Coordination polymer structure and revisited hydrogen evolution catalytic mechanism for amorphous molybdenum sulfide", *Nature Materials*, **15**, pp.640-646.

[5] O. Mabayoje, Y. Liu, M. Wang, A. Shoola, A.M. Ebrahim, A.I. Frenkel, C.B. Mullins (2019), "Electrodeposition of MoS_x hydrogen evolution catalysts from sulfur-rich precursors", *ACS Appl. Mater. Interfaces*, **11(36)**, pp.32879-32886, Doi: 10.1021/acsami.9b07277.

[6] Tuan M. Duong, Anh D. Nguyen, Ly T. Le, Loan T. Nguyen, Phong D. Tran (2019), "Insights into the electrochemical polymerization of $[Mo_3S_{13}]^{2-}$ generating amorphous molybdenum sulfide", *Chem. Eur. J.*, **25(60)**, pp.13676-13682.

[7] H. Vrubel, X. Hu (2013), "Growth and activation of an amorphous molybdenum sulfide hydrogen evolving catalyst", *ACS Catalysis*, **3(9)**, pp.2002-2011.

[8] J.D. Benck, Z. Chen, L.Y. Kuritzky, A.J. Forman, T.F. Jaramillo (2012), "Amorphous molybdenum sulfide catalysts for electrochemical hydrogen production: insights into the origin of their catalytic activity", *ACS Catal.*, **2(9)**, pp.1916-1923.

[9] J. Tan. W. Yang, Y. Oh, H. Lee, J. Park, J. Moon (2018), "Controlled electrodeposition of photoelectrochemically active amorphous MoS_x Cocatalyst on Sb_2Se_3 photocathode", *ACS Appl. Mater. Interfaces*, **10(13)**, pp.10898-10908, Doi: 10.1021/acsami.8b00305.

[10] X.J. Chua, M. Pumera (2018), "Molybdenum sulfide electrocatalysis is dramatically influenced by solvents used for its dispersions", *ACS Omega*, **3(10)**, pp.14371-14379.

Doi: 10.31276/VJSTE.61(4).14-28

The 50 cm telescope of Hoa Lac observatory: an introduction

Nguyen Thi Thao[1, 2*], Mai Thuy Dung[1], Pham Vu Loc[1], Nguyen Thi Kim Ha[1], Pham Ngoc Diep[1], and Pierre Darriulat[1]

[1]Department of Astrophysics, Vietnam National Space Center, Vietnam Academy of Science and Technology
[2]Graduate University of Science and Technology, Vietnam Academy of Science and Technology

Received 20 September 2019; accepted 12 November 2019

Abstract:

The Vietnam National Space Center has recently established an observatory in Hoa Lac, near Ha Noi. The observatory is equipped with a 50 cm diameter Ritchey-Chrétien optical telescope. The authors report on first measurements illustrating its performance and demonstrate its excellence as a training tool for university students at bachelor's and master's degree levels.

Keywords: **astronomy, CCD camera, telescope.**

Classification number: **2.1**

1. Description of the telescope

The Hoa Lac observatory (105º 32'' 31'' E, 21º 01' 07'' N, near sea level) of the Vietnam National Space Center (VNSC) was commissioned in June 2018. It hosts a 50 cm (f/8) Ritchey-Chrétien reflecting telescope [1] equipped with a CCD array in the focal plane. Fig. 1 displays photographs of the observatory and of the telescope. A similar telescope equips the Nha Trang VNSC observatory in Hon Chong. Here, we report on measurements illustrating the performance of the former.

1.1. Optics

The telescope is of the Ritchey-Chrétien type, a variant of the Cassegrain design. It includes a primary mirror which reflects the light onto a smaller coaxial secondary mirror. The secondary mirror produces the image on the focal plane located behind the primary mirror and then the light beam passes through the small central hole of the primary mirror (Fig. 2). The Ritchey-Chrétien design uses hyperbolic mirrors aimed at suppressing off-axis optical errors such as coma and spherical aberration, but it introduces some

Fig. 1. Left: the Hoa Lac observatory telescope, installed in the dome and equipped with field rotator and camera. Right: the Hoa Lac observatory with the telescope dome in the foreground.

*Corresponding author: Email: ntthao02@vnsc.org.vn

astigmatism. Each mirror has a nominal reflectivity of 96% and a wave-front peak-to-valley precision of a fifth of a wavelength at λ=632 nm. Small diffraction spikes caused by light diffracting around the support vanes of the secondary mirror are present on images of bright sources. The focal length, nominally 4 m, can be finely adjusted by shifting the secondary mirror along its axis.

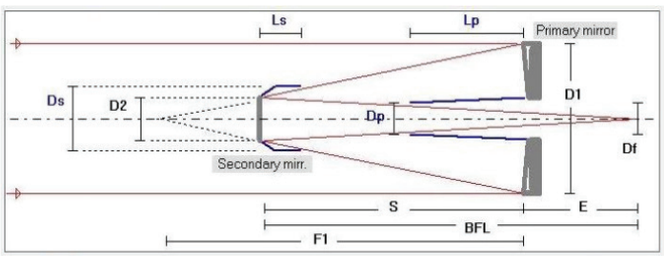

Fig. 2. Schematic of the telescope optics. The main dimensions are as follows: primary curvature radius=3500 mm; secondary curvature radius=2294 mm; primary to secondary distance=1105 mm; secondary mirror diameter (D_2)=200 mm, magnification=2286, back focal length=1475 mm; linear obstruction=48%; aperture ratio=8; light-shield length (L_s=128 mm and L_p=588 mm); light shield diameter (D_s=240 mm and D_p=150 mm); effective focal length=4 m; primary focal length (F_1^p)=1750 mm; primary diameter (D_1)=500 mm; distance between the primary mirror and the focal plane (E)=370 mm; field diameter (D_f)=50 mm.

1.2. Drive

The telescope mount is of the altitude-azimuth (altazimuth) type. The image of the environment of a star to which the telescope is pointing rotates in the image plane as the star is moving. The rotation of the image is maximal when pointing to the north pole (i.e. 90^0 declination). It is compensated by having the CCD array of the camera on a rotating support, called the field rotator. However, in the present work, the field rotator has not been used. The telescope can be driven on tracking mode for exposure times exceeding a fraction of a second. For example, near the equator, when the telescope points to a fixed direction, the field of view is typically covered in a time of only 2 minutes, or about 30 ms per pixel.

1.3. Camera

The CCD camera (Finger Lakes Instrumentation, PL16801) [2] uses a 4096×4096 pixel array with an individual pixel size of 9×9 μm^2. Each pixel covers an angle of 0.46×0.46 arcsec^2, meaning it has a field of view of 31.7×31.7 arcmin^2. The quantum efficiency exceeds 50% and peaks between 600 and 700 nm, as displayed in Fig. 3. Peltier elements cool the array to the required temperature, however, not lower than ~50^0 below ambient. Read-out proceeds at 8 MHz, meaning in practice a read-out time of 4 s per frame. However, the read-out time can be decreased by grouping together neighbouring pixels or selecting a sub-frame, with both options being available by software. Saturation occurs at a level of 10^5 electron units (eu). The signal is sampled by a 16-bit analog-to-digital converter (ADC), each ADC unit (ADCu) being equal to 1.7 eu.

Hysteresis in the CCD array, producing so-called residual bulk images (RBI), is caused by the presence of saturated pixels from the preceding exposure. It can be eliminated by illuminating the array with a ring of light emitting diodes before exposure, a procedure known as RBI pre-flood, which is also available by software. However, this technique has not been used in the present work.

1.4. Monitoring and control

A flow chart of the monitoring and control operation is displayed in the right panel of Fig. 3. It uses the Sky X Pro software [3] to streamline various tasks, which are, in turn, handled by other software, such as Maestro [4] for the telescope movements. A detailed description of the available tasks is beyond the scope of the present introduction. However, it is sufficient to mention that the movements of the telescope and dome are coupled and can be adjusted either in fixed or tracking mode. The pointing direction can be specified either by its horizontal coordinates or by its equatorial coordinates. Each picture is accompanied by a header that summarizes data of relevance, such as latitude, longitude, equatorial and horizontal coordinates of the CCD centre, calendar date, universal time, local sidereal time and local hour angle, exposure time, position of the secondary mirror, and CCD temperature.

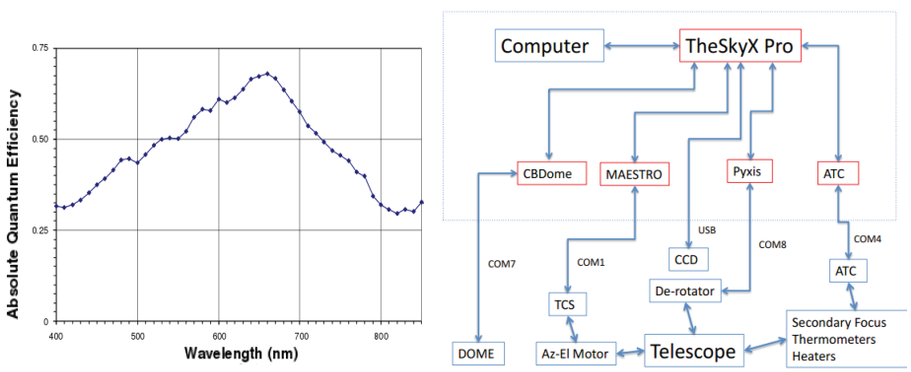

Fig. 3. Left: wavelength dependence of the quantum efficiency of the CCD array. Right: flow chart of the monitoring and control tasks.

2. The CCD camera: bias frames, dark frames and flat field frames

Basic properties of the CCD array and of the telescope optics have been measured by recording reference images referred to as bias frames, dark frames, and flat field frames. They are needed for a proper interpretation of the telescope images. The present section describes and analyses the associated data.

2.1. Bias frames and dark frames

Bias frames and dark frames are recorded with no light reaching the CCD array, the CCD shutter being closed and the telescope cap in position. The frames are recorded at different exposure times, t, during which charge is allowed to accumulate in the CCD pixels. A dark frame having zero exposure time, or more precisely, the minimum possible exposure time of 1 ms, is called a bias frame. This appellation refers to a common bias that is applied to each pixel in order to guarantee that all measured charges are well above zero and within the range of the ADC (16 bits, 65536 ADCu). The bias has been adjusted to produce a charge of approximately 1000 ADC units (ADCu). We refer to this bias as the pedestal.

2.1.1. Thermal noise, dark current and read-out noise:

The distribution of the charges measured in each of the $(4096)^2$ pixels is observed to be Gaussian to an excellent precision and nearly constant from frame to frame with a common standard deviation of some 10 ADCu. Table 1 and Figs. 4 to 6 summarize measurements of bias and dark frames for a number of combinations of exposure time, t, and temperature, T.

A typical distribution of pixel charges is shown in Fig. 4 (left). A Gaussian fit to the charge distribution gives a mean value of Q_0 +1000 ADCu with a standard deviation of σ_0 ADCu. Table 1 lists values of Q_0 and σ_0 for different combinations of temperature and exposure time. The Gaussian fit describes the measured distribution down to ppm level on the low charge side, which is remarkable, but reveals the presence of an excess of high charges. We measure the importance of this high charge tail as the ratio R_{hi} between the number of pixels having a charge larger than $Q_0+5\sigma_0$ and a charge smaller than $Q_0+5\sigma_0$.

The dispersion of the pixel charge distribution depends only slightly on temperature and exposure time; the smallest and largest values of σ_0 listed in Table 1 differ by less than 1 ADCu. On the contrary, Q_0 displays a small linear increase with exposure time as illustrated in Fig. 4 (right) and an exponential increase with temperature; it is well described by a form Q_0=-1.3+7.40 (1+0.0112 t) exp(0.112 T), where Q_0 is in units of ADCu, t in s, and T in ^{0}C. Both thermal noise, associated with the dark current thermally generated in the CCD array, and read-out noise, associated with the noise inherent to the read-out amplifier preceding the ADC, contribute to Q_0 and σ_0. The exponential temperature dependence with a characteristic temperature of around 10^0 is typical of silicon devices. Indeed, the dependence on temperature of the dark current [5] takes the form exp(-$\Delta E/kT$) where ΔE is the activation energy and k Boltzmann constant. Developing this expression about the mean temperature, T_0, we obtain, to first order in the temperature span, a dependence of the form exp($\Delta E \times T/kT_0^2$), which for T_0=270K gives ΔE=0.112kT_0^2=0.7 eV, consistent with expectation. The low value of σ_0, equivalent to 15 to 20 electrons, demonstrates the high quality of the CCD array. When adding the charges of n pixels, the relative contribution of the noise decreases as $1/\sqrt{n}$ as long as n does not exceed 1000 or so; however, for larger pixel samples, other contributions to the noise prevent further decrease.

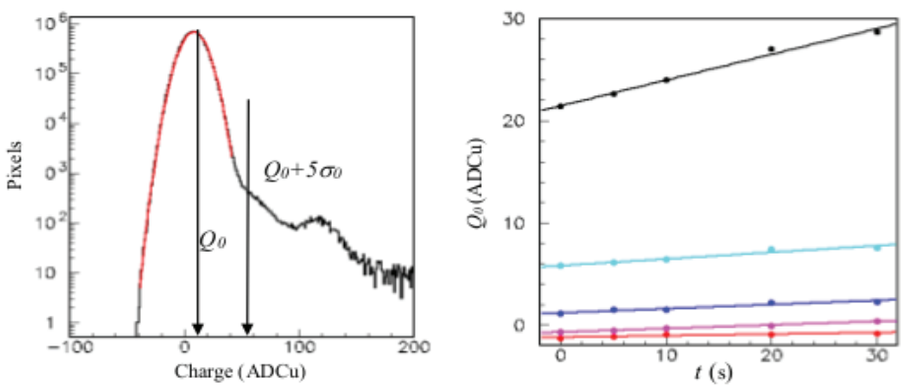

Fig. 4. A typical dark frame (t=20 s and T=0°C). Left: distribution of the pixel charges (in excess of a nominal pedestal of 1000 ADCu). The bin size is 1 ADCu. The red curve is a Gaussian fit having mean Q_0 and rms σ_0. The arrows show the value of Q_0 and of $Q_0+5\sigma_0$, the latter being used to measure the value of R_{hi} (see text). Right: dependence of Q_0 on temperature, T, and exposure time, t (s in abscissa). Colours are red, purple, blue, magenta and black for T=-25°C, -20°C, -10°C, 0°C, and 10°C, respectively.

2.1.2. Non-uniformity of the charge distribution on the pixel array:

We use coordinates x and y on the pixel array, measured in pixel size (1 px=9 μm). Read-out proceeds by shifting charges downward (decreasing y) in columns of increasing x; namely the first pixel read-out is (x, y)=(4096, 1), followed by (4096, 2) and so on up to (4096, 4096) for the last column; then we have (4095, 1)… (4095, 4096)… (1, 1)… (1, 4096). The distribution of charges on the CCD array is illustrated in Fig. 5 (left) and is observed to be non-uniform. Such non-uniformity is known to be present in all CCD arrays and is largely due to contaminations in the fabrication process. In particular, in the present case, pixel columns having x<~300 contain higher charges and, among these, pixels with y<300 contain even higher charges (Fig. 5 right). We measure this lack of uniformity with two numbers, Δ_x and Δ_{xy}. Δ_x is the difference between the mean pixel charge in pixel columns having x≤300 and pixel columns having x>300; Δ_{xy} is the difference between the mean charges contained in pixels having x≤300 and y≤300 and those contained in pixels having x≤300 and y>300. Table 1 shows that both Δ_x and Δ_{xy} are nearly independent of temperature and exposure time, with the exception of Δ_{xy}, nearly cancelling for bias frames. On average, over all measurements listed in Table 1, Δ_x=1.15±0.12 ADCu and Δ_{xy}=3.35±0.18 ADCu for dark frames, and Δ_{xy}=0.2±0.1 ADCu for bias frames. It is therefore sufficient to look at the dark frame having the lowest values of temperature and exposure time, -25^{0}C and 5 s respectively, to see the effect of the non-uniformity of the pixel charge distribution over the CCD array. This is illustrated in Fig. 6 that displays projections of the charge map over the x and y axes, both over the full range of 4096×4096 px^2 and over the restricted environment of the (x, y)=(0, 0) corner of the array, of size 300×300 px^2. The enhancements at low x and y values are described by exponentials having amplitudes of 17 ADCu in x and 10 ADCu in y with decay lengths of 67 pixels in x and 103 pixels in y.

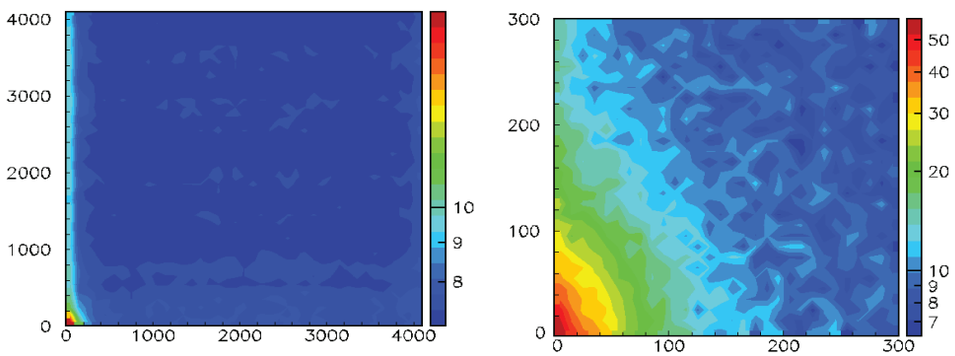

Fig. 5. A typical dark frame (t=20 s and T=0^{0}C). Left: map of the pixel charges (in excess of a nominal pedestal of 1000 ADCu) not exceeding $Q_0+5\sigma_0$. Each (x, y) bin of the map is averaged over 100×100 pixels. Right: zooming on the left panel close to the lower-left corner of the CCD array (x=y=0). Each (x, y) bin of the map is now averaged over 10×10 pixels.

Table 1. Bias and dark frames. Summary of results obtained for different values of the temperature (T) and of the exposure time (t).

T (^{0}C)	t (s)	Q_0 (ADCu)	σ_0 (ADCu)	R_{hit}	Δ_x (ADCu)	Δ_{xy} (ADCu)
-25	0	-1.3	9.46	6.0 10^{-7}	0.9	0.3
	5	-1.1	9.47	2.3 10^{-5}	1.1	3.1
	10	-0.9	9.47	3.5 10^{-5}	1.1	3.4
	20	-0.9	9.48	5.9 10^{-5}	1.1	3.6
	30	-0.8	9.48	7.5 10^{-5}	1.1	3.6
-20	0	-0.7	9.47	9.5 10^{-7}	0.9	0.3
	5	-0.5	9.48	3.2 10^{-5}	1.1	3.1
	10	-0.3	9.48	4.5 10^{-5}	1.1	3.4
	20	-0.1	9.49	7.8 10^{-5}	1.2	3.4
	30	0.4	9.50	1.1 10^{-4}	1.1	3.6
-10	0	1.	9.52	2.1 10^{-6}	0.9	0.0
	5	1.1	9.53	5.1 10^{-5}	1.2	3.2
	10	1.5	9.54	9.4 10^{-5}	1.2	3.4
	20	2.2	9.55	2.0 10^{-4}	1.2	3.4
	30	2.3	9.56	4.0 10^{-4}	1.2	3.5
0	0	5.8	9.65	2.1 10^{-6}	1.0	0.2
	5	6.1	9.67	1.2 10^{-4}	1.2	3.2
	10	6.4	9.68	3.4 10^{-4}	1.3	3.2
	20	7.4	9.71	8.5 10^{-4}	1.3	3.5
	30	7.6	9.73	1.3 10^{-3}	1.3	3.4
10	0	21.4	10.07	4.7 10^{-6}	1.1	0.2
	5	22.6	10.10	4.8 10^{-4}	1.3	3.0
	10	24.0	10.20	1.0 10^{-3}	1.3	3.2
	20	27.0	10.30	1.8 10^{-3}	1.3	3.2
	30	28.7	10.41	2.5 10^{-3}	1.3	3.6

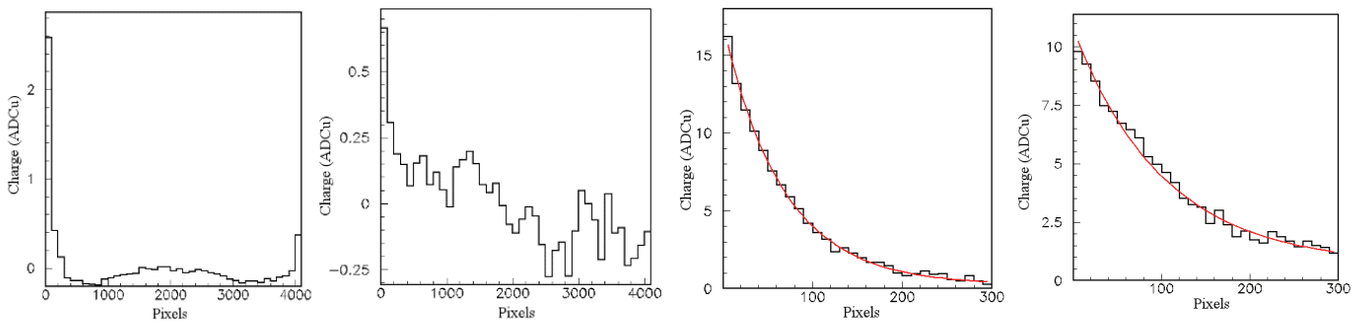

Fig. 6. Dark frame having *t*=5 s and *T*=-25^{0}C. Projections on the *x* (left) and *y* (middle-left) axes of the whole charge map (pedestal subtracted). Middle-right and right: same as the left panels for the 300×300 pixels^2 lower-left square of the CCD array. Curves are exponential fits (see text).

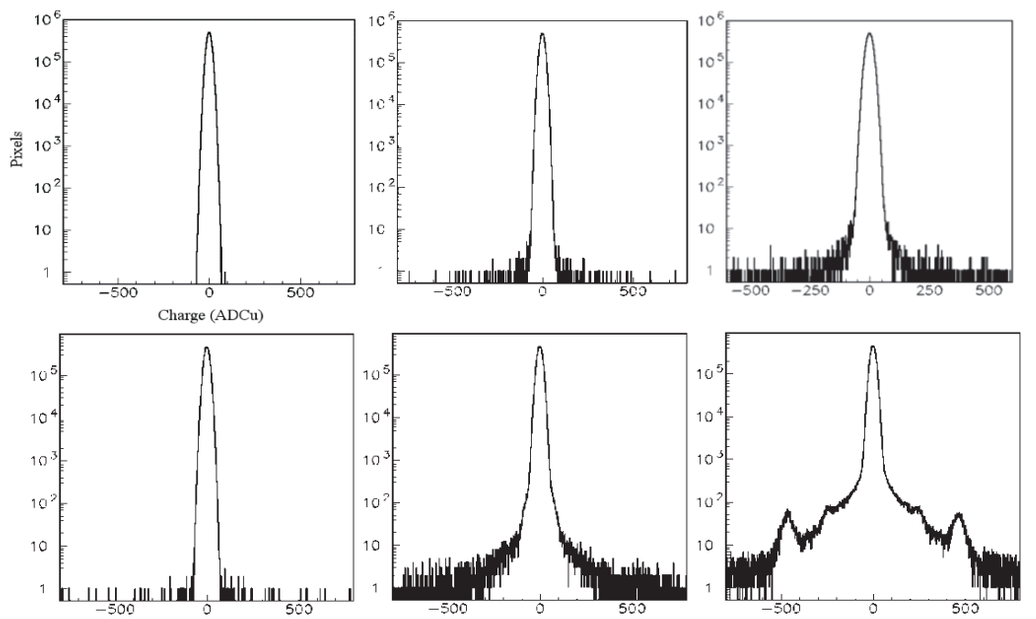

Fig. 7. Warm pixels. Distributions of the difference between the charges (ADCu) contained in two adjacent pixels (having *y* values differing by one unit and the same value of *x*). Upper panels: *T*=-25^{0}C; lower panels: *T*=10^{0}C; left panels: bias frames; central panels: *t*=5 s; right panels: *t*=30 s.

2.1.3. Warm pixels:

In the preceding section, we studied pixels having a content not exceeding a typical value of $Q_0+5\sigma_0$. However, the maps of pixels having larger charges display isolated points associated with what is called warm pixels, due to charge leakages across the CCD array caused by contamination during production. Warm pixels are easily identified as containing a charge much higher than their immediate neighbours in the array. Fig. 7 and Table 2 display distributions of the difference between the charges contained in two adjacent pixels for various combinations of exposure time and temperature. Warm pixels are seen to populate wings of these distributions having amplitudes that depend on both temperature and exposure time. To a very good approximation, their amplitude is proportional to exposure time; the proportionality factor R_{hot} is listed in the last column of Table 2; its distribution as a function of temperature is shown in Fig. 8 (left); it increases exponentially as 20 exp(0.09 *T*) (s^{-1}) with again a characteristic temperature of around 10^0.

Table 2. Number of pairs of adjacent pixels containing charges differing by more than 1000 ADCu.

	0	5 s	10 s	20 s	30 s	R_{hot} (s^{-1})	$20e^{0.09T}$
-25^{0}C	0	13	19	42	62	2.2	2.1
-20^{0}C	0	17	31	68	108	3.4	3.3
-10^{0}C	0	39	90	192	268	8.8	8.1
0^{0}C	0	100	219	414	615	20.8	20.0
10^{0}C	1	253	525	1021	1521	51.2	49.2

However, the shape of the distribution of the charges contained in warm pixels is independent of temperature and exposure time; as illustrated in Fig. 8 (right) it decreases exponentially with a common characteristic charge of between 800 and 900 ADCu. When a pixel is warm in a given combination of temperature and exposure time, it is also warm in any other combination having either a larger temperature or a larger exposure time (or both): being warm is a property of the pixel, which justifies the denomination.

Fig. 9 displays the dependence of R_{hi} (defined in Section 2.1.1 and listed in Table 1) on exposure time and temperature. It increases exponentially with temperature, approximately as R_{hi}=3.5 10^{-5} exp(0.08 T) $t^{1+0.008T}$, again displaying a characteristic temperature at the scale of 10^0. The question then arises of the relation between the tail of the charge distribution measured by R_{hi} and warm pixels. We answer it in the typical case of the (t=20 s, T=0^{0}C) dark frame illustrated in Fig. 4. We consider charges Q in the tail of the distribution (Q>1047 ADCu) and study the correlation between Q-1007 ADCu (defining tail charges) and Q- $Q_{neighbour}$ (defining warm pixels, $Q_{neighbour}$ being the charge of the adjacent pixel in the read-out sequence). Fig. 9 (middle and right) shows that essentially all tail charges are from warm pixels, namely are isolated.

The bumps seen at ~120 ADCu in Fig. 4 and at ~240 ADCu and ~480 ADCu in the lower right panel of Fig. 7 represent a small fraction of the warm pixel population. They are uniformly distributed over the CCD array and are only present for temperatures equal to or larger than 0^{0}C. In contrast with other warm pixels that display a temperature-independent and exponentially decreasing charge distribution, their charges cluster about values that depend on exposure time and temperature. We fail to understand what causes their presence.

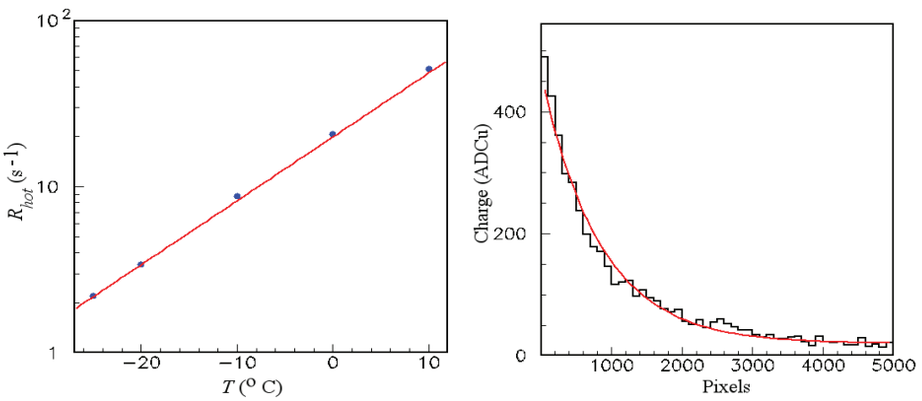

Fig. 8. Warm pixels. Left: dependence of R_{hot} (s^{-1}) on temperature T (^{0}C). Right: charge distribution of hot pixels (in excess of the charge of the adjacent pixel charge increased by 1000 ADCu). The curve is an exponential fit of the form exp(-Q/841).

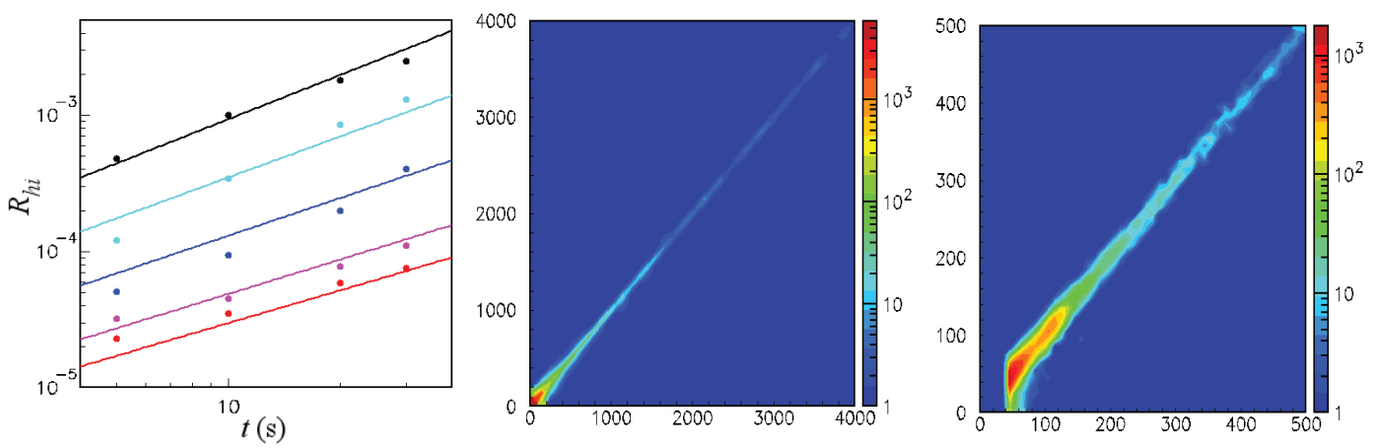

Fig. 9. Warm pixels. Left: dependence of R_{hi} (ordinate) on t (s, abscissa) for different values of the temperature: -25^{0}C (red), -20^{0}C (purple), -10^{0}C (blue), 0^{0}C (magenta) and 10^{0}C (black); the curves are fits of the form R_{hi}=3.5 10^{-5} exp(0.08 T) $t^{1+0.008\ T}$. Middle and right: (t=20 s, T=0^{0}C) dark frame; correlation between tail charges Q and warm pixels. The abscissa is Q-1007 ADCu for Q>1047 ADCu and the ordinate is Q-$Q_{neighbour}$. The right panel is a zoom of the middle panel at lower Q values.

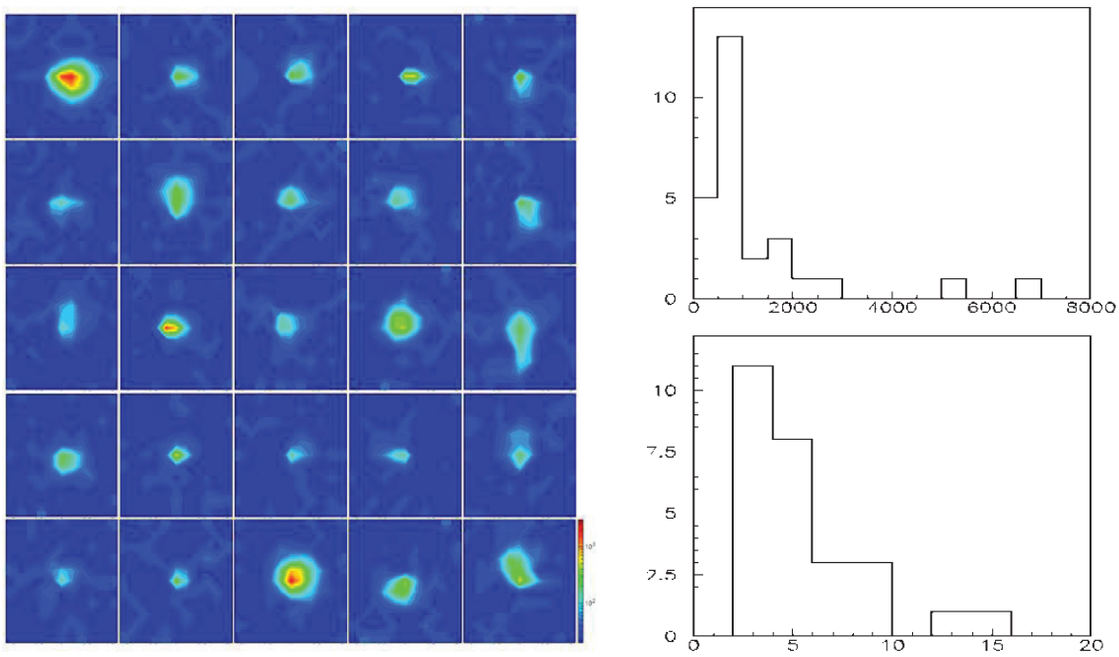

Fig. 10. Cosmic rays. Left: charge maps of 25 of the 27 recorded cosmic ray impacts (see text). Each map is 11×11 px^2, namely 0.1×0.1 mm^2 in area. A common colour scale (ADCu) is used for all maps (shown in the lower right corner). Right: distribution of the charges (ADCu, upper panel) and of the number of pixels hit (lower panel) for the 27 detected cosmic ray impacts.

2.1.4. Cosmic rays:

We expect cosmic rays to cross the ~14 cm^2 of the CCD array at a rate of approximately one every 4 s [6, 7]. In order to detect a significant sample, we record 25 bias frames at T=-25^{0}C and select pixel charges exceeding Q_0+8σ_0. We find five warm pixels, easily identified by their isolation, generally present in several frames (respectively 8, 7, 5, 2 and 1) and 27 clusters of a few pixels that are associated with cosmic ray impacts on the CCD array. Their number is consistent with the time during which the array is sensitive, slightly more than half the read-out time on average. Their maps are displayed in Fig. 10 (left) and the distribution of their charges (~1400 ADCu on average) and of the number of pixels in the cluster (~6 on average) in Fig. 10 (right). These values conform with expectation; minimum ionizing muons lose some 1.8 MeV per g/cm^2 of silicon, meaning ~400 eV/μm for a silicon density of 2.3 g/cm^3. The average 1400 ADCu (~2400 electrons) correspond, therefore, for a production of an electron per 3.6 eV, to a track length of ~20 µm, namely a depleted sensitive layer thickness at the ~10 µm scale.

2.2. Flat field frames

In addition to the non-uniformity of the charge distribution measured in bias and dark frames that has been revealed in the preceding sections, vignetting can be expected to cause the response of a pixel to a given photon flux to depend on its location in the array. Vignetting occurs when light reflected by the primary mirror misses the secondary mirror; it is more important for sources that are farther off axis and results in a loss of illumination that increases with the distance, r, of the pixel from the centre of the array.

Flat field frames were recorded in November 2018 at twilight pointing to altitudes for which the sky brightness was reasonably uniform over the field of view, and to azimuths opposite to the setting Sun, with an illumination of typically half saturation. As an illustration of the main features, measurements made on a flat field frame recorded at T=0^{0}C and t=20 s are displayed in Fig. 11 after a pixel-by-pixel subtraction of the dark frame taken under the same conditions of temperature and exposure time. The subtracted charge, ΔQ, peaks above an irregular background. We characterize its profile by the mean $<\Delta Q>$ and the standard deviation, σ_q, of a Gaussian fit to the peak. Here, $<\Delta Q>$=40430 ADCu and σ_q=370 ADCu. We measure the importance of the background by the deviation from unity of the ratio, R, between the charge contained within 5σ_q of $<\Delta Q>$ and the total charge summed over the whole

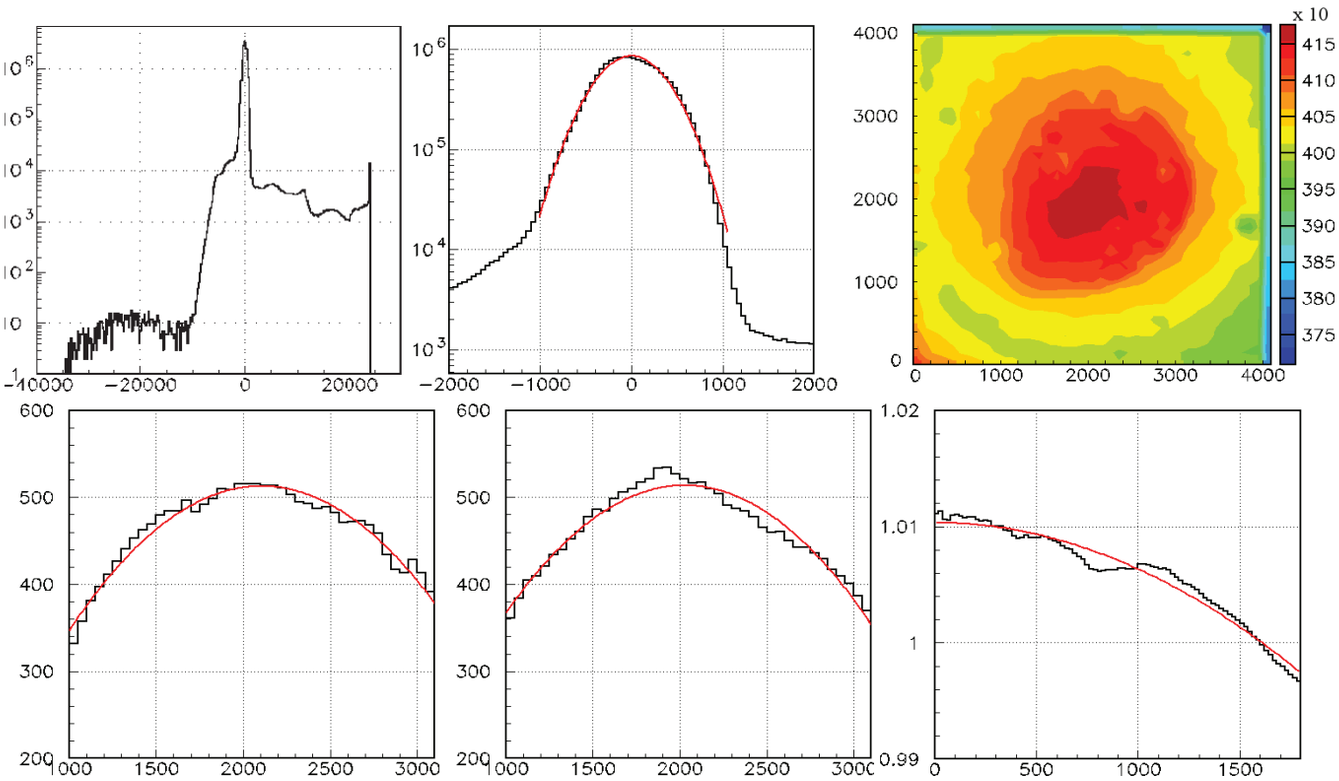

Fig. 11. Flat field frame (dark frame subtracted) recorded at (T=0^{0}C, t=20 s). Upper-left and upper-middle panels: charge distribution after subtraction of $<\Delta Q>$, the middle panel being a zoom of the left panel about the origin. The curve in the upper-middle panel is a Gaussian fit. Upper-right panel: distribution of the mean charge per pixel (there are 100×100 pixels in each bin of the histogram, the colour scale is in units of 100 ADCu). Lower-left and lower-middle panels: projections on the x and respectively y axes of the central square of the charge, with both x and y contained in the interval [1000, 31000] px; a constant charge has been subtracted from ΔQ and the curves are parabolic fits used to measure $<x>$ and $<y>$. Lower-right panel: dependence of $R=\Delta Q/<\Delta Q>$ on r for r<1800 px; the red curve is a fit of the form $R/R_0=1-\lambda(r/1000)^2$.

array. Here, $1-R_q$=7.4%, which is two orders of magnitude larger than the corresponding value of R_{hi} (8.5 10^{-4}) listed in Table 1. The distribution of ΔQ over the CCD array is shown in the upper-right panel of Fig. 11. Using a colour scale confined to a narrow window centred on$<\Delta Q>$ reveals very clearly a central enhancement, spanning some 5% of the central value from centre to edge. The illumination is seen to be slightly off-centre. We evaluate the coordinates ($<x>$,$<y>$) of its centre by making parabolic fits of the projection on the x- and y- axes of the charge distribution of the central 2100×2100 px^2 of the array, where $<x>$=2104 px and $<y>$=2026 px. We define r in each pixel, (x, y), as $r=[(x-<x>)^2+(y-<y>)^2]^{½}$. The dependence of $\Delta Q/<\Delta Q>$ on r is then fitted to the central disc r <1800 px to the form $R=R_0[1-\lambda(r/1000)^2]$. If the non-uniform illumination were due to vignetting, we would expect the values of $<x>$, $<y>$, and λ to be independent of the values of T and t. However, this is not at all the case.

The flat field frames recorded at temperatures below 0^{0}C are found to behave very differently from those recorded at positive temperatures. As will become apparent from what follows, the reason is the presence of ice between the CCD array and the glass window that covers it, forming a pattern of very small droplets acting as lenses in front of the pixels.

Indeed, visual inspection of the CCD array at temperatures below 0^{0}C reveals the presence of frozen condensation. Such a pattern is shown in Fig. 12 for a small but typical region of the flat field frame recorded at T=-25^{0}C and t=30 s; also shown on the figure is the charge distribution recorded over the whole array, with values of $<Q>$= 20989 ADCu, σ_q=254 ADCu and $1-R_q$=0.198, compared with R_{hi}=7.5 10^{-5} for the corresponding dark frame (Table 1). A small cluster of some 20 pixels is observed to surround the largest charge pixel associated with each water droplet. This is illustrated in the right panel of Fig. 12, which displays

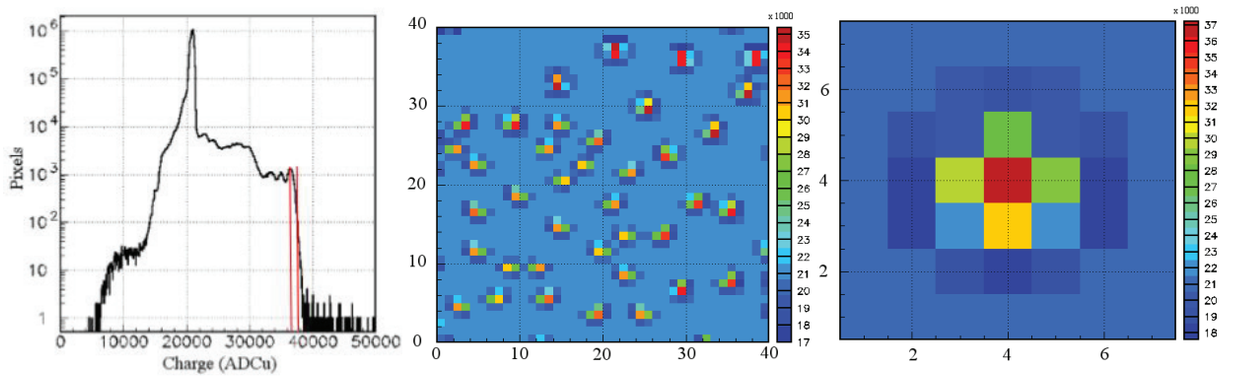

Fig. 12. Flat field frame recorded at (*T*, *t*)=(-25^{0}C, 30 s). Left panel: charge distribution (ADCu). Middle panel: typical pattern as observed in the small square of the CCD array defined as 1500<*x*<1540 px and 3000<*y*<3040 px. Right panel: charge pattern averaged over 4966 squares of 7×7 px^2, centred on a pixel selected for having a charge between 37000 and 38000 ADCu (between the red lines shown on the left panel).

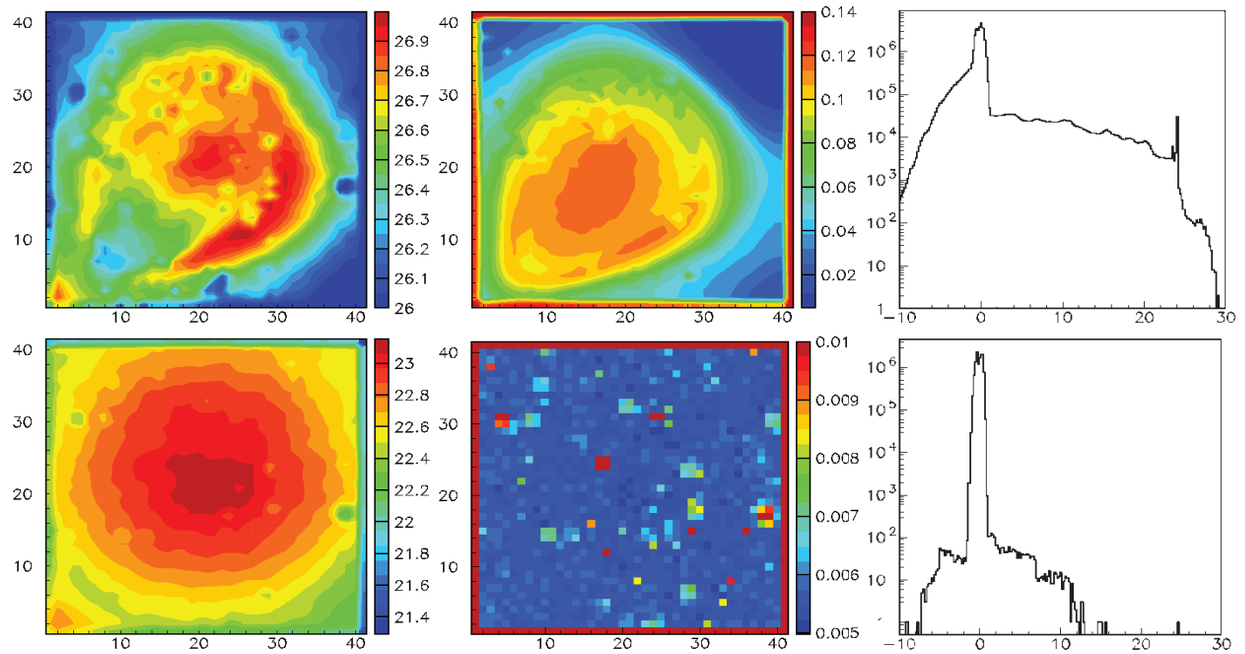

Fig. 13. Flat field frames averaged over 12 frames recorded at *T*=-25^{0}C, -20^{0}C and -10^{0}C for *t*=5, 10, 20 and 30 s (upper panels) and over 3 frames recorded at *T*=10^{0}C for 10, 20 and 30 s (lower panels). The left panels show the maps of $\langle \Delta Q \rangle_{sub}$ (*x* and *y* in units of 100 px, colour scale in units of 1000 ADCu), the middle panels the map of $\sigma_{sub}/\langle \Delta Q \rangle_{sub}$ and the right panels the charge distribution ($\langle \Delta Q \rangle$ subtracted).

the cluster shape averaged over some 5000 cases of high charge pixels (37000<*Q*<38000 ADCu) and centred on that pixel. Interestingly, it reveals the presence of a ring of charges lower than average at a distance of some 20 μm from the central pixel, approximately compensating for the central excess and supporting the interpretation in terms of a lensing effect of ice droplets.

The observed pattern of droplets is invariant for successive frames taken without warming up the CCD array to positive temperatures, independently from the precise values of temperature and exposure time. On the contrary, when the CCD is warmed up and cooled again a different pattern is observed. This, together with the facts that the phenomenon is absent from temperature below 0^{0}C dark frames (for which the CCD array is however covered with ice) and that 1-R_q is considerably higher than R_{hi} gives

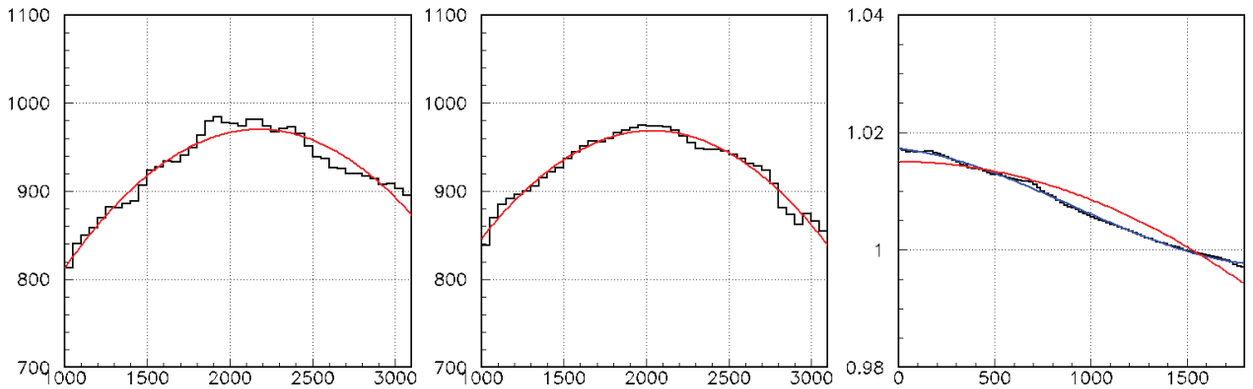

Fig. 14. Flat field frames averaged over 3 frames recorded at T=10^{0}C for 10, 20 and 30 s. The left panels show the distributions of ΔQ used to calculate $\langle x \rangle$ and $\langle y \rangle$; a constant charge has been subtracted from ΔQ and the curves are parabolic fits used to measure $\langle x \rangle$ and $\langle y \rangle$. The right panel shows the dependence on r of R/R_0. The curves show a fit of the form $R/R_0 = 1 - \lambda(r/1000)^2$ (red) and a third degree polynomial fit (blue).

evidence for the interpretation in terms of ice droplets. We illustrate this further in Fig. 13, which compares 12 flat field frames recorded at temperatures below 0^{0}C for different exposure times and 3 flat field frames recorded at 10^{0}C for t=10, 20 and 30 s. The differences are spectacular. As a measure of the effect, we calculate in each square of 100×100 pixels the mean charge $\langle \Delta Q \rangle_{sub}$ and the rms with respect to the mean σ_{sub}. The ratio $\sigma_{sub}/\langle \Delta Q \rangle_{sub}$ is found to be essentially the same for each combination of temperature below 0^{0}C and exposure time; its map is displayed in the middle panels of Fig. 13. Its shape, for temperatures below 0^{0}C, is the same as that of the frozen condensation observed visually.

The above results make it clear that negative temperature flat field frames cannot be used to evaluate the effect of vignetting. We use instead the three flat field frames recorded at T=10^{0}C with exposure times of 10, 20, and 30 s that are illustrated in the lower panels of Fig. 13. Table 3 and Fig. 14 show that they give consistent results and their dispersion is used to evaluate uncertainties. The values of $\langle x \rangle$ and $\langle y \rangle$ are measured as -14±4 px and 129±7 px, respectively, away from the centre of the array. The value of λ is (6.3±0.2) 10^{-3} but the fit is poor. A third-degree polynomial gives a much better fit with R=1.017 [1 - 0.306 10^{-2} (r/1000) - 0.124 10^{-1} (r/1000)^2 + 0.453 10^{-2} (r/1000)^3]. We retain from this analysis that the centre to edge difference of illumination due to vignetting does not exceed 3%.

Table 3. Dependence of $\Delta Q = Q_{flat} - Q_{dark}$ on the pixel coordinates x and y on the CCD array. The quantities listed are defined in the text.

T (0C)	t (s)	$\langle \Delta Q \rangle$ (ADCu)	σ_q (ADCu)	$1-R_q$ (10^{-6})	$\langle x \rangle$	$\langle y \rangle$	λ (10^{-3})
10	10	13494	144	93.4	2039	2187	6.64
	20	21112	211	70.3	2031	2171	6.29
	30	29162	274	33.9	2032	2174	6.15
Mean		-	-	-	2034	2177	6.33
RMS		-	-	-	4	7	0.21

2.3. Summary

In summary, the analysis of bias and dark frames has demonstrated the high-quality performance of the CCD array with a Gaussian charge distribution down to ppm level and a standard deviation at the level of 9 to 10 ADCu (~16 electrons). A few well-defined pixels, called warm pixels, representing a fraction of the total increasing from ppm level at -25^{0}C to permil level at 10^{0}C, deviate from the Gaussian distribution and produce a high charge tail with an exponential charge distribution typically decreasing by a factor 2 every 600 ADCu (~1000 electrons). They are distributed uniformly over the CCD array.

The thermal noise and dark current display an exponential temperature dependence consistent with a Boltzmann distribution and doubling every 6 to 8^{0}C.

The distribution of the charge is uniform over most of the CCD array, increasing only at the lower edges of the x and y

distributions (over typically 70 and 100 pixels respectively).

Cosmic rays have been detected during the exposure and read-out times, at a rate of a few tenths of Hz. They produce small clusters of 6 pixels on average carrying a mean charge of some 2000 to 3000 electrons.

The analysis of flat field frames has revealed significant water condensation behind the front glass window of the CCD array when operating at temperatures below 0^0C. In practice, we have been able to overcome this problem by keeping the CCD array in a dry atmosphere between observations, as humidity may take more than a day before building up significantly on the CCD array. The precise cause of this default, leak or outgassing, needs to be identified and corrected. The analysis of flat field frames recorded at 10^0C has revealed a small misalignment of the image on the CCD array, at millimetre level in y, and a vignetting causing a difference of illumination not exceeding 3% between centre and edge.

3. Geometry and astrometry

In order to evaluate possible misalignments of the system, reference stars have been observed with different exposure times, at different altitudes and azimuths. Here, we simply illustrate the main results by using a set of observations performed on December 17th, 2018 (Julian date JD=2458469.5).

Each picture is associated with a header that lists, among other information, the values of the calendar date, of the universal time UT and of the azimuth and altitude, az and alt, of the telescope (centre of the CCD array) as measured from the encoders of the associated movements. Knowing the equatorial coordinates of the star being observed, right ascension ra and declination dec (as obtained from the Simbad database [8], accounting for the star proper motion) and the location of the telescope on Earth (as obtained from GPS measurements and compared with values quoted by Google [9]), latitude lat=21.021^0 and longitude $long$=105.543^0, we can calculate the horizontal coordinates of the star, azimuth az_0 and altitude alt_0, using the equations below:

$$\sin(alt_0)=\sin(lat)\,\sin(dec)+\cos(lat)\cos(dec)\cos(lha)$$

$$\sin(az_0)= -\sin(lha)\cos(dec)/\cos(alt_0)$$

$$\cos(az_0)=[\sin(dec)-\sin(lat)\sin(alt_0)]/[\cos(lat)\cos(alt_0)].$$

Here, lha is the local hour angle, equal to the difference between the local sidereal time LST and the right ascension of the star, ra_0. The local sidereal time is the sum of Greenwich sidereal time, GST, and longitude, $long$. The Greenwich sidereal time is obtained from the value of universal time, UT, using the relation below (in hours):

$$GST=6.656306+0.0657098242*(JD-2445700.5)+1.0027379093*UT,$$

where JD is the Julian date [10]. Namely lha is expressed in degrees (modulo 360^0) as

$$lha=LST-ra_0=GST+long-ra_0.$$

Measuring the coordinates x and y of the star on the CCD array, we can then infer the horizontal coordinates of the centre of the CCD array, (az*,alt*) by correcting az_0 and alt_0 by the offsets (x-2048)px/cos(alt) and (y-2048)px where px=1.28^0 10^{-4} is the angular acceptance of a pixel.

Table 4 compares the values of the true horizontal coordinates of various stars at various times and the corresponding values listed in the picture headers.

Table 4. Summary of observations made on December 17th, 2018.

x (px)	y (px)	UT (hr)	az (^{0})	alt (^{0})	Δaz (^{0})	Δalt (^{0})
β Cas, ra=2.2973^0, dec=59.1488^0						
1966	1953	11.80915	356.8463	51.2952	2.1459	-0.3107
2030	2288	11.81715	356.7341	51.2438	2.1448	-0.3087
1998	2202	11.81963	356.7042	51.2533	2.1386	-0.3069
1858	1870	11.82212	356.6749	51.2963	2.1109	-0.3031
1714	2291	11.83088	356.5044	51.2440	2.0178	-0.2897
1972	1684	11.83340	356.5733	51.2982	2.1706	-0.3097
2131	1995	11.83615	356.5427	51.2509	2.2063	-0.3134
1950	2295	11.84230	356.4072	51.2177	2.1086	-0.2997
2094	2077	11.84508	356.4187	51.2319	2.1836	-0.3095
φ Aqr, ra=348.5809^0, dec=-6.0489^0						
1726	2053	11.48577	210.3983	59.3232	-0.3479	0.2809
1795	2029	11.48980	210.5243	59.2951	-0.3075	0.2786
1877	1998	11.49316	210.6336	59.2710	-0.2633	0.2747
2082	1913	11.49824	210.8210	59.2352	-0.1541	0.2647
2150	2080	11.50173	210.9094	59.1875	-0.1374	0.2636
1711	1989	11.50722	210.9593	59.1823	-0.3353	0.2867
2103	2209	11.51156	211.1424	59.1062	-0.1648	0.2703

2054	2141	11.51474	211.2222	59.0946	-0.1773	0.2733
2007	2070	11.51830	211.3129	59.0797	-0.1879	0.2754
γ Cas, ra=14.1772^0, dec=60.7167^0						
3228	2720	11.97788	4.5780	49.6847	2.5984	-0.4827
2630	2576	11.98138	4.4379	49.7334	2.3787	-0.4543
2186	2406	11.98423	4.3388	49.7759	2.2235	-0.4350
1408	1866	11.98730	4.2038	49.8803	1.9679	-0.4014
2520	1459	11.99048	4.4044	49.8721	2.4277	-0.4633
2842	2287	11.99331	4.3625	49.7626	2.4827	-0.4682
2436	2457	11.99628	4.2393	49.7658	2.3124	-0.4447
1970	2112	11.99998	4.1418	49.8315	2.1640	-0.4250
Bellatrix, ra=81.2828^0, dec=6.3497^0						
1687	2208	13.78427	103.9007	44.9081	0.6547	-1.1264
1714	2110	13.78725	103.9379	44.9592	0.6709	-1.1286
1954	1877	13.79060	104.0200	45.0149	0.7718	-1.1425
1992	1962	13.79272	104.0421	45.0384	0.7786	-1.1431
2365	2183	13.79574	104.1140	45.0352	0.8930	-1.1593
1781	2065	13.79874	104.0504	45.1201	0.6951	-1.1305
1844	2047	13.80141	104.0854	45.1560	0.7183	-1.1334
1852	2056	13.80434	104.1113	45.1960	0.7199	-1.1323
2080	1963	13.80697	104.1794	45.2314	0.8071	-1.1447
Aldebaran, ra=83.0017^0, dec=-0.2991^0						
2378	2145	13.22196	91.2207	51.6741	1.0915	-1.2121
1937	2220	13.22510	91.1490	51.7338	0.9090	-1.1869
2001	1813	13.22794	91.2102	51.8187	0.9683	-1.1939
2042	1891	13.23064	91.2254	51.8445	0.9774	-1.1961
2191	2208	13.23328	91.2410	51.8709	1.0103	-1.1661
1944	2179	13.23596	91.2112	51.8912	0.9131	-1.1872
2095	1974	13.23884	91.2730	51.9475	0.9913	-1.1976
Mintaka, ra=68.9805^0, dec=16.5084^0						
2069	2532	13.88839	112.0897	41.7553	0.6864	-1.1010
2000	2375	13.89097	112.1155	41.8112	0.6739	-1.0989
1822	1962	13.89371	112.1423	41.9032	0.6417	-1.0956
1883	1922	13.89634	112.1807	41.9375	0.6639	-1.1008
2179	2182	13.89942	112.2396	41.9321	0.7432	-1.1131
2087	2124	13.90195	112.2534	41.9752	0.7151	-1.1105
Alpheratz, ra=2.0976^0, dec=29.0896^0						
2235	2281	15.37633	292.9245	35.8846	1.4869	0.5647
1895	2279	15.37946	292.8840	35.8617	1.3876	0.5824
2343	1583	15.38277	292.9901	35.8760	1.5581	0.5509
2424	1926	15.38550	292.9770	35.7958	1.5528	0.5502
2157	2034	15.38843	292.9361	35.7587	1.4649	0.5652

We perform linear fits to the differences $\Delta az=az-az^*$ and $\Delta alt=alt-alt^*$ of the form:

$$\Delta az_{lin}=\Delta az_0+\Delta az_1\, alt+\Delta az_2\, cos(az)+\Delta az_3\, sin(az)$$

$$\Delta alt_{lin}=\Delta alt_0+\Delta alt_1\, alt+\Delta alt_2\, cos(az)+\Delta alt_3\, sin(az).$$

The distributions of the differences $\Delta az-\Delta az_{lin}$ and $\Delta alt-\Delta alt_{lin}$ are displayed in Fig. 15. Gaussian fits give standard deviations of 0.091^0 and 0.016^0 respectively. The parameters of the linear fits are listed in Table 5.

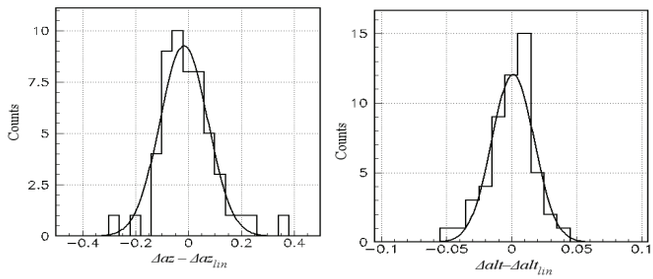

Fig. 15. Distributions of $\Delta az-\Delta az_{lin}$ (left) and $\Delta alt-\Delta alt_{lin}$ (right) as described in the text for the measurements associated with the observations listed in Table 4.

Table 5. Values of the parameters of the linear fits to $\Delta az-\Delta az_{lin}$ and $\Delta alt-\Delta alt_{lin}$.

	Δ_0	Δ_1	Δ_2	Δ_3
Azimuth	1.4580	-9.84 10^{-3}	1.2635	6.81 10^{-2}
Altitude	-0.2047	-1.56 10^{-3}	-0.1157	-0.9185

They are dominated by the dependence on az and, at a typical altitude of 50^0, they can be crudely approximated by the simpler forms

Δaz=1.0^0+1.3^{0}cos(az-3^0) and Δalt =-0.3^0-0.9^{0}sin(az+7^0).

This suggests a dominant contribution from a tilt of the telescope axis. Indeed, measuring such a tilt by the associated Euler angles φ, ψ and β and calling $\alpha=\varphi+\psi$, a rotation of (x, y, z) into (x', y', z') is defined by only two parameters, α and β, to first order in the Euler angles:

$x'=x-\alpha y$; $y'=\alpha x+y-\beta z$; $z'=\beta y+z$.

Differentiating the relations that give the horizontal coordinates as a function of the equatorial coordinates, we obtain

$\Delta az=\alpha-\beta$tan(alt)cos(az) and $\Delta alt=\beta$sin(az),

suggesting $\alpha\sim$1.0^o and $\beta\sim$1.1^o. Here α measures a rotation about vertical and β measures the tilt with respect to vertical.

A detailed evaluation of the uncertainties attached to the measurement of the horizontal coordinates of a star requires a preliminary correction for such a tilt and is beyond the

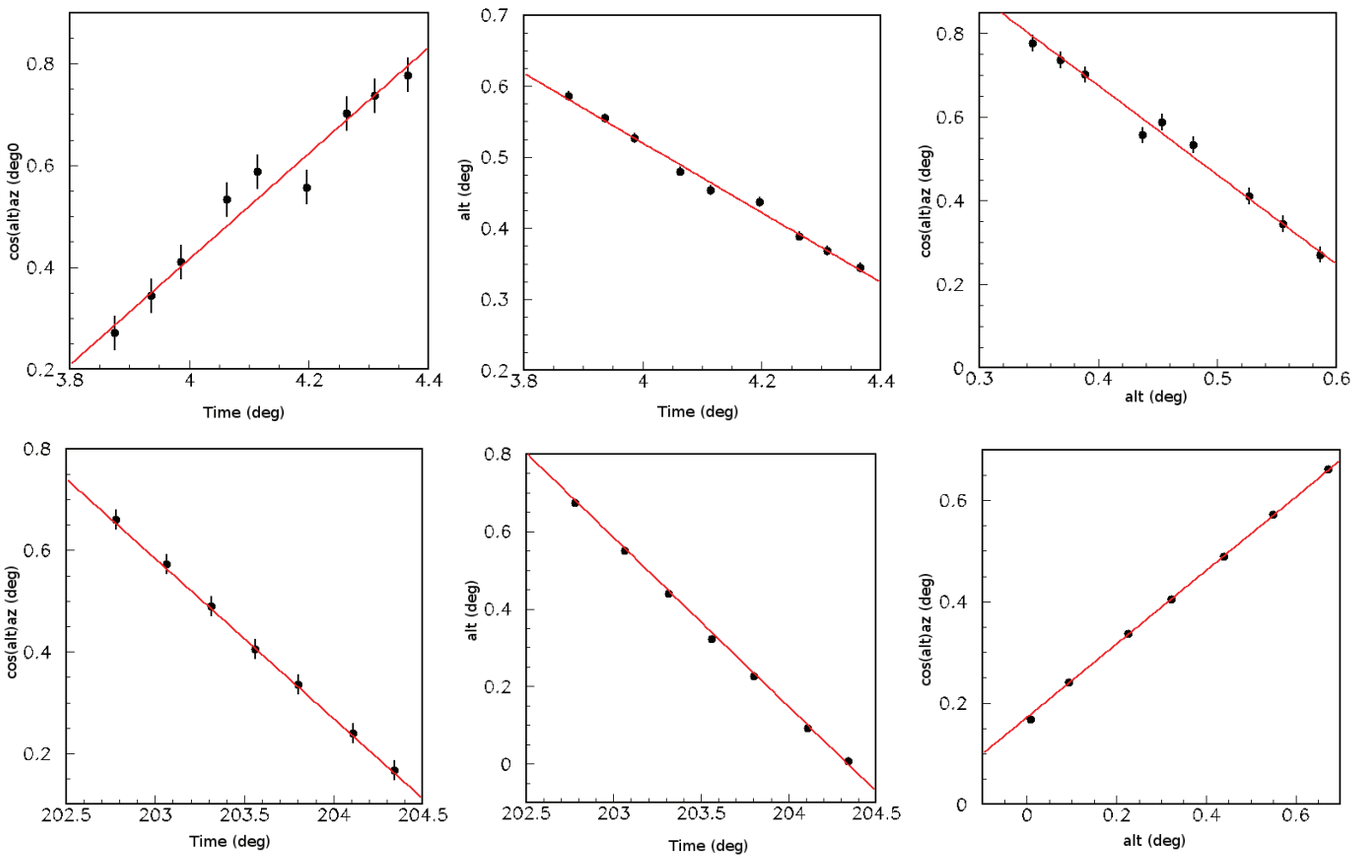

Fig. 16. Dependence of cos(*alt*)*az* (left) and *alt* (middle) over time. Right: dependence of cos(*alt*)*az* over *alt*. Both time and horizontal coordinates are measured in degrees. The upper panels are for observations of φ Aqr made on 17 December 2018 and the lower panels for observations made of Merak (β Ursae Majoris) on 17 May 2019.

scope of the present article. Assuming that the time elapsed since the construction of the observatory is sufficient for the building to have settled to a precision better than a tenth of a degree, it would be advisable to fine-adjust the orientation of the telescope mount to correct for the tilt. Pointing errors are expected at the level of ±5 arcsec~10 px. Ultimately, one should be able to reach precisions of this order of magnitude when measuring the horizontal coordinates of the target. However, this will require more detailed analyses than performed in the present introductory presentation.

Another illustration of the dispersion of successive measurements is displayed in Fig. 16 using observations of φ Aqr made on 17 December 2018 and observations of β Ursae Majoris (Merak) made on 17 May 2019 (Julian date *JD=2458620.5*). Average horizontal coordinates of the telescope pointing were (*az, alt*)=(210.9^0, 59.2^0) for the former and (331.2^0, 45.0^0) for the latter. Linear fits to the dependence on time of the star offsets measured in the CCD array after correction for the different pointing directions provide evaluations of the quantities cos(*alt*)*daz/dt*, *dalt/dt* and cos(*alt*)*daz/dalt* listed in Table 6 together with their true values and the standard deviations of the measurements with respect to the linear fits. Within the uncertainties induced by the tilted geometry, reasonable agreement between the measured and true values of the measured quantities is observed. The values of the standard deviations, particularly small in the case of Merak, confirm the conclusions that were obtained from the analysis of the data listed in Table 4.

Table 6. Movements of φ Aqr and β Ursae Majoris as observed on 17 December 2018 and 17 May 2019, respectively.

	φ Aqr			Merak		
	cos(alt) daz/dt	*dalt/dt*	*cos(alt) daz/dalt*	*cos(alt) daz/dt*	*dalt/dt*	*cos(alt) daz/dalt*
Measured values	1.04	-0.49	-2.14	-0.31	-0.44	0.73
True values	1.12	-0.48	-2.46	-0.32	-0.45	0.72
Standard deviations	0.034	0.007	0.020	0.006	0.009	0.001

4. Conclusions

The exploratory and introductory measurements that have been performed over the past year and that are described

in the present article have demonstrated the high quality of the Hoa Lac observatory telescope as a scientific instrument of outstanding potential in terms of training bachelor's and master's degree students. It is now essential to make sure that the important investment that the acquisition of such an instrument represents is made use of as efficiently as possible. In particular, it must be made accessible to those who are most likely to make good use of it, namely university students and amateur astronomers.

Ideally, a scientific instrument should be granted a yearly operation and maintenance budget at the level of a significant percentage, say 5 to 10%, of the initial investment cost. Ideally also, for a proper exploitation of an optical telescope, weather conditions should be such that the fraction of clear nights during which observations can be performed should well exceed 50%. Unfortunately, in the present case, none of these two conditions can be realised. The operation and maintenance budget available for the exploitation of the telescope is negligible and cloud coverage is such that less than 10% of the nights are clear enough to make observations possible [11]. In order to overcome these handicaps, active cooperation with universities and astronomer clubs is mandatory.

The potential of the telescope as a training tool is twofold: it covers the fields of pure instrumentation and of astronomy observations. The present article has given an idea of what the former may include, continuing the exploratory measurements that have been described in order to reach a detailed understanding of the telescope geometry and perform observations of the highest possible quality. In particular, the horizontal coordinates of the orientation of the "*altaz*" rotation axes of the telescope mount need to be accurately measured, together with the precise location of the optical axis and of the CCD array. Detailed properties of the optical system need to be studied. Third party access to the software should be available. Saturation of the CCD array currently prevents taking pictures of bright targets such as the Moon and planets and solutions have to be found to overcome this problem. The pointing accuracy should be optimized. A system or procedure allowing for operation at temperatures below 0^0C without ice formation on the CCD array needs to be implemented.

For what concerns astronomy observations, in addition to collecting pictures of the highest possible quality, a study of bright, short period variable stars is an example of the kind of observations that could be made in the period during which cloud coverage is not too important, typically between October and April. Fig. 17 shows pictures of two nebulae that illustrate the current performance of the telescope optics.

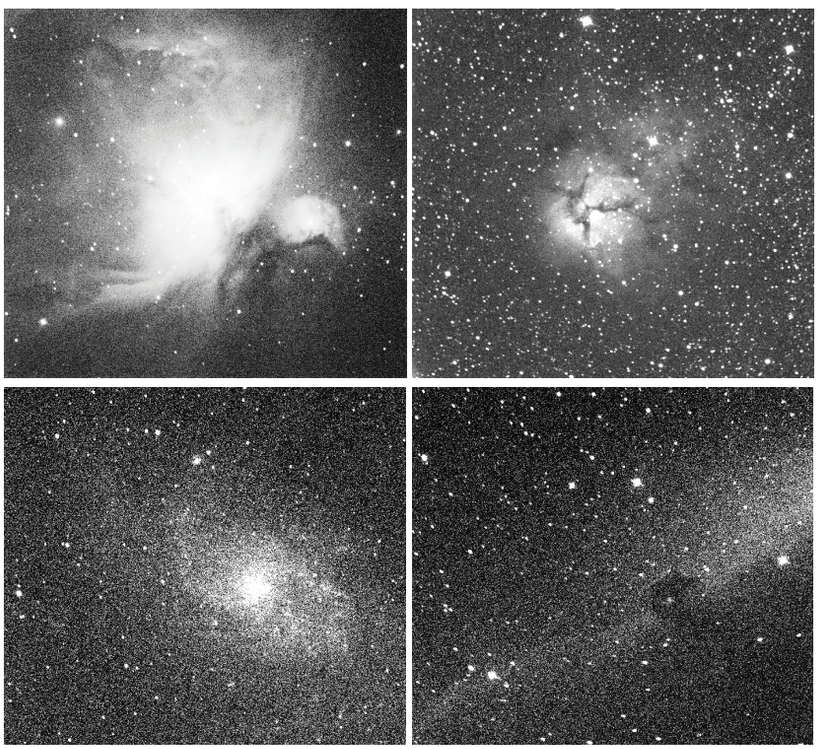

Fig. 17. Up left: picture of the Orion Nebula (100 s exposure time, 19 January 2018). Up right: picture of the Trifid Nebula (30 s exposure time, 19 January 2018). Down left: picture of the Triangulum Galaxy (60 s exposure time, 19 January 2018). Down right: picture of the Horsehead Nebula (60 s exposure time, 4 July 2018).

The research work of the team of the Department of Astrophysics of the Vietnam National Space Center, who is authoring the present article, covers a domain of astronomy and astrophysics essentially disconnected from what the Hoa Lac telescope can access [12]; it uses instruments, such as the Atacama Large Millimeter (submillimeter) Array [13] having sensitivities and angular and spectral resolutions four orders of magnitude larger. Yet, the team will always be available to provide advice and guidance to potential users.

In summary, the opportunity of using the optical telescope of Hoa Lac observatory should not be missed by universities and amateur astronomer clubs. To the former it provides access to a highly performing scientific instrument, with which bachelor and master students can be trained and learn the constraints of rigor and professionalism inherent to the practice of science. To the latter, it offers an opportunity to observe the night sky with one of the best instruments available in the country.

ACKNOWLEDGEMENTS

We thank the anonymous referee for a number of useful comments that helped with improving the quality of the manuscript. We are grateful to the members of the Department of Astrophysics of the Vietnam National Space Center, in particular Dr. Do Thi Hoai, Dr. Pham Thi Tuyet Nhung and Dr. Pham Tuan Anh, for help and useful discussions. This research is funded by the Graduate University of Science and Technology under grant number GUST.STS.NV2017-VL01. Financial support from the Vietnam National Space Center and from the World Laboratory is acknowledged.

The authors declare that there is no conflict of interest regarding the publication of this article.

REFERENCES

[1] http://www.marcontelescopes.com/azienda.php, Marcon-RC500, JEA Technical Solutions Ltd, info@jea-ts.co.uk.

[2] https://www.onsemi.com/pub/Collateral/KAF-16801-D.PDF.

[3] http://www.bisque.com/help/TheSkyXSAEAndPro/index.htm#t=Chart_Navigation.htm.

[4] http://www.astrometric.com/products/telescope-control/.

[5] R. Widenhorn, M. Blouke, A. Weber, A. Rest, and E. Bodegom (2002), "Temperature dependence of dark current in a CCD", *Sensors and camera systems for scientific, industrial, and digital photography application III*, Proceedings of SPIE - The International Society for Optical Engineering, **Vol.4669**, Doi: 10.1117/12.463446

[6] P.N. Dinh, et al. (2003), "Measurement of the Zenith angle distribution of the cosmic muon flux in Hanoi", *Nuclear Physics B*, **661(1-2)**, pp.3-16.

[7] P.N. Dinh, et al. (2002), "Measurement of the vertical cosmic muon flux in a region of large rigidity cutoff", *Nuclear Physics B*, **627(1-2)**, pp.29-42.

[8] M. Wenger, et al. (2000), "The SIMBAD astronomical database. The CDS reference database for astronomical objects", *Astronomy and Astrophysics Supplement*, **143**, pp.9-22.

[9] https://www. maps.google.com/.

[10] O. Montenbruck (1989), *Practical Ephemeris Calculations*, Springer Verlag and http://www.onlineconversion.com/julian_date.htm.

[11] https://weatherspark.com/y/116009/Average-Weather-in-Hanoi-Vietnam-Year-Round.

[12] https://vnsc.org.vn/dap/publications.htm.

[13] https://www.almaobservatory.org/en/home.

Partial nitrification of piggery wastewater as pre-treatment for anammox process using flat sheet membrane bioreactor

Hung Dang Thien[1], Dan Nguyen Phuoc[1*], Thanh Bui Xuan[2], Joon Yong Soo[3]

[1]Centre Asiatique de Recherche sur l''Eau (CARE) - University of Technology, Vietnam National University, Ho Chi Minh city
[2]Faculty of Environment and Natural Resources - University of Technology, Vietnam National University, Ho Chi Minh city
[3]Institute of Advances in Science and Technology - Dankook University, Republic of Korea

Received 20 August 2019; accepted 3 December 2019

Abstract:

A lab-scale flat sheet membrane bioreactor (MBR) system was used for the treatment of piggery wastewater to produce an effluent with the appropriate ratio of nitrite:ammonia (1:1 to 1:1.3) as a pre-treatment for the anammox process. The feed wastewater, which was the effluent of a biogas digester, contained 253±49 (n=60) mg.l^{-1} as COD, 231±18 mg.l^{-1} as N-ammonia, 223±19 mg.l^{-1} as total Kjeldalh nitrogen (TKN), alkalinity of 1433±153 mg.l^{-1} as $CaCO_3$, and pH=7.5±0.3. This study aimed to determine the suitable hydraulic retention time (HRT) and alkalinity to yield the appropriate influent for the annamox process. The results showed that the suitable effluent of the partial nitrification with ratio of nitrite:ammonia 1.0:1.1 at HRT of 7h30, equivalent to total nitrogen loading of 0.77 kgNm^{-3}d^{-1}. The nitrite accumulation rate (NAR) was 82% at HRT of 7h30, whereas NAR were 11 and 63% at HRT of 12h30 and 8h45, respectively, due to the high growth of nitrite oxidation bacteria (NOB) at long HRTs. As increasing alkalinity of up to 1600 mg.l^{-1} and pH of 8.0 at HRT of 8h45, NAR was increased from 63 to 73%, ratio of ammonia:nitrite reduced from 1.0:1.8 to 1.0:1.6 and free ammonia concentration reached to 20.2 mg.l^{-1} nitrogen. This shows that the increase of alkalinity inhibited strongly NOB.

Keywords: **flat-sheet membrane, partial nitrification, piggery wastewater.**

Classification numbers: **2.2, 5.1**

Introduction

Currently, nitrogen removal from wastewater using biological processes mainly follows the trend of nitrification-denitrification, which is a method from recent decades that removes nitrogen through nitrite. Conventional nitrogen removal processes require two stages, the first stage is nitrification, which requires a large amount of oxygen. The second stage demands a supply source of carbon in case that the ratio of C to N in the influent is not high enough. Therefore, the treatment cost is large and it requires a lot of technology. In 1995, Dutch scientists explored a new biological process in which nitrogen was transferred to remove a high concentration of ammonia with a low ratio of C to N [1]. This is known as the anammox process. In this process, ammonia is oxidized by nitrite under anaerobic conditions without a supply source of organic matter to form nitrogen molecules. The reaction process is described as follows [2]:

$NH_4^+ + 1.32\ NO_2^- + 0.066\ HCO_3^- + 0.13\ H^+ \rightarrow 1.02\ N_2 + 0.26\ NO_3^- + 0.066\ CH_2O_{0.5}N_{0.15} + 2.03\ H_2O$.

Compared to conventional nitrification/denitrification in activated sludge systems, nitrogen removal through anammox-based technology is an innovative method that eliminates the necessity of an organic carbon source for nitrification. Further, anammox-based technology consumes lower energy for aeration, has lower excess sludge production, and lower CO_2 emissions [3]. This technology is a combination of two processes consisting of partial nitrification followed by the anammox process. Nitrogen removal efficiency of the anammox process depends largely on partial nitrification. The suitable ratio of NH_4^+-N/NO_2^--N for the anammox process ranges from 1:1 to 1:1.3 [4]. Recent research has shown that the combination of partial nitrification and anammox could economize 20-30% of the consumed

**Corresponding author: Email: npdan@hcmut.edu.vn*

oxygen and 40% of the organic carbon source [5-7]. Besides, it could reduce the volume of the treatment tank up to 40% [8], and the nitrification rate through nitrite is 1.5 to 2 times faster than the conventional process [9]. Recent studies on partial nitrification, as well as nitrite accumulation, focus on the following affected factors [10-13]: (1) high temperature (30-40^{0}C): the growth rate of ammonia-oxidizing bacteria (AOB) is faster than nitrite-oxidizing bacteria (NOB), hence, there is a nitrite accumulation at high temperature; (2) Operation at low dissolved oxygen (DO) levels causes the cell structure of AOB to utilize oxygen more easily than the NOB's cell structure, thus, NOB is suppressed at low DO concentrations, which leads to an increase in the rate of nitrite accumulation; (3) Control of pH, free ammonia concentration (FA), and free HNO_2 (FNA); (4) Substrate concentration and ammonia loads in the influent: AOB were divided into two groups, namely, fast-growth and slow-growth. The fast-growth bacteria group has a great attraction to influent with a high concentration and load of ammonia, thus, nitrification accumulation occurs more easily than for an influent with low concentration and load of ammonia [14, 15]; (5) Sludge retention time: AOB has a shorter growth time than NOB, therefore we could determine the suitable sludge retention time to eliminate the NOB from the treatment system. A study on partial nitrification using a hollow fibre membrane with synthetic wastewater at <0.1 $mg.l^{-1}$ DO and nitrogen load of 0.9 $kgNm^{-3}d^{-1}$ showed that nearly 50% of the ammonia in the influent was transformed into nitrite [16]. Similar results in another study that used a tubular membrane on synthetic wastewater showed the suitable amount of alkalinity to reach the NH_4^+-N/NO_2^--N 1:1 ratio was 1500 $mg.l^{-1}$ $CaCO_3$ at the operational conditions of <1 $mg.l^{-1}$ DO, 510 $mg.l^{-1}$ of influent ammonia, and a retention time of 24h [17]. Regarding livestock wastewater, another study using sequencing batch reactor (SBR) technology with an influent ammonia load of 1.47 g/l/d NH_4^+-N found the nitrite formation rate was 0.91 $gl^{-1}d^{-1}$ NO_2^--N and the NH_4^+-N/NO_2^--N ratio was 1.38:1.00 [18]. According to research that examined the effects of COD concentration on partial nitrification with piggery wastewater with a TOC concentration of more than 2000 $mg.l^{-1}$, it was found that AOB was suppressed and the nitrite accumulation rate decreased [19]. Currently, most MBRs use hollow fibre membranes. In comparison with a hollow fibre MBR, the flat sheet MBR can achieve a unique advantage of high flux, longer service life, and high recovery rate. Research on flat sheet MBR for partial nitration has not been widely published.

Therefore, this study aims: (i) to evaluate the performance of partial nitritation using flat sheet MBR with control of the parameters DO, pH, and HRT to produce the suitable NO_2^--N:NH_4^+-N effluent ratio for the subsequent anammox process and (ii) to assess the effect of alkalinity on partial nitrification.

Materials and methods

Materials

The feed wastewater used in this study was collected from the effluent of a biogas tank in a pig farm with a hydraulic retention time of 20 d. The characteristics of the feed wastewater are described in Table 1.

Table 1. Characteristics of feed wastewater.

Parameter	Unit	Average value (±STD)
pH		7.5±0.3 (n=60)
Alkalinity	$mg.l^{-1}$ $CaCO_3$	1433±153 (n=45)
TSS	$mg.l^{-1}$	223±21 (n=25)
BOD_5	$mg.l^{-1}$	131±17 (n=15)
COD	$mg.l^{-1}$	253±49 (n=60)
NH_4^+-N	$mg.l^{-1}$	231±18 (n=60)
T-N	$mg.l^{-1}$	256±19 (n=25)
NO_2^--N	$mg.l^{-1}$	<1 (n=15)
NO_3^--N	$mg.l^{-1}$	8±1 (n=15)
T-P	$mg.l^{-1}$	89±15 (n=15)

STD: standard deviation.

The feed wastewater had a low concentration of biodegradable substances, the ratio of BOD_5/COD was less than 0.5, so that the organic matter removal efficiency by biological processes may be low. However, the wastewater contained a high amount of nutrients such as T-P and T-N, and the ratio of C/N or BOD_5/TKN was less than 0.5.

Seed sludge used in this experiment was taken from the secondary sedimentation tank of a domestic wastewater treatment plant. The initial concentration of the feed sludge was introduced into the reactor at MLSS at 4000 $mg.l^{-1}$.

Flat sheet MBR (Fig. 1)

The experimental model had a length x width x height of 20 cm x 12 cm x 40 cm, respectively, which is equivalent to a total volume of 9.6 l and working volume of 6 l. This study used two flat membranes with total area of 0.1067 m^2. The membrane was made of polypropylene and polyester, and was put on a PVC plastic frame. The average diameter of the pores were 0.23 µm and it was a product of the GS Yuasa Corporation (Japan).

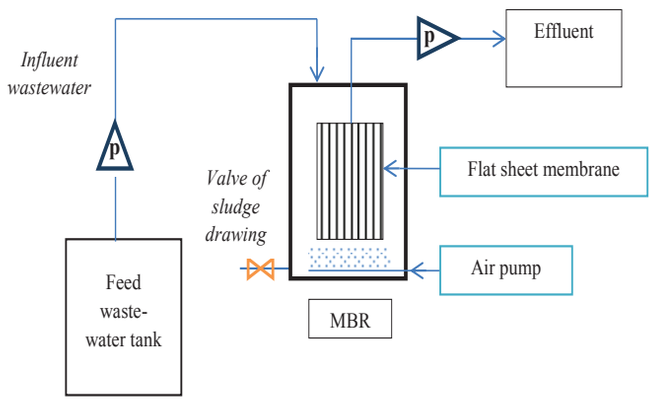

Fig. 1. Schematic diagram of the flat sheet MBR.

Experiment set-up

The feed wastewater was allowed to settle for 1h to remove suspended solids before running the experiment. The inlet pump that introduced wastewater into the MBR tank was controlled by an automatic floating valve. This study was conducted under room temperature conditions (day: 28-32^{0}C and night: 25-27^{0}C). To inhibit NOB growth, low DO levels ranging from 1.4 to 1.8 mg.l^{-1} were maintained using an air adjusting valve [20, 21]. The running mode of the membrane was 8 min ON and 2 min OFF. The transmembrane pressure (TMP) was measured by an electrical pressure gauge. When the TMP reached 20 kPa, the membrane surface was washed manually using a brush [20].

This study was conducted under different hydraulic retention times (Table 2), namely, 12h45 (TN1), 8h45 (TN2, TN3), and 7h30 (TN4). The effect of alkalinity on the partial nitrification process was carried out at a HRT of 8h45 (TN4) by adding $NaHCO_3$ into the feed wastewater to reach an alkalinity of 1600 mg.l^{-1} as determined by the concentration of $CaCO_3$. The pH value of the influent of four experiments was adjusted in the range from 8.0 to 8.5 [21].

Table 2. Operation conditions of the experiment.

Notation	HRT h min	L_{TN} kgN.m^{-3}.d^{-1}	L_{COD} kgCOD.m^{-3}.d^{-1}	flux l.m^{-2}.h^{-1}	Note
TN1	12h45	0.47	0.43	5.5	
TN2	8h45	0.69	0.84	6.4	
TN3	8h45	0.60	0.63	6.4	Bicarbonate addition to influent
TN4	7h30	0.78	0.70	7.5	

Analysis methods

The following parameters: TKN, NH_4^+-N, NO_2^--N, NO_3^--N, COD, and alkalinity were analysed according to standard methods provided by APHA AWWA, 20th, 1998. The pH value was measured by a pH meter (pH211, Hana instrument, Italia). The DO content was measured by a DO meter (WTW 410i, Germany). The rate of nitrification accumulation was calculated as follows:

$$NAR\ (\%) = \frac{NO_2^- - N}{NO_2^- - N + NO_3^- - N} \times 100\%.$$

The FA concentration was calculated by the following equations:

$$FA\ (mgN.l^{-1}) = \frac{TAN}{1 + \left(\frac{10^{-pH}}{K_{e,NH_3}}\right)}$$

$$K_{e,NH_3} = e^{\frac{-6344}{273+T}}$$

where TAN is the total ammonium as nitrogen (mgN.l^{-1}), T is the reaction temperature (^{0}C), and FA is the free ammonia concentration (mgN.l^{-1}).

Results and discussion

Change of nitrogen concentration

Figure 2 (at TN1) showed that most of the influent N-NH_4^+ was oxidized into its NO_3^--N form. The effluent nitrogen concentration had a ratio of N-NH_4^+:NO_2^--N:NO_3^--N of 1:1.9:14.7 (in terms of nitrogen). According to Ref. [22], an FA concentration higher than 3.5 mgN.l^{-1} inhibited NOB growth. However, in this experiment, a low FA concentration of 0.7 mgN.l^{-1} did not inhibit the growth of NOB, and the all nitrite was fully oxidized into nitrate. In addition, high amounts of alkalinity was consumed (90.6% of initial alkalinity). Ref. [23] has shown that the oxidation of ammonia and the oxidation of nitrite can occur at the same time. Ref. [20]

demonstrated that the optimal dissolved oxygen of an MBR should be between 0.8-0.9 mg.l^{-1}. Thus, the DO content is the key factor controlling NOB inhibition. The DO concentration was adjusted to be less than 1.0 mg.l^{-1} since the experiment TN2 was conducted. Fig. 3 showed that almost all ammonia had already been oxidized, so the nitrification accumulation reached a low level, with a NAR of 11.2%.

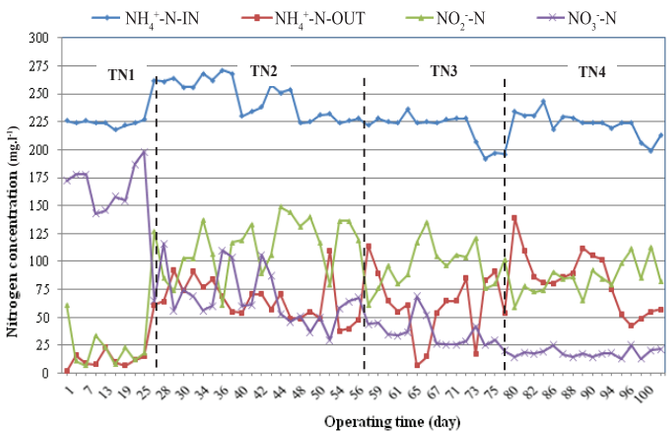

Fig. 2. Changes of nitrogen in the experiments.

In comparison with TN1, a decrease of hydraulic retention time and an increase of nitrogen load of TN2 affected a change in the nitrogen of the effluents and the ratio of N-NH_4^+:NO_2^--N:NO_3^--N was 1:1.8:1 (in term of nitrogen). As presented above, much more nitrite was formed resulting in nitrite accumulation and decreased nitrate concentration, thus an increase of NAR (63.6%) during this experiment. These outcomes could be explained by the consumed alkalinity during the ammonia oxidation in this experiment, which was smaller than that of the TN1 experiment (only 81%). Thus, the pH value in the reaction tank did not decrease rapidly (7.39), and the average FA concentration in this experiment was 6.29 mgN.l^{-1}. According to the figure, a correlation can be seen between FA, FNA, and the growth of nitrification bacteria with the influent that has a high ammonia concentration (>200 mg.l^{-1}) and an FA ranging from 1-10 mgN.l^{-1} (in the second area). The FA concentration was the main factor behind the suppression of NOB [23]. Therefore, in the TN2 experiment, the rate of nitrite oxidation was low and the NAR increased much more than in TN1. However, the NO_3^--N formed in this experiment still made up a high percent of the effluent (27.1%). The FA concentration of 6.29 mg.l^{-1} only suppressed a part of the NOB group and, thus, the ratio of NH_4^+-N:NO_2^--N, which was 1:1.8 (in term of nitrogen), was not appropriate since the requirement ranges from 1:1 to 1:1.3. To reach the appropriate ratio for the anammox process, reducing the hydraulic retention time is necessary.

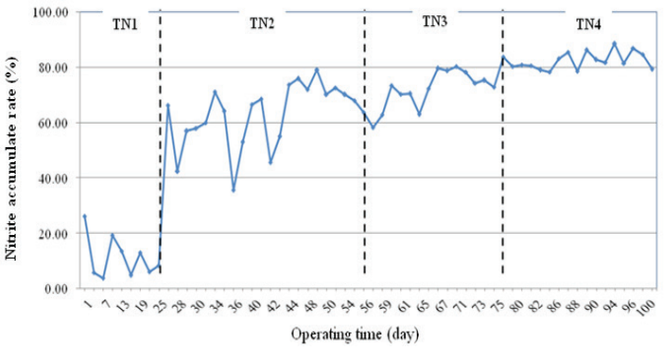

Fig. 3. Rate of nitrite accumulation in the experiments.

In the TN4 experiment, the HRT was adjusted from 8h45 to 7h30. The experimental results in Fig. 3 showed that NH_4^+-N was oxidized and the NO_3^--N concentration in the effluent was very low. The change of nitrogen in the effluent had a ratio of N-NH_4^+:NO_2^--N:NO_3^--N of 1:1.1:0.2 (in term of nitrogen) and a NAR of 82.3%. Therefore, the NH_4^+-N:NO_2^--N ratio at this hydraulic retention time was in a suitable range for the anammox process. This could be explained by the decrease of ammonia oxidation time, as the consumed alkalinity was very low (only 44.4% of the initial alkalinity), so the pH value in the reaction tank was maintained at a high level (7.59). The FA concentration in this experiment continuously increased to reach 9.1 mgN.l^{-1}, thus a strong suppression of NOB occurred. Besides, according to Refs. [14, 15], when the nitrogen load increases up to a suitable value, it is easy for nitrite accumulation or partial nitrification to occur.

Effects of Bicarbonate (HCO_3^-)

The nitrification process consumed a large amount of alkalinity (1 g NH_4^+-N requires 7.07 g alkalinity in terms of $CaCO_3$), so the pH value and FA concentration also decreased rapidly [24]. This reduced the ability of NOB suppression. Therefore, to raise nitrite accumulation, it is necessary to amend the alkalinity. The TN4 experiment (Fig. 4), after an alkalinity amendment of the influent, the nitrogen concentration had a ratio of NH_4^+-N:NO_2^--N:NO_2^--N of 1:1.6:0.6 (in terms of nitrogen) and a NAR of 72.8%. The alkalinity used in the TN3 experiment was 54%. The nitrite accumulation process increased, and the NOB growth was much more suppressed. The pH value of the reactor in this

experiment was always kept at a high level (7.99) and the FA concentration significantly rose to reach the value of 20.2 mgN.l^{-1}, same as the results reported by Refs. [20, 25].

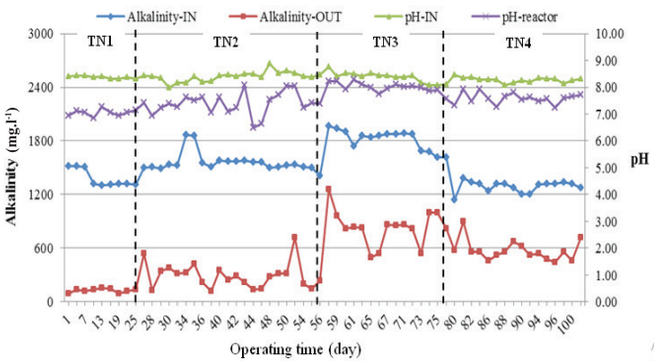

Fig. 4. Change of pH value and alkalinity in the experiments.

Assessment of organic matter removal efficiency

In the TN1 experiment (Fig. 5), the average COD removal efficiency was 41.6%, which was pretty low in comparison to other regular MBR tanks. A reason for this is that the oxygen supply (DO 1.4-1.8 mg.l^{-1}) was much lower than the required amount of oxygen to oxidize organic matter and the influent ratio of BOD_5/COD was less than 0.5, thus the amount of refractory organic compounds was large and the COD removal efficiency by biological process was low. Similarly, for the TN2, TN3, and TN4 experiments, the COD removal efficiencies were low 18.1, 10.5, and 14.29%, respectively.

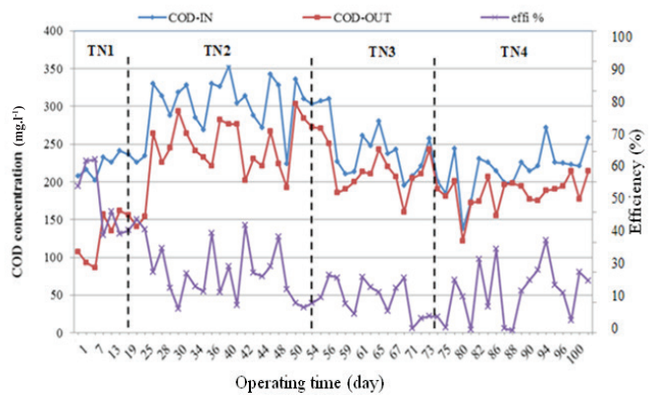

Fig. 5. COD removal efficiency versus operation time.

Conclusions

The appropriate hydraulic retention time for partial nitrification of piggery wastewater using a flat membrane is 7h30 at DO levels ranging between 0.8-1.0 mg.l^{-1}. When the alkalinity was amended in the influent to over 1600 mg.l^{-1}, the pH of the reactor was maintained at 8.0 and the FA concentration reached 20.2 mgN.l^{-1}. This increased the ability of NOB suppression and thus nitrite accumulation increased. The organic removal efficiency (COD) was low in this experimental model, as the highest efficiency was only 41.6%.

ACKNOWLEDGEMENTS

The authors deeply thank Japanese International Cooperative Association JICA-Supreme for financial aids and the technical support of Faculty of Environment and Natural Resources - University of Technology, Vietnam National University, Ho Chi Minh city for this study.

The authors declare that there is no conflict of interest regarding the publication of this article.

REFERENCES

[1] A.A. Van de Graaf, P. de Bruijn, L.A. Robertson, M.S.M. Jetten, J.G. Kuenen (1996), "Autotrophic growth of anaerobic ammonium oxidizing micro-organisms in a fluidized bed reactor", *Microbiology*, **142(8)**, pp.2187-2196.

[2] M. Strous, J.G. Kuenen, M.S.M. Jetten (1999), "Key physiology of anaerobic ammonium oxidation", *Appl. Environ. Microbiol.*, **65**, pp.3248-3250.

[3] A. Bertino (2010), *Study on one-stage partial nitritation-anammox process in moving bed biofilm reactors: a sustainable nitrogen removal*, Master Thesis, Stockholm, Royal Institute of Technology.

[4] I. Schmidt, O. Sliekers, M. Schmid, E. Bock, J. Fuerst, J.G Kuenen, M.S.M. Jetten, M. Strous (2003), "New concepts of microbial treatment processes for the nitrogen removal in wastewater", *FEMS Microbiol. Rev.*, **27**, pp.481-492.

[5] G. Ciudad, O. Rubilar, P. Munoz, G. Ruiz, R. Chamy, C. Vergara, D. Jeison (2005), "Partial nitrification of high ammonia concentration wastewater as a part of a shortcut biological nitrogen removal process", *Process Biochemistry*, **40**, pp.1715-1719.

[6] W. Jianlong, Y. Ning (2004), "Partial nitrification under limited dissolved oxygen conditions", *Process Biochemistry*, **39**, pp.1223-1229.

[7] N.H. Johansen, N. Suksawad, P. Balslev (2004), "Energy saving processes for nitrogen removal in organic wastewater from food processing industries in Thailand", *Water Science and Technology*, **50**, pp.345-351.

[8] Y.Z. Peng, Y. Chen, C.Y. Peng, M. Liu, S.Y. Wang, X.Q. Song, Y.W. Cui (2004), "Nitrite accumulation by aeration controlled in sequencing batch reactors treating domestic wastewater", *Water Science and Technology*, **50**, pp.35-43.

[9] U. Abeling, C.F. Seyfried (1992), "Anaerobic-aerobic

treatment of high-strength ammonium wastewater - nitrogen removal via nitrite", *Water Science and Technology*, **26(5-6)**, pp.1007-1015.

[10] O. Turk, D.S. Mavinic (1989), "Maintaining nitrite build-up in a system acclimated to free ammonia", *Water Res.*, **23**, pp.1383-1388.

[11] L. Kuai and W. Verstraete (1998), "Ammonium removal by the oxygenlimited autotrophic nitrification-denitrification system", *Appl. Environ. Microbiol.*, **64**, pp.4500-4506.

[12] S.K. Rhee, J.J. Lee, S.T. Lee (1997), "Nitrite accumulation in a sequencing batch reactor during the aerobic phase of biological removal", *Biotechnol. Lett.*, **19**, pp.195-198.

[13] A. Pollice, V. Tandoi, C. Lestingi (2002), "Influence of aeration and sludge retention time on ammonium oxidation to nitrite and nitrate", *Water Res.*, **36(10)**, pp.2541-2546.

[14] H. Sliegris, S. Reithaar, P. Lais (1998), "Nitrogen loss in a nitrifying rotating contactor treating ammonium rich leachate without organic carbon", *Water Sci. Technol.*, **37(4-5)**, pp.589-591.

[15] V.N. Dongen, M.S.M Jetten, M.C.M. Van Loosdrecht (2001), "The SHARON- Anammox process for treatment of ammonium rich wastewater", *Water Sci. Technol.*, **44(1)**, pp.153-160.

[16] S. Wyffels, S.W.H. van Hulle, P. Boeckx, E.I.P. Volcke, O. van Cleemput, P.A. van Rolleghem, W. Verstraete (2004), "Modelling and simulation of oxygen-limited partial nitritafition in a membrane-assisted bioreactor (MBR)", *Biotechnol. Bioengineering*, **86**, pp.531-542.

[17] Y.J. Feng, S.K. Tseng, T.H. Hsia, C.M. Ho, W.P. Chou (2007), "Partial nitrification of ammonium-rich wastewater as pretreatment for anaerobic ammonium oxidation (Anammox) using membrane aeration bioreactor", *Journal of Bioscience and Bioengineering*, **104(3)**, pp.182-187.

[18] M. Albert, B. Matias Vanotti, A.S. Ariel (2011), "Partial nitritation of swine wastewater in view of its coupling with the Anammox process", *Proceedings of First International Anammox Symposium*, pp.9-16.

[19] C.D.P. Marina, K. Airton, G. Caroline, Casagrande, M.S. Hugo (2011), "Influence of COD concentration on the partial nitritation", *Proceedings of First International Anammox Symposium*, pp.25-30.

[20] H. Xiaowu, U. Kohie, W. Qiaoyan, Y. Yuki (2016), "Fast start-up of partial nitritation as pre-treatment for Anammox in membrane bioreactor", *Biochemical Engineering Journal*, **105**, pp.371-378.

[21] L. Michele, P. Falas, R. Orlane, W. Arne, A.T. Thomas, et al. (2016), "Mainstream partial nitritation and anammox: long-term process stability and effluent quality at low temperatures", *Water Research*, **101,** pp.628-639.

[22] G.M. Wong-Chong, R.C. Loehr (1978), "Kinetics of microbial nitrite nitrogen oxidation", *Water Res.*, **12**, pp.605-609.

[23] A.C. Anthonisen, R.C. Loehr, T.B.S. Prakasam, E.G. Srinath (1976), "Inhibition of nitrification by ammonia and nitrous acid", *J. Water Pollut. Control Fed.*, **48(5)**, pp.835-852.

[24] M. Henze, P. Harremoes, J.L.C. Jansen, E. Arvin (2002), *Wastewater treatment: biological and chemical processes*, Springer.

[25] S. Uemura, S. Suzuki, K. Abe, A. Ohashi, H. Harada, M. Ito, H. Imachi, T. Tokutomi (2011), "Partial nitrification in an airlift activated sludge reactor with experimental and theoretical assessments of the pH gradient inside the sponge support medium", *Int. J. Environ. Res.*, **5(1)**, pp.33-40.

Analysing the impact of hydropower dams on streamflow in the Be river basin

Tran Thi Kim Ngan, Dao Nguyen Khoi*

Faculty of Environment, University of Science, Vietnam National University, Ho Chi Minh city

Received 22 September 2019; accepted 25 November 2019

Abstract:

The aim of the present study is to assess the effect of hydropower dams on the streamflow in the Be river basin using the Soil and Water Assessment Tool (SWAT). Model calibration and validation of SWAT were conducted using the historical data collected from two stream gauges, namely Phuoc Long and Phuoc Hoa, and the obtained results indicated that SWAT shows a good reliability in reproducing streamflow with R^2>0.90 and NSE>0.70 for both periods of calibration (1980-1990) and validation (1991-1993). Considering the results of SWAT's calibration, the hydrological impact on the streamflow needs to be taken into consideration. The study results show that the separate impact of each hydrological dam (Thac Mo reservoir, Can Don reservoir, and Srok Phu Mieng reservoir) significantly increases streamflow in the dry season (89-101%) and decreases it in the wet season (6-33%). Moreover, there is a considerable rise in the dry season (89%) and a significant decline in the wet season (33%) of streamflow under the combined impact of the three dams.

Keywords: **Be river basin, hydrological dams, streamflow, SWAT model.**

Classification numbers: **2.3, 5.1**

Introduction

Changing climate is identified as one of the crucial challenges facing humanity in the 21st century. The mitigating measures for global warming require renewable energy sources to meet the increasing demand of energy consumption, which is mainly driven by factors contributing to population growth and economic development. Hydrological dams used as renewable energy sources represent a high potential for the reduction of greenhouse gases. Additionally, these dams contribute to meeting socio-economic development requirements, which is why the construction and development of dams have greatly increased in river basins.

The construction of dams has negative effects on hydrological regimes, sedimentation, ecosystems, fisheries, and the daily livelihoods of the surrounding and downstream inhabitants [1]. Specifically, an artificial reservoir affects the natural water quality, as well as the hydrological regimes of the river that depend on storage capacity and operation [2]. Hence, assessing the effect of hydrological dams on streamflow in the river basin is necessary for supporting management and providing useful information on scientific aspects.

The Be river basin has been established as a potential development site for a large number of hydrological dams. The cascade hydropower plant is relatively far in its development in this basin, which includes stages at the Thac Mo reservoir, Srok Phu Mieng reservoir, Can Don reservoir, and irrigation systems in Phuoc Hoa. There have been several studies assessing the water resources in this area, however, almost all of them concentrate on the impact of changing climate and land use [3, 4], and none of them take the effects of hydrological dams on streamflow into consideration. Therefore, the aim of the present study is

*Corresponding author: Email: dnkhoi@hcmus.edu.vn

to investigate the effect of dams on the streamflow in the Be river basin. For this purpose, the modelling approaches, particularly the SWAT model, were selected due to their effectiveness and their wide popularity for simulating river basins.

Study area

The Be river basin is one of the four largest tributary basins of the Dong Nai river system, stretching from latitudes 11^{0}10'-12^{0}16' N to longitudes 106^{0}36'-107^{0}30' East (Fig. 1). The total catchment area is larger than 7800 km^2 and the area had a population of about 1.5 million in 2010. It includes three provinces: Binh Phuoc, Binh Duong, and Dak Nong. The basin has a tropical monsoon climate with has two individual seasons, including wet season (lasting from May to October) and dry season (November to April). In the wet season, the flood peak occurs in September and October, with the precipitation accounting for about 85-90% of the total annual rainfall in this basin [3].

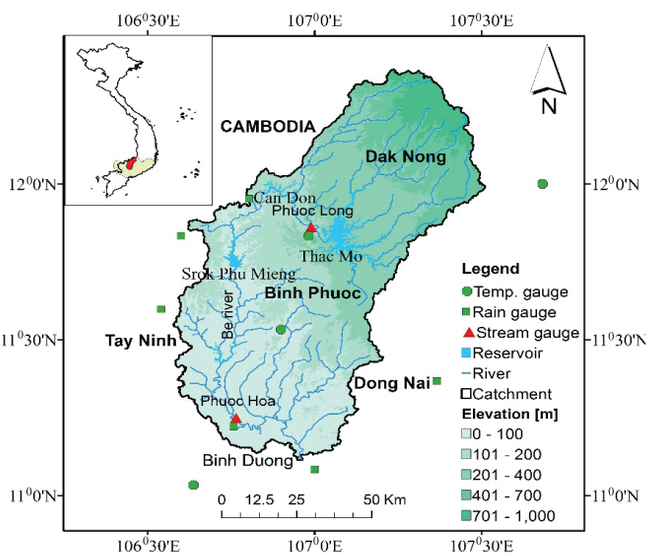

Fig. 1. Location of the Be river basin.

The terraced morphological structure of the Be river basin brings about considerable potential for hydrological dams. In the recent past, three reservoirs have been operated in the Be river, including Thac Mo (1995), Can Don (2004), and Srok Phu Mieng (2006), all of which were responses to the growing demand for electricity from the thriving southern economy (Fig. 1). The current capacity of hydropower reaches 1 billion kWh/year and is continuously increasing. In addition to these three dams, an irrigation system has been constructed in Phuoc Hoa to regulate the streamflow in the basin.

Materials and methods

SWAT model

SWAT, which is a distribution model based on physical processes, was chosen to simulate the streamflow in the Be river basin. The model was established by the United States Department of Agriculture (USDA) in the early 1990s to estimate the impact of land management practices and climate change on water, sediment, and nutrient over large spatial areas and long time periods. One of the main principles of this model is to simulate streamflow from rainfall and other regional physical characteristics [5].

To analyse large catchment areas in SWAT, the areas are partitioned into various sub-watersheds, which are then further subdivided into hydrological response units (HRUs) with homogeneous characteristics concerning soil, land use, and slope. Each HRU of the SWAT model simulates its hydrological cycle according to the following water balance equation [5]:

$$SW_t = SW_0 + \sum_{i=1}^{t}(R_{day} - Q_{surf} - E_a - W_{seep} - Q_{gw}), \quad (1)$$

wherein SW_t [mm] is the total soil water content, SW_0 [mm] is the initial soil water content, t [d] is the time, R_{day} [mm] is the precipitation, Q_{surf} [mm/d] is the surface runoff, E_a [mm] is the amount of ET (evapotranspiration), W_{seep} [mm] is the amount of water entering the ground layer, and Q_{gw} [mm/d] is the parameter for the groundwater discharge.

In the SWAT model, the reservoir is one of the main tributaries of the basin area. The reservoirs water balance is evaluated based on the following equation:

$$V = V_{stored} + V_{flowin} - V_{flowout} + V_{pcp} - V_{evap} - V_{seep}, \quad (2)$$

wherein V [m^3] is the final water volume at the end of the day, V_{stored} [m^3] is the initial water storage at the beginning of the day, V_{flowin} [m^3] is the water volume flowing into the reservoir, $V_{flowout}$ [m^3] is the surface runoff, V_{pcp} is the precipitation volume of reservoir in day (m^3 H_2O), V_{evap} [m^3] is the evaporation volume of the reservoir, and V_{seep} [m^3] is the water loss volume from leakage.

SWAT model set-up

The simulation process on the Be river basin is implemented via ArcSWAT, which is an updated version of the SWAT model. In order to set up the SWAT model, there

are five steps as follows: (1) data preparation (Table 1), (2) delineation of the sub-basin, (3) Hydrologic Response Unit (HRU) definition, (4) weather data input, and (5) calibration and validation using sequential uncertainty fitting with the SUFI - 2 algorithm. Then, the model is run under reservoir scenarios.

Table 1. Data collection in this study.

Data type	Description	Source
DEM	Elevation, slopes and lengths, a spatial resolution of 90 m	USGS-Hydro-SHEDS
Land use	Land use types in 2005	Sub-National Institute of Agricultural Planning and Projection (Sub-NIAPP)
Soil	Soil type, a spatial resolution of 1 km	Food and Agriculture Organization (FAO)
Weather	Daily precipitation (mm) and temperature (^{0}C) during 1978-2013 at 9 meteorological stations	Hydro-Meteorological Data Centre (HMDC)
Hydrology	Daily streamflow (m^3/s) at Phuoc Long and Phuoc Hoa stations	Hydro-Meteorological Data Centre (HMDC)
Reservoir	Reservoir parameters and discharge flow at three hydropower: Thac Mo, Can Don and Srok Phu Mieng	The hydropower in Thac Mo, Can Don and Srok Phu Mieng

The simulation result of the SWAT model is compared against the monitoring data using statistical parameters such as the coefficient of determination (R^2), Nash-Sutcliffe (NSE), and error percentage (PBIAS). The assessment standard is based on the study of [6] as described in Table 2.

Table 2. Model performance evaluation criteria for streamflow.

Effective simulation	R^2	NSE	PBIAS
Very good	0.85-1.00	0.80-1.00	≤±5%
Good	0.75-0.85	0.70-0.80	±5-10%
Satisfactory	0.60-0.75	0.50-0.70	±10-15%
Not satisfactory	≤0.60	≤0.50	>±15%

Result and discussion

Calibration and validation of the SWAT model

SWAT was established for the study area, and calibration results were simulated for the periods without the impact of a reservoir before 1993. The most sensitive parameters were selected for calibrating the streamflow in accordance with the study of [4]. Table 3 illustrates the SWAT-calibrated parameters for simulating streamflow.

Table 3. SWAT parameters calibrated for simulating streamflow.

No.	Parameter	Description	Min-Max value	Calibrated value
1	v_EPCO	Factor of compensation of water consumption by plants	0-1	0.77
2	r_SOL_K	Saturated soil hydraulic conductivity (mm h-1)	-0.25-0.25	-0.19
3	v_CH_N2	Manning coefficient for the main channel (s m-0.33)	-0.01-0.3	0.17
4	v_GW_REVAP	Coefficient of water rise to saturation zone (dimensionless)	0.02-0.2	0.19
5	v_CH_K2	Effective hydraulic conductivity of the channel (mm h-1)	-0.01-500	203.95
6	r_SOL_ALB	Soil Albedo (dimensionless)	-0.1-0	0.03
7	r_CN2	Number of the initial curve for the moisture condition AMCII (dimensionless)	-0.5-0.13	-0.21
8	v__GWQMN	Water limit level in the shallow aquifer for the occurrence of base flow (mm)	0-500	2296.71
9	v__GW_DELAY	Time interval for recharge of the aquifer (days)	0-500	23.79
10	v_ALPHA_BF	Baseline flow recession constant (days)	0-1	0.99

v: replaced value, r: ratio value.

Figures 2 and 3 compare simulated and observed daily streamflow for the calibration (1980-1990) and validation (1991-1993) periods. The results show an agreement between the observed and simulated data, shown in Table 4. However, the simulated streamflow value on the flooding and dry season, as well as the peak flood, does not fit with the observed value. This is caused by an uneven spatial rain gauge distribution and errors during the measurement process. Evidently, the range of R^2 varied from 0.90 to 0.91, NSE varied from 0.77 to 0.80, PBIAS varied from -14% to 9% for the calibration period, and the range of R^2 varied from 0.91 to 0.93, NSE varied from 0.82 to 0.86, PBIAS varied from 4% to 10% for the validation period. In general, the results of the calibration and validation steps indicate that SWAT can simulate streamflow in the Be river basin, the results of which could be used for investigating the impact of hydropower and reservoir on the streamflow.

Table 4. The calibration and validation result of streamflow at two stations.

Station	Calibration (1980-1990)			Validation (1991-1993)		
	R^2	*NSE*	*PBIAS*	*R^2*	*NSE*	*PBIAS*
Phuoc Long	0.90	0.80	9%	0.91	0.82	10%
Phuoc Hoa	0.91	0.77	-14%	0.93	0.86	4%

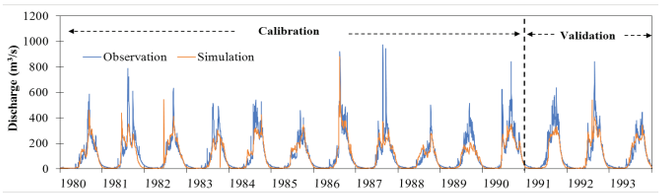

Fig. 2. The comparison between simulated and observed daily streamflow at the Phuoc Long station for the calibration period (1980-1990) and the validation period (1991-1993).

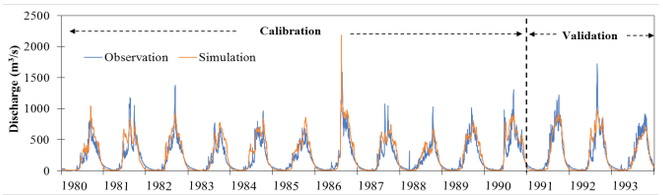

Fig. 3. The comparison between simulated and observed daily streamflow at the Phuoc Hoa station for the calibration period (1980-1990) and the validation period (1991-1993).

The impact of hydropower on streamflow

After the calibration and validation steps for streamflow without the impact of hydropower (1980-1993), the reservoir parameters involving discharge were used to evaluate the change of streamflow under reservoir impact. Figs. 4-6 illustrate the flow discharge simulation results at the Phuoc Hoa station, and show that they are affected by the three hydropower plants Thac Mo (in operation since 1995), Can Don (in operation since 2004), and Srok Phu Mieng (in operation since 2006). Considering the simulation results of the SWAT model, it is recognized that the SWAT model with the reservoir module satisfactorily simulate streamflow in the Be river basin under the impact of hydropower. The resulting statistical parameters concerning the effectiveness of the SWAT model's simulation are shown in Table 5.

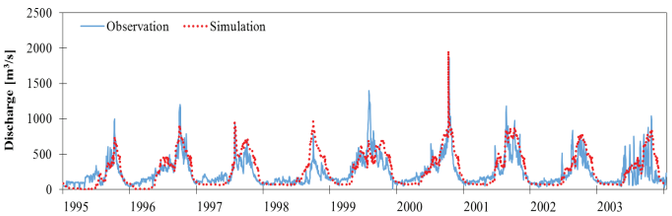

Fig. 4. The comparison between simulated and observed daily streamflow at the Phuoc Hoa station under Thac Mo hydropower operation (1995-2003).

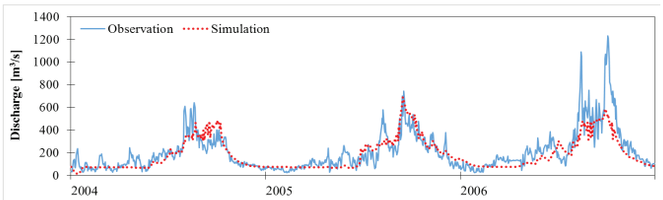

Fig. 5. The comparison between simulated and observed daily streamflow at the Phuoc Hoa station under Thac Mo and Can Don hydropower operations of (2004-2006).

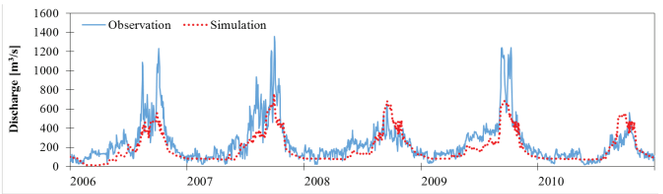

Fig. 6. The comparison between simulated and observed daily streamflow at the Phuoc Hoa station under the Thac Mo, Can Don, and Srok Phu Mieng hydropower operations of (2006-2010).

Table 5. The effectiveness of streamflow simulation at the Phuoc Hoa station under the hydropower scenarios.

Station	Thac Mo (1995-2003)			Thac Mo and Can Don (2004-2006)			Tha Mo, Can Don and Srok Phu Mieng (2006-2010)		
	R^2	*NSE*	*PBIAS*	R^2	*NSE*	*PBIAS*	R^2	*NSE*	*PBIAS*
Phuoc Hoa	0.77	0.42	-9%	0.81	0.64	11%	0.80	0.55	23%

With the streamflow simulation results under the impact of hydropower being satisfactorily reliable, the study investigates the impact of hydropower utilization on the Be river streamflow during the period of 2006-2013 under three scenarios: Scenario (1) - without hydropower, Scenario (2) - only one hydropower plant (Thac Mo, Can Don, or Srok Phu Mieng), and Scenarios (3) - the combination of the three hydropower plants.

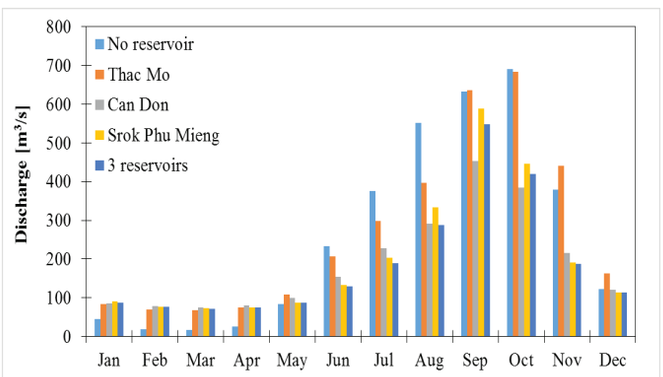

Fig. 7. Average monthly water discharge for three simulation scenarios during the period of 2006-2013.

Figure 7 illustrates the average monthly water discharge for the three scenarios. The result shows that streamflow in the dry season (December to May) is higher than normal conditions when the interventions of hydropower are operated to regulate water in the entire basin, contributing significantly to water scarcity during this period. By contrast, in the rainy season, the water discharge on river could be reduced in hydropower scenarios due to the storage volume of the reservoirs.

Table 6. The change in percentage ratio of streamflow under hydropower scenarios in Be river basin during 2006-2013 periods.

Season	Trend	Thac Mo	Can Don	Srok Phu Mieng	Three hydropower
Dry	Increase	101%	93%	89%	87%
Rainy	Decrease	6%	38%	33%	37%

Based on the quantified results seen in Table 6, the study indicates that dams regulate water in the lower river leading to an increased streamflow by 101, 93, and 89%, at the Thac Mo, Can Don, and Srok Phu Mieng stations, respectively, and 87% for the combined three hydropower plants, in comparison to the scenario without hydropower use in the dry season. On the other hand, the role of the hydropower dams in regulating flooding, and, as a result, mitigating its damage in the lower river could be significant if they are managed accordingly. When hydro-electric plants such as Thac Mo, Can Don, and Srok Phu Mieng begin operating, the water discharge in the rainy season decreases gradually by 6, 38, and 33%, respectively, and the three-dam scenario declines by 37% in comparison to the scenario without the use of hydropower.

Conclusions

In this study, the impact of hydropower reservoir operation on streamflow was investigated using the SWAT model. The results can be briefly described as follows: (1) SWAT could simulate the streamflow for the Be river basin with the satisfactory accuracy; (2) considering the separate effect of hydropower reservoir operation (Thac Mo, Can Don, and Srok Phu Mieng), streamflow discharge in the dry season increases by 89-101% and decreases by 6-33% in the rainy season; (3) streamflow increases by 89% in the dry season and decreases by 37% in the wet season.

In addition to the obtained results, there is a limitation related to the unavailability of discharge data from reservoirs. Thus, collection of this additional data should be considered to improve the results of the model. In general, the study results could be used for reference purposes aimed to support local authorities for sustainable water resource management through the enhanced understanding of the impacts of hydropower reservoirs on the streamflow in the study area. There are also suggestions for further research related to the separate and combined impacts of climate change, land use change, and potential development of hydropower in the Be river basin.

ACKNOWLEDGEMENTS

This research is funded by Vietnam National University, Ho Chi Minh city (VNU-HCM) under grant number B2019-18-07.

The authors declare that there is no conflict of interest regarding the publication of this article.

REFERENCES

[1] A.R. Timo, O. Varis, L. Scherer, M. Kummu (2018), "Greenhouse gas emissions of hydropower in the Mekong river basin", *Environmental Research Letter*, **13(3)**, Doi:10.1088/1748-9326/aaa817.

[2] J. Hecht, G. Lacombe (2014), "The effects of hydropower dams on the hydrology of the Mekong basin", *State of Knowledge Series 5*, Vientiane, Lao PDR, CGIAR Research Program on Water, Land and Ecosystems (WLE), 16pp.

[3] D.N. Khoi, T. Suetsugi (2014), "The responses of hydrological processes and sediment yield to land use and climate change in the Be river catchment, Vietnam", *Hydrological Processes*, **28(3)**, pp.640-652.

[4] L.V. Thang, D.N. Khoi, H.L. Phi (2018), "Impact of climate change on streamflow and water quality in the upper Dong Nai river basin, Vietnam", *La Houille Blanche*, **1**, pp.70-79.

[5] S.L. Neitsch, J.G. Arnold, J.R. Kiniry, J.R. Williams (2009), "Soil and water assessment tool, theoretical documentation: version 2009", *Agricultural Research Service and Texas A&M Blackland Research Center*, 597pp.

[6] D.N. Moriasi, J.G. Arnold, M.W.V. Liew, R.L. Bingner, R.D. Harmel, T.L. Veith (2007), "Model evaluation guidelines for systematic quantification accuracy in watershed simulation", *Transactions of the ASABE*, **50(3)**, pp.885-900.

 Doi: 10.31276/VJSTE.61(4).40-47

Removal of natural organic matter from water by coagulation and flocculation to mitigate the formation of chlorine-disinfection by-products: a case study at Chinaimo water treatment plant, Vientiane capital, Laos

Inthavongkham Phanutda and Ngo Anh Dao Ho*

Faculty of Environment and Labour Safety, Ton Duc Thang University

Received 12 August 2019; accepted 22 November 2019

Abstract:

The reaction between natural organic matter (NOM) and chlorine during disinfection of water potentially forms trihalomethanes (THMs), which are classified as dangerous, carcinogenic disinfection by-products. Thus, this study aimed to investigate the removal of NOM by using coagulation and flocculation via jar tests of the raw water collected from the Chinaimo water treatment plant in Laos. Several different coagulants, such as $Al_2(SO_4)_3$ (alum), polyaluminium chloride (PAC), and iron chloride ($FeCl_3$), and the flocculant polyacrylamide (PAM) were examined to determine the optimal operational conditions (i.e. coagulant dosage, flocculant dosage, and initial pH). The removal efficiency was evaluated by turbidity, NOM measured as total and dissolved organic carbon (TOC and DOC), ultraviolet absorbance at 254 nm (UV-254), and trihalomethane formation potential (THMFP). Results showed that 60 mg/l of alum, 40 mg/l of PAC, and 80 mg/l of $FeCl_3$ were the optimal dosages for coagulation, while a 0.2-0.3 mg/l of PAM was effective for flocculation. Optimal initial pH values of 7.0, 6.0, and 8.0 were found for the alum, PAC, and $FeCl_3$ coagulants, respectively. At the optimal conditions, the removal efficiency of turbidity was over 90% in all cases, which was higher than that of NOM (i.e. DOC of 31-42%, TOC of 19-52%, UV-254 of 17-39%, THMFP of 44-48%).

One sentence summary: NOM can be removed from water by coagulation-flocculation with $Al_2(SO_4)_3$ (alum) at a dosage of 60 mg/l, PAM dosage of 0.2 mg/l, and adjusted pH of 7.0.

Keywords: **disinfection by-products, flocculation and coagulation, natural organic matter, trihalomethanes, trihalomethane formation potential.**

Classification numbers: **2.3, 5.1**

Introduction

Chlorination is widely used for disinfection of water and wastewater since it is efficient, easily supplied and operated, and cost effective. Most municipal water treatment plants in Laos use chlorine (Cl_2) for disinfection [1, 2]. However, it has also been discovered that the use of chlorine poses potential health risks due to the formation of disinfection by-products (DBPs), such as trihalomethanes, which are recognised as carcinogenic halo-organic compounds.

THMs are formed from the chemical reaction of natural organic matter (NOM) and Cl_2 during the disinfection process. NOM is widely described as a complex mixture of organic compounds that occur naturally in groundwater and surface water. Two common types of NOM are humic acids and fulvic acids, which cause colour and odour in water bodies [3]. The presence of NOM in water sources does not cause serious effects on the human's health, but problems arise when water sources containing NOM are treated with Cl_2 and other chlorine related compounds during the disinfection stage. Chlorination of water containing NOM is believed to be the most important precursor to the formation of THMs and it enables the growth of microorganisms in the treatment unit or distribution system [4, 5]. Typically, four types of THMs are found in chlorinated water, including chloroform ($CHC1_3$), dichlorobromomethane ($CHCl_2Br$), dibromochloromethane ($CHBr_2Cl$), and bromoform ($CHBr_3$) [6]. THMs are also reported to be the dominant

*Corresponding author: Email: hongoanhdao@tdtu.edu.vn

species of DBPs, followed by haloacetic acids (HAAs) in water systems [6]. The total concentration of THMs and the formation of individual THM species in chlorinated water strongly depend on the concentration and properties of NOM, type of disinfection chemical and dose, and operational conditions (e.g. reaction time, temperature, and pH). Legislation has been strictly regulated to control allowable DBP levels in drinking water. The maximum contaminant level for THMs is set at different levels in developed countries, such as 80 µg/l in the US, 250 µg/l in Australia, 100 µg/l in Canada, 10 µg/l in Germany, and 100 µg/l in the EU [7]. Moreover, according to the World Health Organization (WHO) and the United States Environmental Protection Agency (US EPA), the limits for a total of five HAAs and bromate in drinking water are 60 µg/l and 10 µg/l, respectively [8]. Some negative effects of THM exposure due to the usage of chlorinated public water supplies (e.g., drinking and bathing) are low birth weight, small gestational size, and cancer [9, 10].

A conventional water treatment system normally comprises of coagulation-flocculation, sedimentation, rapid sand filtration, and disinfection. Coagulation-flocculation process is used to remove common physical parameters of surface water, such as suspended solids, turbidity, and colour. For NOM removal, it was reported that treatment efficiency was strongly affected by many factors, including the characteristics of raw water (e.g., nature and properties of NOM particles) and operational conditions (e.g., type and dose of coagulants/flocculants, pH, ionic strength, temperature, and turbidity) [11]. Other advanced treatments, such as adsorption with activated carbon, ion exchange, electro-coagulation, bio-filtration, membrane filtration, and advanced oxidation, have been investigated for NOM removal [5]. However, in terms of cost, coagulation and flocculation is generally considered to be an effective and economical option for NOM removal compared to other advanced alternatives, especially in the case of large-capacity water treatment plants [11]. Thus, the removal of NOM from surface water by using coagulation-flocculation technique should be investigated in detail, and performed at a real water treatment plant to demonstrate the practical applicability.

The Chinaimo Water Treatment Plant (CWTP) is a main water supply source of Vientiane, the capital of Laos. CWTP was established in 1980 with an initial capacity of 40,000 m^3/day. Currently, the plant is operated with a capacity of 120,000 m^3/day to supply tap water for 156,335 households over the 7 districts of Vientiane. A conventional water treatment process is designed and operated at CWTP, in which raw water is collected from the Mekong River at the water intake and pumping station located on the boundary of Xaysathan (upstream side) and Phonsavang village (downstream side). The current water treatment process at CWTP focuses on removal of common pollutants, such as turbidity, colour, and microorganisms. Although the water quality currently produced by CWTP satisfies the national standard (i.e., Ministry of Natural Resources and Environment, Decree No. 81/MONRE issued in 2017 [12]) and is safe for people's health, the removal of NOM has been not considered during the treatment.

Therefore, the objective of this study is to investigate the optimal operational conditions for NOM removal by chemical coagulation and flocculation, which was carried out through a case study at CWTP. The optimal initial pH of water, types and optimal dosages of coagulants (i.e., alum as $Al_2(SO_4)_3$, PAC and $FeCl_3$), and flocculant dosages (i.e., PAM) for NOM removal via jar tests were examined. The treatment efficiency is evaluated by considering the removal percentage of turbidity and NOM, in which NOM is measured by total and dissolved organic carbon, ultraviolet absorbance at a wavelength of 254 nm, and trihalomethane formation potential.

Materials and methods

Raw water samples collection, preservation, and characterisation

Raw water samples are collected from the water intake of CWTP by using the grab sampling method with 10 high density polyethylene (HDPE) tanks with 20 l capacity. The grab sampling procedure includes 2 sampling times, where the interval between samples is 16 hours, thus the experimental water samples were obtained from mixed samples. The sampling procedure was taken at a specific time when the pumping station is operating at the average daily flow rate. Since the pH and dissolved oxygen (DO) of the water sample can change rapidly once the sample is removed from the flow, these parameters were measured on-site during the grab sampling.

Afterwards, all samples were preserved by sodium thiosulfate ($Na_2S_2O_3$) to eliminate biological reaction, hydrolysis of organic compounds and complexes, and water evaporation. It was reported that $Na_2S_2O_3$ is a satisfactory dechlorinating agent that neutralizes any residual halogen and prevents the continuation of bactericidal actions during the transfer and chilling of samples at 4^0C.

The properties of raw water were characterized by physical-chemical parameters including pH, temperature, turbidity, TOC, DOC, UV-254, THM content, and THMFP. The above factors are important to assess the occurrence of NOM in water. Due to the heterogeneous and undefined character of NOM, surrogate parameters (i.e., TOC, DOC, and UV-254) are normally used for measurement [6]. Also, UV-254 provides an indication of NOM concentration and the DBPs formation potential when Cl_2 is added for disinfection [13].

Jar test experimental design

Jar test apparatus: in this study, a common jar test apparatus containing six paddles corresponding to six 1.0-l beakers (i.e., B1-B6) was used. An rpm gauge at the top-centre of the system allowed the control of mixing speed in all beakers (i.e. 20 rpm in 3 mins for initial rapid mixing or 200 rpm in 17 mins for slow mixing flocculation). The jar test system simulates the coagulation and flocculation process at CWTP to investigate the practicability of removal of suspended colloids and organic matter from water. Thus, the jar test control procedure was based on the real operational parameters at CWTP.

Coagulants and flocculants preparation: during the jar test experiments, alum, PAC, and $FeCl_3$ were used as coagulants, while PAM was used as the flocculant. The preparation of the above reagents is described below.

- Coagulants, including alum, PAC, and $FeCl_3$, at different dosages (i.e., 10, 20, 40, 60, 80, and 100 mg/l) were prepared from their corresponding 1% stock solutions and distilled water.

- The flocculant PAM, at different dosages (i.e., 0.05, 0.10, 0.15, 0.20, 0.25 and 0.30 mg/l), was prepared from a 0.01% (100 mg/l) stock solution. PAM is an anionic organic polymer used widely in water treatment as a coagulant aid with inorganic coagulants to enhance performance due to its high molecular weight and long polymer chains.

Samples preparation: raw water samples were used to test with the three coagulants (i.e., $Al_2(SO_4)_3$, PAC, and $FeCl_3$) in duplicate experiments. A total of 576 samples were used during the jar test experiments. The alkalinity and pH of all samples were measured first. Then, a pH adjustment was carried out by using 1 N NaOH and 1 N HNO_3 solutions.

Jar test experimental design: a summary of the jar test experiments is presented in Table 1. During the experiments, 3 types of coagulants, including alum, PAC, and $FeCl_3$, and flocculant PAM were used. Each substance was divided into 4 experiments (Table 1).

The experiments were conducted by varying the dosage of the 3 coagulants in a range of 10-100 mg/l and flocculant in a range of 0.05-0.30 mg/l at an initial pH range of 4.0-9.0. During experiments 1, 2 and 3, the turbidity, DOC concentration, and UV-254 value were measured and considered to determine the optimal dosage of coagulant, pH, and flocculant. In experiment 4, all parameters, including turbidity, DOC, TOC, UV-254, and THMFP, were simultaneously evaluated to compare the treatment efficiency between different coagulants.

The jar test operation was conducted at room temperature conditions (20^0C) in a duplicate-mode experimental design. All chemicals were analytical grade supplied by Water Specialist Supply Co., Ltd (www.wssthailand.com). The solutions and reagents were prepared by using distilled water.

Analytical methods and calculation

All samples before analysis were preserved according to the standard methods of APHA, AWWA, and WEF (2005) [14]. The physical and chemical parameters were then analysed and measured under laboratory conditions in accordance with the standard of APHA, AWWA, and WEF [14]. Specifically, the pH was determined by using a pH meter (Model: Eutech, cyber scan 510 PC) and turbidity was measured by using a turbidity meter (Model: HACH 2100 P). The UV-254 absorbance measurements were carried out by a UV/vis Spectrometer (Model: Jasco V-530 at a wavelength of 254 nm with a 1 cm quartz cell). Before UV-254 analysis, the samples were filtered through a prewashed membrane filter with pore size of 0.45 µm to remove turbidity. For NOM parameters, the TOC measurement was performed with a TOC analyser (Model: Tekmar-Dohrman Phoenix 8000), whereas for DOC, samples were firstly filtered through glass-fibre filters (GFC) of pore size 0.45 µm before TOC analysis. THM concentration was determined by the liquid-liquid extraction gas chromatographic method, in which the total concentration of the four THMs (chloroform, bromodichloromethane, dibromochloromethane, and bromoform) was reported as TTHM in units of µg/l. The

Table 1. Summary of Jar test experiments.

No.	Experiment 1			Experiment 2			Experiment 3			Experiment 4		
	Coagulant dose (mg/l)	*pH initial*	*PAM dose (mg/l)*	*Coagulant dose (mg/l)*	*pH initial*	*PAM dose (mg/l)*	*Coagulant dose (mg/l)*	*pH initial*	*PAM dose (mg/l)*	*Coagulant dose (mg/l)*	*pH initial*	*PAM dose (mg/l)*
1	10	7.0	0.10	a	4.0	0.10	a	b	0.05			
2	20	7.0	0.10	a	5.0	0.10	a	b	0.10	a	b	c
3	40	7.0	0.10	a	6.0	0.10	a	b	0.15			
4	60	7.0	0.10	a	7.0	0.10	a	b	0.20			
5	80	7.0	0.10	a	8.0	0.10	a	b	0.25	Be corresponding to each coagulant		
6	100	7.0	0.10	a	9.0	0.10	a	b	0.30			

Coagulant: $Al_2(SO_4)_3$, PAC, and $FeCl_3$; flocculant: anion polymer (PAM); a: optimal coagulant dose obtained from experiment 1; b: optimal pH obtained from experiment 2; c: optimal flocculants dose obtained from experiment 3.

TTHM measurement was carried out by a head-space gas chromatograph ECD detector (Model: Perkin Elmer, Autosystem XL) and column Supelco 241 35-U PTE^{tm}-5 under the following conditions: carrier gas N_2 and He flow rates of 2 ml/min, injection temperature of 220^{0}C, oven temperature of 55^{0}C for 15 min, and detector temperature of 300^{0}C. The THMFP was determined by measuring THMs formed after adding Cl_2 (~20 mg/l) to all samples within a reaction time of 4 h at 35^{0}C. THMFP was calculated from the difference in concentration between the instantaneous THMs (inst THMs) and terminal THMs (term THMs). Inst THMs is the THM concentration in water measured while sampling. In contrast, the total THMs (TTHM) or term THMs is the THM concentration measured at the end of the reaction between Cl_2 and precursor in the water supply system.

Results and discussion

Characterisation of raw water

The characterisation results of raw water collected from the Mekong river at the CWTP water intake is presented in Table 2. Specifically, the pH was in a range of 7.48-8.20 and turbidity was 13.00-15.60 NTU. Organic substances measured in the form of DOC, TOC, UV-254, and THMFP, were detected in large quantities (i.e., 1.82-3.98 mg/l, 2.61-4.72, 0.054-0.514 cm^{-1}, and 87.53 µg/l, respectively). However, the concentrations of total THMs were not detected (≤1) in the raw water since disinfection with Cl_2 had not yet occurred at this stage and, thus, the reaction between organic substances and Cl_2 has not taken place.

Table 2. Characteristics of raw water collected at CWTP water intake.

Parameter	Unit	Raw water	National Standard (Lao PDR)
pH		7.4-8.2	5-9
Turbidity	NTU	13.0-15.6	<20
Dissolve organic carbon (DOC)	mg/l	1.82-3.98	2[3]
Total organic carbon (TOC)	mg/l	2.61-4.72	4[4]
Ultraviolet at 254 nm (UV-254)	cm^{-1}	0.054-0.514	-
Total THMs[1]	µg/l	ND[2]	-
THMFP	µg/l	87.53	-

[1]Total THMs is measured and calculated by the concentration of $CHCl_3$, $CHBrCl_2$, $CHBr_2Cl$, and $CHBr_3$; [2]ND= Not detected due to the detection limit of the analysis method; [3]According to US-EPA standard; [4]According to WHO standard.

As compared to the Laos National Standard of Raw Water Sources issued by the Ministry of Natural Resources and Environment, Decree No. 81/MONRE (2017), the water quality at the CWTP water intake satisfied the regulations. For NOM parameters (i.e., TOC, DOC, UV-254) and DBPs (i.e., TTHMs and THMFP), there is still no standard to apply to raw water in Laos at the moment. The results of raw water characteristics were then used as a background data to evaluate the removal efficiency during the coagulation - flocculation simulated by the jar test experiments conducted in this study.

Optimal conditions for coagulation - flocculation and water treatment efficiency

Optimal dosage of coagulants: a jar test experiment was carried out to determine the optimal dosage of coagulants. The $Al_2(SO_4)_3$, PAC, and $FeCl_3$ concentrations were varied in a range of 10.0-100.0 mg/l, corresponding to beakers 1-6, whereas an initial pH of 7.0 and an PAM polymer dose of 0.10 mg/l were kept constant. The results were evaluated based on turbidity, DOC, and UV-254 of the water samples pipetted from beaker after static settling.

Specifically, the turbidity decreased linearly along with the increase of $Al_2(SO_4)_3$ dosage (Fig. 1). The highest turbidity removal efficiency, 97.31%, corresponding to a turbidity of 0.35 NTU, was obtained at an $Al_2(SO_4)_3$ dosage of 100 mg/l.

In contrast, when PAC and $FeCl_3$ were used, the turbidity removal efficiency fluctuated with the increase of PAC and $FeCl_3$ dosage. The highest turbidity removal efficiency was 95.04% (i.e., turbidity of 0.65 NTU) at a PAC dosage of 40 mg/l, and 94.80% (i.e., turbidity of 0.78 NTU) at a $FeCl_3$ dosage of 60 mg/l.

In terms of DOC, the concentration measured from settled water fluctuated with an increase of coagulant dosage. Accordingly, the highest DOC removal efficiencies were 34.88, 51.76, and 55.35% (i.e. corresponding to DOC concentration of 1.68, 1.92, and 1.21 mg/l), which were found at alum, PAC, and $FeCl_3$ dosages of 40.0, 40.0, and 60.0 mg/l, respectively.

In the case of alum, the UV-254 sharply fluctuated when alum dosage was increased. In contrast, a slight change was found in the PAC and $FeCl_3$ case. The lowest UV-254 intensity of settled water was 0.0554 cm^{-1}, 0.0528 cm^{-1}, and 0.0842 cm^{-1} obtained for alum, PAC, and $FeCl_3$ dosages of 60, 40, and 100 mg/l, respectively.

Previous studies also investigated the removal of NOM and DBPs in the Tigris river (Baghdad) by using alum and $FeCl_3$ via jar tests [15]. However, the results showed a different trend, in which the increase of alum and $FeCl_3$ dosage resulted in the decrease of turbidity and NOM. Similarly, another study also showed that when the $FeCl_3$ amount was increased from 10 to 80 mg/l, the removal efficiency of NOM also increased [16].

When taking all results (i.e. turbidity, DOC, and UV-254) and the cost aspect into consideration, the final optimal

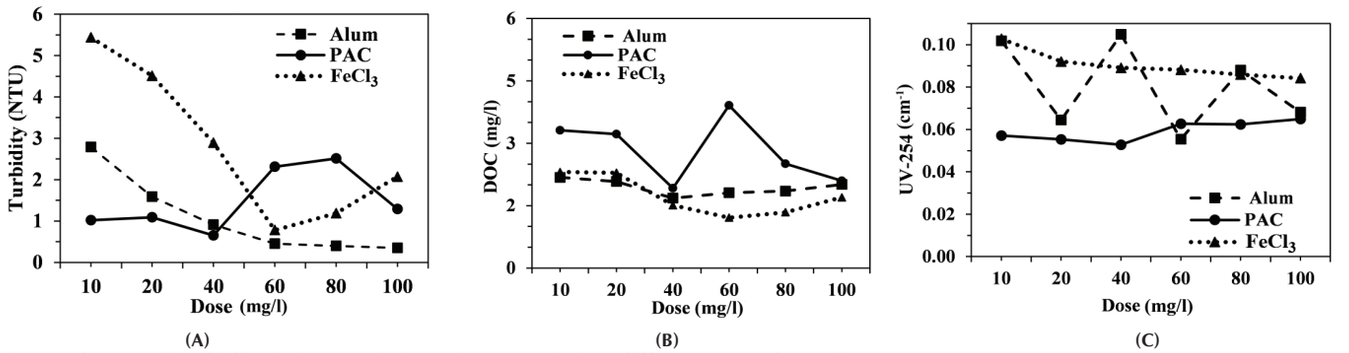

Fig. 1. Change of turbidity (A), DOC (B), and UV-254 (C) at different coagulants dosage.

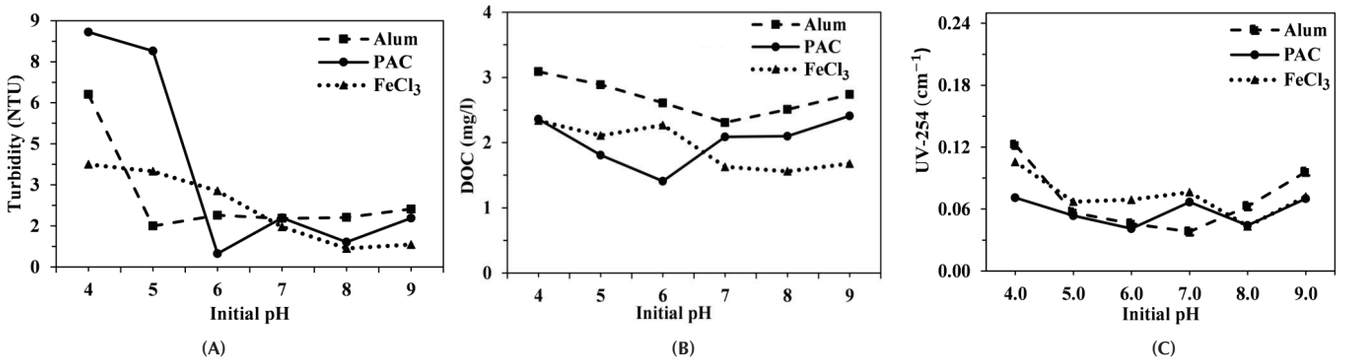

Fig. 2. Change of turbidity (A), DOC (B), and UV-254 (C) at different initial pH.

$Al_2(SO_4)_3$, PAC, and $FeCl_3$ dosage was chosen as 60.0, 40.0 and 80.0 mg/l, respectively. At the chosen $Al_2(SO_4)_3$ dosage of 60 mg/l, the turbidity and DOC removal efficiency was not much different at dosages of 100 and 40 mg/l (Figs. 1A and 1B). Similarly, at the chosen $FeCl_3$ dosage of 80 mg/l, the removal efficiencies of all parameters did not change much (Fig. 1C). These chosen optimal values were then used for further experiments.

Optimal initial pH of raw water: the adjustment of pH is an important factor strongly affecting coagulation and flocculation. In this experiment, the initial pH of the raw water samples was varied in a range of 4.0-9.0, corresponding to beakers 1-6. The optimal dosage of $Al_2(SO_4)_3$ (60 mg/l), PAC (40 mg/l), and $FeCl_3$ (80 mg/l) obtained from Experiment 1, and PAM polymer dose of 0.10 mg/l, were added to all beakers.

Results showed that the turbidity of the settled water in the three cases of coagulants investigated decreased sharply when the initial pH increased from 4 to 5-6 (Fig. 2A). When pH increased to 8-9, the turbidity did not change as much as with the alum, but the turbidity continued to decrease with $FeCl_3$. For PAC, an opposite trend was found, as turbidity increased with high pH. Accordingly, the highest turbidity removal efficiencies were 90.00%, 96.75%, and 95.64% obtained at pH of 5.0, 6.0, and 8.0 for alum, PAC, and $FeCl_3$, respectively.

When DOC was examined, the optimal effective pH value was easily found as the peaks of curves. DOC values of 2.31, 1.41, and 1.56 mg/l were found for alum, PAC, and $FeCl_3$ coagulant, respectively, as seen in Fig. 2B. Accordingly, the highest DOC removal efficiency was 29.57, 43.37, and 34.18% at initial pH values of 7.0, 6.0, and 8.0, respectively. In terms of UV-254, a pH of 7.0, 6.0, and 8.0 was also effective for alum, PAC, and $FeCl_3$, respectively, during the coagulation (Fig. 2C).

Previous studies on the removal of NOM by using coagulation with alum, $NaAlO_2$, and PAC at a pH range of 5.0-10.0 have been conducted [17]. These findings showed that a pH of 6.0-8.0 is optimal for removing NOM. This can be explained by the fact that alum has a low solubility in a pH range of 5.7-6.2. When the alum dosage is added in excess amounts, alum will form $Al(OH)_3$, which enhances the removal of turbidity. In contrast, when the pH is below 5.7, alum will dissolve in water in the form of a cations such as Al^{3+}, $Al(OH)_2^+$, and $Al(OH)^{2+}$. These cationic forms are able to give a neutralization charge at the surface of colloidal particles. On the other hand, if pH is in a basic range, the cationic states will change to $Al(OH)_4^-$.

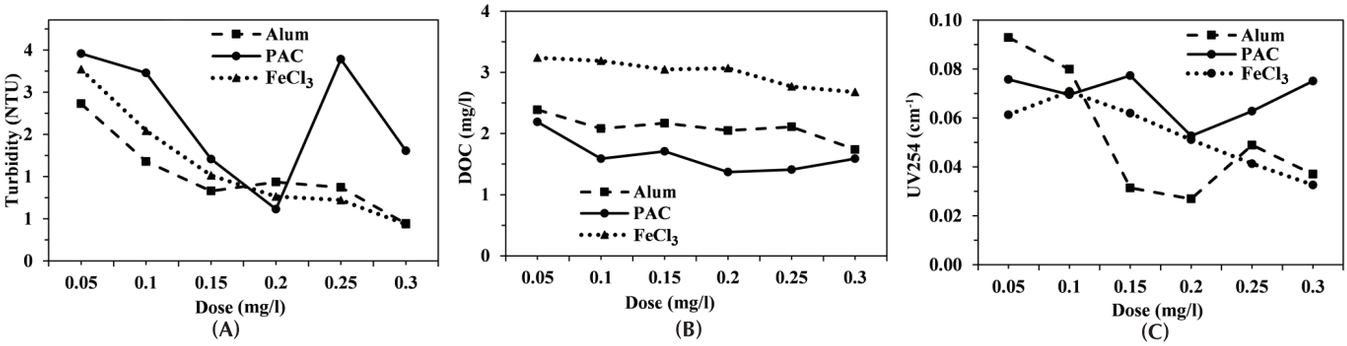

Fig. 3. Change of turbidity (A), DOC (B), and UV-254 (C) at different PAM dosages.

Another study on turbidity and NOM removal used coagulation with PAC and alum in water from the Yellow river of China [18]. The results showed that an initial pH of 6.0 is more efficient to remove turbidity, DOC, and UV-254 with the removal efficiencies of 86%, 45%, and 55%, respectively. With a pH lower than 6.0, PAC will dissolve well in water and change form to a monomer and the cationic polymers $Al_{13}O_4(OH)_{24}^{7+}$, Al^{3+}, and $AlOH^{2+}$. Similarly, when the pH is lower than 8.0, the $FeCl_3$ coagulant will also change to a cationic monomers like Fe^{3+}, $FeOH^{2+}$, and $Fe(OH)_2^+$ [19, 20]. Under this condition, NOM has a high density of negative ions (anion) and coagulants in cation form, which enhance the neutralization and precipitation as well.

In this study, when the three parameters turbidity, DOC, and UV-254 were considered, the optimal initial pH was chosen as 7.0, 6.0, and 8.0 for $Al_2(SO_4)_3$, PAC, and $FeCl_3$, respectively. The above optimal pH values were then used to in further experiments.

Optimal PAM polymer dosage: in this experiment, the PAM polymer dosage was varied in a range of 0.05-0.30 mg/l, corresponding to beakers 1-6. The optimal $Al_2(SO_4)_3$ dosage of 60 mg/l, PAC dosage of 40 mg/l, and $FeCl_3$ dosage of 80 mg/l, obtained from Experiment 1, and corresponding optimal pH of 7.0, 6.0, and 8.0, obtained from Experiment 2, were constant across all beakers.

Figure 3A shows that the increase of polymer dosage promoted the flocculation in the case of alum and $FeCl_3$ coagulants. Specifically, the turbidity of settled water in these cases decreased sharply along with the increase of PAM dosage. However, when the coagulant PAC was used, an increase of PAM polymer dosage over 0.2 mg/l caused a lower performance as the turbidity of water increased. Therefore, in terms of turbidity removal, a PAM dosage of 0.3 mg/l was effective when using coagulant as alum and $FeCl_3$, whereas a PAM dosage of 0.2 mg/l should be used with PAC.

However, the use of PAM polymer had little effect on NOM removal evidenced by DOC. As shown in Fig. 3B, the DOC concentration in all cases changed slightly when PAM dosage was varied. Accordingly, the NOM removal efficiency was around 30-40% in all cases. A PAM dosage of 0.2 mg/l was seemly effective for the alum and PAC cases, whereas a PAM dosage of 0.3 mg/l resulted in high NOM removal for the $FeCl_3$ coagulant.

In terms of NOM removal determined by UV-254, trends different from those measured by DOC were found (Fig. 3C). However, a PAM dosage of 0.2 mg/l still showed as an effective dosage for alum and PAC case. Also, a PAM dosage of 0.3 mg/l caused a high performance in the $FeCl_3$ case.

At the end of this experiment, when all results were considered simultaneously, the optimal dosage of the PAM polymer was chosen as 0.20, 0.20, and 0.30 mg/l for $Al_2(SO_4)_3$, PAC, and $FeCl_3$, respectively. These optimal values were used in the final experiment to compare the performance of different coagulants.

Comparison of different coagulants: experiment 4 was conducted based on the results obtained from experiments 1, 2, and 3. Specifically, the optimal coagulant dosage (i.e., $Al_2(SO_4)_3$ dosage of 60.0 mg/l, PAC dosage of 40 mg/l, and $FeCl_3$ dosage of 80.0 mg/l), optimal initial pH of water sample (i.e. 7.0 with $Al_2(SO_4)_3$, 6.0 with PAC, and 8.0 with $FeCl_3$), and optimal PAM dosage (i.e., 0.20 g/l with $Al_2(SO_4)_3$, 0.20 mg/l with PAC, and 0.30 mg/l with $FeCl_3$), were used. The jar test in experiment 4 compared the removal efficiency of the different coagulants. In this experiment, 5 parameters were considered to evaluate the treatment efficiency, including Turbidity, DOC, UV-254, TOC, and THMFP (Table 3 and Fig. 4).

Table 3. Result of jar test operation for removal of turbidity and NOM from raw water with different coagulants at optimal conditions.

Type of coagulant	Optimal conditions			Influent (C_{in})(*) and effluent (C_{eff})(**) concentration									
	Coagulant (mg/l)	Initial pH	Polymer (mg/l)	Turbidity (NTU)		DOC (mg/l)		TOC (mg/l)		UV-254 (cm^{-1})		THMFP (µg/l)	
				C_{in}	C_{eff}	C_{in}	C_{eff}	C_{in}	C_{eff}	C_{in}	C_{eff}	C_{in}	C_{eff}
$Al_2(SO_4)_3$	60.0	7.0	0.20	14.30	1.29	1.98	1.18	2.61	1.31	0.054	0.035	87.53	45.40
PAC	40.0	6.0	0.20	14.48	1.31	1.82	1.25	2.65	1.26	0.075	0.061	87.53	48.91
$FeCl_3$	80.0	8.0	0.30	14.36	0.73	2.11	1.22	4.72	3.81	0.078	0.047	87.53	45.41

(*)C_{in} values were extracted from the results of raw water characteristic shown in Table 2; (**)C_{eff} values were the results obtained in experiment 4.

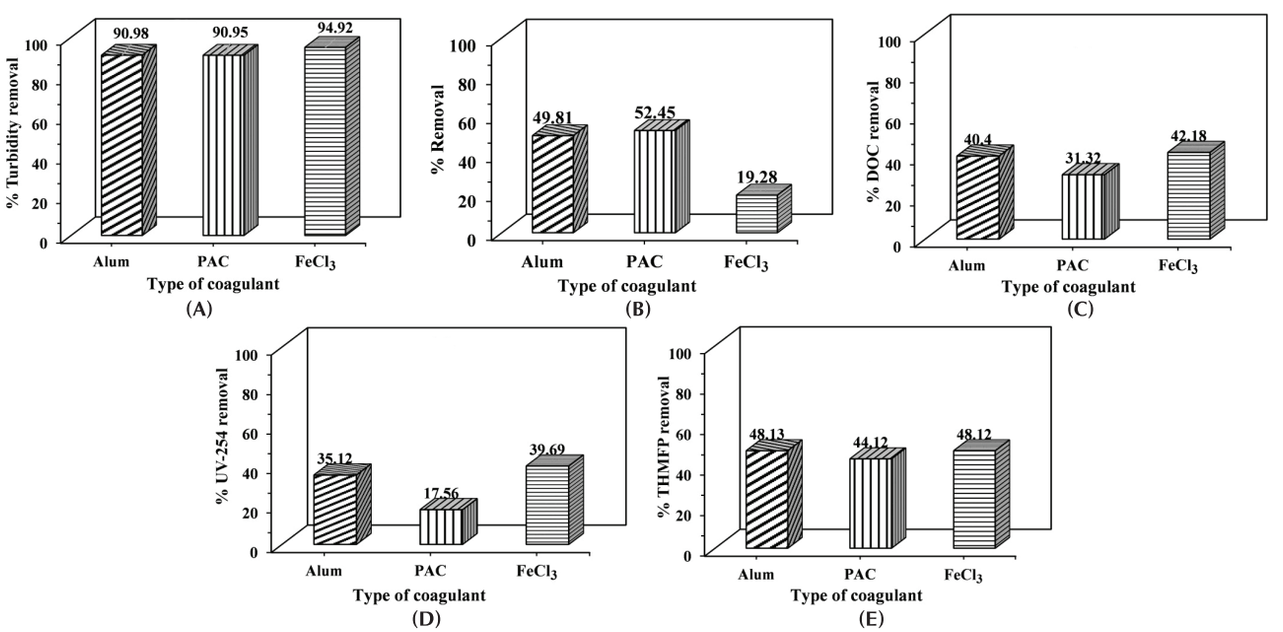

Fig. 4. Removal efficiency of turbidity (A), TOC (B), DOC (C), UV-254 (D), and THMFP (E) at the optimal operational conditions for coagulation and flocculation.

When all results were compared (Fig. 4 and Table 3), the $FeCl_3$ coagulant at an optimal dosage of 80 mg/l showed the highest removal efficiency of turbidity and NOM. Other optimal conditions were pH of 8.0 and PAM polymer dosages of 0.30 mg/l. However, it is practically unsuitable to use $FeCl_3$ as a coagulant in water treatment plant due to its yellow colour, which affects the aesthetics of drinking water.

On the other hand, $Al_2(SO_4)_3$ is more effective than PAC as the turbidity and NOM removal efficiency obtained with $Al_2(SO_4)_3$ was higher than with PAC. The optimal conditions, however, were different. Specifically, a high removal efficiency was achieved at an $Al_2(SO_4)_3$ dosage of 60 mg/l, pH 7.0, and PAM dosage of 0.20 mg/l. Meanwhile, PAC showed maximum effectiveness at an optimal dosage of 40 mg/l, pH 6.0, and PAM dosage of 0.20 mg/l.

Table 4. The cost of coagulants and flocculants.

Type of coagulant	Coagulant dosage (mg/l)	Flocculant dosage (mg/l)	Price of Coagulant dollar/m^3 raw water	Price of Flocculant dollar/m^3 raw water	Total price dollar/m^3 raw water
$Al_2(SO_4)_3$	60.00	0.20	0.042	0.0014	0.0434
PAC	40.00	0.20	0.140	0.0014	0.1414
$FeCl_3$	80.00	0.30	0.112	0.0021	0.1141

Note: $Al_2(SO_4)_3$=0.7 dollar/kilogram(*); PAC=3.5 dollar/kilogram(*); $FeCl_3$=1.4 dollar/kilogram(*); (*)The market price was obtained at the time of purchase, which was issued by Water Specialist Supply Co., Ltd.

When considering the cost of the chemicals in Table 4, ($Al_2(SO_4)_3$=0.7 dollar/kilogram, PAC=3.5 dollar/kilogram and $FeCl_3$=1.4 dollar/kilogram) and the practical situation in the CWTP water supply system, it is recommended to

use $Al_2(SO_4)_3$, instead of PAC and $FeCl_3$. For PAM polymer, the usage is similar. The total cost of chemicals of all three conditions was estimated as 0.0434, 0.1414 and 0.1141 dollar/m^3 raw water, for alum, PAC, and $FeCl_3$, respectively. Therefore, it is concluded that $Al_2(SO_4)_3$ is the most suitable coagulant to use in an actual water production system by adjusting the optimal dosage, initial pH, and flocculant dosage.

Conclusions

This research investigated the optimal operational conditions of the chemical coagulation and flocculation process with different coagulants (i.e. alum, PAC, and $FeCl_3$) to remove turbidity and NOM from surface water collected at the CWTP water intake. The results showed that the optimal dose of coagulants for alum is 60 mg/l, PAC is 40 mg/l, and $FeCl_3$ is 80 mg/l. The increase of coagulant dosage affected the removal efficiency of turbidity and NOM, in which the removal efficiency of turbidity was higher than that of NOM. The optimal initial pH for the coagulation and flocculation process with alum, PAC, and $FeCl_3$ was 7.0, 6.0, and 8.0 respectively. Therefore, in the treatment process for the removal of turbidity and NOM, it is suggested to adjust the initial pH of raw water to the above optimal values to improve the performance. The addition of the anion polymer PAM significantly affected the removal efficiency of turbidity, whereas little effects were found in the case of organic substances. The optimal dose of the anion polymer for flocculation when using different coagulants such as alum, PAC, and $FeCl_3$ were 0.20, 0.20, and 0.30 mg/l respectively. In terms of THMFP, this study showed that the coagulation and flocculation treatment under experimental conditions resulted in high removal efficiencies. Specifically, the THMFP concentration as measured in settled water satisfied the standards of WHO and US-EPA after coagulation-flocculation. Thus, it is concluded that the optimal conditions found during the jar test experiments in this study were able to maximize the treatment efficiency for reducing the formation of THMs. In addition, a comparison of the suitability and cost of the coagulants indicated that the effective coagulant to be applied in CWTP is alum, $Al_2(SO_4)_3$. Actually, this cost effective coagulant is currently being used at CWTP.

ACKNOWLEDGEMENTS

The authors would like to acknowledge the financial grant of master scholarship from Ton Duc Thang University, Vietnam.

The authors declare that there is no conflict of interest regarding the publication of this article.

REFERENCES

[1] Nam Papa Nakhone Luang (2013), *Annual Report in 2013*, Vientiane: Lao PDR.

[2] Nam Papa Nakhone Luang (2018), *Annual Report in 2018*, Vientiane: Lao PDR.

[3] I. Garcia (2011), *Removal of natural organic matter to reduce the presence of Trihalomethanes in drinking water*, Royal Institute of Technology Stockholm, Sweden.

[4] B. Chanya (2009)., *Risk assessment of trihalomethanes exposure from chlorinated swimming pools*, Master Thesis, Silpakorn University, Thailand.

[5] Y. Zhang, X. Zhao, X. Zhang, S. Peng (2015), "A review of different drinking water treatments for natural organic matter removal", *Water Supply*, **15(3)**, pp.442-455, Doi:10.2166/ws.2015.011.

[6] A. Grünwald, B. Šťastný, K. Slavíčková, M. Slavíček (2002), "Formation of haloforms during chlorination of natural waters", *Acta Polytechnica*, **42(2)**, pp.56-59.

[7] G.S. Wang, Y.C. Deng, T.F. Lin (2007), "Cancer risk assessment from trihalomethanes in drinking water", *Science of the Total Environment*, **387(1-3)**, pp.86-95.

[8] World Health Organization (2008), "Incorporating 1st and 2nd addenda", *Guidelines for drinking-water quality, 3th Edition: Volume 1- Recommendations*.

[9] R. Grazuleviciene, M.J. Nieuwenhuijsen, J. Vencloviene, M. Kostopoulou-Karadanelli, S.W. Krasner, A. Danileviciute, G. Balcius, V. Kapustinskiene (2011), "Individual exposures to drinking water trihalomethanes, low birth weight and small for gestational age risk: a prospective Kaunas cohort study", *Environmental Health*, **10(1)**, Doi: 10.1186/1476-069X-10-32.

[10] V. Uyak (2006), "Multi-pathway risk assessment of trihalomethanes exposure in Istanbul drinking water supplies", *Environment International*, **32(1)**, pp.12-21.

[11] R. Fabris, C.W. Chow, M. Drikas, B. Eikebrokk (2008), "Comparison of NOM character in selected Australian and Norwegian drinking waters", *Water Research*, **42(15)**, pp.4188-4196.

[12] Laos Ministry of Natural Resources and Environment (2017), *National Environmental Standards*, Pollution Control Department, Vientiane, Laos.

[13] A. Pabbavong (2003), *Removal of Trihalomethane precursors in water treatment system by coagulation with alum and bentonite*, Khon Kaen Unviersity, Thailand.

[14] American Public Health Association, American Water Works Association, Water Environment Federation (2005), *Standard methods for the examination of water and wastewater*, Washington, D.C.

[15] A.H. Sulaymon, A-F.M. Ali, S.K. Al-Naseri (2009), "Natural organic matter removal from Tigris river water in Baghdad, Iraq", *Desalination*, **245(1-3)**, pp.155-168.

[16] C. Musikavong, S. Wattanachira, T.F. Marhaba, P. Pavasant (2005), "Reduction of organic matter and trihalomethane formation potential in reclaimed water from treated industrial estate wastewater by coagulation", *Journal of Hazardous Materials*, **127(1-3)**, pp.48-57.

[17] M. Kabsch-Korbutowicz (2005), "Effect of Al coagulant type on natural organic matter removal efficiency in coagulation/ultrafiltration process", *Desalination*, **185(1-3)**, pp.327-333.

[18] Z. Yang, B. Gao, Q. Yue (2010), "Coagulation performance and residual aluminum speciation of $Al_2(SO_4)_3$ and polyaluminum chloride (PAC) in Yellow river water treatment", *Chemical Engineering Journal*, **165(1)**, pp.122-132.

[19] H. Ødegaard, S. Østerhus, E. Melin, B. Eikebrokk (2010), "NOM removal technologies-Norwegian experiences", *Drinking Water Engineering and Science*, **3(1)**, pp.1-9.

[20] L. Rizzo, V. Belgiorno, M. Gallo, S. Meric (2005), "Removal of THM precursors from a high-alkaline surface water by enhanced coagulation and behaviour of THMFP toxicity on D. magna", *Desalination*, **176(1-3)**, pp.177-188.

Doi: 10.31276/VJSTE.61(4).48-52

Season-dependent fine root production at a deciduous *Quercus serrata* plantation in Japan

Tran Van Do[1, 2*]

[1]*Silviculture Research Institute, Vietnamese Academy of Forest Sciences, Hanoi, Vietnam*
[2]*JSPS postdoctoral fellow (2012-2014) at Forestry and Forest Products Research Institute, Tsukuba, Japan*

Received 23 July 2019; accepted 23 October 2019

Abstract:

The production of fine roots (diameter ≤2 mm) contributes considerably to carbon cycling in forest ecosystems. Fine roots constitute a significant organic matter pool with high net primary productivity and turnover. In this study, fine root decomposition, mortality, and production were estimated at a *Quercus serrata* Murr. plantation in Japan by using rates of diameter-dependent root mortality, decomposition, and the thickening method employed. Sequential soil core and litter bag techniques were used to collect field data. The experiments were set up in a 20×20 m plot. The data were collected five times (May, August, November, and December 2013, as well as April 2014) during a one-year period, and fine roots were classified into ones with a diameter of ≤1 mm and others of 1-2 mm. The results indicate that fine root decomposition, mortality, and production in a *Q. serrata* plantation are season-dependent and are higher in the summer compared to the winter. In the summer, production reached 1.365 g m^{-2} day^{-1}, while it was lower than 0.132 g m^{-2} day^{-1} in the winter. The total fine root production of the *Q. serrata* plantation was 1.364 tonnes ha^{-1} $year^{-1}$. The mortality was 0.440 tonne ha^{-1} $year^{-1}$, and the amount decomposed to return nutrients to the soil was 0.108 tonne ha^{-1} $year^{-1}$.

Keywords: **climate, continuous inflow method, decomposition, fine root differentiation, time interval.**

Classification number: **3.1**

Introduction

Roots with a diameter of ≤2 mm are called fine roots. Their production plays an important role in forest carbon cycling [1]. Fine roots have high net primary production (NPP) and turnover because of their short longevity - up to several months [1-2]. It has been estimated that fine root production may contribute 75% of the total NPP in a forest [2]. Several factors, including vegetation type, soil fertility, temperature, and precipitation, affect the production of fine roots [1, 3]. Using a global database, Finer, et al. [1] indicated that fine root production and turnover increase from boreal to tropical forests. Fine root production and turnover are estimated by different methods, which may cause different estimations even in the same site [4].

A number of methods exist for estimating fine root production [5-7], and there is no standard method available. Comparative studies indicate significant differences in fine root estimation between methods [8]. The true answer regarding the best method is unknown because each method has potential biases, leading to over- or underestimation [3, 8]. Recently, Tran, et al. [9] developed a new method for estimating fine root production based on the continuous inflow method [7], which assumes that fine roots grow, die, and decompose simultaneously. This method [9] provides more accurate fine root production estimation, as it considers the difference in the amount and decomposition ratios of thinner and coarser fine roots (those of ≤1 mm in diameter and those 1-2 mm in diameter).

The objective of this study is to estimate fine root production at a deciduous *Quercus serrata* Murr. (*Q. serrata*) plantation by using rates of diameter-dependent root mortality, decomposition, and the thickening method employed.

Materials and methods

Study site

This study was conducted in a pure plantation of the deciduous *Q. serrata* at 36^{0}00′30″N, 104^{0}07′54″E in

*Email: dotranvan@hotmail.com

Tsukuba, Japan. Trees were planted with a spacing of approximately 5×4 m. At the time of the experiment, the plantation had a stem height of 12-30 m and a diameter at breast height of 15-35 cm. A one-year field observation revealed that *Q. serrata* trees produce leaves in early April and shed in mid-October. During the December-April period, no leaves are available on trees. The site has an average annual precipitation of 1,283 mm and an average monthly temperature of 13.2^{0}C. The maximum temperature was recorded in August (35^{0}C), while minimum temperature was recorded in January (0.4^{0}C).

Experiment

Data were collected at a 20×20 m plot. Sequential soil cores and litter bag techniques were used to collect data. A tube of 32 mm in diameter and 45 cm in length was used to take soil samples vertically to a depth of 21 cm in May, August, November, and December 2013, as well as April 2014. During each sampling period, 24 soil cores were collected randomly from a 20×20 m plot. The soil collected was washed and sieved through water to separate fine roots. A steel sieve with a mesh size of 0.2 mm was used. Water was poured directly on the soil in the sieve with high pressure to break and wash away soil particles, and then fine roots were recovered manually. The dead and living fine roots were classified by their colour, resilience, and structural integrity. Generally, dead fine roots have a dark/black colour, while living fine roots are bright and yellow-brown in colour. Fine roots were then further classified into two classes as those with a diameter of ≤ 1 mm and those with a diameter of 1-2 mm. Those categorised as fine roots were dried at 80^{0}C until a constant mass and then weighed (accuracy of 0.0001 g) for a mass of live roots (biomass/*B*), as well as that of dead roots (necromass/*N*) for both size classes, separately.

Litter bags (size of 10×15 cm) were made of special cloth, which was produced by Toyobo Co., Osaka, Japan. The cloth had a pore size of 6 µm, which can block the ingrowth of fine roots. Dead fine roots used in the litter bag technique were collected from the field and then oven-dried for a constant mass as mentioned above. Each bag contained a fine root mass of 0.7-1.3 g, which was inserted inside the bag with some fine soil collected from the same site. Before burying them in the field, litter bags were soaked in ordinary water for 24 hours to ensure that the moisture content of the fine roots in the litter bags was similar to that in nature. In total, 60 bags were made and systematically buried in May 2013 at a 20×20 m plot with a distance of 2 m x 2 m between each other. At the same time as the soil core collection (August, November, and December 2013, as well as April 2014), 15 litter bags were collected. The collected bags were washed and sieved with water for the remaining fine roots, which were then oven-dried for a constant mass. The remaining mass was weighed (accuracy of 0.0001 g) and used to estimate the decomposition ratio (γ) by the following equation: {γ = (initial mass - remained mass)/ initial mass}.

Data analysis

The continuous inflow method [7] was applied to estimate fine root production (*P)* (Eq. 1), mortality (*M)* (Eq. 2), and decomposition (*D)* (Eq. 3).

$$P = (B_j - B_i) + (N_j - N_i) + \left[-(N_j - N_i) - \left((N_j - N_i)/\gamma_{ij} + N_i\right) * ln(1 - \gamma_{ij})\right] \quad (1)$$

$$M = (N_j - N_i) + D \quad (2)$$

$$D = -(N_j - N_i) - ((N_j - N_i)/\gamma_{ij} + N_i) * ln(1 - \gamma_{ij}) \quad (3)$$

where B_i and B_j represent the masses of living fine roots (biomass) at times t_i and t_j, respectively ($t_j > t_i$), N_i and N_j denote the masses of dead fine roots (necromass), and γ_{ij} is the decomposition ratio.

The estimation was conducted for two size classes separately (those with a diameter of ≤1 mm and those with a diameter of 1-2 mm). Then, the total decomposition, mortality, and production of all fine roots (those with a diameter of ≤2 mm) were calculated from two classes.

Differences in fine root biomass (the mass of living fine roots) and necromass (the mass of dead fine roots) amongst the five collection periods (May, August, November, and December 2013, as well as April 2014) - as well as in fine root decomposition ratio, production, mortality, and decomposition amongst four collection intervals (May-August, August-November, November-December, and December-April) - were assessed by univariate analysis of variance (ANOVA) and post-hoc tests. All analyses were conducted using SAS 9.2 (SAS Institute Inc., Cary, NC, USA).

Results

The fine root biomass, necromass, and decomposition ratio differed significantly in the five collection periods and collection intervals (Table 1). In 1-2 mm fine roots, the highest biomass was found in December 2013 (94.2 g m^{-2}), while the lowest biomass was observed in May 2013 (33.9 g m^{-2}). The highest necromass in 1-2 mm fine roots was appeared in November 2013 (32.3 g m^{-2}), and the lowest was found in May 2013 (14.8 g m^{-2}). In terms of the decomposition ratio, the highest figure was found during the May-August period (0.00085 day^{-1}), and the lowest was recorded during the December-April period (0.00010 day^{-1}). A similar pattern was found in ≤ 1 mm fine roots. The highest biomass was found in December 2013 (106.3 g m^{-2}),

Table 1. The fine root biomass, necromass, and decomposition ratio (γ_{ij}) (± standard error) of two size classes.

Collection dates	1-2 mm fine roots			≤1 mm fine roots		
	Biomass (g m^{-2})	*Necromass (g m^{-2})*	γ_{ij} *(day^{-1})*	*Biomass (g m^{-2})*	*Necromass (g m^{-2})*	γ_{ij} *(day^{-1})*
May, 2013	33.9±4.5^{a}	14.8±1.6^{a}		63.0±6.1^{a}	27.5±2.2^{a}	
August, 2013	38.0±4.1^{a}	16.1±1.5^{a}	0.00085±.00009^{a}	64.7±6.2^{a}	27.4±2.5^{a}	0.00145±.00015^{a}
November, 2013	60.6±5.8^{b}	32.3±2.9^{b}	0.00038±.00004^{b}	83.6±7.6^{b}	44.7±4.5^{b}	0.00052±.00009^{b}
December, 2013	94.2±9.2^{c}	30.6±2.6^{b}	0.00019±.00001^{c}	106.3±10.1^{c}	34.6±3.2^{c}	0.00021±.00001^{c}
April, 2014	52.4±4.9^{d}	18.2±1.7^{a}	0.00010±.00001^{d}	54.5±4.9^{e}	19.0±1.8^{d}	0.00010±.00001^{d}

Different letters ($^{a, b, c, d, e}$) in a column indicate significant differences of means at p = 0.05.

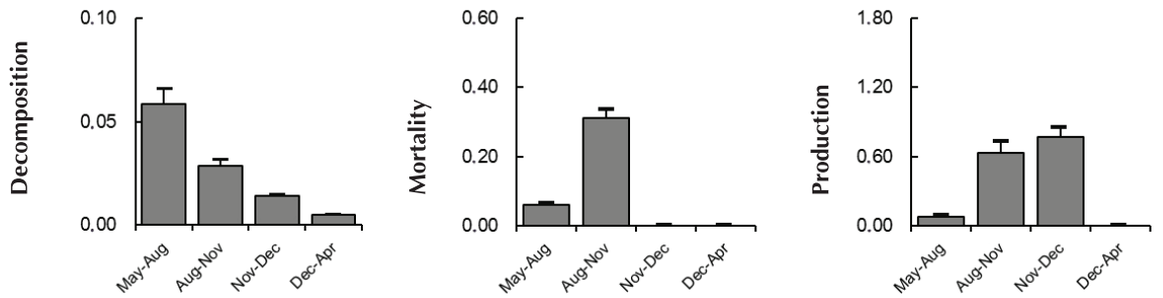

Fig. 1. Decomposition, mortality, and production (g m^{-2} d^{-1}) of ≤1 mm fine roots. Bars indicate + standard error.

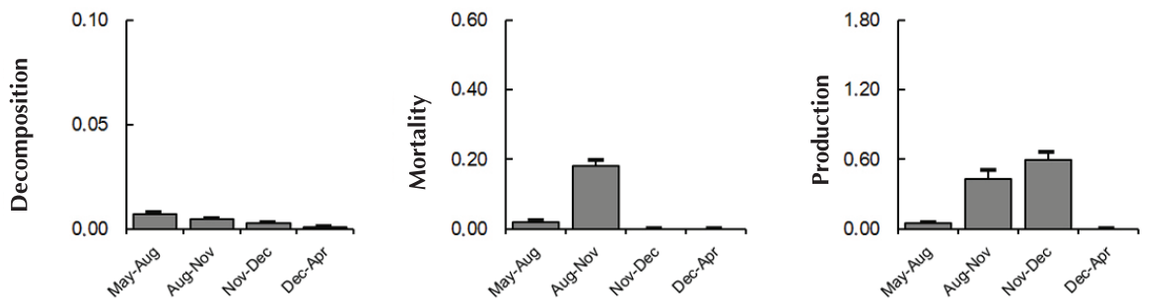

Fig. 2. Decomposition, mortality, and production (g m^{-2} d^{-1}) of 1-2 mm fine roots. Bars indicate + standard error.

while the lowest biomass was discovered in May 2013 (63.0 g m^{-2}). The highest necromass was found in November 2013 (44.7 g m^{-2}), and the lowest was recorded in August 2013 (27.4 g m^{-2}). In terms of the decomposition ratio, the highest figure was found during the May-August period (0.00145 day^{-1}), and the lowest was discovered during the December-April period (0.00010 day^{-1}).

The fine root decomposition, mortality, and production in both size classes of ≤1 mm (Fig. 1) and 1-2 mm (Fig. 2) were season-dependent, and the trends were similar in both classes. The highest decomposition was found during the May-August period (0.058 g m^{-2} day^{-1} for the ≤1 mm class and 0.0072 g m^{-2} day^{-1} for the 1-2 mm class; Figs. 1 and 2), while the lowest decomposition was recorded during the December-April period. The highest mortality was found during the August-November period (0.311 g m^{-2} day^{-1} for the ≤1 mm class and 0.186 g m^{-2} day^{-1} for the 1-2 mm class), and the lowest mortality was observed during the December-April period for both classes. The highest production levels occurred during the November-December period (0.769 g m^{-2} day^{-1} for the ≤1 mm class and 0.595 g m^{-2} day^{-1} for the 1-2 mm class). The lowest production was recorded during the December-April period for both classes.

The total fine root decomposition, mortality, and production of both classes (Fig. 3) had the same trends in each class (Figs. 1 and 2), with the highest decomposition during the May-August period (0.066 g m^{-2} day^{-1}) and the lowest during the December-April period; the highest mortality during the August-November period (0.493 g m^{-2} day^{-1}) and the lowest during the December-April period; the highest production during the November-December period (1.36 g m^{-2} day^{-1}) and the lowest during the December-April period (Fig. 3).

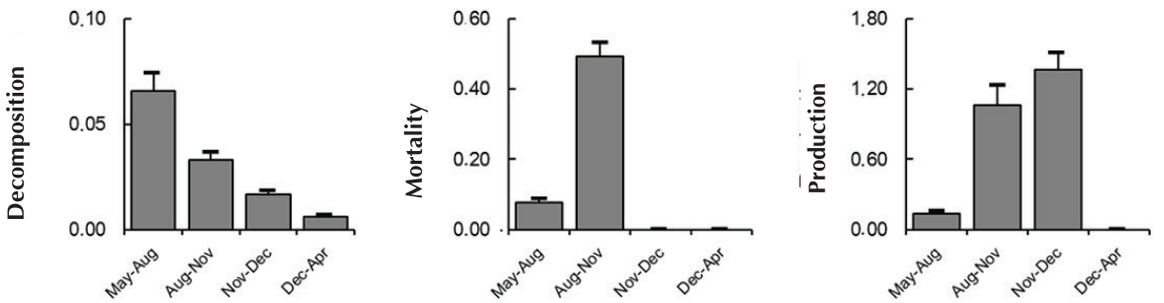

Fig. 3. Decomposition, mortality, and production (g m^{-2} d^{-1}) of all fine roots (≤2 mm). Bars indicate + standard error.

In this study, the *Q. serrata* plantation had a fine root decomposition of 0.108 tonnes ha^{-1} $year^{-1}$, a mortality of 0.440 tonnes ha^{-1} $year^{-1}$, and a production of 1.364 tonnes ha^{-1} $year^{-1}$ (Fig. 4).

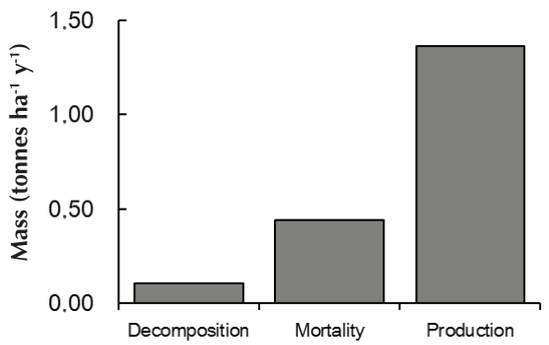

Fig. 4. Total decomposition, mortality, and production of fine roots in a 1-year duration.

Discussion

The fine root production of *Q. serrata* is season-dependent (Figs. 1 and 2). The *Q. serrata* plant produces leaves in the early summer (April) and sheds in the early winter (mid-October). The quick growth of fine roots during the April-May period and the peak during October correspond to leafing and shedding, respectively [10]. Leafing requires energy and nutrients to support the growth of numerous new leaves; therefore, fine roots must grow quickly to meet such requirements, sustaining tree life. During the winter when there are no leaves, trees still require energy while there is no photosynthesis, so they must store energy during photosynthesis. Thus, the high level of fine root production before shedding leaves could be explained by saving energy for the winter.

The decomposition of litter in general and fine roots, in particular, is controlled by several factors, such as environmental conditions (temperature, humidity) and quality of the litter itself (nutrient content) [11-12]. The low decomposition in the present study (Fig. 4) was probably controlled by temperature. Since there is a prolonged winter of 6 months, the temperature dropped to -2^{0}C with snowfall during the field experiment, leading to inhibited microorganism activity for the decomposition of dead fine roots. In addition, *Q. serrata* sheds all leaves in winter, leading to large amounts of organic matter on the forest floor. Therefore, the decomposing fine roots were limited because of the overload of organic matter [13].

The amount of dead fine roots was also low in the present study (Fig. 4; less than 30% production), which indicates less organic matter returning to the soil from fine roots, leading to low soil nutrient content. This phenomenon is probably a physiological reaction of *Q. serrata* to the low temperatures in winter [9-10]. If more fine roots die, then new fine roots must grow in the following year to support the tree's growth. This process requires a great deal of energy, but trees cannot absorb nutrients from the soil or conduct photosynthesis because leaves are not available in the winter. Therefore, the fine root decomposition, mortality, and production of deciduous forests differ from those of evergreen broadleaved forests [14, 15].

Several factors affect fine root production, including forest type and age, climate, and soils. The fine root production in this study was 1.36 tonnes ha^{-1} $year^{-1}$. It was 5.78 tonnes ha^{-1} $year^{-1}$ in a secondary *Q. serrata* forest in Ohtsu, Japan [9]. According to another study, fine root production was 3.65 tonnes ha^{-1} $year^{-1}$ [15] and 1.13 tonnes ha^{-1} $year^{-1}$ in old-growth and secondary [14] evergreen tropical forests, respectively, in Vietnam. Those figures demonstrate the significant difference of fine root production amongst sites. Therefore, estimating fine root production locally is becoming important for a deep understanding of fine root functioning in the forest carbon cycle and nutrient return.

Conclusions

The fine root decomposition, mortality, and production at a *Q. serrata* plantation were estimated based on the continuous inflow method to separate fine roots into two classes: ≤1 mm in diameter and 1-2 mm in diameter.

Mortality and production were season-dependent, and they were higher in the summer as compared to the winter.

The total production of the study forest was 1.364 tonnes ha^{-1} $year^{-1}$, of which mortality accounted for 0.440 tonnes ha^{-1} $year^{-1}$. In a duration of one year, 0.108 tonnes ha^{-1} $year^{-1}$ of dead fine roots decomposed to return nutrients to the soil.

ACKNOWLEDGEMENTS

This research is funded by Japan Society for the Promotion of Science. Comments from anonymous reviewers on the manuscript are highly appreciated.

The author declares that there is no conflict of interest regarding the publication of this article.

REFERENCES

[1] L. Finer, M. Ohashi, K. Noguchi, Y. Hirano (2011), "Fine root production and turnover in forest ecosystems in relation to stand and environmental characteristics", *For. Ecol. Manage.*, **262(11)**, pp.2008-2023.

[2] R.A. Gill, R.B. Jackson (2000), "Global patterns of root turnover for terrestrial ecosystems", *New Phytol.*, **147**, pp.13-31.

[3] Z.Y. Yuan, H.Y.H. Chen (2012), "Indirect methods produce higher estimates of fine foot production and turnover rates than direct methods", *PLOS ONE*, **7(11)**, e48989.

[4] I. Brunner, M.R. Bakker, R.G. Bjork, Y. Hirano, et al. (2013), "Fine-root turnover rates of European forests revisited: an analysis of data from sequential coring and ingrowth cores", *Plant and Soil*, **362(1-2)**, pp.357-372.

[5] H. Majdi, K. Pregitzer, A.S. Moren, J.E. Nylund, G.I. Agren (2005), "Measuring fine root turnover in forest ecosystems", *Plant and Soil*, **276(1-2)**, pp.1-8.

[6] D.F. Metcalfe, P. Meir, M. Williams (2007), "A comparison of methods for converting rhizotron root length measurements into estimates of root mass production per unit ground area", *Plant and Soil*, **301(1-2)**, pp.279-288.

[7] A. Osawa, R. Aizawa (2012), "A new approach to estimate production, mortality and decomposition of fine roots using litter-bag experiments and ordinary soil-core techniques", *Plant and Soil*, **355(1-2)**, pp.167-181.

[8] D.J. Milchunas (2009), "Estimating root production: comparison of 11 methods in shortgrass steppe and review of biases", *Ecosystems*, **12(8)**, pp.1381-1402.

[9] V.D. Tran, A. Osawa, T. Sato (2016a), "Estimation of fine-root production using rates of diameter-dependent root mortality, decomposition and thickening in forests", *Tree Physiology*, **36(4)**, pp.513-523.

[10] V.D. Tran, T. Sato, O. Kozan (2016b), "A new approach for estimating fine root production in forests: a combination of ingrowth core and scanner", *Trees*, **30(2)**, pp.545-554.

[11] T. Bueis, M.B. Turrion, F. Bravo, V. Pando, A. Muscolo (2018), "Factors determining enzyme activities in soils under *Pinus halepensis* and *Pinus sylvestris* plantations in Spain: a basis for establishing sustainable forest management strategies", *Ann. For. Sci.*, **75(1)**, Doi: 10.1007/s13595-018-0720-z.

[12] M.P. Krishna, M. Mohan (2017), "Litter decomposition in forest ecosystems: a review", *Energy, Ecol. Environ.*, **2(4)**, pp.236-249.

[13] D.C. Coleman, D.A.Jr. Crossley, P.F. Hendrix (2004), "Secondary production: activities of heterotrophic organisms-the soil fauna", *Fundamentals of Soil Ecology*, Elsevier Inc., pp.77-171.

[14] V.D. Tran, T. Sato (2018), "Towards carbon certificate in Vietnam: net ecosystem production and basic income for local community", *Environmental Resources Use and Challenges in Contemporary Southeast Asia: Tropical Ecosystems in Transition*, Springer, pp.79-96.

[15] V.D. Tran (2017), "Estimating net ecosystem production of tropical forest". *Sustainable Humanosphere*, **13**, pp.5-6.

Doi: 10.31276/VJSTE.61(4).53-57

A beads-based biofertilizer containing *Bacillus megaterium* for cabbage

T.M. Quynh[1*], N.T.T. Thuy[2], T.X. An[1], N.T. Thom[1], N.V. Binh[1], H.D. Sang[1], T.B. Diep[1], N.T. Ha[3], L.T.M. Luong[3]

[1]Hanoi Irradiation Center, Vietnam Atomic Energy Institute
[2]Faculty of Biology, University of Science, Vietnam National University, Hanoi
[3]Soils and Fertilizers Research Institute

Received 28 May 2019; accepted 8 November 2019

Abstract:

The aim of this study was to study the use of a beads-based biofertilizer in crop production. The study focuses on the production of a beads-based biofertilizer containing spores and vegetative cells of *Bacillus megaterium (B. megaterium)* VACC 118. It also evaluated the quality of the biofertilizer and its effects on the growth and yield of cabbage. The results show that the density of *B. megaterium* in the beads-based biofertilizer reached 4.34×10^{10} CFU/g and did not change after 6 months of storage. The degree of swelling of the beads was 1.57 times after 24 hours of immersion in an alkaline solution. The number of released cells of *B. megaterium* reached 4.2×10^{8} CFU/ml after 1 week of soaking in the alkaline solution. The application of the beads-based biofertilizer with NPK fertilizer increased the rate of folded plant, the fresh weight of head and the yield of cabbages grown in alluvial soil. When the beads-based biofertilizer was used along with a 20% reduction of the recommended NPK dosage, the yield of cabbage still increased by 12.36% compared to the control. This indicates that the beads-based biofertilizer can partially replace for chemical fertilizers.

Keywords: **beads-based biofertilizer, *B. megaterium*, cabbage growth and yield.**

Classification number: **3.1**

Introduction

Fertilization is essential for providing nutrients for the soil to facilitate plant growth and improve crop yields. Fertilizers in general and chemical fertilizer in particular can directly promote plant growth. According to the Food and Agriculture Organization (FAO), chemical fertilizers may be responsible for 55% of the increase in global yields of agricultural products and that each kilogram of NPK fertilizer applied to the crop can produce 10 kg to the yield [1]. However, long-term overuse of these inorganic fertilizers caused serious risks to our environment, affecting both food quality and eco-systems. Therefore, new safety-friendly fertilizers, such as biofertilizers and slow-release fertilizers, have been developed to partly replace inorganic fertilizers [2-5].

In Vietnam, probiotic and biofertilizers have been studied since the late 1980s, but only a few products have been developed by research universities and institutes [6]. Therefore, several imported biofertilizers have recently been approved for use in organic farming and sustainable agriculture. Most of the existing biofertilizers are carrier-based inoculants of nitrogen-fixing, phosphorous-solubilizing, or plant-growth-promoting bacteria. After fertilization, these beneficial microbes can easily colonize in the rhizosphere to deliver nutrients to plants, regulate phytohormones, and control phytopathogens. The microorganisms are encapsulated in carriers to protect them from adverse stress factors (such as pH, temperature, and radiation) during storage. Peat, clay, and bentonite are the most frequently used carriers due to their abundance, availability, and low cost. But, these materials can easily be contaminated due to their high nutrient content [7]. Therefore, polymeric-based carriers have been developed for the production of biofertilizersas these organic compounds can be utilized as a carbon source for bacteria and, therefore, to prolong their survival during storage [8].

* *Corresponding author: Email: tmqthuquynh@gmail.com*

In addition, the polymer molecules can crosslink to form three-dimensional structures that can protect the biofertilizers from contamination.

Alginate gels are widely used as polymer carriers due to their good biodegradability and compatibility. After inoculation, bacteria can incorporate to inthe gel in the wet or concentrated dry beads, which are easy to store, transport, and apply. However, these alginate beads are nonuniform, highly porous, andhave poor mechanical stability because alginate solution is very viscous and weak. Fillers such as starch may be added to the formulation to increase the dry matter in the beads, improving their mechanical resistance and allowing for a gradual release of beneficial microbes into the soil [9]. However, the insolubility and sedimentation of starch in the encapsulating solution can result in an unstable solution. Therefore, modified starch is often added to obtain a regularly dispersed solution for encapsulation, as reported by Ivanova, et al. [10]. Modified starch is easily obtained through irradiation, and this radiation method has proved a useful tool for the modification of natural polymers [11]. In our previous study, we found that modified starch with improved water solubility and dispersion was obtained by gamma irradiation at 3.5 kGy [12]. In addition, the modified cassava starch was also pasteurized during radiation treatment. Therefore, for this study, radiation-modified starch was mixed with sodium alginate to prepare a carrier for biofertilizer.

B. megaterium is a rod-like, gram-positive, plant-growth-promoting microorganism. These bacteria increase the availability of P and K in soil and produce indole acetic acid (IAA), a phytohormone that can improve plant growth. Their vegetative cells completely sporulate through heat inactivation, and the resulting spores, which are resistant to environmental stimuli, can easily germinate again under suitable conditions. Because the spores can survive for long periods in harsh conditions, they can inoculate onto the alginate-starch carriers for the production of biofertilizers that can be stored for longer.

In a recent study, *B. megaterium* VACC 118 strain, a plant-growth-promoting bacteria that can produce to 415 µg/ml of IAA after 5 days of cultivation, was selected from the culture collection of the Soils and Fertilizers Research Institute [13]. In order to produce an environmentally friendly fertilizer that can promote plant growth in unfavourable conditions, contribute to reducing pollution caused by agricultural chemicals and adapt to climate change, we attempted to produce alginate-starch bead carriers containing spores and vegetative cells of *B. megaterium* VACC 118.

Materials and methods

Materials

Cassava starch was purchased from Taiky Food, Vietnam. *B. megaterium* VACC 118 strain was selected from the culture collection of the Soils and Fertilizers Research Institute. Healthy seedlings of cabbage were kindly supplied by the Research Center for Fertilizers and Plant Nutrients at the Soils and Fertilizers Research Institute. All chemicals and reagents were industrial grade.

Methods

Preparation of the bead-based biofertilizer: B. megaterium cells were incubated in King's B for activation and then transferred to soybean extract medium and cultivated at 30^0C in favourable conditions for 5 days for sporulation. The liquid culture at the stationary phase was concentrated to a density of about $1.3\text{-}2.5\times10^{11}$ CFU/ml by centrifugation at 3,000 rpm and then collected for encapsulation.

The process for preparing the biofertilizer is presented in Fig. 1. Briefly, a modified starch was prepared from commercial cassava starch using gamma irradiation, as described in our previous study [12]. This was mixed with a pre-sterilized sodium alginate solution to form a starch-alginate (SA) solution of 2% sodium alginate and 33% modified starch. Then, the concentrated *B. megaterium* culture was homogenized with the SA solution at a volume ratio of 1:2 in a sealed bath and dropped onto a pre-sterilized solution of 2% $CaCl_2$ under magnetic stirrer for precipitation. The resulting beads were stabilized by further stirring for 30 minutes and were then washed with sterile water before drying. All manipulations were performed under aseptic conditions in clean laminar (Fig. 2).

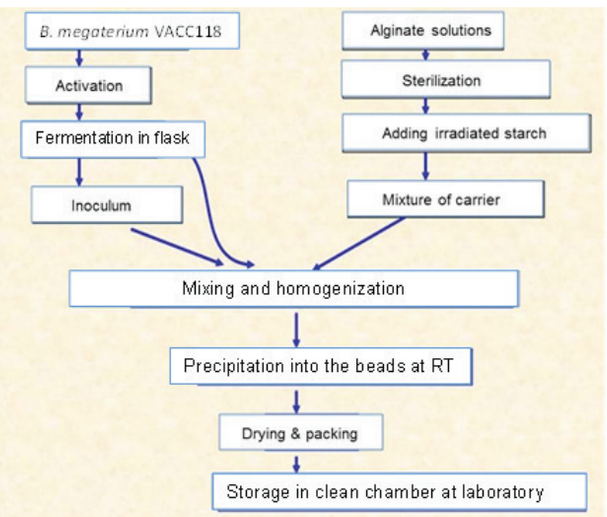

Fig. 1. Experimental process of preparation of bio-fertilizer.

Fig. 2. Production of bio-fertilizer beads in pilot scale.

Evaluation of the beads-based biofertilizer: the dried biofertilizer beads were immersed in a sterile saline solution (NaCl 0.85%, pH 7.0) for 24 hours at room temperature, and the swelling degree in percentage (PS) was measured by obtaining the weight ratio of swollen (W_s) to initial (W_d) beads using the following equation:

$$PS = 100\times(W_s - W_d)/W_d \quad (1)$$

In addition, 1 g of the dried beads wasimmersed in 100 ml of sterile saline for a week under weak stirring at room temperature for release test. The number of released cells in the saline solution was determined after 1, 2, and 7 days. For this experiment, the density of *B. megaterium* was determined by culturing the bacterial cells on a Luria Bertani (LB) agar plate supplemented with L-tryptophanin accordance with TCVN 10784:2015 [13].

The dried beads were packed in aluminium foil and placed in a plastic bag, and the packages were kept in a clean chamber. The effects of storage time on the viability of bacteria in the fertilizer were investigated after 7, 30, 90, and 180 days of storage at room temperature. First, 1 g of the beads were immersed in 10 ml of sterile saline for 30 minutes for hydration. The hydrated beads were moved to 100 ml of a 10% sodium tricitrate solution for a further 30 minutes, gently vortexed into suspension, and plated on LB agar. After incubation at 37^0C for 48 hours, the live cells in the beads were counted.

The effects of the beads-basedbiofertilizer on growth and yield of cabbage: together with NPK, the fertilizer beads were applied to cabbage once at a rate of 20 kg/ha before planting. The healthy seedlings of cabbage were planted in 24 m^2 testing plots containing alluvial soil at Thanh Da, Phuc Tho, Hanoi from January to March 2019. Each treatment was replicated three times. The experiment was arranged according to acompletely randomized block design, and the cabbage fertilized with 120 kg N, 60 kg P_2O_5 and 80 kg K_2O per ha as the control (DC) [14]. Treatments included TN1: NPK plus the beads-based biofertilizer and TN2: 80% NPK plus the beads-based biofertilizer. Plant growth was measured by recording plant height, rate of unfolded plant, head height and weight during the vegetative stage. The whole plot of cabbage heads was harvested, and the productivity of the cabbage and the yield increase were calculated [15].

Statistical analysis: the data were statistically analysed using Excel and IRRISTAT software.

Results and discussion

Quality of the beads-based biofertilizer

The dried beads containing *B. megaterium* VACC118 were prepared as a biofertilizer. The increased water solubility and reduced intermolecular hydrogen bonds of the radiation-modified starch helped the starch molecules to disperse well in the encapsulating solution [12]. Gamma irradiation also resulted in an increase in gelation of the modified starch. The results show that the beads-based biofertilizer has a relatively homogeneous shape and a higher dry matter content and that the *B. megaterium* cansurvive and grow better in the beads of alginate-modified starch.

Table 1. Quality of the beads-based biofertilizer.

Parameter	Measurement	Current regulation
Moisture (%)	9.4	≤30
pH	5.7	≥5
Density of useful cells (CFU/g)	4.34×10^{10}	$\geq10^8$
Salmonella (CFU/g)	Not detected	Negative
E. coli (MPN/g)	Not detected	1.1×10^3

Table 1 shows that the beads-based biofertilizer meets all the current requirements for biofertilizer and that the density of beneficial microbe in the beads-based biofertilizer at $4.34\text{x}10^{10}$ CFU/g, is much higher than the required density. This means that the products can be kept for longer. Moreover, the low moisture content of the product can also limit contamination, further prolonging its storage period. The density of *B. megaterium* in our biofertilizer is similar to the density of *A. brasilense* (10^{10}-10^{11} CFU/g) in the alginate-starch capsules produced by Ivanova, et al. [10] but higher than that ($8.6\text{x}10^8$ CFU/g) of the microbial inoculants produced by Thu Ha Nguyen, et al. [13]. The significant difference in the density of the beneficial microbes can be explained by the different encapsulating cultures.

Table 2. Rate of release of *B. megaterium* from the biofertilizer.

Soaking time (days)	Swelling degree (%)	Number of released cells (CFU/ml)
1	57.0	7.2×10^7
2	–	1.15×10^8
7	–	4.2×10^8

As shown in Table 2, the swelling degree of the beads-based biofertilizer reached 57%, which is equivalent to 1.57 times after 24 hours of immersion. Not only did the weight of the swollen beads increase, but their diameter also expanded after absorbing water, making it easier to releasing the cells from the beads. During the first day, the number of released cells was 7.2×10^7 CFU/ml. It was 1.15×10^8 CFU/ml in the second day and reached 4.2×10^8 CFU/ml after 1 week of soaking. The results suggest that the bacteria were not immobilized to the carrier but could easily move to the rhizosphere after inoculating to the soil. In fact, the release rate of surviving bacteria from the fertilizer to the soil is rather slow, because the dried beads have to be hydrated first.

Table 3. The survival of *B. megaterium* in the beads-based biofertilizer during the storage.

Time of storage (days)	Density of surviving cells (CFU/g)
0	4.34×10^{10}
7	4.26×10^{10}
30	4.18×10^{10}
90	3.75×10^{10}
180	2.31×10^{10}

The viability of the *B. megaterium* cells after 7, 30, 90, and 180 days storage is shown in Table 3. The results show that the density of *B. megaterium* in the beads-based biofertilizer does not appear to change during storage. The density of *B. megaterium* after 6 months storage was still high enough, which suggests that the fertilizer could be stored for longer. In a recent study, Thu Ha Nguyen, et al. [13] reported that the density of *B. megaterium* reduced to 2.6 from 8.6×10^8 CFU/g. However, the biofertilizer in their experiment contained four kinds of microbes mixed with cassava starch and rice bran as the carrier. The fact that various bacteria strains display antagonistic activities may have influenced the development of the microbial population in the inoculant.

According to Altuhaish, et al. [16], the density of surviving bacteria in biofertilizer was not significantly reduced after 3 months of storage. Thirumal, et al. [17] also found that the density of *B. megaterium* in an alginate-based carrier decreased slightly after longer storage periods but was about 7×10^8 CFU/g, meaning that their biofertilizer still in good conditions after 8 months of storage. This indicates that the alginate-based carriers used in the present study can prolong the storage of microbial fertilizers.

The effects of the beads-based biofertilizeron growth and yield of cabbage

Table 4. The effects of the beads-based biofertilizer on growth and yield of cabbage.

Formulation	Rate of folded Plan (%)	Fresh weight of head (kg)	Yield (tones/ha)	Increase (%)
DC	95.8	1.53	43.55	-
TN1	97.0	1.74	49.24	13.07
TN2	96.3	1.72	49.05	12.36
$LSD_{0.05}$			3.71	
CV			4.1	

DC: control (100% NPK as per local standard); TN1: 100% NPK + biofertilizer; TN2: 80% NPK + biofertilizer; $LSD_{0.05}$: least significant difference at 0.05; CV: coefficient of variation.

The effects of the beads-based biofertilizeron the growth and yield of cabbage planted in alluvial soil were determined and are presented in Table 4. The results reveal that the growth and yield of the cabbage inoculated with the beads-based biofertilizer together with NPK were better than the growth and yield of the cabbage treated with NPK only (DC). The application of the beads-based biofertilizer provided nutrients and phytohormones that stimulated plant growth, which resulted in a yield that was 13.07% greater than that of the control. When there commended NPK dosage was reduced by 20%, the yield of cabbage was still 12.36% greater than that of the control. Abou El Magd, et al. also reported a positive effect of biofertilizer on cabbage [18].

Conclusions

The biofertilizer formed from *B. megaterium* VACC118 and an admixture carrier of sodium alginate and radiation-modified cassava starch has a *B. Megaterium* density of $4.34x10^{10}$ CFU/g, which is much higher than the current requirement. The beads-based biofertilizer can easily absorb water and expand to release the living cells in the aqueous medium. The density of *B. Megaterium* did not decrease after 6 months of storage. The application of the beads-based biofertilizer with NPK increased the rate of folded plant, fresh weight of head, and yield of the cabbages grown on alluvial soil. When the beads-based biofertilizer used and the recommended NPK dosage was reduced by 20%, the yield of cabbage was still 12.36% greater than that of the control. This indicates that the beads-based biofertilizer can replace a proportion of chemical fertilizer.

ACKNOWLEDGEMENTS

This work was supported by Vietnam Ministry of Science and Technology with government project of

DTDLCN.19/16. The authors also acknowledge to Hanoi Irradiation Center (VINATOM) and Soils and Fertilizers Research Institute for other supports.

The authors declare that there is no conflict of interest regarding the publication of this article.

REFERENCES

[1] www.fao.org/3/a-i5627e.pdf.

[2] S. Li, Y. Tian, K. Wu, Y. Ye, J. Yu, J. Zhang, Q. Liu, M. Hu, H. Li, Y. Tong, N.P. Harberd, X. Fu (2018), "Modulating plant growth-metabolism coordination for sustainable agriculture", *Nature*, **560(7720)**, pp.595-600, Doi: 10.1038/s41586-018-0415-5.

[3] S. Goyal, K. Chander, M.C. Mundra, K.K. Kapoor (1999), "Influence of inorganic fertilizers and organic amendments on soil organic matter and soil microbial properties under tropical conditions", *Biol. Fertil. Soils*, **29**, pp.196-200.

[4] M. Matos, B.D. Mattos, B.L. Tardy, O.J. Rojas, W.L.E. Magalhães (2018), "Use of biogenic silica in porous alginate matrices for sustainable fertilization with tailored nutrient delivery", *ACS Sustainable Chemistry & Engineering*, **6(2)**, pp.2716-2723.

[5] S. Sandra, B. Vladimir, K. Ivana, L. Miodrag, N. Nada (2018), "Microbial fertilizers: a comprehensive review of current findings and future perspectives", *Spanish Journal of Agricultural Research*, **16(1)**, pp.1-18.

[6] P.V. Toan (2013), *Studies and Applications of Microbial Inoculants in Vietnam*, Vietnam Academy of Agricultural Science, in Vietnamese.

[7] M. Schoebitz, M.D. López, A. Roldán (2013), "Bioencapsulation of microbial inoculants for better soil-plant fertilization: a review", *Agron. Sustain. Dev.*, **33**, pp.751-765.

[8] Y. He, Z. Wu, L. Tu, Y. Han, G. Zhang, C. Li (2015), "Encapsulation and characterization of slow-release microbial fertilizer from the composites of bentonite and alginate", *Applied Clay Science*, **109-110**, pp.68-75.

[9] Y. Bashan, J.P. Hernandez, L.A. Leyva, M. Bacilio (2002), "Alginate microbeads as inoculant carriers for plant growth-promoting bacteria", *Biol. Fertil. Soils*, **35**, pp.359-368.

[10] E. Ivanova, E. Teunou, D. Poncelet (2006), "Alginate based macrocapsules as inoculant carriers for the production of nitrogen fixing biofertilizers", *Chemical Industry and Chemical Engineering Quarterly*, **12(1)**, pp.31-39.

[11] N.M. Adzahan, D.M. Hashim, K.R. Muhammad, A. Rahman, Z. Ghazali, K. Hashim (2009), "Pasting and leaching properties of irradiated starches from various botanical sources", *International Food Research Journal*, **16**, pp.415-429.

[12] Tran Xuan An, Nguyen Van Binh, Hoang Dang Sang, Nguyen Thi Hang, Le Thi Hien, Tran Minh Quynh (2017), "Characterization of cassava starch modified by gamma irradiation", *The Vietnam Conference on Nuclear Science and Technology*, in Vietnamese.

[13] Thu Ha Nguyen, et al. (2016), "Study on production of probiotic for the peanuts cultivated on coastal sand at Nghe An and Binh Dinh provinces", *2nd National Conference on Crop Science*, pp.1124-1131.

[14] Vietnam Technical Regulation (2013), *National Technical Regulation on Testing for Value of Cultivation and Use of Cabbage Varieties*, QCVN 01-120:2013/BNNPTNT (in Vietnamese).

[15] A. Haque, S.K. Bhowal, M. Ali, M. Robbani (2015), "Yield and yiel attributes of cabbage (*Brassica oleracea* var. *capitala* L.) as influenced by soil organic amendments", *Basic Research Jourrnal of Agricultural Review*, **4(12)**, pp.339-344.

[16] A. Altuhaish, Hamim, A. Tjahjoleksono (2014), "Biofertilizer effects in combination with different drying system and storage period on growth and production of tomato plant under field conditions", *Emir. J. Food Agric.*, **26(8)**, pp.716-722.

[17] G. Thirumal, R.S. Reddy, S. Triveni, M.H. Bhave (2017), "Evaluate the shelf life of pseudomonas carrier based biofertilizer stored at different temperatures at different intervals", *Int. J. Pure App. Biosci.*, **5(4)**, pp.1295-1301.

[18] M.M. Abou El Magd, M.F. Zaki, S.A. Abo Sedera (2018), "Bio-fertilization and foliar application of Milagro bio-stimulant in growth, head yield and quality as well as mineral K requirements of Chinese cabbage", *Middle East Journal of Agriculture Research*, **7(4)**, pp.1310-1322.

Doi: 10.31276/VJSTE.61(4).58-63

Determination of protease and chitinase activities from *Paecilomyces variotii* NV01 isolated from Dak Lak pepper soil

Chu Thanh Binh[1, 2*], Tran Van Tuan[2], Tran Bao Tram[3], Bui Thi Viet Ha[2]

[1]*Vietnamese - Russian Tropical Center, Hanoi*
[2]*Department of Microbiology, Faculty of Biology, University of Science, Vietnam National University, Hanoi*
[3]*Center for Experimental Biology, NACENTECH*

Received 20 August 2019; accepted 15 October 2019

Abstract:

The filamentous fungus *Paecilomyces* is currently being developed as a biocontrol agent against plant parasitic nematodes, which often cause black leaf disease in pepper and coffee trees. Nematode eggs and cuticles are the infection sites for biocontrol agents that penetrate those areas by the production of lytic enzymes. *Paecilomyces variotii* NV01 was isolated from pepper soil from the Dak Lak province. The purpose of this work is to study the activity of protease and chitinase in the strain *Paecilomyces variotii* NV01. The protease activity was determined to be 82.3 U/ml in a 0.65% casein substrate concentration after 84 hours of culture, which was 6 folds higher than with a basal medium (12.7 U/ml). Exo-chitinase activity was found to be 37.28 U/ml after 84 hours of culture in a chitin substrate concentration of 0.75%, which is 4 folds greater than the basal medium. It was found that adding Ca^{2+} to the medium drastically altered chitinase activity, increasing it by 10.5%. A 5 mM concentration of Ca^{2+} was found to affect chitinase activity but not protease activity. Furthermore, the percentage of *Meloidogyne* sp. nematodes killed by *Paecilomyces variotii* NV01 after 96 hours of culture was 50.4%. Further study should be carried out in order to use this fungal strain to control plant parasitic nematodes.

Keywords: **chitinase, *Meloidogyne* sp., *Paecilomyces variotii* NV01, protease.**

Classification numbers: **3.1, 3.5**

Introduction

Valuable industrial crops such as pepper and coffee trees are often attacked by nematodes. Peppers growing in areas such as Dak Lak are often infected by nematodes affecting them with yellow, curly leaves and swollen roots that are unable to get nutrients. There is increasing opposition to the use of chemical pesticides for these nematodes because of undesirable environmental side effects. Thus, other methods of biological control are of interest to scientists. For example, fungus can be used as traps, nematode egg parasites, or as drop toxins to kill nematodes. Specifically, *Paecilomyces* sp. has been found as a parasitic egg nematophagous-fungi [1]. Similarly, Dackman, et al. (1989) [2] investigated fungal egg parasites, isolated from the eggs of the cyst nematode *Heterodera avenae*, with respect to their ability to infect cyst nematode eggs of *H. scbachtii*.

The mechanism of the infection process by egg-parasitic fungi may be either mechanical, enzymic, or both. Extracellular enzymes, including serine proteases and chitinases, are shown to be important virulence factors that can degrade the main chemical constituents of the nematode cuticle and eggshell [3]. These enzymes, which play an especially important role during fungal infection against nematodes, can break down the physical and physiological integrity of the cuticles of nematodes and help fungal penetration and colonization [4, 5]. To date, few attempts have been made to determine the effects of purified fungal enzymes on the eggshell of the root knot nematode. Stirling & Mankau (1979) [6] studied the enzymes of nematode egg-parasitic fungus *D. oviparasitica* in a liquid culture supplemented with colloidal chitin. These authors found chitinase activity and suggested this enzyme play a role in penetrating the eggshell, which consists partly of chitin. The cuticle degrading protease P32 was identified from the nematode egg-parasitic fungus *Pochonia rubescens* (syn. *Verticillium suchlasporia*) in 1990 [7].

**Corresponding author: Email: chuthanhbinhvn@gmail.com*

In a previous article, we isolated and sequenced based on the ITS1- 5.8s - ITS2 of NV01 and determined the ability to produce chitinase and protease extracellular enzyme by means of diffusion on agar of *Paecilomyces variotii* NV01. The purpose of the present study is to investigate whether isolated protease and chitinase might play a role in the penetration of eggshells and therefore would be vital to the use of fungi as biological control agents.

Materials and methods

Materials

Paecilomyces variotii NV01 was isolated from pepper soil in the Dak Lak province as per Binh, et al. (2017) [8]. The stock culture was maintained on PDA (Potato-Dextrose-Broth) slants kept at 4^0C.

Meloidogyne sp.: Institute of Ecology and Biological Resources - Vietnam Academy of Science and Technology.

Medium: Czapeck-Dox (CD); C PDB (Potato-Dextrose-Broth); CMA (Corn-Meal-Agar) (Merck); pH 7; T1: CD added 0.65% casein; T2: CD added 0.75% chitin and 5 mM $CaCl_2$ Chitin (BioBasic); Casein: 0.25-0.85% (BioBasic); $CaCl_2$ (Merck).

Chemicals (to determine enzyme activity): Trichloro Aceticacid (TCA) (Merck); DNS (3,5 - Dinitrosalicylic acid (BioBasic, Canada); Folin-Ciocalteau reagent (Merck); Na_2CO_3 (BioBasic, Canada); Coomassie Brilliant Blue G-250 (Merck); Ethanol (Prolab).

Preparation of colloidal chitin: colloidal shrimp cuticle was used as substrates for chitinase activity production. Shrimp cuticle and commercial chitin were treated with phosphoric acid (10 g/100 ml) overnight. Then, several water washings and filtrations were performed until a pH 7 was reached. Substrates were then sterilized and kept at 4^0C (Chávez-Camarillo and Cruz-Camarillo, 1984) [9].

Methods

Enzyme qualification: Paecilomyces variotii NV01 was cultured on PDB, CMA, Czapeck-Dox media at 28-30^0C for 3-5 days in shaking flasks at 200 rpm. The crude enzyme was obtained by centrifuging the culture broth at 10,000 rpm to remove biomass.

Chitinase activity was found through the measure of the reducing sugars using DNS (3,5 - Dinitrosalicylic acid) method (Miller, 1959) [10]. Chitinase activity was measured at 540 nm using a spectrophotometer (SHIMADZU) and calculated by a standard curve based on different concentrations of N-acetyl-glucosamine (Sigma). One unit (U) of chitinase activity was defined as the amount of enzyme that liberated 1 mmol/l of N-acetyl-glucosamine ($y = 0.001x + 0.041$), where y is optical density - OD, x is N-acetyl glucosamine concentration (µg/ml) with $R^2=0.9939$.

Protease activity was essentially determined according to Manachini, et al., 1988 [11] at 37^0C, pH 7.5 in 50 mM phosphate buffer. Dialyzed sample (1 ml) was added to 5.0 ml of casein (0.65%) solution and incubated at 37^0C for 10 min. The reaction was arrested after the incubation period by adding 5.0 ml of Trichloro Acetic acid (110 mM). The residual protein was precipitated after 30 min of incubation and then was pelleted by centrifugation at 1000 x g for 5 min. The supernatant (2 ml) was utilized for a color reaction using Na_2CO_3 (5 ml) and Folin-Ciocalteau reagent (1 ml). The blue color developed was read at 660 nm on UV spectrophotometer. One unit of protease activity is defined as the amount which liberates 1 µg of tyrosine min^{-1} under experimental conditions ($y = 0.904x + 0.0017$), where y is the optical density - OD and x is tyrosine concentration (µg/ml).

Protein content of the culture suspension was determined according to the method of Bradford (1976) [12] using BSA as the standard.

Investigation of the effect of casein concentration on protease activity: the culture medium was supplemented with casein concentrations between 0.25-0.85%. From those experiments, the casein concentration with the highest protease activity was selected. The culture solution was shaken in a 500 ml capacity flask with 100 ml of shaking solution at a speed of 200 rpm at a temperature between 28-30^0C. Each experiment was repeated 3 times.

Effect of incubation P. variotii NV01 *in protease production*: the culture suspension was collected at various times between 24 and 120 h to determine the protease activity and protein content.

Investigation of the effect of chitin concentration on chitinase activity: similar to protease activity experiments, the culture medium was supplemented with chitin concentrations between 0.25-0.85%.

Detection of nematode killing ability (Khan, et al., 2006) [13]: *Paecilomyces variotii* NV01 strain was cultured on T1 and T2 medium, respectively, shaking for 84 h at 30±2^0C at 200 rpm. The culture broth was filtered using Whatman N°1 paper to remove the mycelium. Then, 300 nematodes of *Meloidogyne* sp. were added to 5 ml of culture broth and kept for 96 h at 30^0C. The number of nematodes were counted every 24 h by using a counting dish and counting machine under the microscope. Microscope slides of nematodes

were prepared to determine the dead nematodes, which had a violet colour after staining with Phloxin B reagent.

Results and disscusion

According to the results of the previous article [8], the NV01 strain has extracellular chitinase and protease activity. By diffusion on CD agar plates, the valuable characteristics of this strain can be seen. In this study, we continue to shed light on chitinase and protease activity as well as factors related to the culture medium's affects on enzyme activities.

Selection of protease biosynthesis medium

The selection of optimal culture medium for protease biosynthesis in the NV01 strain is the aim of this study. The protease activity results from the PDB, Czapeck-Dox, and CMA culture media under the culture conditions described in the methods section are presented in Fig. 1. The CD medium had the highest protease activity. The results showed that the CD medium contains a number of mineral elements necessary for protease biosynthesis, which increases protease activity.

The CD medium with the highest protease activity was selected for further studies to find the optimal casein substrate concentration for the NV01 strain.

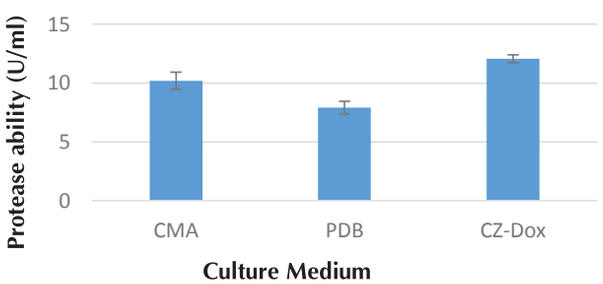

Fig 1. Protease biosynthesis ability.

Effect of casein substrate concentration of Paecilomyces variotii NV01

Figure 2 shows that the NV01 strain has the highest activity with 82.3 U/ml in a concentration of 0.65% casein after 84 h of incubation (Fig. 3). These results are 6 folds higher than with a basal medium (12.7 U/ml) and 1.5 folds higher than the results of Deore, et al. (2013) [14]. In that work, the strain *Paecilomyces variotii* PR-4 was used and it showed that protease activity was 53 U/ml between 96-120 h. Our results suggest that the protease activity of NV01 is the basis for research into applications that kill nematodes or decompose organic matter in soil into an easily absorbed organic ion form.

According to the studies of Khan, et al. (2004) [15] the ability to kill nematodes using the strain *Paecilomyces lilacinus* 251 was based on both protease and chitinase activities.

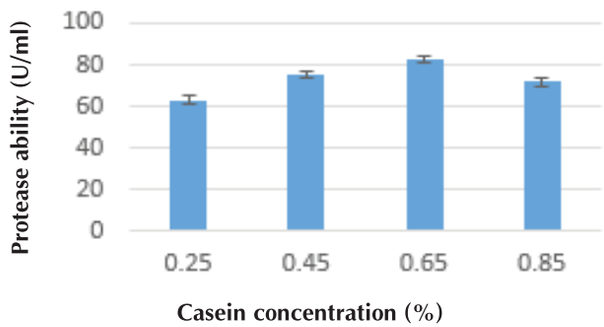

Fig. 2. Effect of casein concentration.

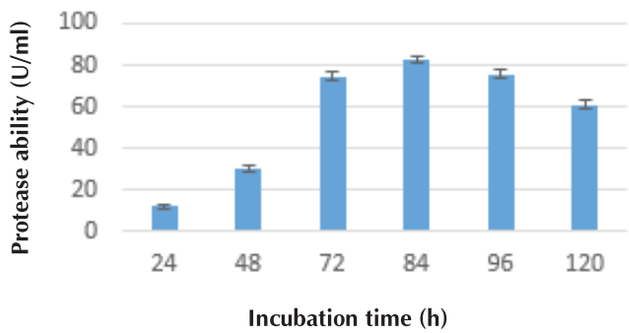

Fig. 3. Incubation time effect.

Effect of chitin substrate concentration

Based on the survey of protease-producing medium, the Czapeck-Dox (CD) medium had a higher protease activity than PDB and CMA. In this experiment, the CD medium was the control medium. According V.N. Nguyen, et al. (2009) [16], the chitinase activity from the culture liquid of *P. variotii* DG-3 was 3.8 U/ml after 12 days with 0.5% chitin added. On that basis, we study the effect of chitin substrate concentration on the chitinase biosynthesis ability of strain NV01. Based on the results of protease activity from NV01, a chitin concentration of 0.25-1% was added to the CD medium.

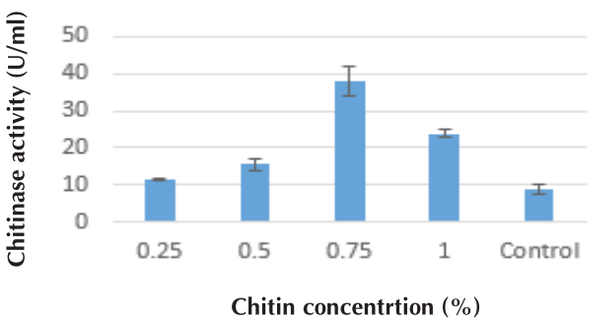

Fig. 4. Chitin substrate concentration.

The results in Fig. 4 show that the chitinase activity of NV01 in the medium supplemented with 0.75% chitin was highest after 84 h of incubation, which is 4 folds higher than the control CD medium. The chitinase activity of the 0.5% chitin substrate was 12.3 U/ml after 84 h. This result is 3 folds higher than what was reported by V.N. Nguyen, et al. (2009) [16] using a 0.5% substrate supplement and 10 folds higher than the 0.75% substrate. The culture time was shortened by 1/3 (for research by V.N. Nguyen, et al. (2009) [16] was 12 days.

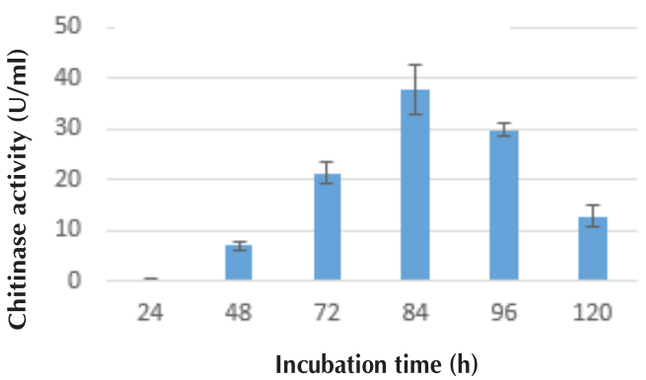

Fig. 5. Incubation time effect.

In Fig. 5, from 72 h to 84 h of culture, the chitinase activity of NV01 strain increased. The enzyme activity decreased after 96 h of culture. The harvest time for chitinase is 84 h. After 84 hours of culture, the metabolites in fungi product is made up of many chitinase activity inhibitors. At the same time, due to the metabolic process of fungi, some trace elements in the medium, which the device needs, has been exhausted [17, 18].

Effect of Ca^{2+} on chitinase and protease activity

Due to its innate ability to produce extracellular enzymes, *Paecilomyces variotii* provides eco-friendly solutions for a variety of biotechnological applications and is a potential source of industrial bioproducts. In addition to substrate concentration and culture conditions, typical trace elements such as Ca^{2+} play an important role in the enzyme activity of microorganisms. Therefore, the culture medium of strain NV01 was supplemented with 5 mM of $CaCl_2$.

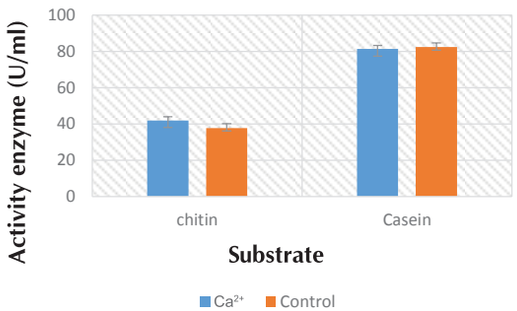

Fig. 6. Influence of Ca^{2+} on enzyme activity of NV01 strain.

Figure 6 shows that chitinase activity increased significantly when compared to the control (without supplementing Ca^{2+}). These results also coincide with studies of chitinase from microorganisms by Kassa (2017) [19], and Annamalai, et al. (2010) [20]. However, protease activity was not influenced and protease does not require $CaCl_2$ for its stability. Our results also show that Ca^{2+} does not influence protease activities. These results are similar to those of protease activity from the strain *Paecilomyces fomosoroseus* reported by Castellanos, et al. (2008) [21].

Perveen and Shahzad (2013), Khan, et al. (2003), and Kopparapu, et al. (2012) [22-24] studied chitinase activity on the *Paecilomyces* species, which is capable of killing nematodes and is used in biological control. Chitinase from *Trichoderma atroviridae* has been introduced to control the golden potato cyst nematode. It can also be used for chitinase enzyme production, which is supposed to be used in commercial formulation [25]. This is the basis for conducting further studies, such as the investigation of nematode killing ability.

Test of killing ability of nematodes

Table 1. Insecticide results of *Paecilomyces variotii* NV01.

Number	Strain	Nematode death rate (%)				
		24 h	*48 h*	*72 h*	*96 h*	*120 h*
0	Control (H_2O)	-	-	-	-	-
1	*Paecilomyces variotii* NV01 (T1 - Protease)	-	2.08	12.74	35.8	35.8
2	*Paecilomyces variotii* NV01 (T2 - Chitinase)	-	1.75	10.7	23.65	23.65
3	*Paecilomyces variotii* NV01 (Protease and Chitinase)	-	2.31	15.6	50.4	50.4

Note: (-) did not die.

Table 1 shows that incubation of the protease and chitinase together had a higher efficiency than T1 and T2 alone. Genier, et al. (2016) [26] aimed to evaluate the action of *Paecilomyces marquandii* proteases on *Ancylostoma* spp L_3. Protease from L_3 reduced action by 41.4%. The NV01 strain between 72-96 h tested the pathogenicity of *Meloidogyne* sp. and destroyed 50.4%. According to the study by Perveen and Shahzad using *P. lilacinus*, *P. variotii*, and *P. fumosoroseus* incubated with the larvae of *M. incognita*. After 24, 48, and 72 h, the number of larvae was counted. Results showed that after 72 h, the ability to kill nematodes was 75% effective [21]. In order to be able to use the fungus for the application of plant parasitic nematode control, further research is needed to improve the activity and appropriate culture conditions. .According to Al-Assas, et al. (2011) [27], *Paecilomyces variotii* reduced the number of nematode root galls and showed the superiority of pesticides based on plant extract over chemical pesticides. The fungus showed a high effectiveness (91.5%) in controlling root-knot nematode, while it was 96.4, 99.7, and 98.9% in DMAC, diazinon and plant extract, respectively. Ahmad, et al. (2019) [28] indicated that out of the five strains of fungus *Paecilomyces variotii*, *Paecilomyces lilacinus*, *Duddingtonia flagrans*, *Trichoderma harzianum*, and *T. asperelum*, only *D. flagrans* could not kill the egg in an in vitro egg culture of *Meloidogyne* sp..Among the remaining 4 strains, *P. lilacinus* showed a significant reduction in eggs by 67.9%, meanwhile the potency of *P. variotii* could kill only 25.1% of the eggs.

Conclusions

Protease activity of *P. variotii* NV01 reached 82.3 U/ml within 84 h of incubation. When 0.65% casein was added, the protease activity was 6 times higher than the basal medium. It is interesting to note that protease activity was not significantly altered by the addition 5 mM of $CaCl_2$ concentration.

Chitinase activity of *P. variotii* NV01 reached 37.28 U/ml within 84 h of incubation with 0.75% chitin, which is 4 folds more than the basal medium. Unlike protease, the chitinase activity increased by 10.5% with the addition of 5 mM $CaCl_2$.

By the method of testing for infectious nematode *Meloidogyne* sp. with *Paecilomyces variotii* NV01, the efficiency reached 50.4% within 96 h. This is the basis for further research on the NV01 strain.

ACKNOWLEDGEMENTS

This research was supported by Department of Microbiology, Faculty of Biology, University of Science, Vietnam National University, Hanoi.

The authors declare that there is no conflict of interest regarding the publication of this article.

REFERENCES

[1] J. Li, C. Zou, J. Xu, X. Ji, X. Niu, J. Yang, X. Huang, K.-Q. Zhang (2015), "Molecular mechanisms of nematode-nematophagous microbe interactions: basis for biological control of plant-parasitic nematodes", *Annual Review of Phytopathology*, **53**, pp.67-95.

[2] C. Dackman, I. Chet, B. Nordbring-Hertz (1989), "Fungal parasitism of the cyst nematode Heterodera schachtii: infection and enzymatic activity", *FEMS Microbiology Ecology*, **5(3)**, pp.201-208.

[3] J. Yang, L. Liang, J. Li, K.-Q. Zhang (2013), "Nematicidal enzymes from microorganisms and their applications", *Applied Microbiology and Biotechnology*, **97(16)**, pp.7081-7095.

[4] X. Huang, N. Zhao, K. Zhang (2004), "Extracellular enzymes serving as virulence factors in nematophagous fungi involved in infection of the host", *Research in Microbiology*, **155(10)**, pp.811-816.

[5] J. Yang, B. Tian, L. Liang, K.-Q. Zhang (2007), "Extracellular enzymes and the pathogenesis of nematophagous fungi", *Applied Microbiology and Biotechnology*, **75(1)**, pp.21-31.

[6] G. Stirling, R. Mankau (1979), "Mode of parasitism of *Meloidogyne* and other nemaitode eggs by *Dactylella oviparasitica*", *Journal of Nematology*, **11(3)**, p.282.

[7] L. Lopez-Llorca (1990), "Purification and properties of extracellular proteases produced by the nematophagous fungus *Verticillium suchlasporium*", *Canadian Journal of Microbiology*, **36(8)**, pp.530-537.

[8] C.T. Binh, B.T.V. Ha, H. Tuyen, N.P. Nhue (2017), "Biological characteristics of strain *Paecilomyces variotii* NV01 isolated in Dak Lak pepper soil", *VNU Journal of Science: Natural Sciences and Technology*, **33(1S)**, pp.42-48.

[9] G. Chávez-Camarillo, R. Cruz-Camarillo (1984), "El sistema quitinolítico de *Serratia marcescens*", *Revista Latinoamericana de Microbiología*, **26**, pp.203-215.

[10] G.L. Miller (1959), "Use of dinitrosalicylic acid reagent for determination of reducing sugar", *Analytical Chemistry*, **31(3)**, pp.426-428.

[11] P.L. Manachini, M.G. Fortina, C. Parini (1988),

"Thermostable protease produced by *Bacillus thermorubber*: a new species of Bacillus", *Appl. Microbiol. Biotechnol*., **28**, pp. 409-413.

[12] M.M. Bradford (1976), "A rapid and sensitive method for the quantitation of microgram quantities of protein utilizing the principle of protein-dye binding", *Analytical Biochemistry*, **72(1-2)**, pp.248-254.

[13] A. Khan, K.L. Williams, H.K. Nevalainen (2006), "Control of plant-parasitic nematodes by *Paecilomyces lilacinus* and *Monacrosporium lysipagum* in pot trials", *Biocontrol*, **51(5)**, pp.643-658.

[14] G. Deore, A. Limaye, Y. Dushing, S. Dhobale, S. Kale, S. Laware (2013), "Screening of protease producing fungi for microbial digestion of seed proteins and synthesis of amino acids-metal nutrient chelates", *Pakistan Journal of Biological Sciences*, **16(2)**, pp.86-91.

[15] A. Khan, K.L. Williams, H.K. Nevalainen (2004), "Effects of Paecilomyces lilacinus protease and chitinase on the eggshell structures and hatching of *Meloidogyne javanica* juveniles", *Biological Control*, **31(3)**, pp.346-352.

[16] V.N Nguyen, I.-J. Oh, Y.-J. Kim, K.-Y. Kim, Y.-C. Kim, R.-D. Park (2009), "Purification and characterization of chitinases from *Paecilomyces variotii* DG-3 parasitizing on *Meloidogyne incognita* eggs", *Journal of Industrial Microbiology & Biotechnology*, **36(2)**, p.195.

[17] W. Chan Cupul, G. Heredia Abarca, D. Martinez Carrera, R. Rodríguez Vázquez (2014), "Enhancement of ligninolytic enzyme activities in a *Trametes maxima-Paecilomyces carneus* co-culture: key factors revealed after screening using a Plackett-Burman experimental design", *Electronic Journal of Biotechnology*, **17(3),** pp.114-121.

[18] S. Kim, H. Hwang, C. Xu, Y. Na, S. Song, J. Yun (2002), "Influence of nutritional conditions on the mycelial growth and exopolysaccharide production in *Paecilomyces sinclairii*", *Letters in Applied Microbiology*, **34(6)**, pp.389-393.

[19] F. Kassa (2017), *Production and Characterization of Alkaline Chitinase and Protease from an Alkaliphilic Actinomycete*, Thesis MSc, Addis Ababa University.

[20] N. Annamalai, S. Giji, M. Arumugam, T. Balasubramanian (2010), "Purification and characterization of chitinase from Micrococcus sp. AG84 isolated from marine environment", *African Journal of Microbiology Research*, **4(24)**, pp.2822-2827.

[21] M. Castellanos, J.R. Cruz-Camarillo, E. Aranda, T. Mier, C. Toriello (2008), "Relationship between protease and chitinase activity and the virulence of *Paecilomyces fumosoroseus* in *Trialeurodes vaporariorum* (Hemiptera: Aleyrodidae)", *Revista Mexicana de Micología*, **28**, pp.71-80.

[22] Z. Perveen, S. Shahzad (2013), "A comparative study of the efficacy of *Paecilomyces* species against root-knot nematode *Meloidogyne incognita*", *Pakistan Journal of Nematology*, **31(2)**, pp.125-131.

[23] A. Khan, K. Williams, M.P. Molloy, H. Nevalainen (2003), "Purification and characterization of a serine protease and chitinases from *Paecilomyces lilacinus* and detection of chitinase activity on 2D gels", *Protein Expression and Purification*, **32(2)**, pp.210-220.

[24] N.K. Kopparapu, P. Zhou, S. Zhang, Q. Yan, Z. Liu, Z. Jiang (2012), "Purification and characterization of a novel chitinase gene from *Paecilomyces thermophila* expressed in *Escherichia coli*", *Carbohydrate Research*, **347(1)**, pp.155-160.

[25] K. Abbasi, D. Zafari, R. Wick (2017), "Evaluation of chitinase enzyme in fungal isolates obtained from golden potato cyst nematode *(Globodera rostochiensis)*", *Zemdirbyste-Agriculture*, **104(2)**, pp.179-184.

[26] H.L.A. Genier, J.H.D. Queiroz, F.R. Braga, F.E.D.F. Soares, J.V.D. Araújo, I.R. Pinheiro (2016), "Nematicidal activity of *Paecilomyces marquandii* proteases on infective larvae of *Ancylostoma* spp.", *Brazilian Archives of Biology and Technology*, **59**, Doi:10.1590/1678-4324-2016160218.

[27] Al-Assas, W. Naffaa (2011), "Effectiveness of *Paecilomyces variotii*, plant extraction of Hemlock Conium maculatum and some pesticides in controlling Root-knot nematode *Meloidogyne incognita* on tomato", *The Arab Journal for Arid Environments*, **4(1)**, pp.48-54.

[28] R. Ahmad, B. Sidi, D. Endrawati, F. Ekawasti (2019), "*Paecilomyces lilacinus* and *P. variotii* as a predator of nematode and trematode eggs", *IOP Conference Series: Earth and Environmental Science*, IOP Publishing.

Doi: 10.31276/VJSTE.61(4).64-69

Transgenerational effects of the plasticizer di-2-ethylhexyl phthalate on survival, growth, and reproduction of *Daphnia magna*

Thi-Phuong-Dung Le[1*], Van-Tai Nguyen[1], Thi-My-Chi Vo[1], Nghia-Hiep Bui[2], Thanh-Son Dao[1]

[1]*University of Technology, Vietnam National University, Ho Chi Minh city*

[2]*Department of Environmental Engineering, Dayeh University, Taiwan*

Received 6 September 2019; accepted 21 November 2019

Abstract:

In this study, we conducted a chronic toxicity assessment of di-2-ethylhexyl phthalate (DEHP) on the life history traits of *Daphnia magna* across three generations. In the first generation, the neonates (called F0 *Daphnia*) were raised in a control environment (C, toxin-free medium) or in a medium containing DEHP at three concentrations 5, 50, and 500 µgl^{-1}, abbreviated as P5, P50, and P500, respectively. The offspring from the F0 control (called F1 *Daphnia*) were raised in toxin-free medium (denoted as C-C). However, the offspring from the P500 exposure were split into two groups: (i) the first group was raised in a toxin-free, control medium (denoted as P-C) and (ii) the second group was raised again in a medium containing 500 µgl^{-1} DEHP (denoted as P-P). The offspring from the F1 (called F2 *Daphnia*) were split again and treated in the same manner as F1, resulting in C-C-C, P-P-C, and P-P-P. The exposure time for each generation (F0, F1, F2) was 21 days. The survival and reproduction of *D. magna* over the three generations (F0, F1 and F2) were recorded daily during the 21 days of incubation. The body length of the animals in the F0 was measured by the end of incubation. The results showed that the survival rate of *D. magna* in the control and DEHP treatments was similar, while the DEHP strongly enhanced the reproduction of *D. magna* in the F0 and F1 generations. However, in the F2 generation, the survival rate for P-P-C and P-P-P was only 45-50% compared to the control. Consequently a much lower accumulative neonate proportion in DEHP treatment was found, around 50% compared to the control. The reduction in survivorship and reproduction of *D. magna* in the F2 generation and the smaller body length of the P500 treatment is a consequence of energy cost and trade-off under the chronic effects of DHEP. The results revealed that the population development of the micro-crustacean may lead to an extinction upon continuous exposure to high phthalate concentrations in natural water bodies. *In situ* monitoring on phthalates and zooplankton in aquatic ecosystems is suggested.

Keywords: **chronic effects, life traits, micro-crustacean, plastic additives.**

Classification number: **5.1**

Introduction

Global production of plastic materials has increased twenty-fold over the last fifty years, exceeding 300 million tonnes in 2015 [1]. Worldwide, a great amount of plastic waste is left unmanaged [2] and, more seriously, less than 5% of discarded plastic materials has been recovered [3]. Consequently, the continuous increase of plastic use over time has negative effects on the environment, especially water bodies. Plastics are known to contain a great number of additives, e.g., bisphenol A and phthalates, among others. Phthalates and their isoforms are among the most commonly used solvents in various industrial and consumer products, and the global production of phthalates is estimated to be between 6 and 8 million tons annually [4]. The existence of phthalates in the environment has been reported by many countries such as Finland, Denmark, Germany, Japan, China, Thailand, Poland, Sweden, and Italy [5]. While bisphenol A is known as both an oestrogen agonist and an androgen antagonist, impacting both reproduction and development in crustaceans and insects, phthalates have been shown to cause molecular and whole-organism effects in vertebrates and invertebrates [6]. Besides, phthalates desorbed from plastic have been known to accumulate in the gut of organisms resulting in disorder of biological processes such as endocrine disruption and behavioural alterations [7].

**Corresponding author: Email: phuongdungbp94@gmail.com*

Zooplankton have a central position in the food chain of aquatic ecosystems. Chemical substances leaching from many plastic products were shown to cause acute toxic effects (immobility) for *Daphnia magna*, with the 48 h-EC_{50} of leachates ranging from 5 to 80 g plastic material per L [8]. Giraudo, et al. (2015) found that the plasticizer Tris (2-butoxyethyl) phosphate (TBOEP) caused the mortality of 50% of the test *D. magna* within a 48 h exposure at a concentration of around 147 mgl^{-1} [9]. So far, there have only been a few investigations on the effects of plastic additives on freshwater micro-crustaceans such as *D. magna*. Plastic additives have also impacted gene transcription related to proteolysis, protein synthesis, and energy metabolism in *D. magna*. The plasticizer di-2-ethylhexyl phthalate (DEHP) at the concentration of 811 μgl^{-1}, significantly reduced the survivorship in *D. magna* after 21 days of treatment [10]. However, the same authors observed an impairment by DEHP exposure on genetic (RNA, DNA) and biochemical levels and hydrocarbon storage of the animal at a lower concentration, 158 μgl^{-1}, within 7 days of incubation. Recently, Wang, et al (2018) found that DEHP strongly influenced on the antioxidant and biotransformation enzyme activities in *D. magna* [11]. TBOEP at low concentration (10 μgl^{-1}) resulted in the reduction of body size (width and length), reproduction, and moulting in *D. magna* over three generational exposures [12].

Although the toxicity of plastic microspheres to several aquatic organisms has been tested and reported, the detrimental impacts of plastics and plasticizers on aquatic animals are underestimated [13]. The responses of aquatic animals and, in particular, zooplankton to microplastics and plastic additives upon long-term exposures are not yet fully understood [7, 14]. Therefore, in this study, we assessed the effects of DEHP at a concentration range of 5-500 μgl^{-1} on the life history traits of *D. magna* across three generations in laboratory conditions.

Materials and methods

The *Daphnia magna* (from Micro BioTest, Belgium) was raised in an ISO medium [15] and fed *ad libitum* with the live green alga *Chlorella* sp. and YTC, a rich nutrient mixture [16]. The alga *Chlorella* was cultured in a Z8 medium [17]. The animals were incubated under laboratory conditions at a temperature of 25±1^{0}C, light intensity of less than 1000 Lux, and a photo regime of 14 h light: 10 h dark [15, 18].

Di-2-ethylhexyl phthalate (DEHP, 99.5%), dissolved in MeOH at a concentration of 1000 mgl^{-1} (Aldrich Sigma), was used for the experiment. The stock was kept at 4^{0}C prior to the test implementation.

The experimental set up was conducted according to Dao, et al. (2010) and APHA (2012) with a minor modification [15, 18]. Briefly, the neonates of *D. magna* (<24 h old) were used for the chronic test and the experiment was conducted over 3 generations of *Daphnia*. In the first generation, the neonates (called F0 *Daphnia*) were raised in a control medium (denoted as C, a toxin-free medium) or in a medium containing DEHP at three concentrations: 5, 50, and 500 μgl^{-1}, abbreviated as P5, P50 and P500, respectively. The test concentrations of the phthalate in this study were based on the concentrations found in the environment, which is up to 460 μgl^{-1} [5]. The offspring from the F0 control (called F1 *Daphnia*) were raised in toxin-free medium (C-C). However, the offspring from the P500 were split into two groups: (i) the first group was raised in control medium (P-C), and (ii) the second group was raised in a medium containing DEHP (500 μgl^{-1}, P-P). The offspring from the second generation (called F2 *Daphnia*) were collected and split in the same manner as those from F1, resulting in C-C-C, P-P-C, and P-P-P (Fig. 1). We chose the offspring from the P500 for the transgenerational experiment because we believed that the P50 exposure would not cause significant effects on the life traits of the F1 and F2 *D. magna* generations because previous research found no observable effects on the bioindicators of *D. magna* (e.g. genetic and cellular levels, and life traits) were observed at a 158 μgl^{-1} concentration of DEHP [10]. However, a concentration of 811 μgl^{-1} DEHP impaired the survival, reproduction, and biochemical responses of *D. magna* on the 21st day of experiment [10]. Hence, we expected the P500 exposure might result in detrimental influences on *D. magna* in the F1 and F2 generations.

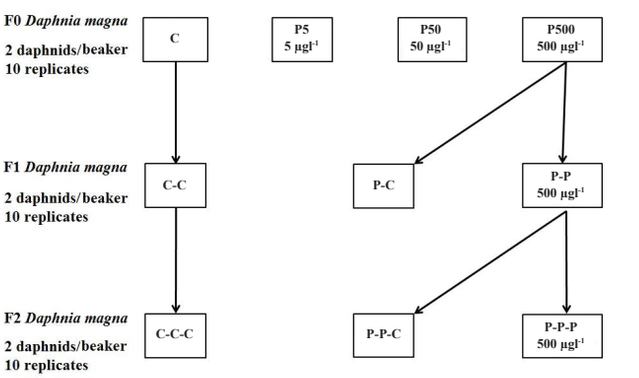

Fig. 1. Experimental setup. The first column shows the C, C-C, and C-C-C raised toxic-free medium exposures to *Daphnia* in the F0, F1, and F2 generations, respectively. The first row shows the C, P5, P50, and P500 exposures of *Daphnia* in F0 raised in 0, 5, 50, and 500 µg DEHP l^{-1}, respectively. P-C and P-P-C denote the exposures of *Daphnia* offspring of DEHP-exposed mothers in F0 and F1, respectively, raised in non-toxic medium. P-P and P-P-P denote exposures of *Daphnia* to DEHP-exposed mothers in F0 and F1, respectively, raised in a toxic medium of 500 µg DEHP l^{-1}.

In each generation and each treatment (control or DEHP exposure), 20 neonates were used and incubated in 10 glass beakers (2 neonate *Daphnia* per beaker, n=10; Fig. 1). The animals were fed and maintained in the laboratory conditions as mentioned above. The test medium and food were totally renewed 3 times per week and the incubation time for each treatment lasted 21 days. The life traits of the mother *D. magna,* including survival and reproduction, were recorded daily. By the end of experiment, the body size of the mother *Daphnia* in the F0 were measured on a microscope (Optika) coupled with a digital camera.

The Kruskal-Wallis test was applied in SigmaPlot (version 12.0) to determine the significant difference of the body size of F0 *D. magna* from the control and DEHP exposures.

Results and discussion

Effects of DEHP on survival of Daphnia magna

In the first generational experiment (F0), the survival rate of *D. magna* in the control and DEHP exposures was between 95% and 100% (Fig. 2A). The mortality of the animals in the second generational experiment (F1) was 85% (P-P), 95% (control), and 100% (P-C), as seen in Fig. 2B. In the third generational treatment (F2), the survival rate of the control was 95%, however, that of the P-P-C and P-P-P was 50% and 45%, respectively (Fig. 2C).

Seyoum and Pradhan (2019) reported that DEHP at concentrations up to 3900 μgl^{-1} did not result in any lethality or reduction of the hatching rate of *D. magna* within 48 h and 96 h, respectively, of incubation [4]. This record is similar to *D. magna* survival rate in control and DEHP treatments in our study. It has been evidenced that isoforms of phthalates (e.g. benzyl butyl phthalate, diethyl phthalate, mono-(2-ethylhexyl) phthalate, DEHP) at concentrations of 100 μgl^{-1} to 5 mgl^{-1} negatively influence the feeding behaviour of aquatic animals [7]. The values of the 48 h-LC_{50} of plastic additives and leachates on *D. magna* were reported to withstand quite a high range of the chemical and material concentrations, e.g., up to 147 mg TBOEP l^{-1} and 80 g plastic l^{-1} [8, 9]. Knowles, et al. (1987) found a reduction of genetic synthesis (DNA) and genetic ratio (RNA/DNA) in *D. magna* exposed to DEHP (158 μgl^{-1}) for 7 days [10]. Additionally, DEHP at concentrations of 60-100 μgl^{-1} significantly altered the activities of the antioxidant enzymes superoxide dismutase and catalase and the biotransformation enzyme glutathione S-transferase in *D. magna* within 2 days of exposure [11]. Hence, one might expect concentrations of 5-500 μgl^{-1} DEHP to cause adverse influences on biochemical and physiological responses on the F0 and F1 *D. magna* in our study, however, the impacts were apparently not strong enough to reduce the survivorship of the animals. Also, the survival rate of *D. magna* exposed 158 μgl^{-1} DEHP was similar to that of the control [10], which supports our observation in the F0 experiment (Fig. 2A). Giraudo, et al. (2015) reported that the plastic additive TBOEP did not cause mortality on *D. magna* at concentrations between 147-1470 μgl^{-1} [9]. Hence, the toxicity of DEHP and TBOEP to *D. magna* survival is comparable.

Differently, in the F2 generation, the *D. magna* pre-exposed to DEHP strongly reduced their survival within the first 4 days of incubation (Fig. 2C) regardless of being raised in a DEHP-containing medium or not. Phthalates were reported to impair the exposed animals on a molecular, cellular, and organ level [7]. The 811 μgl^{-1} DEHP exposure strongly reduced the total protein and glycogen content in *D. magna* after 21 days of exposure [10]. Therefore, an energy cost occurs when the animals are exposed to the toxin. The reduction of survival rate in the F2 generation in our study could be explained by: (i) there was already an energy cost and some impairment in the DEHP-exposed F1 *D. magna* and its offspring (F2) because DEHP could cause adverse effects on the development of the newborns [5, 10], and (ii) the impairment was only strong enough after 2 generational exposures to the DEHP. Hence, the F2 *D. magna* with prior disorder/damage would not be healthy enough to maintain normal life activities and die as a consequence. Thus, the toxicity of plasticizers to zooplankton should not be assessed within one generation, but by multiple generations.

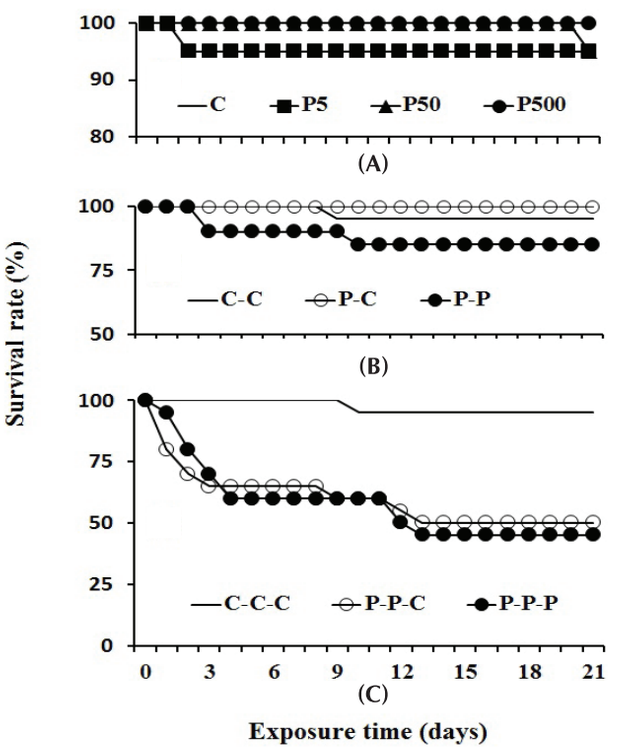

Fig. 2. Survival rate of the (A) first, (B) second, and (C) third generation of *Daphnia magna* exposed to DEHP. Abbreviations are the same as in Fig. 1.

Effects of DEHP on reproduction of Daphnia magna

The total neonates produced by the mother *D. magna* in the control, P5, P50, and P500 exposures were 545, 779, 1031, and 612, respectively. Therefore, in the F0 experiment, the total neonates of the P5, P50, and P500 relative to the control was 143%, 189%, and 112%, respectively (Fig. 3A). In the F1 experiment, the total neonates of the P-C and P-P relative to the control was 108% and 127%, respectively (Fig. 3B). Conversely, the total neonates of the P-P-C and P-P-P exposures relative to the control in the F2 experiment was 53 and 55%, respectively (Fig. 3C).

The plasticizer TBOEP (147-1470 μgl^{-1}) did not significantly alter the reproduction of *D. magna* during 3 weeks of treatment [9]. In contrast, DEHP at lower concentrations (e.g. 5 and 50 μgl^{-1}) resulted in a reproduction stimulation of the *D. magna* in the current study. Therefore, the influence of DEHP on *Daphnia* reproduction is much stronger than that of TBOEP.

Knowles, et al. (1987) proved that DEHP (from 158 μgl^{-1}) inhibited some biochemical components in *D. magna*. However, no significant impact on those components were observed when the animals were exposed to DEHP at concentrations up to 72 μgl^{-1} [10]. However, a DEHP concentration of 390 μgl^{-1} could increase the reproduction of *D. magna* up to 1.5 times compared to the control [4]. This helps to explain the enhancement of the total offspring in the DEHP-exposed mother *D. magna* compared to the control in the current study (Fig. 3A). Also, the remarkable increase of reproduction in the lower DEHP concentration exposures (P5 and P50) and slight increase in the reproduction of the higher DEHP concentration treatment (P500) is observed in our study (Fig. 3A). This may be explained by an energy cost of the high DEHP concentration treatment (P500 > 158 μgl^{-1}), which was reported elsewhere [10].

The reproduction of DEHP-treated *D. magna* in the F1 generation of our study was still a little higher than that of control. Phthalates and their isoforms are known to cause impairment of the reproduction of fish and aquatic mammals, including problems with fertility [5]. However, our results indicated oestrogen-like effects of the DEHP, i.e. a reproduction stimulation, on *D. magna,* as reported elsewhere [4]. It is likely that different species would have different responses to the same pollutants. Therefore, more investigations of this subject using phthalates are recommended to clarify the observed reproduction stimulation.

In the third generational exposure, F2, we found the total offspring in the pre-DEHP treated *D. magna* remarkably decreased, regardless if the animals were raised in a DEHP-containing medium or toxin-free medium (Fig. 3C). The fecundity of *D. magna* also significantly decreased, but the survival rate did not decrease after three generational exposures to the plasticizer TBOEP [12]. However, it is important to note that the 50% drop in total reproduction of the P-P-C and P-P-P exposures should be closely related to the total number of *D. magna* mothers in the experiment. Around 45-50% of the total number of *D. magna* mothers was lower in the P-P-C and P-P-P, starting from the 4th day to the end of experiment (Fig. 2C), and the accumulative neonates in the pre-DEHP incubations were reduced. Anyway, the population development of *D. magna* would continuously decrease in natural water bodies upon the presence of high phthalate concentrations for a long period of time. *In situ* monitoring of chemical concentrations and zooplankton population development is suggested for extrapolation in aquatic ecosystems.

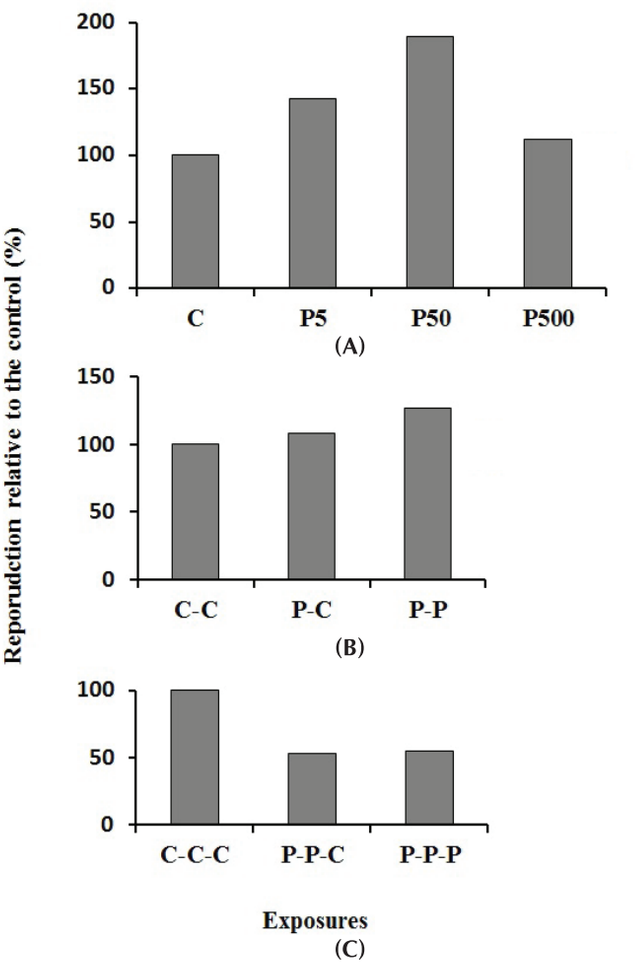

Fig. 3. Total neonates relative to control in the first (A), the second (B), and the third (C generations of *Daphnia magna* exposed to DEHP. Abbreviations as in the Fig. 1.

Effects of DEHP on body length of Daphnia magna

The body length of the mother *D. magna* at the age of 21 days in the control, P5, and P50 were similar, and ranged between 2883 and 2884 mm. However, the body length of the animal in the P500 exposure was 2580 mm, which is significantly shorter than that of the control (p=0.004, Kruskal-Wallis test; Fig. 4).

The similar body length measured of the *D. magna* in the control, 5 μgl^{-1}, and 50 μgl^{-1} DEHP concentrations in this study is in line with the previous observation by Giraudo, et al., (2015, 2017) testing with TBEOP [9, 12]. However, in an exposure to a higher DEHP concentration (500 μgl^{-1}), the *D. magna* was smaller size than in the control (Fig. 4), which is in line with a previous investigation of Seyoum and Pradhan (2019) [4]. The authors recorded a reduction of body length in *D. magna* exposed to around 390 μgl^{-1} of DEHP over the period of 14 days [4]. As previously mentioned, phthalates could impair aquatic animals at the genetic, cellular, tissue, and individual levels [7]. In the treatment with DEHP, it is believed that *D. magna* would be affected by the chemical. The animal could maintain their normal activities and deal with the biochemical and physiological alterations inside its body [10]. Then, the animal needs to balance its total energy for all of its life processes. Therefore, exposure to high concentrations of DEHP would lead to an energy cost in the *D. magna* that results in a trade-off between its growth and other activities. Maybe at low DEHP treatments (e.g. 5 and 50 μgl^{-1}), the *D. magna* could balance all processes and it could grow normally. However, at a higher chemical level incubation (500 μgl^{-1}), the animal has to face a trade-off that consequently slows down its development, hence, growing to smaller size than usual.

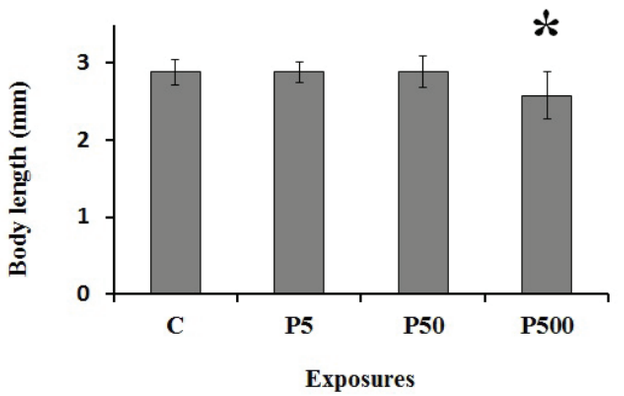

Fig. 4. Body length of the first generation of *Daphnia magna* exposed to DEHP at different concentrations. The asterisk indicates a significant difference of the body length between control and exposure (p=0.004, Kruskal-Wallis test). Abbreviations are the same as in Fig. 1.

Conclusions

This study, from the best of our knowledge, is the first to assess the effects of DEHP on the life history traits of *D. magna* across three generations. Survivorship of the animal exposed to the chemical was slightly reduced in the first and second generations. However, a high mortality proportion of 45-50% occurred in the DEHP exposures in the third generation. Acting as an endocrine disrupting compound, DEHP strongly stimulated the reproduction of *D. magna* in the first two generations (F0 and F1). However, the total accumulative offspring of *D. magna* was significantly reduced in the F2 generation, which is closely related to the survival rate of the pre-DEHP exposed mother *D. magna*. This shows that the population development of micro-crustacean may lead to an extinction upon continuous exposure to high phthalate concentrations in natural water bodies. The reduction in survivorship and reproduction of *D. magna* in the third generation and the smaller body length of the *D. magna* in the 500 μgl^{-1} DEHP treatment should be a consequence of energy cost and trade-off due to chronic effects of the chemical. Phthalates have been widely found in natural environment, but their toxicity to tropical aquatic animals has not been fully understood. Therefore, further investigations on the occurrence, distribution, and fate of phthalates, as well as their detrimental impacts on aquatic ecosystems, are highly suggested.

ACKNOWLEDGEMENTS

This research is funded by Vietnam National Foundation for Science and Technology Development (NAFOSTED) under grant number 106.99-2019.39, and under the framework of the Jeunes Équipes Associées à l'IRD Program (JEAI) supported by The French National Research Institute for Sustainable Development (IRD).

The authors declare that there is no conflict of interest regarding the publication of this article.

REFERENCES

[1] G. Suaria, C.G. Avio, A. Mineo, G.L. Lattin, M.G. Magaldi, G. Belmonte, S. Aliani (2016), "The Mediterranean plastic soup: synthetic polymers in Mediterranean surface waters", *Scientific Report*, **6**, pp.37551.

[2] J.R. Jambeck, R. Geyer, C. Wilcox, T.R. Siegler, M. Perryman, A. Andrady, R. Narayan, K.L. Law (2015), "Plastic waste inputs from land into the ocean", *Science*, **347**, pp.768-771.

[3] H.S. Auta, C.U. Emenike, S.H. Fauziah (2017), "Distribution and importance of microplastics in the marine environment a review of the sources, fate, effects and potential solutions", *Environmental International*, **102**, pp.165-176.

[4] A. Seyoum, A. Pradhan (2019), "Effects of phthalates on development, reproduction, fat metabolism and life span in *Daphnia*

magna", *Science of the Total Environment*, **654**, pp.969-977.

[5] P. Wowkonowicz, M. Kijenska (2017), "Phthalate release in leachate from municipal lanfills of central Poland", *PLOS ONE*, **12(3)**, e0174986.

[6] M. Cole, P. Lindeque, C. Halsband, T.S. Galloway (2011), "Microplastics as contaminants in the marine environment: a review", *Marine Pollution Bulletin*, **62**, pp.2588-2597.

[7] W.C. Li, H.F. Ste, L. Fok (2016), "Plastic waste in the marine environment: a review of sources, occurrence and effects", *Science of the Total Environment*, **566-567**, pp.333-349.

[8] D. Lithner, J. Damberg, G. Dave, A. Larsson (2009), "Leachates from plastic consumer products - screening for toxicity with *Daphnia magna*", *Chemosphere*, **74**, pp.1195-1200.

[9] M. Giraudo, M. Douville, M. Houde (2015), "Chronic toxicity evaluation of the flame retardant tris (2-butoxyethyl) phosphate (TBOEP) using *Daphnia magna* transcriptomic response", *Chemosphere*, **132**, pp.159-165.

[10] C.O. Knowles, M.J. McKee, D.U. Palawski (1987), "Chronic effects of Di-2-ethylhexyl phthalate on biochemical composition, survival and reproduction of *Daphnia magna*", *Environmental Toxicology and Chemistry*, **6**, pp.201-208.

[11] Y. Wang, T. Wang, Y. Ban, C. Shen, Q. Shen, X. Chai, W. Zhao, J. Wei (2018) "Di-(2-ethylhexyl) phthalate exposure modulates antioxidant enzyme activity and gen expression in juvenile and adult *Daphnia magna*", *Archives of Environmental Contamination and Toxicology*, **75**, pp.145-156.

[12] M. Giraudo, M. Dube, M. Lepine, P. Gagnon, M. Douville, M. Houde (2017), "Multigenerational effects evaluation of the flame retardant tris (2-butoxyethyl) phosphate (TBOEP) using *Daphnia magna*", *Aquatic Toxicology*, **190**, pp.142-149.

[13] Y. Chae, Y.J. An (2017), "Effects of micro-and nanoplastics on aquatic ecosystems: current research trends and perspectives", *Marine Pollution Bulletin*, **142**, pp.624-632.

[14] D. Eerkes-Medrano, R.C. Thompson, D.C. Aldridge (2015), "Microplastics in freshwater systems: a review of the emerging threats, identification of knowledge gaps and prioritisation of research needs", *Water Research*, **75**, pp.63-82.

[15] T.S. Dao, L.C. Do-Hong, C. Wiegand (2010), "Chronic effects of cyanobacterial toxins on *Daphnia magna* and their offspring", *Toxicon*, **55**, pp. 1244-1254.

[16] US Environmental Protection Agency (US. EPA) (2002), *Methods for Measuring the Acute Toxicity of Effluents and Receiving Waters to Freshwater and Marine Organisms,* 5th ed, EPA-821-R02-012, Office of Water, Washington, DC.

[17] J. Kotai (1972), "Instructions for preparation of modified nutrient solution Z8 for Algae", *Norwegian Institute for Water Research,* p.5, Blindern, Oslo.

[18] American Public Health Association (APHA) (2012), *Standard Methods for the Examination of Water and Wastewater,* 22nd edition, Washington DC.

Doi: 10.31276/VJSTE.61(4).70-75

Toxicity of non-microcystin producing *Microcystis wesenbergii* isolated from the Tri An reservoir

Pham Thanh Luu[1, 2*]

[1]*Graduate University of Science and Technology, VAST, Vietnam*
[2]*Institute of Tropical Biology, VAST, Vietnam*

Received 5 August 2019; accepted 18 November 2019

Abstract:

Harmful cyanobacterial blooms have become a global threat to human health and aquatic biota around the world. While the ecotoxicity of cyanobacterial toxins such as microcystins (MCs) has been studied extensively, the toxicity of non-toxin producing cyanobacteria has not been evaluated to the same extent. In this study, five strains of *Microcystis wesenbergii* were isolated from the Tri An reservoir and cultured under laboratory conditions. Microscopic observation was used for morphological identification. The MCs concentration was measured by high-performance liquid chromatography (HPLC). The microcrustacean (*Daphnia magna*) was exposed to different concentrations of crude extracts in a series of acute (48 h) and sub-chronic (15 day) toxicity experiments. The acute assay showed that crude extract from all isolated strains of *M. wesenbergii* generated toxic effects on *D. magna*, but no variant of MCs was detected in the cultures of *M. wesenbergii*. The 48 h EC_{50} values of crude extracts of *M. wesenbergii* on *D. magna* ranged from 307.2-491.5 mg dry weight (dw)/l. Sub-chronic exposure of *D. magna* to the crude extract of *M. wesenbergii* at concentrations of 1, 10, 40, and 120 mg dw/l resulted in a decline of survival rates with dose dependence. Both maturation and reproduction of parent *D. magna* were inhibited with increasing concentrations of crude extract. This finding indicated that crude extracts from non-MC-producing *M. wesenbergii* isolated from the Tri An reservoir had significant acute and chronic toxic effects on *D. magna*.

Keywords: **acute, cyanobacteria, *Daphnia*, non-microcystins producing, Sub-chronic.**

Classification number: **5.1**

Introduction

Cyanobacterial blooms in eutrophic freshwater ecosystems have become an environmental concern worldwide [1]. *Microcystis* is one of the most common planktonic freshwater cyanobacterium, which frequently causes bloom-forming and toxin-producing genus in continental aquatic ecosystems. *Microcystis* is known to produce various toxins such as microcystins (MC), other bioactive peptides, alkaloid groups, and lipopolysaccharides (LPS) [2], all of which may generate toxic effects on aquatic organisms as well as human beings. In its natural environment, *Microcystis* blooms may contain either MC-producing or non-MC-producing strains [3]. However, previous studies have primarily focused on isolated MC or cyanobacterial extracts containing MC, but the roles of other toxic compounds present within a complex cyanobacterial extract have not been studied to the same extent [4]. There has been some evidence that various other cyanobacterial metabolites, including LPS, alkaloid groups or unknown secondary metabolites, and non-specific factors also contribute significantly to the adverse effects associated with blooms [4, 5].

In their natural environment, aquatic animals may be directly exposed to toxic cyanobacteria via feeding on toxic cyanobacterial cells or be indirectly exposed via ingestion of water contaminated with dissolved cyanotoxins [6]. Microcrustaceans play critical roles in aquatic ecosystems, serving as both feeders and consumers. As a filter-feeder, microcrustacean *Daphnia* spp. are potential consumers of planktonic cyanobacteria. These filter feeders are therefore seriously affected by the presence of toxic second metabolites released into the water column during cyanobacterial blooms or after the collapse of toxic cells at the end of the blooms [7]. Because of relatively

*Email: thanhluupham@gmail.com

high sensitivity to toxicants, rapid reproduction, and short lifetime, *D. magna* has been used extensively for ecotoxiclogical studies. Several studies [4, 7, 8] have examined the toxic effects of cyanobacterial bloom and MCs on *D. magna* in laboratory conditions. Acute exposure of *Daphnia* to cyanotoxins resulted in inhibition of filtration rate, decrease in swimming movements, and even death [4, 8]. Among chronic effects, literature reports decreased fecundity and population growth rate [7, 9]. Despite not producing MCs, some non-toxic cyanobacteria caused a significant increase of biotransformation enzyme activities from the exposed *D. magna* after a longer incubation [10]. However, the adverse effects of non-microcystin producing on microcrustaceans species in natural environments, where they may be exposed to a complex cyanobacterial biomass, remain somewhat unclear.

The non-microcystin producing *M. wesenbergii* are proliferate in many lakes, rivers and reservoirs in Vietnam. Little is known about their toxicity in the aquatic environment. In this study, we isolated five strains of the *M. wesenbergii* from the Tri An reservoir and maintained them in laboratory conditions. Microscopic observation was used for morphological identification. The MCs concentration was measured by HPLC. In addition, the toxic effects of a crude extract of *M. wesenbergii* on the freshwater *D. magna* were investigated.

Materials and methods

Blooms collection and isolation of cyanobacteria

Bloom samples from the Tri An reservoir were collected on surface water during July of 2017 (Fig. 1). Samples were then brought to the laboratory. Observation under microscope indicated several cyanobacteria dominant in the samples including *Microcystis*, *Oscillatoria*, and *Anabaena*. The colonies of the *M. wesenbergii* was identified under a microscope (Olympus CK40-F200) equipped with a digital camera (Olympus, Tokyo, Japan). Taxonomic classification was based on the system of Komárek and Anagnostidis (2005) [11]. For isolation, single colonies of *M. wesenbergii* were picked out by micro-pipetting. After several times washing in milli-Q water, the colonies were transferred into tubes with Z8 medium and grew at a temperature of 28^{0}C under a 12:12 h light:dark cycle at an intensity of 50 µmol photons/m^2/s. The biomass of *M. wesenbergii* was collected onto GF/C fiberglass filters at stationary phase. After drying completely at 45^{0}C, the samples were kept at -20^{0}C prior to the experiment.

Fig. 1. Collection of water bloom samples in the Tri An reservoir.

Crude extract preparation and analysis

The crude extracts of *M. wesenbergii* were prepared according to the method of Pietsch, et al. (2001) [12]. Briefly, a 1.0 g dry weight (dw) biomass of *M. wesenbergii* was dissolved into 100 ml milli-Q water and frozen at -70^{0}C, then thawed at room temperature. Then, the samples were sonicated for 3 min. This freeze-thaw-sonicate cycle was repeated five times. After centrifugation at 4000 rpm for 10 min, the supernatant was collected and kept at -20^{0}C. Subsamples of the crude extract were used for the measurement of MC by HPLC according to the methods reported previously by Pham, et al. (2015) [13]. Briefly, 100 µl of the supernatants was centrifuged at 4000 rpm for 15 min. The supernatant was collected into new glass tubes and dried completely. The MC's content in the samples were collected by re-constitute in 500 µl of 100% MeOH. MC concentrations were analyzed by an HPLC system with UV-visible photodiode array (PDA) detector (Shimadzu 10A series, Kyoto, Japan). Three commercial MCs included MC-RR, -LR, and -YR from Wako company (Osaka, Japan) were used as internal standards.

Acute and sub-chronic bioassays

D. magna Straus purchased from the MicroBioTests Inc, Belgium has been permanently maintained for more than 3 years under controlled conditions: temperature 25 ± 1^{0}C and 14:10 h light:dark cycle in the ISO medium. The animals were fed by a mixture of viable green algae *Chlorella* sp. and *Scenedesmus* sp. Neonates less than 24 h were isolated for toxicity experiments.

Acute toxicity bioassays were performed according to the Protocol 202 of the Organization for the Economical Cooperation and Development (OECD) [14]. Briefly, *D. magna* neonates (<24 h old) were maintained in an ISO

medium with crude extracts of *M. wesenbergii*. At least six different concentrations with a dilution factor of 0.5 were tested in triplicate with 10 neonates per replicate. Test containers were placed at a controlled temperature of 25 ± 1^0C and a 14:10 h photoperiod during 48 h. The 48 h immobility of cladocerans was used to determine the half maximal effective concentration (EC_{50}) values with the 95% confidence interval by using the SPSS software.

Sub-chronic tests were performed with the crude extract of *M. wesenbergii* at four sublethal concentrations of supernatant (equal to 1, 10, 40, and 120 mg dw/l) and a control. Sub-chronic tests were done by using 50 ml beaker cups with 20 ml of ISO medium or exposure solutions. Neonates of *D. magna* less than 24 h in age were used. Each treatment contained 15 replicates (n=15). Test solutions were renewed every two days. A mixture of *Scenedesmus* sp. and *Chlorella* (approximately $1x10^6$ cells/ml) was provided as food for *Daphnia* in a two-day period. The mortality, maturation and production of live offspring were observed. The parent daphnid was checked daily for numbers of neonates per clutch. Reproduction was calculated by using the average of the number of neonate per female. The sub-chronic test was examined for 15 days. One-way ANOVA and Kruskal-Wallis test (Sigma Plot, version 12) was applied for calculations of the significant difference of the maturation and reproduction of *D. magna* between control and treatments.

Results and discussion

Isolation and morphological characteristics

Microscopic observation of the cyanobacterial bloom samples revealed the dominance of *Microcystis* spp. (mainly *M. aeruginosa*, *M. wesenbergii*, and *M. botrys*) and the less frequent occurrence of other genera (*Dolichospermum*, *Arthrospira*, *Planktothrix*, *Pseudanabaena*, and *Cylindrospermopsis*). Results of the present study are in accordance with previous observations that *Microcystis* was dominant group and the most common bloom-forming species in Vietnamese waters [7, 13, 15].

From bloom samples, five strains of *M. wesenbergii* were isolated and cultured in Z8 medium. Morphology examination from both field and isolated samples indicated that *M. wesenbergii* species forms elongate, often lobate, and sometimes spherical colonies that are commonly composed of sub-colonies with a distinct refractive mucilage edge. In nature, a sub-colony of this species is 15-100 µm in diameter and contains from a few (2-3) to many (>150) cells, depending on the age of the colony. Cells are more or less evenly spread throughout the colony, are 5.5-8.5 µm in diameter, and have many spherical aerotopes. Cells are slightly dark under a high magnification microscope. Colonies of this species forms an agar-like substrate that is soft and often breaks up in culture (Fig. 2).

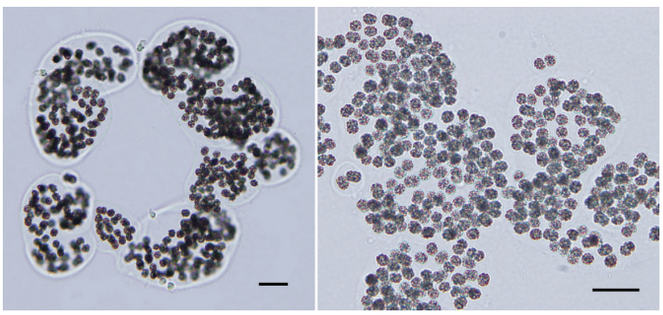

Fig. 2. Morphology of *M. wesenbergii* (scale bar: 20 µm).

M. wesenbergii is a common species of phytoplankton and sometimes forms surface blooms in many lakes and rivers worldwide. In Vietnam, the water bloom of *M. wesenbergii* has been reported from the Dau Tieng and Tri An reservoirs [7, 13], Hoan Kiem, and Nui Coc lake [15].

Measurement microcystins concentration from cultures

Results of HPLC analysis indicated that the water bloom samples contained two variants of MCs including (MC-RR and MC-LR) with the highest concentration ranged from 778.2±12.6 µg/g dw (Fig. 3B and Table 1). But none of the isolated strains of *M. wesenbergii* produced microcystins (Fig. 3A). Three variants of MC, including MC-RR, MC-LR, and MC-RR from water blooms and isolated *Microcystis* species with the maximum concentration of 2130 µg/g dw have been reported from the Dau Tieng reservoir. Many strains of *M. aeruginosa* isolated from the Dau Tieng reservoir were reported to produce MC [13] but none of the strains of *M. wesenbergii* were MC-producing. It is possible that *M. aeruginosa* was the main toxin producer in the Dau Tieng reservoir. From the Tri An reservoir, Dao, et al. (2010) [7] reported four variants of MC, including MC-LR, MC-RR, MC-LA, MC-LY, and one unknown variant in the scum samples but none were found in the cultures. This may be a small number of strains of *Microcystis* were included in the examination. In this study several MCs variants were detected from the water bloom which indicated that the cyanobacterial community from the Tri An reservoir contained MC-producing and non-MC-producing cyanobacteria. Probably, the *M. wesenbergii* species is a non-toxic species. Further study is needed to determine the MC producers from the Tri An reservoir.

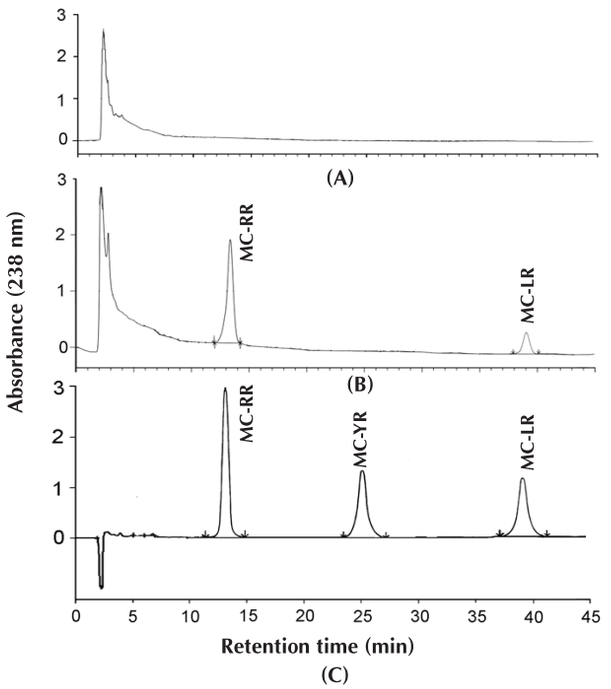

Fig. 3. HPLC-chromatograms of (A) *M. wesenbergii*, (B) water bloom samples, and (C) microcystin standards.

Acute bioassays with D. magna

During the acute test, the survival of *D. magna* in the control was higher than 90%, and the highest concentration of crude extract (1.5 g/l) caused 100% mortality of *Daphnia* daphnids after 48 h. Therefore, the test met the requirement of the OECD (2004) [14] guideline for the acute test. The calculated 48 h EC_{50} for the crude extracts of *M. wesenbergii* and water bloom samples are shown in Table 1. Although MCs were not detected in crude extracts of *M. wesenbergii*, all samples caused acute toxicity on *D. magna*. The EC_{50} values of crude extracts of *M. wesenbergii* on *D. magna* after 48 h ranged from 307.2-491.5 mg dw/l (Table 1). The water bloom samples containing high concentrations of MCs also caused the highest toxicities to cladocerans. The calculated 48 h EC_{50} value is 279.4 mg dw/l at 95% confidence interval (Table 1).

Table 1. List of samples used for acute test with microcystin concentration and 48 h EC_{50} values.

Strain name	Samples name	MC (µg/g dw)	48 h EC_{50} (mg dw biomass/l)
MW1	*M. wesenbergii*	ND	491.5
MW2		ND	307.2
MW3		ND	386.3
MW4		ND	383.1
MW5		ND	311.6
BL-TA	Water bloom samples	778.2±12.6	279.4

ND: no detectable microcystins.

Previous studies [16-18] have demonstrated various toxic effects on feeding behaviour and reproduction of daphnids after exposure to cyanobacterial cells or their purified toxins. However, the toxicity of the complex extract from non-MC-producing cyanobacteria is not examine in the same extent. Herrera, et al. (2014) [19] reported that the EC_{50} values 48 h of a cyanobacteria bloom contained MC-LR (538 µg/g dw) collected from a reservoir in Colombia on *Daphnia* sp. were from 175-336 mg dw/l. The results of this study indicated that the toxic effects of non-MC-producing *M. wesenbergii* are somewhat lower than the water blooms samples. Probably, these water blooms samples contained other toxic compounds that contribute toxic effects other than MCs. The present results confirmed the toxic effect of non-MC-producing strains of *M. wesenbergii* on *D. magna*. In a recent study, Pawlik-Skowrońska, et al. (2019) [20] compared the toxic effects of purified MC and the extracts from *Microcystis*, *Planktothrix* and *Dolichospermum* on *Daphnia pulex*, and found that the toxicity of the crude extracts to *D. pulex* was higher than that from pure cyanotoxins. Authors reported that other toxic compounds present in the cyanobacterial extracts such as non-ribosomal oligopeptides and LPS may contribute to the toxic effects on cladocerans. The findings of this research are consistent with previous studies that natural extract from cyanobacteria contains various toxic compounds that may even be more toxic than cyanotoxins [4, 5, 9]. Further study is needed to understand the toxic effects of these compounds in cyanobacteria from the Tri An reservoir.

Sub-chronic toxicity and reproduction bioassay

Sub-chronic toxic effects of crude extracts of *M. wesenbergii* (strain MW2) on *D. magna* over a period of 15 days revealed that the crude extracts of non-MC-producing *M. wesenbergii* had dose-dependent toxic effects on the survival of *D. magna* (Fig. 4).

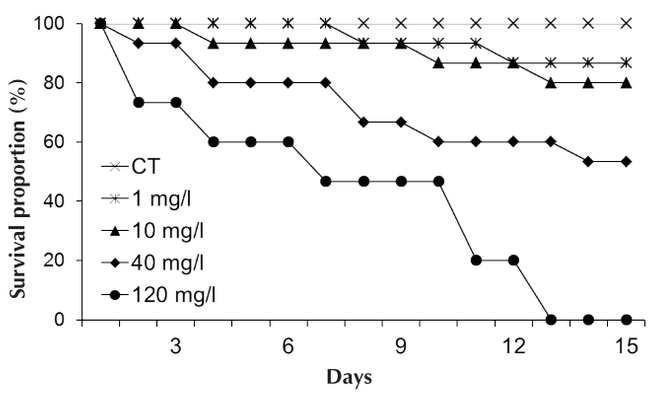

Fig. 4. Effects of crude extracts of *M. wesenbergii* on survival of *D. magna*.

No deaths of daphnids was recorded in the control treatment. But a mortality rate of 13% of the exposed daphnids was recorded in the treatment with 1 mg/l. The survival decreased to 80% in the 10 mg/l treatment by the end of the experiment. Only about 50% of daphnids survived in the 40 mg/l treatment. At the highest crude extract treatment (120 mg/l), mortality occurred quickly starting from day 2 and all the daphnids died after 13 days of exposure (Fig. 4).

Results of the maturation age and average number of offspring per female of *D. magna* exposed to different concentration of crude extracts of *M. wesenbergii* are shown in the results indicate that crude extracts of non-MC-producing *M. wesenbergii* at a concentration of 10 mg/l or higher inhibited the maturation and reproduction of parent daphnids. In the control and 1 mg/l treatments, there was no significant difference of maturation age between the two groups, where the maturation age of the daphnid was 5.4±0.3 days and 5.2±0.5 days, respectively. But the maturation ages of the exposures with 10 mg/l, 40 mg/l and 120 mg/l are significantly longer than the CT (Fig. 5A).

wesenbergii significantly delayed maturity age and caused a decline in the number of offspring of the parent daphnids. Smutná, et al. (2014) [4] exposed *D. magna* to both MC-containing and non-MC-containing cyanobacterial water bloom samples in a series of acute (48 h) and chronic (21 day) toxicity experiments. Results showed that high acute toxicity was observed for 6 of the 8 crude biomass samples. The chronic exposure assays indicated the complex biomass, the crude aqueous extract, and the microcystin-free extract all elicited similar and significant lethal effects on *D. magna*. The authors confirmed that cyanobacterial water blooms are highly toxic to zooplankton (both acutely and chronically) at environmentally relevant concentrations. Dao, et al. (2010) [7] reported malformation of neonates and cessation of the eggs/embryos of *D. magna* caused by cyanobacterial toxins from crude extract. In addition, the production of nonviable eggs and reduced fertility in *D. magna* were observed after exposure to toxic cyanobacteria [21]. The present study supports the previous findings that both toxic and non-toxic cyanobacteria exert significantly toxic effects on cladocerans.

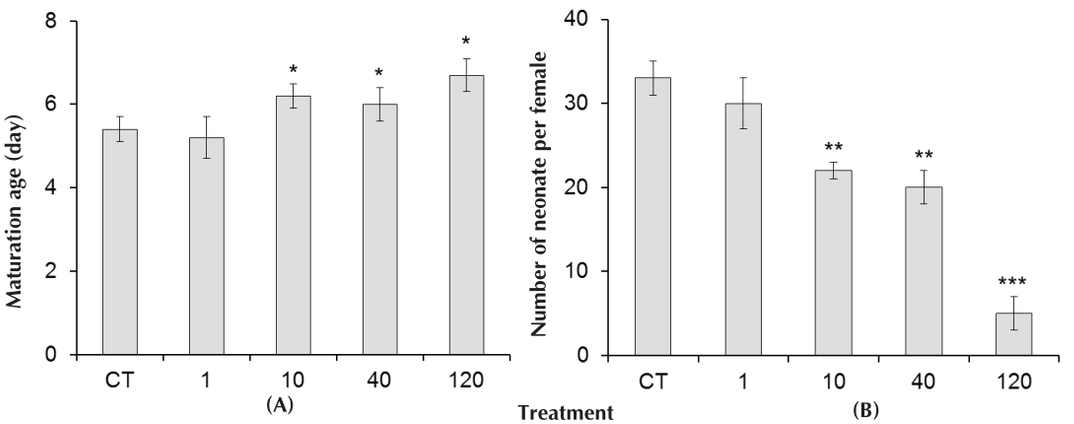

Fig. 5. Maturation age (A) and number of offspring per female (B) of *D. magna* exposed to different concentration of crude extracts of *M. wesenbergii*. Asterisks indicate significant difference between control (CT) and exposures.
*: p<0.05; **: p<0.01; ***: p<0.001.

During 15 days of the experiment, one parent *D. magna* in the CT treatment produced about 33±2 offspring, which was not significantly different than the 1 mg/l treatment. However, the treatment with 10, 40, and 120 mg/l resulted in significant decreases of the number of offspring per female (Fig. 5B). The reproduction results indicated that there is a concentration-response pattern in the parent daphnids exposed to crude extracts of non-MC-producing *M. wesenbergii.* Previous studies have confirmed the adverse effects of toxic cyanobacteria on *D. magna*. The toxicity includes inhibition of filtration rate, decrease in swimming movements, and fecundity or reduction population growth rate [7-9]. However, little is known about the chronic effects of non-MC-producing on cladocerans. The findings of this study revealed that crude extracts of non-MC-producing *M.*

Conclusions

This study demonstrated that the bloom samples from the Tri An reservoir contained MCs, but no MC variant was detected from the cultures of five isolated strains of *M. wesenbergii*. The crude extracts from non-MC-producing *M. wesenbergii* isolated from the Tri An reservoir had significant acute and chronic toxic effects on *D. magna*. The present findings indicate that metabolites other than MC are likely to be responsible for the observed toxic effects, and that toxins produced from cyanobacteria may play only a minor role in the overall ecotoxicity of cyanobacterial blooms. MC producers and the toxicity mechanism of these unknown metabolites remain to be explored and need further investigation.

ACKNOWLEDGEMENTS

This research was founded by Vietnam National Foundation for Science and Technology Development (NAFOSTED) under grant number 106.04-2018.314.

The author declares that there are no conflicts of interest regarding the publication of this article.

REFERENCES

[1] T.L. Pham, M. Utsumi (2018), "An overview of the accumulation of microcystins in aquatic ecosystems", *J. of Environ. Manage.*, **213**, pp.520-529.

[2] E. Dittmann, et al. (2015), "Natural product biosynthetic diversity and comparative genomics of the cyanobacteria", *Trends Microbiol.*, **23(10)**, pp.642-652.

[3] S. Le Manach, et al. (2018), "Physiological effects caused by microcystin-producing and non-microcystin producing *M. aeruginosa* on medaka fish: a proteomic and metabolomic study on liver", *Environ. Pollut*., **234**, pp.523-537.

[4] M. Smutná, et al. (2014), "Acute, chronic and reproductive toxicity of complex cyanobacterial blooms in *D. magna* and the role of microcystins", *Toxicon*, **79**, pp.11-18.

[5] B. Burýšková, et al. (2006), "Toxicity of complex cyanobacterial samples and their fractions in *Xenopus laevis* embryos and the role of microcystins", *Aquat. Toxicol.*, **80(4)**, pp.346-354.

[6] T.L. Pham, et al. (2016), "Microcystin accumulation and biochemical responses in the edible clam *Corbicula leana* P. exposed to cyanobacterial crude extract", *J. Environ. Sci*., **44**, pp.120-130.

[7] T.S. Dao, L.C. Do-Hong, C. Wiegand (2010), "Chronic effects of cyanobacterial toxins on *D. magna* and their offspring", *Toxicon*, **55(7)**, pp.1244-1254.

[8] A.S. Ferrão-Filho, et al. (2009), "Biomonitoring of cyanotoxins in two tropical reservoirs by cladoceran toxicity bioassays", *Ecotoxicol. Environ. Saf*., **72(2)**, pp.479-489.

[9] N.A. Herrera, L.F. Echeverri, A.S. Ferrão-Filho (2015), "Effects of phytoplankton extracts containing the toxin microcystin-LR on the survival and reproduction of cladocerans", *Toxicon*, **95**, pp.38-45.

[10] T.S. Dao, R. Ortiz-Rodríguez, L.C. Do-Hong, C. Wiegand (2013), "Non-microcystin and non-cylindrospermopsin producing cyanobacteria affect the biochemical responses and behavior of *D. magna*", *Int. Rev. Hydrobiol*., **98(5)**, pp.235-244.

[11] J. Komárek, K. Anagnostidis (2005), "Cyanoprokaryota 1. Teil: Oscillatoriales", *Phycologia*, **38(6)**, p.544.

[12] C. Pietsch, et al. (2001), "The effects of a cyanobacterial crude extract on different aquatic organisms: evidence for cyanobacterial toxin modulating factors", *Environ. Toxicol*., **16(6)**, pp.535-542.

[13] T.L. Pham, T.S. Dao, K. Shimizu, D.H. Lan-Chi, M. Utsumi (2015), "Isolation and characterization of microcystin-producing cyanobacteria from Dau Tieng reservoir, Vietnam", *Nova Hedwigia*, **101(1-2)**, pp.3-20.

[14] OECD (2004), *Daphnia sp. Acute Immobilization Test, OECD Guideline for Testing of Chemicals No.202*.

[15] T. Duong, et al. (2014), "The occurrence of cyanobacteria and microcystins in the Hoan Kiem lake and the Nui Coc reservoir (North Vietnam)", *Environ. Earth Sci.*, **71(5)**, pp.2419-2427.

[16] A. Ghadouani, et al. (2004), "Effects of *M. aeruginosa* and purified microcystin-LR on the feeding behavior of *D. pulicaria*", *Limnol. Oceanogr*., **49(3)**, pp.666-679.

[17] W. Chen, L. Song, D. Ou, N. Gan (2005), "Chronic toxicity and responses of several important enzymes in *D. magna* on exposure to sublethal microcystin-LR", *Environ. Toxicol.*, **20(3)**, pp.323-330.

[18] R. Ortiz-Rodríguez, C. Wiegand (2010), "Age related acute effects of microcystin-LR on *D. magna* biotransformation and oxidative stress", *Toxicon*, **56(8)**, pp.1342-1349.

[19] N. Herrera, et al. (2014), "Effects of a cyanobacterial bloom sample containing microcystin-LR on the ecophysiology of *D. similis*", *Toxicol. Rep.*, **1**, pp.909-914.

[20] B. Pawlik-Skowrońska, M. Toporowska, H. Mazur-Marzec (2019), "Effects of secondary metabolites produced by different cyanobacterial populations on the freshwater zooplankters *Brachionus calyciflorus* and *Daphnia pulex*", *Environ. Sci. Pollut. Res.*, **26(12)**, pp.11793-11804.

[21] S. Gustafsson, K. Rengefors, L.A. Hansson (2005), "Increased consumer fitness following transfer of toxin tolerance to offspring via maternal effects", *Ecology*, **86(10)**, pp.2561-2567.

Doi: 10.31276/VJSTE.61(4).76-81

Exploiting WebGis technology to build an environmental database to support the environmental management of Ho Chi Minh city

Phu Cuong Tran*, Thi Van Tran

University of Technology, Vietnam National University, Ho Chi Minh city

Received 29 July 2019; accepted 22 November 2019

Abstract:

Recently, climate change and its effects have been significantly influenced by human life. Human activities, mostly from urbanization, are the main contributors to the pollution of soil, water, and air, which has been proven by several observations and studies. However, it is necessary to raise awareness, by including support from society as a whole, in order to maximize the efficiency of environmental campaigns. In this work, the geodatabase model of geographic information system (GIS) combined with the WebGIS system based on ArcGIS server technology was employed to build environmental database for Ho Chi Minh city, which will be used by the HCM-SSED system (Ho Chi Minh city - system for sharing environmental database). This system supports the environmental administration with the management, updating, and sharing of environmental databases, as well as providing environmental information to the community quickly and efficiently.

Keywords: **environment database, GIS, sharing environmental databases, WebGIS.**

Classification number: **5.1**

Introduction

It is obvious that pollution is a controversial issue that has attracted tremendous interest of many countries and communities around the world. Pollution and climate change negatively affect our ecosystem and living conditions, through the air we breathe, the water we drink, and the soil we cultivate our crops to eat.

With its intuitive capabilities and object positioning characteristics, GIS is one of the best tools in terms of environment management. GIS can pinpoint the location of emission sources and project its spreading potential. Many developed countries around the world have applied GIS to effectively manage their environment. The main advantage of GIS is that users can search and extract information from the database quickly and easily, so that management can make practical and accurate decisions. In addition, we live in the era of technology and sharing information using the sharing function of this tool will greatly support management's efforts to catch up with this new trend. Therefore, the combination of the internet and GIS system will bring great efficiency to the management and distribution of environmental data to citizens.

Ho Chi Minh city is the largest city in Vietnam in terms of population size, economic development, level of urbanization, and is an important cultural and educational hub of the country. Together with its great socio-economic achievements, Ho Chi Minh city is also facing certain challenges in urban management. For example, a dramatic increase in urban population, lack of infrastructure, proper planning, and management systems. As the living conditions increase gradually, people are more considerate of their quality of life and the effects of pollution on their soil, water, and air. However, the current system cannot offer an efficient method to provide accurate information

*Corresponding author: Email: 1670387@hcmut.edu.vn

to the community, and this has led to little improvement of the people's awareness to support local administrators with solving environment issues. In order to build green and smart cities as the provisioned by the government, Ho Chi Minh city has a short period of time to employ an innovative solution to manage and educate its citizens by providing suitable information.

Based on those necessities, this paper presents the construction of the HCM-SSED system based on a WebGIS environmental database in order to support the city with their efforts to update, manage, and share environmental data and information to the community quickly and effectively.

Database and system structure

Building database

Data collection: data is provided by the Ho Chi Minh city Department of Natural Resources and Environment and is divided into two groups as follows:

- The administrative data of Ho Chi Minh city, such as maps of the land use status in 2005 in scales of 1/500 and 1/1000 in .dgn format, the terrain background in scales of 1/2000 and 1/5000, also in .dgn format, basic geographical information of the 24 districts at district level and 322 areas at ward/commune level in .mdb (geodatabase) format, a cadastral map with land boundaries and addresses in 2005 in scales of 1/500 and 1/1000 in .mdb format (geodatabase), and a topographical map in scales of 1/2000 and 1/5000 in .mdb format [1].

- Thermatic data on the water and air environment extracted from the data synthesis process of the Centre for Resources and Environment Monitoring. Then spatial and attribute data are merged and stored in the same database to allow for fast and accurate updates, searches, statistics, and data extraction tasks.

Standardized data: the surveyed and collected map data sources include many different formats such as data from paper maps and digital data (MicroStation, MapInfo, and AutoCAD). Then, each type of data is converted and edited accordingly. For the data extracted from paper maps, it is scanned and digitized into AutoCAD format, the coordinates are adjusted and checked for geometric errors. Similarly, for digital data, its coordinates will be adjusted and checked for geometric errors, and then updated with attribute information. All these steps are completed through the use of ArcGIS, which also was used to build standardized background data layers and thematic data according to the Geodatabase model.

Geodatabase is a spatial data model provided by the company Esri that is used for storing, accessing, and processing GIS data, and it is controlled by database management systems such as SQL servers. Geodatabase is an ideal storage model for geographic features due to its outstanding data structure that allows extensive data to be saved in the form of a data table. There are two geodatabase models: geodatabase one user (personal geodatabase) and geodatabase multiple users (enterprise geodatabase). It stores the structure and collection of objects, attributes, relationships between attributes, and relationships between objects in the form of specific spatial and attribute data. The geodatabase model has the nature of an object-oriented data model. This model and data structure provide high data integrity and efficiency [2].

Building the database: the process of building a database for HCM-SSED is shown in Fig. 1. After data collection, based on the objectives of the research, a review of the current status of data is conducted and the role of the data for a particular topic is analysed, thereby establishing a criteria framework for each data. Then, the data is standardized for the processes of converting and linking spatial and attribute data. Finally, the object-oriented database is designed with 3 levels (concepts, logic, and physics) to construct the data structure, define topology, declare the coordinate system, define relationships, and apply data rules to the geodatabase.

- Conceptual database design: the properties of objects and the relationships between them are identified and defined based on the professional procedures for the management and distribution of the environmental database given by the Centre for Environmental and Resources Monitoring, thereby building a conceptual model using the entity link model.

- Logical database design: the primary key, foreign key of each object, and domain for the attributes are identified. In the logical model, the data is specified in the form of tables, frames, and steps on the WebGIS system. From there, a logical model is built through the use of relational data models.

- Design of physical database: the description of a physical model is directly related to the selection of technical solutions and compatibility with software such as storage structure, technical facilities to ensure the operation of the system through a defined geometry, properties for each data, and the defined relationship between data layers corresponding to geodatabase components.

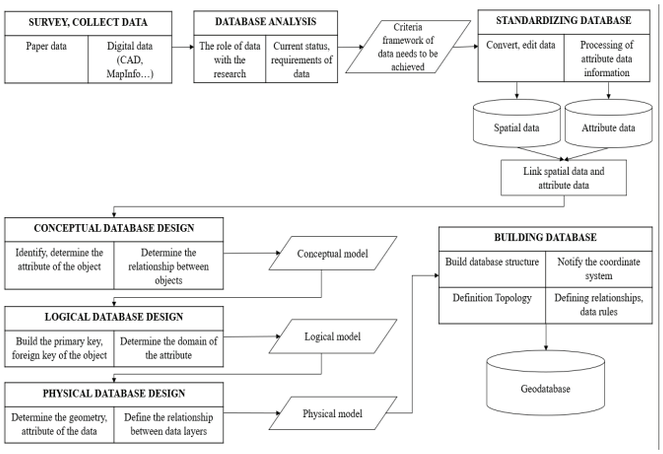

Fig. 1. Procedure of building HCM-SSED's database.

System structure

HCM-SSED (Fig. 2) is built through the combination of ArcGIS server technology and SQL server database management system [3] and is designed to store spatial objects along with attribute information of object layers and associated data sources monitored by time. Spatial and non-spatial data are stored and managed uniformly in the same database so users can update, search, count, and extract data in a convenient and easy way. Environmental databases are designed to serve multiple users and allows multiple user access at the same time.

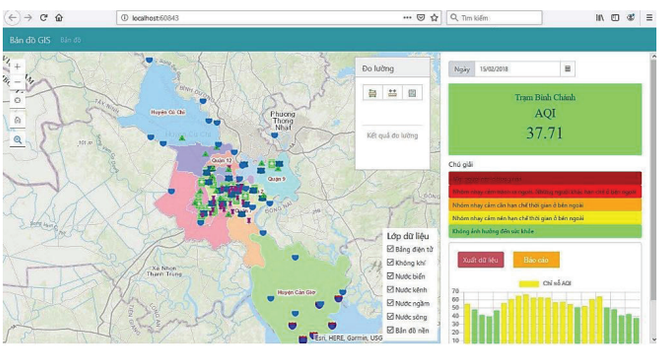

Fig. 2. Interface of HCM-SSED system.

The overall structure of the HCM-SSED system (Fig. 3) is based on three main layers including the web layer, application layer, and database layer. System users will communicate via the web interface to send their desired requests to the server via the Internet. After receiving the request from the user, the server will access the database to retrieve the desired data and then return it to the user [4]. Geographic data includes both spatial and non-spatial data and managed by SQL. The spatial database is used to manage and retrieve spatial data that is placed on the data server. Based on data management components, server applications and server models calculate spatial information through specific functions. The information processing procedure used to extract the maps is based on the IIS platform, ArcGIS service, and ArcGIS server. Meanwhile, the procedure used to access the attribute information on the web is coded in .NET language [5].

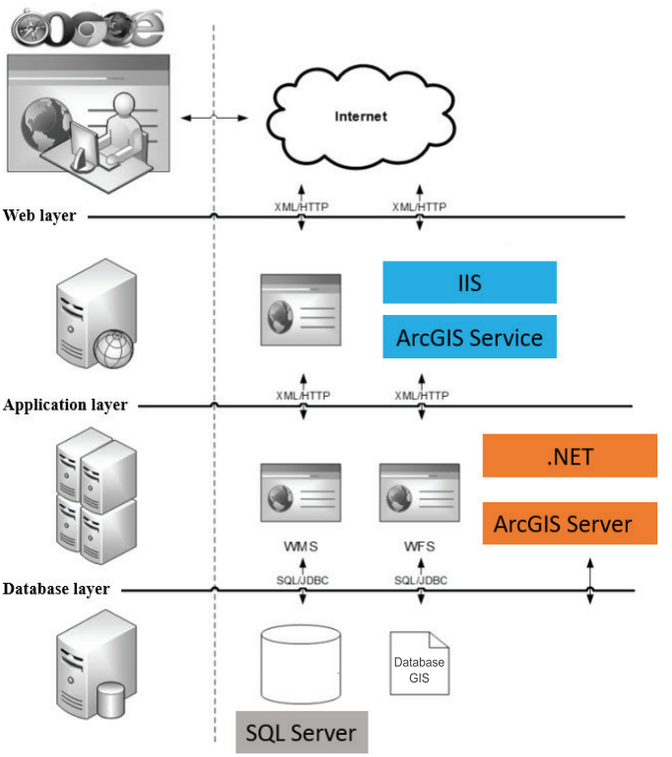

Fig. 3. Overall structure of HCM-SSED.

System operation

Functions of HCM-SSED

HCM-SSED is constructed as an information system for air and water environmental monitoring and uses ArcGIS Server technology with the following information groups (Fig. 4):

- Air: this group contains information related to air monitoring stations such as their name, station code, coordinates, address, and detailed monitoring indicators such as SO_2, CO, NO_2, O_3, TSP, PM_{10}, $PM_{2.5}$, and Pb.

- River water: this group contains information related to river water monitoring stations such as name, station code, coordinates, address, and detailed monitoring indicators such as BOD_5, COD, DO, Coliform, turbidity, salinity, E. coli, NH_4, temperature, PO_4, TSS, Cd, Cu, Fe, Mn, Pb, and Cr^{6+}.

- Canal water: this group contains information related to river water monitoring stations such as name, station code, coordinates, address, and detailed monitoring indicators such as BOD_5, COD, DO, Coliform, turbidity, salinity, E. coli, NH_4, temperature, PO_4, TSS, Cd, Cu, Fe, Mn, Pb, and Cr^{6+}.

- Groundwater: this group contains information related to groundwater monitoring stations such as name, station code, coordinates, address, and detailed monitoring indicators such as As, Cd, CN, Coliform, Cr^{6+}, Cu, hardness, E. coli, Fe, Mn, NO_3, NH_4, Pb, pH, SO_4, TDS, Zn in the Pleistocene, the upper Pliocene, and the lower Pliocene layers.

- Seawater: this group contains information related to sea monitoring stations such as name, station code, coordinates, address, and detailed monitoring indicators such as As, Cd, Coliform, Cu, Hg, NH_4, Pb, pH, oil in seawater, and bottom mud.

- Electronic board: this group contains the information related to the electronic board placed on main routes in Ho Chi Minh city such as name, table code, coordinates, address, and information about environmental quality from the air and water monitoring stations near the monitoring areas.

- Information: this group gathers data and information on monitoring indicators from air and water monitoring stations as a basis for calculation of the AQI (air quality index) and WQI (water quality index) environmental quality indicators.

- Model: includes two models for calculating the AQI and WQI.

- Report: this group will gather information about AQI and WQI calculation results by station and time. All the statistical data shown in charts and reports will be given in the report format of the Centre for Monitoring Environmental and Resources.

- Permission: this group will gather functions for HCM-SSED such as configuration of user permissions according to specific permission lists.

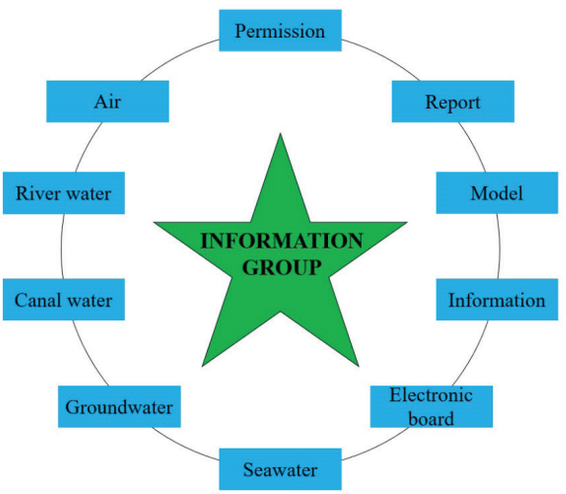

Fig. 4. Information grouping in HCM-SSED.

Based on the information groups, the organizational model of HCM-SSED is systematically designed with main functions such as the introduction of the HCM-SSED homepage interface, user permission interface, WQI and AQI calculation models, monitoring stations information, monitoring indicators index, reports, and maps. The main contents of the functions are shown in Fig. 5.

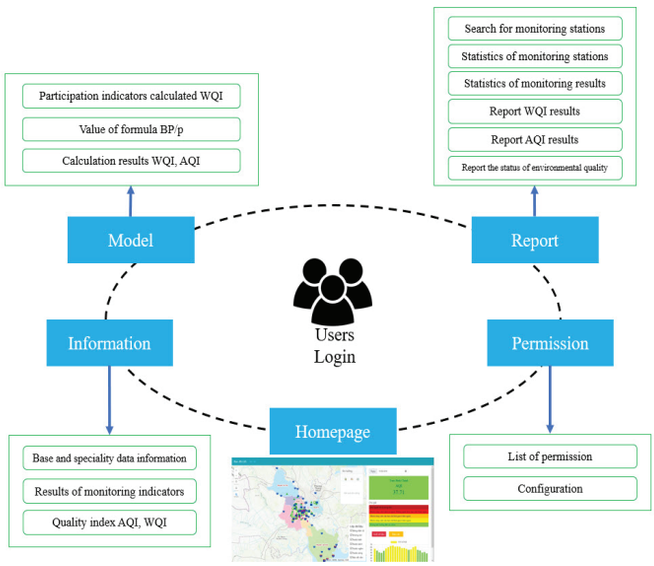

Fig. 5. Functions in HCM-SSED.

The information function includes the display of thematic maps and base maps (Fig. 6), zoom in/out functionality, map movement, and an on/off toggle for the display of data layers. In addition, users can view the results of monitoring indicators, such as the water and air quality indexes of each monitoring station.

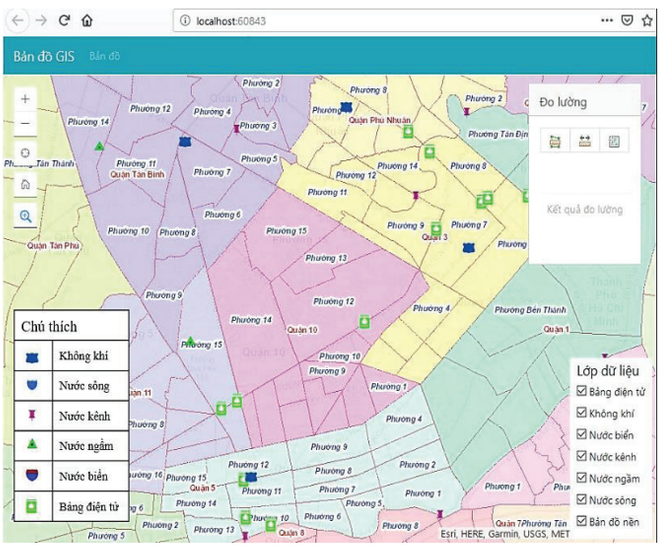

Fig. 6. Interface of the map display function.

The report function includes information searching (Fig. 7) where the HCM-SSED system allows its users to find the location of monitoring stations by administrative boundaries to assist with the handling of information and decision making.

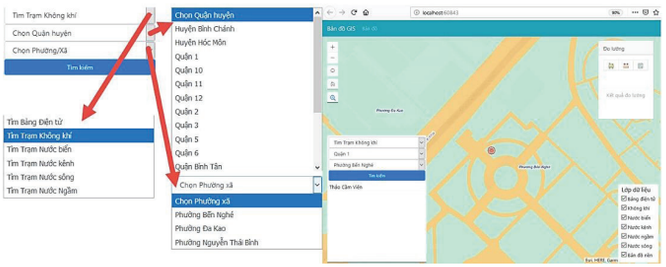

Fig. 7. Interface of information searching function.

The reporting function demonstrates the role of database sharing (Fig. 8), where environmental information via reporting and statistical functions allow users to monitor environmental quality with the AQI and WQI by time, and also view statistical criteria and interactive maps, which can generate analytical and evaluation information. Users can download data and view environmental reports using data export and reports (Fig. 9). In parallel with the display of monitoring station data, data transmission and linkage to the digital board are also implemented to support database sharing within the community.

Fig. 8. Interface of report and statistical functions in the sharing environment database.

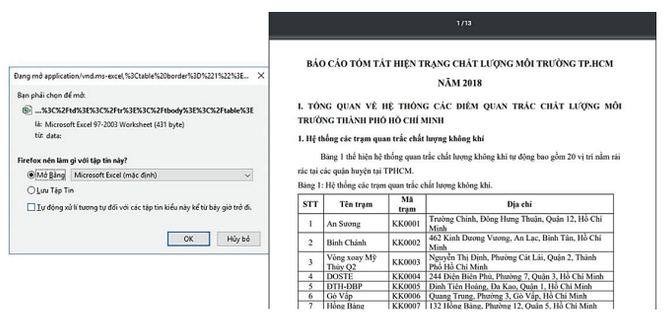

Fig. 9. Results of the data export and report functions.

Mechanism to allow permission and share databases

HCM-SSED is designed for many different users. Each user has a particular level of permissions set by the system administrator, such that each user may have different permissions to different functions (Fig. 10).

Fig. 10. Interface of permission setting function.

The system is divided into 2 types of users, management and normal. Details of the contents that these types of users can access are demonstrated in Table 1.

Table 1. Functional requirements of HCM-SSED by user type.

Function	Users	
	Management	***Common user***
Map interaction	Change map scale (zoom in, zoom out) Set map scale Move the map View full map Measure distance View object information	Change map scale (zoom in, zoom out) Set map scale Move the map View full map Measure distance View object information
Map display	Background map layers: ESRI maps, roads, parcel land, river, boundary administration by district or ward/commune Thematic map layers: air, river water, canal water, sea water, and groundwater monitoring data Turn on/off the data layer	Background map layers: ESRI maps, roads, parcel land, river, boundary administration by district or ward/commune Thematic map layers: air, river water, canal water, sea water, and groundwater monitoring data Turn on/off the data layer
Information access	Access to base data: roads, river, parcel land, according to boundary administration (district, ward/commune) Access thematic data: monitoring data of air, river water, canal water, sea water, groundwater according to boundary administration, by time Export data with Excel filetype by time	Access to speciality data: monitoring data about air, river water, canal water, sea water, groundwater according to boundary administration, by time Export data with Excel filetype by time
Statistic, report	Perform environmental statistics and reports for professional work in the department	Perform a simple environmental statistics and reports
User management	Search, view, edit, delete, create new account	

Conclusions

It is indisputable that environmental pollution is a problem that requires a sophisticated solution and an improved management system to evaluate and perform quick action under certain circumstances. Therefore, a WebGIS system with its many advantages plays a critical role to provide a solution for the local government to share and communicate environmental information to the community via HCM-SSED. The study has surveyed, collected, analysed, and built an environmental database specializing in the air and water monitoring of Ho Chi Minh City with 5 main data layers including air, river water, canal water, groundwater, and seawater monitoring stations. Building the GIS database as a centralized database also helps users to access and update data synchronously. If all departments and units at the Centre for Environmental and Resources Monitoring can update the data using a single database, the issues of fragmented, asynchronous data would be avoided. In addition, HCM-SSED is built with a user-friendly interface and functions that are very simple and easy to use. Building the system on in Web environment with a centralized database will also make the distribution and management of environmental data much simpler to control and upgrade. Furthermore, the web environment has the benefits of fast and convenient data extraction and distribution, which is beneficial to all citizens in the community.

The authors declare that there is no conflict of interest regarding the publication of this article.

REFERENCES

[1] https://hcmgis.vn/wpcontent/uploads/2018/01/VUC2012_HCMC_GISCenter_HienTrangUngDungGISTaiTpHCM.pdf>.

[2] http://www.landviser.net/content/building-geodatabase-arcmap-10-desktop>.

[3] ESRI (2004), "Introduces ArcGIS server, broadens capabilities for ArcIMS and ArcSDE: ArcGIS 9 expands serverside GIS capabilities", viewed 11 July 2019, from:<https://www.esri.com/news/arcnews/spring04articles/arc9-special/arcgis9-expands.html>.

[4] A. Markos (2014), "The role of (Web GIS) the development of tourism - in the case of Bahir Dar town and its surroundings, Amhara region, Ethiopia", *Radix International Journal of Research in Social Science*, **3(11)**, pp.15-20.

[5] B. Agrios (2009), *Getting Started with ArcGIS Server*, 2009 ESRI Education user conference.

Doi: 10.31276/VJSTE.61(4).82-87

Chronic effects of lead and arsenic on life history traits of *Daphnia magna*

Le-Thu Quach[1], Thi-My-Chi Vo[2], Van-Tai Nguyen[2], Thanh-Son Dao[2*]

[1]Ho Chi Minh city University of Food Industry

[2]University of Technology, Vietnam National University, Ho Chi Minh city

Received 22 August 2019; accepted 12 November 2019

Abstract:

Anthropogenic activities such as industrial production, mining, agriculture and transportation are among the main causes for the increase of trace metal concentrations in the environment, especially in water bodies. In this study, we evaluated the chronic impacts of lead (Pb) and arsenic (As) on *Daphnia magna*, a crucial organism to aquatic ecosystems, at several concentrations (0, 5, 25, 50, 150 and 250 µgl^{-1} of Pb and 0, 5, 25, 50 µgl^{-1} of As) for 21 days. The organism's life history traits, including survivorship, maturation, and reproduction, were recorded daily. In addition, the survival rate of the offspring exposed to 50 µgl^{-1} Pb was also recorded when the animals were raised in (i) a Pb-containing medium and Pb-free medium for 8 days. The results showed that As, at all the test concentrations, did not only negatively affect the survival and cause a delay the maturation, but also reduced the reproductive performance of the animal, especially at the highest concentration. Compared to the control, the survivorship and reproduction of the *D. magna* exposed to Pb at the highest concentrations (150 and 250 µgl^{-1}) declined dramatically, and it took a longer time to reach maturity. On the other hand, almost all of the recorded life history traits of the organisms exposed to 5, 25 and 50 µgl^{-1} of Pb were relatively similar to those from the control. However, Pb at the concentration of 50 µgl^{-1} had detrimental effect on survival of *Daphnia*'s F1 generation after the 8-day experiment. An abnormality of the metal-exposed *D. magna* was also observed. An impairment of the daphnids was observed upon exposures to As and Pb at concentrations within the Vietnam guideline values for surface water safety. Hence, further investigations are suggested to adjust the guidelines related to As and Pd for the protection on environmental quality and ecological health.

Keywords: **chronic effects, *Daphnia magna*, guideline, life history traits, trace metals.**

Classification number: **5.1**

Introduction

Over the past decades, trace metals have been one of the most serious chemical contaminants causing environmental pollution and potential toxicity to human health and organisms [1, 2]. Some trace metals (e.g. Cu, Cr, Mg, Mn, Zn, Ni, Fe and Co with the concentration less than 10 µgl^{-1}) are essential elements for the physiological and biochemical functions of organisms [3], yet when exceeding a certain concentration, they could cause negative effects [4]. Besides, some other trace meals such as Pb, As, Cd, Hg are not only non-essential elements for biological functions of organisms, but also potent toxins to living things [5-7]. They can adversely affect cellular organelles and components, such as cell membranes, mitochondria, lysosomes, endoplasmic reticula, nuclei, some metabolic enzymes, detoxification processes, and damage repair mechanisms [8, 9], hence trace metals interfere with critical life processes of organism. Recently, there has been an abundance of evidence of aquatic pollution caused by trace metals worldwide [10-12]. In Vietnam, due to rapid economic development, the surface water quality is under constant threat of trace metal contamination, especially with Pb and As [13, 14]. Trace metals are naturally and commonly occurring elements in the Earth's crust, however in surface water, the main sources of trace metal, particularly As and Pb, are emission from anthropogenic activities e.g. metal plating, fishing operations, battery manufacturing, fertilizers and pesticides in agriculture, and smelting of ores [4, 15].

Both Pb and As are classified as top human carcinogens [5]. Additionally, Pb and As are non-essential elements for organisms and considered a major cause of aquatic environmental pollution due to the mechanism of chronic bioaccumulation and toxicity at low concentrations [16]. The presence of Pb in the environment was shown to cause behavioural abnormalities, hearing deficits, neuromuscular weakness, and shown to impair cognitive functions in human being as well as wildlife [17]. Regarding As,

*Corresponding author: Email: dao.son@hcmut.edu.vn

exposure to this chemical might affect several different organ systems including skin, respiratory, cardiovascular, immune, genitourinary, reproductive, gastrointestinal, and nervous system [18, 19].

Microcrustaceans (e.g. *D. magna*) play an important role in aquatic ecosystems as they are vital intermediate trophic level organisms responsible for the passage of matter and energy between primary producers and top predators [20]. Hence, in order to assess the ecological risk of Pb and As, a large number of studies have been completed on the chronic and semi-chronic effects of Pb and As on the life history traits of zooplankton. Many studies [21-24] indicated that there were various detrimental impacts on the health of test organisms when they were exposed to trace metals. In surface water, As and Pb could reach concentrations of 0.64 mgl^{-1} (see in the study of Frisbie, et al. (2002) [25]) and 6.3 mgl^{-1} (see in the study of Vuković, et al. (2011) [26]), respectively. For environmental and ecological safety in Vietnam, the As and Pb concentrations should not exceed 50 μgl^{-1} [27]. However, the question of whether there is any the impact of these trace metals on *D. magna* at low concentrations during a long-term exposure and across generations has not been addressed. Therefore, this study aims to evaluate the chronic effects of Pb and As at concentrations ranging from 5-250 μgl^{-1} on the life history traits and the next generation of *D. magna*.

Materials and methods

Materials

D. magna was obtained from MicroBio Test (Belgium) and has been cultured in a medium called ISO [28] for many generations under laboratory conditions (temperature of 25±1^{0}C and a photoperiod of 14 h light: 10 h dark at a light intensity of around 1000 Lux) [29]. Both the stock chemicals $Pb(NO_3)_2$ and $As(NO_3)_3$ at a concentration of 1000 mgl^{-1} were purchased from Merck (Germany) and stored at the temperature of -4^{0}C prior to the experiment.

Experimental set up

The chronic experiments were performed according to the guideline of APHA (2012), US. EPA (2002) and Dao, et al. (2017) [29-31] with minor adjustments. Briefly, prior to the experiment, 50 healthy female *Daphnia* were collected and incubated in the 1 l glass beaker containing 800 ml of ISO medium and fed with a mixture of green alga (*Chlorella* sp.) and YTC (yeast, cerrophyl and trout chow digestion). Afterwards, offspring less than 24 hours old were randomly selected for the chronic experiments.

In the first test, 2 neonates were incubated together in one 50 ml polypropylene cup containing 40 ml ISO medium and exposed to either Pb at a concentration of 5, 25, 50, 150, and 250 μgl^{-1} or As at a concentration of 5, 25, and 50 μgl^{-1}. Moreover, a control was prepared by culturing the offspring in the same way as mentioned above in a metal-free medium. There were 15 replicates (n=15) in each treatment and the test organisms were cultured under the conditions as mentioned above. The food (a mixture of *Chlorella* sp. and YTC) and medium were completely renewed three times per week. During the experimental period of 21 days, the life history traits of *D. magna*, such as survivorship, maturation, and reproductive performance, were monitored daily and carefully recorded.

The offspring of *D. magna* (<24 hours in age) in the control and 50 μgl^{-1} of Pb exposure were collected and used for the second test. Briefly, the offspring from the control were continued to culture in the control medium. Meanwhile, the neonates from 50 μgl^{-1} of Pb exposure were separated into 2 groups: i) those continuing to culture in the control medium and ii) those continuing to be exposed to 50 μgl^{-1} of Pb. In each treatment with the offspring, 30 offspring were used and incubated in 15 polypropylene cups (n=15), hence two offspring were placed in one cup. This experiment was run under the same laboratory conditions as mentioned above. The test terminated after 8 days of incubation and the survival of organisms was recorded.

Data analyses

Sigma Plot version 12.0 was used for the data processing. The Kruskal-Wallis test was applied for calculating the statistically significant difference of the maturation of *D. magna* between the control and trace metal exposures.

Results and discussion

Effects of Pb and As on the survivorship of D. Magna

As showed in Fig. 1, at the end of the experiment, all *D. magna* were still thriving in the control sample. Similarly, the survival rate of the organisms exposed to the lowest concentrations (5, 25 and 50 μgl^{-1}) of Pb was 100% during the 21 experimental days. However, after only 3 days of experiment, exposure to Pb at the concentrations of 150 and 250 μgl^{-1} caused a dramatic reduction of 20 and 77% of the total daphnids, respectively. By the end of the test, all *D. magna* exposed to the two highest concentrations of Pb had died (Fig. 1A). During the 8 first days, the survival of the organisms exposed to As at concentrations ranging from 5-50 μgl^{-1} remained steady at 100%, the same as those in the control sample, but this significantly decreased during the remainder of the As exposure. Finally, only 30, 63, and 17% of the total number of *D. magna* exposed to 5, 25, and 50 μg As l^{-1}, respectively, remained alive (Fig. 1B).

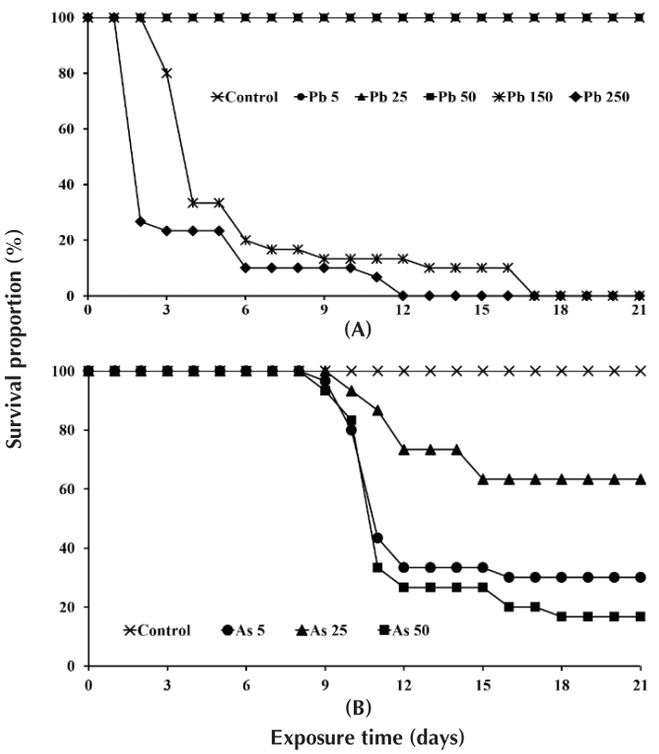

Fig. 1. Survivorship of *D. magna* from control and exposures during 3 experimental weeks (n=30 at the beginning). Samples denoted Pb 5, Pb 25, Pb 50, Pb 150, Pb 250 are animals exposed to 5, 25, 50, 150, 250 μgl^{-1} Pb, respectively, and As 5, As 25, As 50 denote animals exposed to 5, 25, 50 μgl^{-1} As, respectively.

Aquatic animals upon exposure to high metal concentrations would suffer from several impacts such as organ dysfunction, physiological imbalance, and enzyme inhibition/stimulation [32-35]. Pb is a neurotoxic chemical that can affect an organism's gills (respiratory system), cause renal dysfunction, enzymatic inhibition, and anemia [36, 37], resulting in increased energy cost for normal activity and maintenance of the animals. Besides, the metal may reduce food filtering, consequently lowering energy intake [38]. To summarize, in the presence of metals (e.g. Pb), *D. magna* would suffer an energy cost and consequently a decline in the survivorship. Additionally, our results were in line with the previous study of Regaldo, et al. (2013), although the survival of *D. magna* exposed to 30 μgl^{-1} Pb reached 100%, those exposed to this chemical at 90 and 270 μgl^{-1} declined to 10% after 15 days [21].

In the As exposure experiments, the animals exposed to As at a moderate concentration of 25 μgl^{-1} had a higher survival rate than those exposed to 5 μgl^{-1} and 50 μgl^{-1} concentrations. This phenomenon might be explained by hormesis, a term used to refer to a biphasic dose response characterized by a low-dose stimulation and a high-dose inhibition [39]. Further investigations on the physiological and biochemical responses of *D. magna* upon exposure to As are suggested to clarify this response.

Effects of Pb and As on the maturation of D. Magna

A metal may affect an organism in more than one way [40], hence, the time it takes for animals to reach maturity can be affected by exposure to Pb and As. In the control and Pb treatments (5-50 μgl^{-1}), the maturity age of *D. magna* was around 4 days. However, exposure to Pb at the two highest concentrations, 150 and 250 μgl^{-1} Pb, the maturation of *Daphnia* was prolonged to 12 and 8 days, respectively (Fig. 2A).

There was no statistically significant difference in the age to maturation between the control and those exposed to 25 μgl^{-1} As. The animals incubated in As at a concentration of 5 and 50 μgl^{-1} delayed their maturation compared to the control, and they did not mature until the ages of approximately 5 and 6 days, respectively (Fig. 2B). Overall, exposure to trace metals caused a postponement of the maturation of the animals, especially the microcrustaceans, that were observed in several previous investigations [31, 41, 42]. Trace metals at high concentration could negatively impair the respiratory function of daphnids [33] and inhibit their sodium uptake leading to an increased energy cost for maintenance [32], which may help to explain the postponement on the maturation.

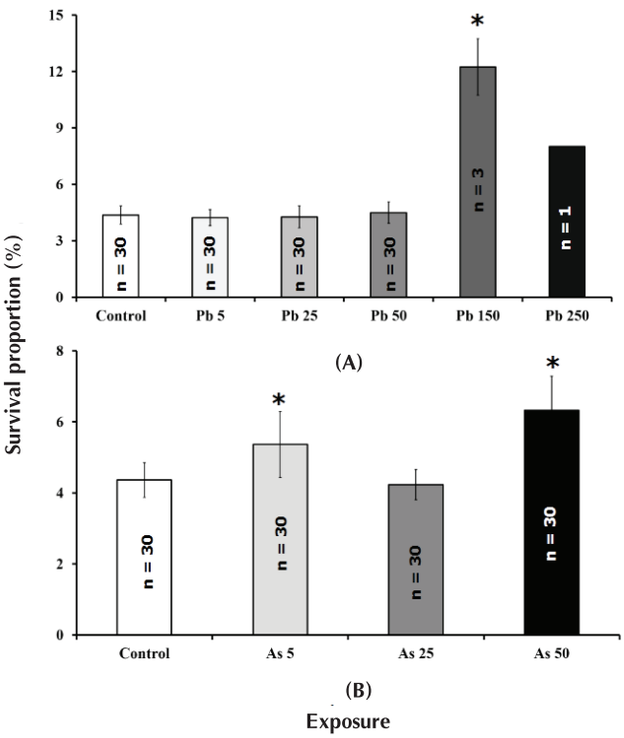

Fig. 2. Maturity age of *D. magna* (mean value ±SD) chronically exposed to Pb and As. Abbreviations given in Fig. 1. The asterisk indicates a statistically significant difference between the control and exposures by the Kruskal Wallis test (*: p≤0.001).

Effects of Pb and As on the reproduction of D. Magna

During the three weeks of incubation, the total number of offspring in the control was 3301, which was comparable to the total neonates in the exposures to Pb at low concentrations of 5, 25 and 50 μgl^{-1}. In contrast, the accumulative offspring in the 150 and 250 μgl^{-1} Pb exposures were only 42 and 5, respectively, which is much far lower than those in the control (Table 1). Regarding all the As exposures, a decline in the reproductive performance of *D. magna* was recorded. The As treatments (5, 25 and 50 μgl^{-1}) resulted in a reduction to 14, 35, and 7%, respectively, as compared to the total offspring in control (Table 1). That could be explained by the detrimental impacts on the organism mentioned above, such as the increase in mortality and postponement of the maturation. Moreover, the clutch size (the number of eggs per clutch) of the animals exposed to Pb at the highest concentration was smaller than those in the control (Fig. 3).

Table 1. Accumulative offspring of *D. magna* during the 21 experimental days. Abbreviations are the same as in Fig. 1.

	Control	Pb 5	Pb 25	Pb 50	Pb 150	Pb 250	As 5	As 25	As 50
Total neonates	3301	3503	3404	3358	42	5	455	1159	246

This observation in consistent with a previous study of Enserink, et al. (1995) [22] in which the reproduction of *D. magna* was negatively influenced by Pb. In detail, exposure to Pb at a concentration of 920 μgl^{-1} resulted in the loss of large number of eggs of the female *D. magna* and a decrease in embryo size. More seriously, several abnormal responses of the organism exposed to 50 μgl^{-1} of As were recorded, such as broken and adhesive eggs and neonatal mortality in the chamber (Fig. 4). These phenomena could significantly contribute to the decrease of the number of offspring laid by the female exposed to Pb or As.

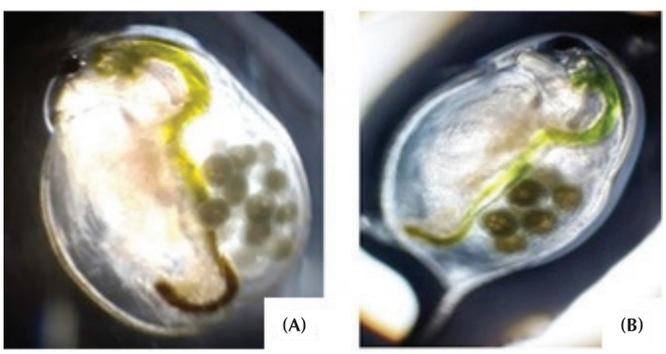

Fig. 3. The difference in the clutch size of female *D. magna* between the control (A) and exposure to 250 µg Pb l^{-1} (B).

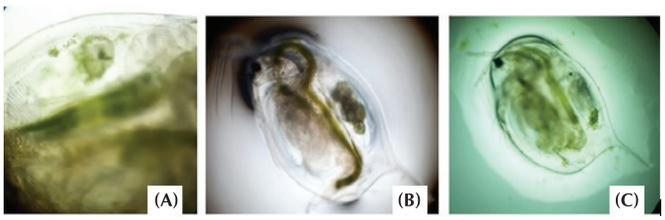

Fig. 4. Several abnormalities in *D. magna* exposed to 50 μgl^{-1} As; broken egg (A); adhesive eggs (B); death of neonate in the brood chamber of its mother (C).

Effects of Pb on the survival of the next generation of D. magna

When organisms from the mothers of the control samples were allowed to continue to rear in a metal-free medium (C/C), the survival rate was 83% (Fig. 5), which was within the requirement of the toxicity test according to APHA (2012) [29]. More seriously, the survival of the offspring of the Pb-exposed mothers incubated in both non-metal (E/C) and metal-containing medium (E/E) dramatically declined to 3 and 17%, respectively (Fig. 5). The survival rate of E/C and E/E was not significantly different but within a similar range to a chronic test according the APHA (2012). Recently, Araujo, et al. (2019) [24] showed that negative and adverse effects (e.g. malformations, Pb aggregation in neonates' dorsal region, reddish extremities, production of males, ephippia, aborted eggs, changes in egg colour) occurred through nine generations in both the temperate *D. magna* and tropical *D. similis* after long-term exposure to 50 μgl^{-1} of Pb. To our knowledge, this was the first investigation on the trans-generation effects of Pb on *D. magna* survival.

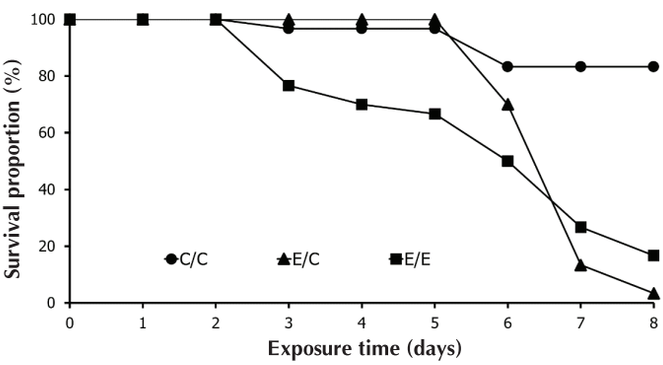

Fig. 5. Survivorship of the descendants of *D. magna* from the control and exposure to 50 μgl^{-1} of Pb during 8 experimental days (n=30 at the beginning). C/C: organisms laid in control and allowed to continue to incubate in the control medium; E/C: organisms laid in control and exposed to 50 μgl^{-1} of Pb; E/E: organisms laid in 50 μgl^{-1} of Pb and allowed to continue to culture in the same medium.

Conclusions

The results of this study proved that As and Pb at concentrations within the Vietnam guideline values for surface water safety (QCVN 08-MT:2015/BTNMT; column B1 for both Pb and As are 50 μgl^{-1}) caused several detrimental impacts on the life history traits of daphnids (e.g. survivorship, maturation, reproductive performance, and transgenerational survivorship). Therefore, more attention should be paid to the presence, distribution, and fate of trace metals in aquatic environment. Additionally, further investigations e.g. effects of a combination of more than two metals, bio-accumulation or mechanism of negative effects, are suggested in order to gain a greater understanding of the toxicity of these contaminants on aquatic organisms and ecosystems.

ACKNOWLEDGEMENTS

The authors would on like to thank Assoc. Prof. Dr. Pham Hong Nhat, University of Food Industry, for his valuable comments on this manuscript.

The authors declare that there is no conflict of interest regarding the publication of this article.

REFERENCES

[1] J.O. Reinhold, A.J. Hendriks, L.K. Slager, M. Ohm (1999), "Transfer of microcontaminants from sediment to chironomids, and the risk for the Pond bat Myotis dasycneme (Chiroptera) preying on them", *Aquatic Ecology*, **33(4)**, pp.363-376.

[2] P.K. Bharti (2012), *Heavy Metals in Environment*, Lambert Academic Publishing GmbH & Co. KG.

[3] D.A. Davis, D.M. Gatlin (1996), "Dietary mineral requirement of fish and marine crustaceans", *Reviews in Fisheries Science*, **4(1)**, pp.75-99.

[4] M. Jaishankar, T. Tseten, N. Anbalagan, B.B. Mathew, K.N. Beeregowda (2014), "Toxicity, mechanism and health effects of some heavy metals", *Interdisciplinary Toxicology*, **7(2)**, pp.60-72.

[5] U.S. Agency for Toxic Substances and Diseases Registry (ATSDR) (2007), *Toxicological Profile for Arsenic*, Atlanta, Georgia.

[6] P. Govind (2014), "Heavy metals causing toxicity in humans, animals and environment", *Journal of Chemical and Pharmaceutical Science*, **3(12)**, pp.172-174.

[7] W. Vincent, A. Hou, G.N. Meng (2015), "Source of lead pollution, its influence on public", *International Journal of Health, Animal Science and Food Safety*, **2(1)**, pp.18-31.

[8] K.S. Squibb, B.A. Fowler (1981), "Relationship between metal toxicity to subcellular systems and the carcinogenic response", *Environmental Health Perspectives*, **40**, pp.181-188.

[9] S. Wang, X. Shi (2001), "Molecular mechanisms of metal toxicity and carcinogenesis", *Molecullar and Cellular Biochemistry*, **222(1-2)**, pp.3-9.

[10] Z. Wang, L. Yao, G. Liu, W. Liu (2014), "Heavy metals in water, sediments and submerged macrophytes in ponds around the Dianchi Lake, China", *Ecotoxicology and Environmental Safety*, **107**, pp.200-206.

[11] M. Hassan, M.A.T.M.T. Rahman, B. Saha, A.K.I. Kamal (2015), "Status of heavy metals in water and sediment of the Meghna river, Bangladesh", *American Journal of Environmental Sciences*, **11(6)**, pp.427-439.

[12] E. Antico, S. Cot, A. Ribo, I. Rodriguez-Roda, C. Fontas (2017), "Survey of heavy metal contamination in water resources in the Municipality of Torola, El Salvador, through in situ sorbent extraction", *Water*, **9(11)**, Doi: 10.3390/w9110877.

[13] T.V. Tran, D.K. Nguyen, P.B. Nguyen, N.S. Nguyen, Q.T. Dinh, P.D. Nguyen, S. Emilie, H. Seunghee (2016), "Distribution of heavy metals in surface water, suspended particulate matter, sediment and clam (*Meretrix lyrata*) from downstream of Saigon-Dongnai river, Vietnam", *Journal of Science and Technology*, **54(2A)**, pp.207-213.

[14] T.H.M. Tran, K.G. Nguyen (2018), "Metal and metalloid concentrations in soil, surface water, and vegetables and the potential ecological and human health risks in the northeastern area of Hanoi, Vietnam", *Environ. Monit. Assess.*, **190(11)**, Doi: 10.1007/s10661-018-6994-7.

[15] P. Sharma, R.S. Dubey (2005), "Lead toxicity in plants", *Brazilian Journal of Plant Physiology*, **17(1)**, pp.35-52.

[16] J. Duffus (2002), "Heavy metals - a meaningless term? (IUPAC Technical Report)", *Pure and Applied Chemistry*, **74(5)**, pp.793-807.

[17] G. Flora, D. Gupta, A. Tiwari (2012), "Toxicity of lead: a review with recent updates", *Interdisciplinary Toxicology*, **5(2)**, pp.47-58.

[18] C.O. Abernathy, Y.P. Liu, D. Longfellow, H.V. Aposhian, B. Fowler, R. Goyer, R. Menzer, T. Rossman, C. Thompson, M. Walkes (1999), "Arsenic: health effects, mechanisms of actions and research issues", *Environmental Health Perspectives*, **107(7)**, pp.593-597.

[19] T. Yoshida, H. Yamauchi, S.G. Fan (2004), "Chronic health effects in people exposed to arsenic via the drinking water: dose-response relationships in review", *Toxicology and Applied Pharmacololy*, **198(3)**, pp.243-252.

[20] R. Sterner (2009), *Role of Zooplankton in Aquatic Ecosystems*, Encyclopedia of Inland Water, pp.678-688.

[21] L. Regaldo, U. Reno, S. Gervasio, H. Troiani, A.M. Gagneten (2013), "Effect of metals on *Daphnia magna* and cladocerans representatives of the Argentinean fluvial littoral", *Environmental Biology*, **35(4)**, pp.689-697.

[22] E.L. Enserink, M.J.J. Kerkhofs, C.A.M. Baltus, J.H. Koeman (1995), "Influence of food quantit and lead exposure on maturation in *Daphnia magna* evidence for a trade-off mechanism", *Functional Ecology*, **9(2)**, pp.175-185.

[23] C.S. Theegala, A.A. Suleiman, P.A. Carriere (2007), "Toxicity and biouptake of lead and arsenic by *Daphnia pulex*", *Environmental Science and Health*, **42(1)**, pp.27-31.

[24] G.S. Araujo, M.D. Pavlaki, A.M.V.M. Soares, D.M.S. Abessa, S. Loureiro (2019), "Bioaccumulation and morphological traits in a multi-generation test with two *Daphnia* species exposed to lead", *Chemosphere*, **219**, pp.636-644.

[25] S.H. Frisbie, R. Ortega, D.M. Maynard, B. Sarkar (2002), "The concentrations of arsennic and other toxic elements in Bangladesh's drinking water", *Environmental Health Perspectives*, **110(11)**, pp.1147-1153.

[26] Z. Vuković, M. Radenković, S.J. Stanković, D. Vuković (2011), "Distribution and accumulation of heavy metals in the water and sediments of the river Sava", *Journal of the Serbian Chemical Society*, **76(5)**, pp.795-803.

[27] Ministry of Natural Resources and Environment (2015), *National Technical Regulation QCVN 08-MT:2015/BTNMT dated December 21st, 2015 on surface water quality*.

[28] OECD guidelines for the testing of chemicals (1998), *Guideline 211: Daphnia magna Reproduction Test*.

[29] American Public Health Association, American Water Works Association and Water Environment Federation (2012), *Standard Methods for the Examination of Water and Wastewater (22nd Edition)*, Washington, DC.

[30] US Environmental Protection Agency (2002), *Methods for Measuring the Acute Toxicity of Effluents and Receiving Waters to Freshwater and Marine Organisms (5th ed. EPA-821-R02-012)*, Washington, DC.

[31] T.S. Dao, V.N. Le, B.T. Bui, V.K. Dinh, W. Claudia, T.S. Nguyen, C.T. Dao, V.D. Nguyen, T.H. To, L.S.P. Nguyen, T.G. Vo, T.M.C. Vo (2017), "Sensity of tropical micro-crustacean (*Daphnia lumholtzi*) to trace metals tested in natural water of the Mekong river", *Science of Total Environment*, **574(1)**, pp.1360-1370.

[32] M. Grosell, C. Nielsen, A. Bianchini (2002), "Sodium turnover rate determines sensitivity to acute copper and silver exposure in freshwater animals", *Comp. Biochem. Physiol. C Toxicol. Pharmacol.*, **133(1-2)**, pp.287-303.

[33] E.F. Pane, C. Smith, J.C. McGeer, C.M. Wood (2003), "Mechanisms of acute and chronic waterborne nickel toxicity in the freshwater cladoceran, *Daphnia magna*", *Environmental Science and Technology*, **37(19)**, pp.4382-4389.

[34] J.C. Amiard, C. Amiard-Triquet, S. Barka, J. Pellerin, P.S. Rainbow (2006), "Metallothioneins in aquatic invertebrates: their role in metal detoxification and their use as biomarkers", *Aquatic Toxicology*, **76(2)**, pp.160-202.

[35] K. Dinh Van, L. Janssen, S. Debecker, M. De Jonge, P. Lambret, V. Nilsson-Ortman, L. Beroets, R. Stocks (2013), "Susceptibility of a metal under global warming is shaped by thermal adaptation along a latitudinal gradient", *Global Change Biology*, **19(9)**, pp. 2625-2633.

[36] G.R. Reddy, M.R. Basha, C.B. Devi, A. Suresh, J.L. Baker, A. Shafeek, J. Heinz, C.S. Chetty (2003), "Lead induced effects on acetylcholinesterase activity in cerebellum and hippocampus of developing rat", *Int. J. Dev. Neurosci.*, **21(6)**, pp.347-352.

[37] S. Hernández-Flores, R. Rico-Martínez (2006), "Study of the effects of Pb and Hg toxicity using a chronic toxicity reproductive 5-day test with the freshwater rotifer *Lecane quadridentata*", *Environ. Toxicol.*, **21(5)**, pp.533-540.

[38] L. Janssens, K. Dinh Van, S. Debecker, L. Bervoets, R. Stoks (2014), "Local adaptation and the potential effects of a contaminant on predator avoidance and antipredator responses under global warming: a space-for-time substitution approach", *Evolutionary Applications*, **7(3)**, pp.421-430.

[39] M.C. Newman (2010), *Fundamentals of Ecotoxicology*, CRC Press, pp.214-218.

[40] M. Vaal, J.T. Van der Wal, J. Hermens, J. Hoekstra (1997), "Pattern analysis of the variation in the sensitive of aquatic species to toxicants", *Chemosphere*, **35(6)**, pp.1291-1309.

[41] L. Coniglio, R. Baudo (1989), "Life-tables of *Daphnia obtusa* (Kutz.) surviving exposure to toxic concentrations of chromium", *Hydrobiologia*, **188(1)**, pp.407-410.

[42] P.T. Tran, L.C. Do-Hong, T.S. Dao (2014), "Long-term impacts of copper and chromium on survivorship, maturation, fecundity and growth of *Daphnia magna*", *Vietnam J. Sci. and Tech.*, **52(3A)**, pp.309-315.

Doi: 10.31276/VJSTE.61(4).88-94

Remote sensing technology-based estimation of atmospheric CO_2 concentration to support efforts to reduce greenhouse gas emissions

Nguyen Hoang Tan Truong, Thi Cam Huong Le, Duong Xuan Bao Ha, Thi Van Tran*

University of Technology, Vietnam National University, Ho Chi Minh city

Received 2 August 2019; accepted 20 November 2019

Abstract:

Due to the strong development of agricultural and industrial activities in this day and age, the widespread use of fossil fuels has caused the concentration of greenhouse gases in the atmosphere to significantly increase. With a high concentration of greenhouse gases comes an increase in the temperature of the Earth, which contributes to the acceleration of climate change. This paper presents a remote sensing technique capable of determining atmospheric CO_2 concentrations from spectral radiation values obtained by satellite images, thereby simulating the distribution of CO_2 concentrations over the entire city of Ho Chi Minh. This study uses two data sources: Greenhouse Gases Observing Satellite (GOSAT) and Moderate Resolution Imaging Spectroradiometer (MODIS) images. Calculation results show that throughout the city the average CO_2 concentration in the first 6 months of 2019 has a minimum value of 360 ppm and maximum value of 410 ppm; these values change monthly and depend on the type of surface land cover. The highest concentration of CO_2 is found over areas of water, bare land, and urban land. On the contrary, over green areas and forests, the CO_2 concentration values are about 360-370 ppm. These results are a suitable reference available to support strategic planners focused on CO_2 emission management, and suggest that expanding urban vegetation to increase the absorption capacity of carbon will contribute to the reduction of the greenhouse effect.

Keywords: **CO_2, GOSAT, greenhouse effect, MODIS.**

Classification number: **5.2**

Introduction

In the 21st century, climate change is one of the most concerning issues to citizens all over the world. One of the many faces of this problem is global warming due to the greenhouse effect. Greenhouse gases, which are the main cause of the greenhouse effect, are able to absorb long-wavelength radiation of sunlight reflected from the Earth surface. Greenhouse gases include variety of gases, but CO_2 is the most important one. Therefore, the measurement of atomic CO_2 concentrations in the atmosphere is essential. Moreover, atomic CO_2 concentration is a required input for climate models, ecology models, and carbon cycle models. Climate change has become an international issue and global warming is one of many signs of this issue. Vietnam is one of the countries most impacted by this environmental problem. Despite accounting for only 1% of the atmosphere, greenhouse gases play a significant role as a cover of the Earth. This cover is responsible for preventing the escape of the heat from sunlight so that it stays inside the atmosphere longer and warms the planet. Without this blanket, the Earth's temperature would decrease by 30^0C. However, this blanket is becoming thicker because of human activities, such as burning of fossil fuels, changes in land use, and deforestation, all of which lead to the increase of global temperatures (Phan and Luu, 2006) [1].

Until now, there are three common research methods for estimating CO_2 according to the Intergovernmental Panel on Climate Change (IPCC). These methods include ground surveys, modelling, and remote sensing. It is crucial to expand the use of space technology in the study of atmospheric greenhouse gases because of its accuracy, efficiency, and low cost in observing and monitoring these gases, especially while ground-based measurements remain temporally and spatially limited. With the above advantages, the successful launch of Japan's GOSAT satellite increases the possibility of using remote sensing for the estimation of

*Corresponding author: Email: tranthivankt@hcmut.edu.vn

atmospheric CO_2 concentration.

In 2012, Guo, et al. [2] published research estimating the global CO_2 concentration based on MODIS images from NASA's TERRA satellite and GOSAT data. In 2014, J. Tao, et al. [3] calculated the CO_2 concentration for urban areas of Wu Han city by combining satellite images (Landsat 8) with on-site data (traffic density and CO_2 concentration) and used a Bayesian Network to analyse the correlational relationship between them. Then, the correlation was described by a regression model of CO_2 concentration, land cover, and traffic density. In 2015, M. Guo, et al. [4] applied a method from their previous 2012 research for a larger scale area, East Asia, with an improvement in validation. In this research, results from a regression model was compared to the measurements from three ground stations in the area. The comparisons demonstrated the largest difference was approximately +10.03 ppm and the overall fluctuation was 4.5 ppm. In 2018, J. Han, et al. [5] developed a model for estimating CO_2 concentrations of the Yellow River delta using the nightlight-based method. This model not only utilised remote sensing data (Landsat images) but also integrated statistical data such as fuel consumption and traffic surveys.

This paper presents the application of remote sensing to establish the spatial distribution of atmospheric CO_2 concentrations in Ho Chi Minh city, in order to support environment managers in the monitoring and reduction of impacts of the greenhouse effect.

Fig. 1. Study area.

The study area is Ho Chi Minh city, which has a decreasing altitude from North-West to South-East and the coast area, which has a mangrove forest site. The urban area of the city, one of the most ancient towns in Vietnam, is located in the centre and expands gradually and widely (Fig. 1).

Data and methods

Data

GOSAT data: contains values of XCO_2, which is the total column number of moles of CO_2 per mole dry air, is processed and stored as an HDF5 file. GOSAT data is classified into four levels: 1, 2, 3 and 4. Each level contains information from two different sensors and channels. The data used in this study was level 2 data, named as L2_FTS_SWIR, which contains the CO_2 information.

The GOSAT satellite completes a global coverage scan in 100 min. This satellite is equipped with a high accuracy instrument, which can observe 56,000 points on the Earth and is capable of tracking down a carbon source, as well as the path of greenhouse gases in the atmosphere. The total column of CO_2 described is the amount of CO_2 atoms in a unit of surface area.

MODIS data: in this study comes from a MODIS product, which is directly related to the processes of respiration and photosynthesis in plants. According to the study by [2], nine input parameters from MODIS products were selected to represent three main groups: 1) a variable representing the surface energy balance: LST (land surface temperature); 2) a group of four variables representing the physiological processes of plants: NDVI, EVI, LAI, FPAR; 3) a group of four variables representing the exchange of carbon between vegetation and the atmosphere: NPP, GPP, GN, NG. These acronyms are defined as NDVI: normalized differential index; EVI: enhanced vegetation index; LAI: the leaf area index; FPAR: fraction of photosynthetically active radiation; NPP: net primary production; GPP: the gross primary production; GN = GPP - NPP; and NG = NPP/GPP.

Data is collected daily and contains both the GOSAT data and MODIS data products. The temporal resolution of the MODIS products in this study is 8 days.

Method

The statistical methods used in this study, which are correlational analysis and linear regression modelling, establish the relationship between the XCO_2 parameter and the nine physical-ecological parameters that have a significant influence on the carbon cycle.

The nine parameters extracted from MODIS products, together with the GOSAT data, form a multi-variable regression equation, which is then used to estimate the atmospheric CO_2 concentration. The regression model is constructed from 24 sets of the 9 variables of MODIS products (independent variables), which include LST, NDVI, EVI, LAI, FPAR, GPP, NPP, NG, GN and CO_2 data of GOSAT (the dependent variable) during the years 2009-2015. The regression method is a stepwise regression, which gradually inputs from single to multi-variable in each step. During the stepwise regression process, statistical indicators are recorded to verify their correlational relationship with suitable tests.

The spatial and temporal resolution of the GOSAT CO_2 data is 2.5^0x2.5^0 and 6 h, respectively. MODIS products have the spatial resolution of 1 km and 0.5 km. Before being used for analysis, the data set must be converted to a resolution of 2.5^0x2.5^0. After completion of the regression model, atmospheric CO_2 concentration distribution modelling for any specific day will be built on MODIS products of that day. The data set is constructed by selecting days that have both GOSAT and MODIS data.

Results and discussion

Correlational analysis and linear regression model of CO_2 and nine parameters

The relationship between the independent and dependent variables commonly takes the form of a linear equation. For a lot of cases, in reality, the relationship can be non-linear, however, in order to simplify calculations, it is acceptable to approximate non-linear relationships as linear if there are no significant differences between the two. In some cases, when the relationship has been not yet identified, it can also be assumed as linear [6]. For this reason, to establish the relationship between dependent and independent variables in this study, the authors have used linear regression.

A scatter plot is used to demonstrate the pattern of the data sets (Fig. 2). The figure shows a correlational relationship. While XCO_2 and LST increase gradually with time, NDVI and EVI, which represent parameters related to vegetation, have the opposite pattern. This result can be explained due to the mutual effect of vegetation area decrease and temperature increase, which then leads to the reduction of photosynthesis followed by the rise of CO_2 concentration.

From the dataset of GOSAT and MODIS, a stepwise regression process allows a step-by-step observation of the relationship between each of the 9 dependent variables from MODIS and the independent variable XCO_2 from GOSAT. These observations provide comprehensive knowledge for future selection of input variables for the regression model. From these observations, the LST parameter is excluded, and the rest of the 8 parameters (EVI, NDVI, LAI, FPAR, GPP, NPP, GN, NG) have correlational relationship with XCO_2, as seen by the "sig" indicator, which denotes correlations lower than 1 or 5% (Table 1).

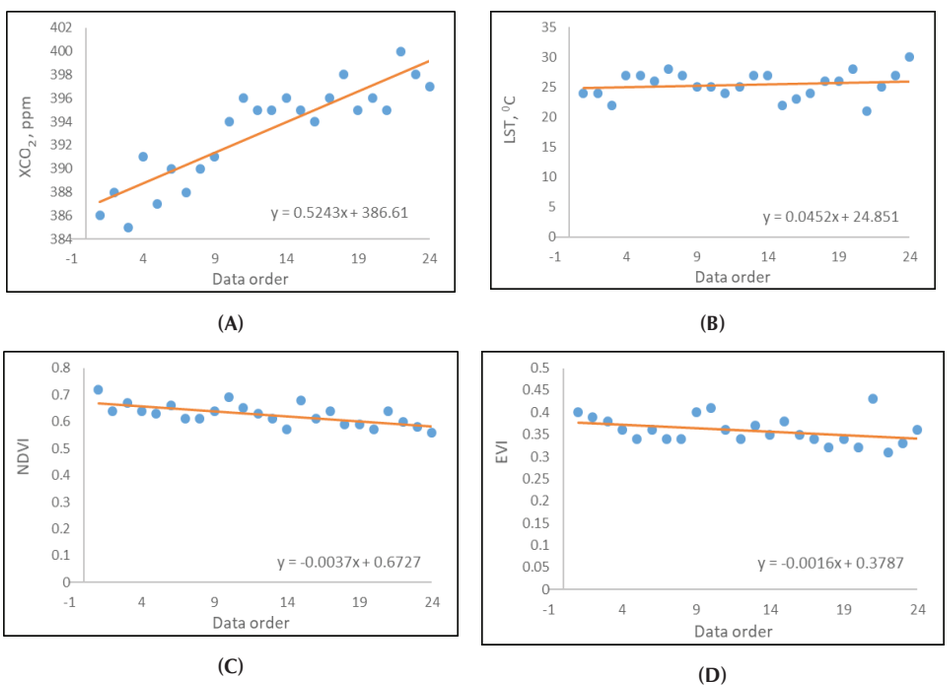

Fig. 2. Input data for models: (A) XCO_2, (B) LST, (C) NDVI, (D) EVI.

Table 1. Correlation Analysis.

	LST	EVI	NDVI	LAI	FPAR	GPP	NPP	GN	NG
XCO_2 - Sig	0.472	0.028 *	0.002 **	0.002 **	0.006 **	0.003 **	0.001 **	0.018 *	0.001 **

Note: **: 0.01 level; *: 0.05 level.

Despite the considerable correlation indicator of those variables, it does not mean that all of them will appear in the regression model. To accurately and completely verify these relationships, a stepwise regression is conducted. In the stepwise process, XCO_2 is the independent variable, and the 8 variables (EVI, NDVI, LAI, FPAR, GPP, NPP, GN, NG), which have been previously identified as having a correlation with XCO_2, are the dependent variables. Stepwise regression is helpful for eliminating variables that are unrelated and can potentially degenerate the regression equation. The result of this process is the below six equations which include single or multiple variables:

Independent variables: NPP ($R=0.618$, $VIF_{mean}=1$) (1)

Independent variables: NPP, EVI ($R=0.855$, $VIF_{mean}=1.2$) (2)

Independent variables: NPP, EVI, FPAR ($R=0.886$, $VIF_{mean}=4.5$) (3)

Independent variables: NPP, EVI, FPAR, NG ($R=0.922$, $VIF_{mean}=3.9$) (4)

Independent variables: NPP, FPAR, NG, LAI ($R=0.945$, $VIF_{mean}=16.4$) (5)

Independent variables: NPP, EVI, FPAR, NG, LAI ($R=0.947$, $VIF_{mean}=18.7$) (6)

Among these equations, the ones selected have the highest correlation index (R). Then, the VIF index is observed to consider the multicollinearity [6]. Multicollinearity is when there is a correlation between predictors (i.e. independent variables) with in a model. Its presence can adversely affect regression results. VIF stands for variance inflation factor. A rule of thumb for interpreting the VIF is as follows: if the VIF is 1, then they are not correlated; a VIF of 1-5 denotes moderate correlation; and a VIG>5 means they are highly correlated [7]. The results show that among the six equations, only equation (1) has a low correlation index (R=0.618), the others have a moderate correlation, and R varies from 0.85 to 0.95. Equations (3), (4), (5), and (6) have a high VIF index. This means that there is multicollinearity in these equations, which indicates that the dependent variables not only regress with the independent but also with each other. This phenomenon significantly influences the R index, making the R index artificially high. Thus, equation (3), (4), (5), and (6) must be eliminated, which leaves the remaining equations (1) and (2). Between the two equations, equation (2) has a higher R index of R=0.855, compared to R=0.618 for equation (1). Consequently, equation (2) is selected as the final model for the estimation of the atmospheric CO_2 concentration of the study area. The form of equation (2) is given below:

$$XCO_2 = 400.275 - 0.042 * NPP - 52.72 * EVI \quad (7)$$

Establishing the map of atmospheric CO_2 concentration distribution

Equation (7) is used to model the distribution of the atmospheric CO_2 concentration for the study area. The NPP and EVI parameters for the study area are derived from the MODIS products with a resolution of 0.5 km. This paper models the CO_2 concentration during the period of the first six months of 2019, on the days that MODIS data available. Fig. 3 presents the model.

The model demonstrates that the 390-400 ppm region is mostly located in an urban area, which has sparse and unevenly distributed vegetation. The 380-390 ppm region appears in the suburbs of Binh Chanh, Nha Be, District 9, Hoc Mon, and Cu Chi, which is mostly covered by agriculture. The evergreen mangrove forests caused the CO_2 concentration of the Can Gio district to fluctuate from 360 to 370 ppm, but remained lower than the other areas.

During the peak of the dry season, February - April and the first half of May, the red area denoting 390-400 ppm CO_2 is found around the downtown area, which accounts for 20-25% of the city area. At the beginning of June, the rainy season begins and thus the vegetation grows and thrives. Consequently, there is an increase of photosynthesis and the CO_2 concentration reduces, which is seen by the shrinking red region.

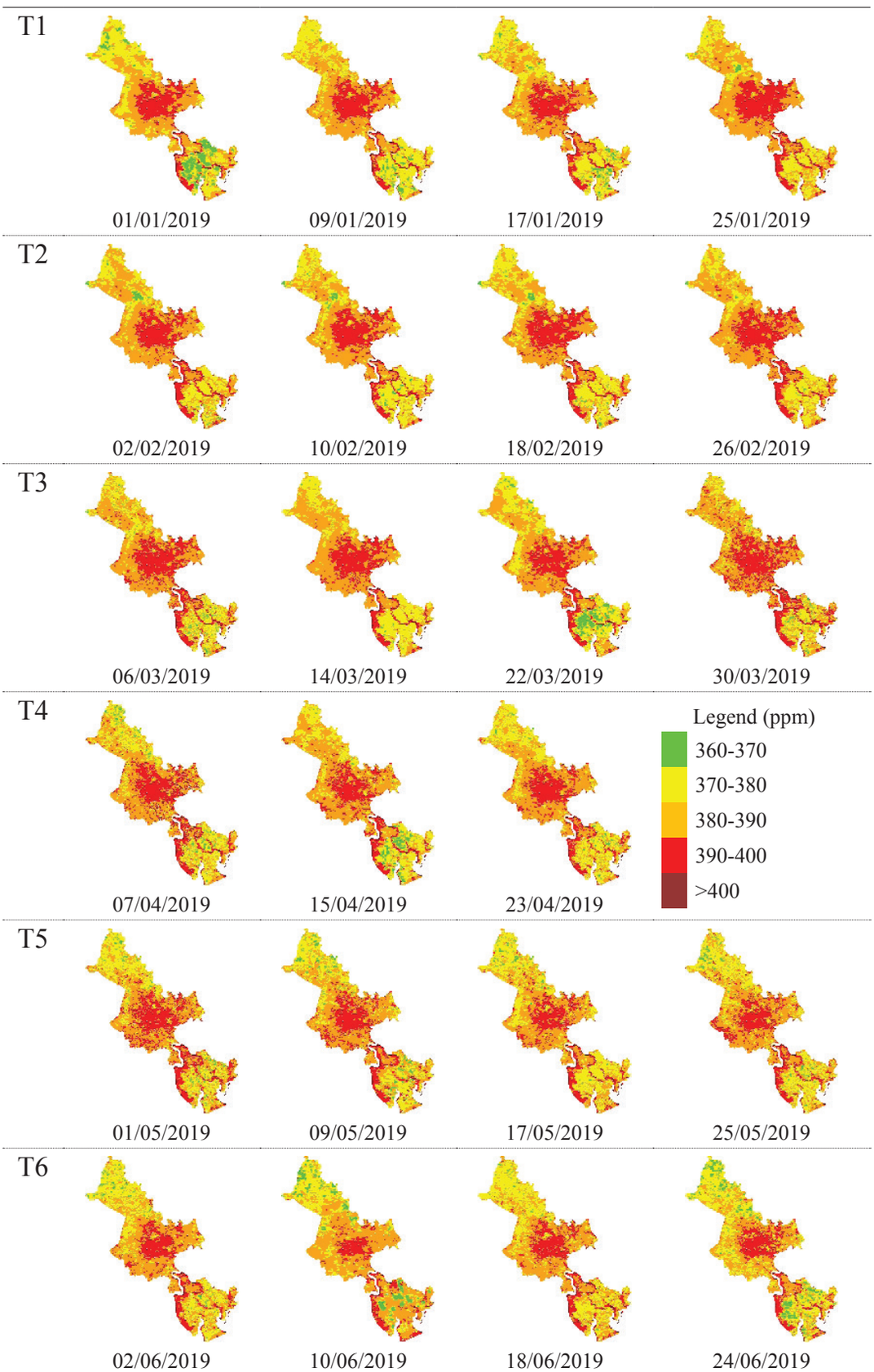

Fig. 3. Spatial distribution of atmospheric CO_2 concentration in first half of 2019.

Figure 4 shows the extrema of the CO_2 concentrations found in the study area during first half of 2019. The minimum line has high fluctuations and a downward trend starting from the beginning of dry season to the beginning of wet season. The lowest CO_2 concentration of Ho Chi Minh city is 365 ppm. Meanwhile, the maximum line has a more stable pattern around 405.66 ppm, which increases 0.1 ppm every 8 days (along with the MODIS data). Among of them, April has the highest CO_2 concentration of approximately 410 ppm. In Ho Chi Minh city, April is characterized as the hottest month of the year, when the majority of agriculture is uninhibited, causing heightened emissions of CO_2 from the land to the atmosphere.

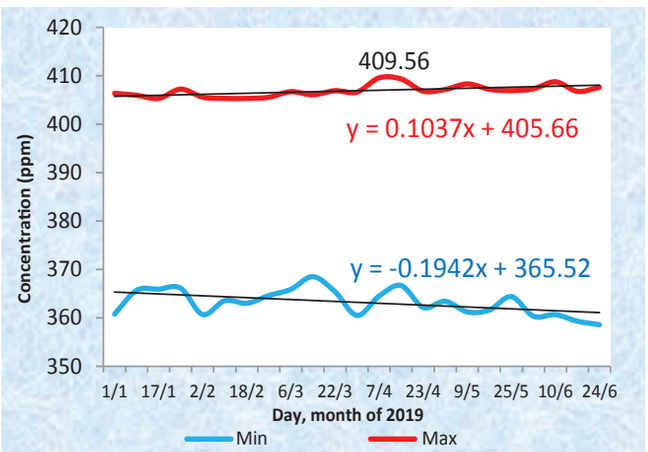

Fig. 4. Extrema of CO_2 concentration in the first 6 months of 2019.

Figure 5 and Table 2 represent the average concentration of CO_2. It can be seen that in the first half of 2019, the average CO_2 concentration of the city is 384 ppm and has an unstable pattern. Meanwhile, the monthly minimum average decreases from January (beginning of dry season) to June (beginning of rain season), ranging from 360 to 365 ppm. The maximum average CO_2 concentration shows the opposite pattern, with values between 405 and 408 ppm.

Figure 6 and Table 3 indicate the proportion of the study area at different concentration ranges. The range of 370-400 ppm CO_2 comprises 20 to 60% of the study area. Specifically, the 380-390 ppm range covers the majority of the study area, which accounts for nearly half of the city, 42 to 59%. The others two ranges, 360-370 ppm and >400 ppm, cover the smallest areas, which vary from 0.2 to 7% of the total study area.

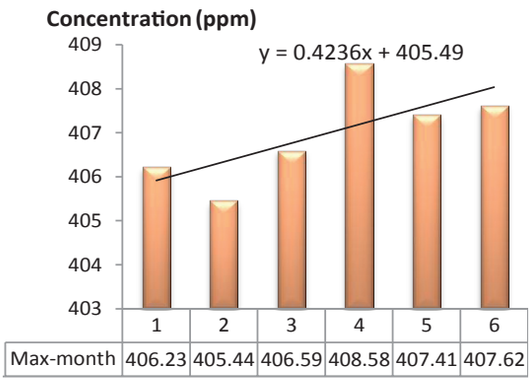

Fig 5. Extreme values of CO_2 concentrations averaged monthly for the first 6 months of 2019.

Table 2. Statistics of extreme data in the first half of 2019.

Month	Min-month	Max-month	Mean-month
1	364.62	406.23	383.77
2	362.96	405.44	384.70
3	365.07	406.59	384.84
4	364.44	408.58	384.33
5	362.65	407.41	383.97
6	359.72	407.62	383.16
Average	363.24	406.98	384.13

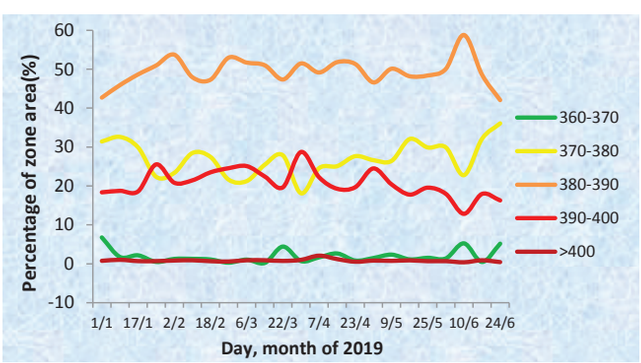

Fig 6. Percentage of total study area for CO_2 concentration ranges in Ho Chi Minh city during the first 6 months of 2019.

Table 3. Percentage of total study area for CO_2 concentration ranges during the first 6 months of 2019.

CO_2 concentration area (ppm)	Min (%)	Max (%)
360-370	0.21	6.76
370-380	18.11	36.08
380-390	42.05	58.79
390-400	12.83	28.72
>400	0.38	2.08

Validation

This paper successfully constructs a multi-variable regression model for the estimation of atmospheric CO_2 concentration of Ho Chi Minh city, based on two data sources: CO_2 from GOSAT and MODIS products. The GOSAT satellite is the first world satellite programmed to observe two greenhouse gases, CO_2 and CH_4. It is from the collaboration efforts of Japan Ministry of Environment, Japan National Institute of Environment Studies, and Japan Aerospace Exploration Agency. It has remained on duty since 2009. From that moment until now, GOSAT continually provides CO_2 data, which is widely used by researchers from every corner of the world. This data has been validated as global coverage data, has high accuracy and precision, and an error range of only 1 ppm to 4 ppm [4].

The MODIS products are used as a bridge in this study, where a physical-ecological equation is developed to interpret the atmospheric CO_2 concentration in a higher resolution than what is currently available. The input variables represent surface-energy balance, and the relationship between the physical-ecological characteristics of vegetation and the exchange of carbon between land and atmosphere. MODIS products appear frequently in academic research and is a credible resource. This approach wipes out the disadvantages of absent ground-based measurement stations, thus, provide a method for observing and quantifying the CO_2 concentration. The limit of this paper is the lack of in-situ measurement validation, which is also the general problem of the Vietnamese monitoring system. This limit inspires the authors to improve future studies.

Conclusions

The method of combining remote sensing with statistical models to calculate the atmospheric CO_2 concentration is suitable for the conditions of Vietnam since there is a lack of ground measurements of CO_2. Currently, environmental management only focus on carbon monoxide CO. This paper successfully models the distribution of CO_2 concentration of Ho Chi Minh city during a period spanning the first 6 months of 2019. This result shows that the monthly average CO_2 concentration varies from 360 ppm to nearly 409 ppm. Unfortunately, this range is within the warning range given by international scientists that stated the global CO_2 has crossed 350 ppm and is continually increasing over 400 ppm. The resulting CO_2 concentration depends accordingly on the type of land cover, where lower concentrations exist in areas that have dense vegetation and higher concentrations are found in areas with sparse vegetation. Therefore, in effort to reduce atmospheric CO_2 concentration and the impacts of climate change, especially in urban areas, increased vegetation areas play a central role.

The authors declare that there is no conflict of interest regarding the publication of this article.

REFERENCES

[1] Phan Minh Sang and Luu Canh Trung (2006), *Carbon Absorption*, Handbook of Forestry.

[2] M. Guo, X. Wang, J. Li, K. Yi, G. Zhong, H. Tani (2012), "Assessment of global carbon dioxide concentration using MODIS and GOSAT data", *Sensors*, **12**, pp.16368-16389.

[3] J. Tao, Y. Zhou, W. Wu, L. Yu (2014), *Estimating Carbon Dioxide Concentrations in Urban Areas from Satellite Imagery Using Bayesian Network*, The Third International Conference on Agro-Geoinformatics, Beijing, pp.1-7.

[4] M. Guo, J. Xu, X. Wang, H. He, J. Li, L. Wu (2015), "Estimating CO_2 concentrations during the growing season from MODIS and GOSAT in East Asia", *International Journal of Remote Sensing*, **36(17)**, pp.4363-4383.

[5] J. Han, X. Meng, H. Liang, Z. Cao, L. Dong, C. Huang (2018), "An improved nightlight-based method for modelling urban CO_2 emissions", *Environmental Modelling and Software*, **107**, pp.307-320.

[6] Nguyen Tran Que and Vu Manh Ha (2008), *Economic Statistics*, Publisher of VNU Hanoi.

[7] https://www.statisticshowto.datasciencecentral.com/variance-inflation-factor/, Accessed in 09/26/2019.

Table of contents in 2019

Vietnam Journal of Science, Technology and Engineering (VJSTE): Manuscript Template

General Instructions on using this template and submitting a manuscript to VJSTE: Thank you for preparing a manuscript for submission to VJSTE. Using this template, or following the guidelines below, will help us in processing your paper. Our goal is to be able to identify each section of your manuscript so that we can accurately record the title, authors, abstract, etc. and also be able to enrich it by including reference links and an accurate layout.

You can submit your paper at http://vietnamscience.vn

So that we can identify the parts of your paper, and even if you do not use our template, please begin each section with the specific key words listed below. Please do not use paragraph breaks in the title, author list, or abstract.

Title

Authors

Affiliations

Abstract

One Sentence Summary

Main Text

Acknowledgements

References

Several of these headings are optional, for example, not all papers will include a one-sentence summary, figures or tables.

Please use the .docx format (all version after Word 2007).

More specific formatting instructions are provided in the actual template, which follows.

Title: How to Format a Science Paper (replace with your real title)

Authors: The author list should be one single paragraph (no breaks). Authors should be listed by first name or initial followed by last name and separated by commas. Use superscript numbers to link affiliations, and symbols *†‡ for author notes. For example, X. Jones[1]*, P. Smith[1,2]

Affiliations:

[1]Affiliations should be preceded by superscript numbers corresponding to the author list, and each affiliation should end with a period.

[2]Each affiliation should be a separate paragraph.

*Correspondence to: include the email addresses or telephone number of the corresponding author(s). Please use the asterisk (*) symbol for the corresponding author information.

Abstract: The abstract should be about 100-150 words, and organized in this structure: An opening sentence that sets the question that you address and is comprehensible to the general reader, background content specific to this study, results, and a concluding sentence. It should be one paragraph only.

One Sentence Summary: A brief summary of the main result of your paper, without excessive jargon and less than 150 characters.

Main Text: In general, this should include a brief (1-2 paragraph) introduction, followed by a statement of the specific scope of the study, followed by results and then interpretations. Please avoid statements of future work or claims of priority, and avoid repeating the conclusions at the end.

All of the Figures and Tables should be cited in order (which should be cited as, for example, figure S1, and table S1). You can include page breaks if you would like to place the figures within the text.

Subheads: These can be included in Research Articles or Reviews and should be brief.

Equations can be included. We do not recommend using the native Word 2007, 2008, 2010 or 2011 equation editor. This can in some cases produce less reliable MathML, the online markup language we use, which may result in display errors. Instead, use the legacy equation editor in word (Insert menu; select insert object; select word equation) or use Mathtype (recommended). If you enter equations in simple LaTeX, check that they will convert accurately (Word 2007 and higher can convert simple LaTeX equations).

Fig. #: (Begin each figure caption with a label, "**Fig. 1.**" for example, as a new paragraph.).

Fig. 1. The figure caption should begin with an overall descriptive statement of the figure followed by additional text. They should be immediately after each figure. Figure parts are indicated with capital letters (**A**). If you prefer, you can place both the actual figures and captions logically through the text near where they are cited rather than at the end of the file (but not both). If a paragraph in the main text begins with the name of a figure, write out "Figure" in full (e.g., <para>"Figure 1 shows….").

Fig. 2. You can place graphics above each equation as part of this file.

Table #: (Begin each table caption with a label "**Table 1.**", etc.) as a new paragraph.

Table 1. Start this caption with a short description of your table. Format tables using the Word Table commands and structures. Do not create tables using spaces or tabs characters.

Acknowledgments: The acknowledgments should include a statement about where the data reported in the paper are presented, archived, or available. If in an archive, include the accession number or a placeholder for it. Please also include relevant funding information such as grant numbers and funding agencies. You can also include a statement of author contributions here. The acknowledgements can be multiple paragraphs.

References:

References should be cited in bracket with a number [1]. Multiple reference citations are separated by commas [2, 3] or if a series, dashes [4-6].

References are listed in numerical order, and in the same order in which they are cited in text. The reference list should include all and only those references you have cited in the text. The reference list appears at the end of the paper.

Please include the above heading "References".

Please do not mix in references with explanatory notes.

The reference consist of: Family name(s) and initials of all authors (year of publication), "Titles of journal articles" (optional), *Title of journal, book or other publication*, **volume(number)**, page numbers.

Example of a reference list:

[1] T. Binzoni, T.S. Leung, D. Boggett, D.T. Delpy (2002), "A new near infrared laser-Doppler flowmeter for deep tissue perfusion monitoring", *MAGMA*, **14,** pp.74-75.

[2] T. Binzoni, T.S. Leung, D. Boggett, D.T. Delpy (2003), "Non-invasive laser Doppler perfusion measurements of large tissue volumes and human skeletal muscle blood RMS velocity", *Phys. Med. Biol.*, **48(1)**, pp.2527-2549.

ISSN 2525-2461

Vietnam Journal of Science, Technology and Engineering

DECEMBER 2019 • VOL.61 NUMBER 4

EDITORIAL OFFICE

113 Tran Duy Hung Str., Cau Giay Dist., Hanoi

Tel: (84.24) 39436793; Fax: (84.24) 39436794

Email: khcnvn@most.gov.vn

Website: vietnamscience.vn

PUBLICATION LICENCE

No.1153/GP-BTTTT 26th July 2011

No.2528/GP-BTTTT 26th December 2012

No.592/GP-BTTTT 28th December 2016